

**Structure formation, crystallization and dynamics
in different semicrystalline polymers**

Dissertation

zur Erlangung des Doktorgrades der Naturwissenschaften
(Dr. rer. nat.)

der

Naturwissenschaftlichen Fakultät II
Chemie, Physik und Mathematik

der Martin-Luther-Universität
Halle-Wittenberg

vorgelegt von

Frau Mareen Schäfer
geb. am 29.07.1991 in Regensburg

Erstgutachter: Prof. Dr. Kay Saalwächter
Zweitgutachter: Prof. Dr. Jörg Kreßler
Drittgutachter: Prof. Dr. Michael Ryan Hansen

Tag der öffentlichen Verteidigung: 15.07.2021

Contents

1	Introduction	3
1.1	Crystallization in polymer systems	3
1.2	Structural and dynamical analysis	7
1.3	Aim and outline	8
2	Scientific Background	10
2.1	Description of a polymer chain	10
2.2	Dynamics in an entangled polymer systems	12
2.3	Crystallization of semicrystalline polymers from the melt	14
2.3.1	Nucleation of polymer crystallites	14
2.3.2	Crystal growth and structure formation	16
2.3.3	Role of entanglements	18
2.3.4	Parameters influencing the semicrystalline morphology	20
2.4	Structure formation in bimodal M_w -distributed systems	22
2.5	Crystallization of statistical copolymers	24
2.6	Structure formation of comb-like polymers	27
3	Experimental Methods	29
3.1	Fundamentals of nuclear magnetic resonance (NMR)	29
3.1.1	Nuclear spin	29
3.1.2	Spin interactions	32
3.1.3	Relaxation	35
3.1.4	Motions	39
3.2	Static ^1H time-domain NMR	41
3.2.1	FID experiment in a multi-phase system	41
3.2.2	Saturation recovery	43
3.2.3	Proton multiple quantum (MQ) NMR	44
3.3	^{13}C structural NMR	48
3.3.1	Polarization transfer	48
3.3.2	Torchia method for T_1 measurement	51
3.3.3	DIPSHIFT	52
3.3.4	Spin Diffusion	53
3.4	Polarized optical microscopy	55
4	Results	58
4.1	Paper I: Intracrystalline dynamics in oligomer-diluted PEO	60
4.2	Paper II: Asymmetric co-unit inclusion in statistical copolyesters	67
4.3	Paper III: Structure and dynamics in a polymorphic nanophase-separated stiff comblike polymer	79

5 Summary, conclusions and outlook	90
A So far unpublished results	94
A.1 Estimation of a reference entanglement density for molten PCL by evaluating the amplitude of the OACF at τ_e	94
A.2 Effects on crystallization and entanglement density caused by oligomer dilution of poly(ϵ -caprolactone)	97
A.3 Effect of the crystallization conditions on the pseudo-eutectic behavior in statistical PBSA copolyesters	107
Bibliography	116
Remarks on the format of citations	128
Erklärung	129
Acknowledgements	130
Publications	132
Curriculum vitae	133

1 | Introduction

1.1 Crystallization in polymer systems

Synthetic polymers are built from numerous monomer units linked by covalent bonds to organic long-chain molecules [1]. The first man-made plastic material, nitrocellulose, was produced by Alexander Parkes as early as 1856 [2]. However, the commercial production of polymer systems began only 50 years later with the development of Bakelite (polyoxybenzylmethyleneglycolanhydride) in 1907 and the start of technical production in 1910 [3, 4] as well as the manufacturing of polyvinylchlorid (late 1920s), polystyrene (1930) and polyethylene (1933). The discovery of polyethyleneterephthalate (PET) in 1941 [5] initiated the mass production of synthetic polymers in the 1940s to 1950s [6]. During that time-period Hermann Staudinger reported that the properties of synthetic macromolecules strongly depend on their molecular weight, chemical structure [1, 7] and their ability to crystallize [8]. The understanding on a microscopic level of the structure formation, crystallization and the dynamics of the various polymeric systems is crucial to tune the material properties as well as the processability, a possible biodegradability [9, 10] and thus the end-use application [11].

The monomeric unit and the microstructure of the polymer chain is an important point regarding the final properties of the product. A polymer constituted by only one repeat unit is called homopolymer. If two different repeat units are covalently joined to form a single polymer chain one speaks of copolymers.[12] Depending on the chemical composition of each monomer unit as well as the sequence in which the building blocks are bonded, the properties of the final copolymer morphology diverge [13, 14]. Another important feature to tune the properties of either homo- or heteropolymers is the polymer architecture, e.g linear, star or comb-like [15]. Randomly branched chains, as in the case of low density polyethylene, are important for the manufacturing of bottles and packaging material [15]. For repeat units with non-symmetric substitution patterns, e.g. CH-CH_3 in polypropylene, the tacticity, which means the stereochemical connectivity of the groups, can influence a potential polymer crystallization process [15, 16]. Depending on the flexibility of the polymer chain one also distinguishes flexible and stiff macromolecules. In the former, the building blocks of the polymer chain can have conformations with bond angles diverging from 180° and

are therefore capable of forming entanglements in the melt. When crystallized from the isotropic melt, the entanglements hinder the complete crystallization of the flexible polymers, resulting in a semicrystalline morphology.[17, 18] Stiff macromolecules are characterized by a collinear connection of the stiff monomeric units, with less entanglements in the melt, but capable of forming ordered liquid-crystalline solutions above their melting temperature [19–21]. Appending flexible side chains of various lengths to the otherwise stiff chain increases the flexibility, enhances the processability and results in a reduction of the melting point [17]. The final structure of these comb-like polymers, for example poly(1,4-phenylene 2,5-dialkoxyterephthalate), can often be described by a layered two-phase system [22].

The ability of polymers to crystallize depends on the regularity of the chemical composition as well as the configuration along the chain and the presence of long sequences of monomeric units [23]. Branched polymers, or polymers with side-chains as well as heteropolymers, especially with random sequence configuration, have a decreased ability to crystallize [24–26]. The properties, which influence the structure formation of crystallizable macromolecules into a two-phase system of rigid and amorphous regions, are not yet fully understood. In this work the structure formation, crystallization and the relevant dynamics will be investigated for several polymeric systems.

The structure formation of the semicrystalline morphology of flexible polymers crystallized from the entangled melt is one main research focus in this thesis. The semicrystalline structure, when crystallized from the coiled conformation in the melt, can be described on a mm-to- μm - scale by the formation of spherulites, which grow radially from a nucleation point and reach diameters from several $\sim 100 \mu\text{m}$ up to cm. On a sub- μ -scale the structure is characterized by ordered crystalline lamellae, with polymer chains in a helical conformation, which are separated by disordered, more mobile amorphous regions.[18] The crystallization process is depicted schematically in Figure 1.1.

Several crystallization theories attempt to explain the microscopic processes which cause the formation of the observed semicrystalline morphologies with a certain crystal and amorphous thickness. The established Hoffman-Lauritzen theory [27], the rate-theory model by Sadler and Gilmer [28] or the intramolecular nucleation model [29] focus in their explanations on the derivation of a growth rate equation and the resulting formation of ordered lamellae with a defined crystal thickness. The growth kinetics are limited by either an entropic or enthalpic barrier caused by secondary nucleation.[30] Other approaches attempt to explain the formation of a certain lamellae thickness as a step-wise process, as a result of reorganization processes, such as intracrystalline dynamics or the formation of a mesophase during crystallization [31–37]. However, in most models the influence of the topological

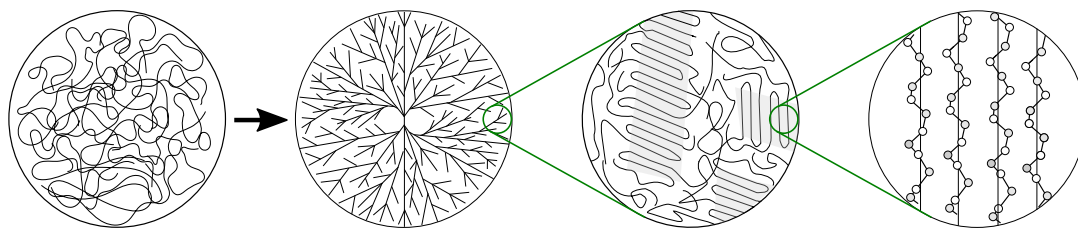


Figure 1.1: Schematic representation of a the macroscopic, microscopic and crystalline structure of a flexible polymer crystallized from the melt. Adapted from reference [18].

constraints, given by the entanglements in the amorphous phase are, with a few exceptions [32, 34, 36], not taken into account. More recent theoretical and experimental studies indicate that entanglements influence the growth process [36] and structure [34, 38] of the crystalline lamellae and are also considered as a limiting factor for the final crystal thickness [39]. Especially the density of entanglements in the amorphous phase and melt is regarded as a controlling factor of the structure formation [40] and the early stages of the crystallization process [41]. According to molecular dynamics simulations, regions with less entanglements crystallize faster and form thicker lamellae [42].

Another crucial point that influences the semicrystalline morphology, is the existence or absence of an intracrystalline mobility and a related crystalline-amorphous large-scale diffusion in so-called crystal-mobile polymers [16, 43, 44]. The presence of this α_c -relaxation in semicrystalline polymers leads to a higher crystallinity [45] and a morphology with a well-defined amorphous thickness [44]. In contrast, crystal-fixed polymers form stable crystals with a defined thickness undergoing steady reorganization during heating [46]. It is assumed that the morphology of the model crystal-mobile polymer poly(ethylene oxide) (PEO) is controlled by the amorphous phase rather than the preselected crystal thickness, the role of the entanglement density in the melt prior to crystallization and in the amorphous phase is not yet clear [44].

In more complex polymeric systems, such as copolymers with a random comonomer distribution, additional factors influencing the formation of a semicrystalline morphology are present. The crystal formation is potentially hindered by the random occurrence of minority co-units, often resulting in a reduction in the overall crystallinity and crystal thickness with increasing comonomer content. Thus, the structure formation strongly depends on a possible inclusion of co-units from one comonomer into the crystal structure of the other. One distinguishes between isomorphism, isodimorphism and total exclusion of the minority component from the crystal.[47] All three crystallization scenarios are depicted in Figure 1.2. In isomorphous copolymers both comonomers are capable of forming one joint crystal structure for the complete composition case, but only if strict molecular requirements, such as similar

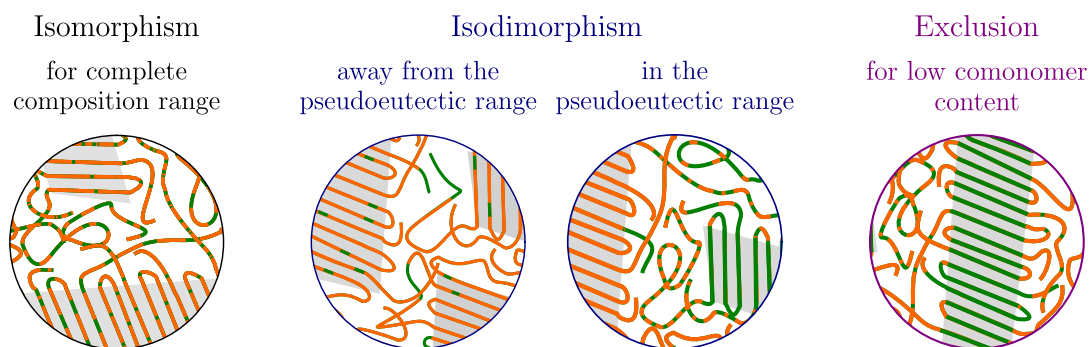


Figure 1.2: Schematic representation of the semicrystalline morphology in random copolymers with isomorphous and isodimorphous behavior and for total exclusion. For isodimorphism the different morphologies for compositions close to and away from the pseudoeutectic range are shown. Isomorphism and exclusion are depicted with copolymers having a low comonomer content. Increasing the comonomer content would subsequently lead to an amorphous polymer in case of total exclusion.

and compatible chain conformations, lattice symmetry, unit cell parameters, total miscibility in the melt and a similar rate of crystallization, are fulfilled. The final semicrystalline properties can be described by a linear extrapolation of the properties of the pure homopolymers.[13, 14] In most copolymers these strict requirements are not fulfilled and either a complete exclusion of one component from the crystal of the second comonomer or only a limited inclusion (isodimorphism) is observed. In the first case the copolymer will not be able to crystallize for nearly equimolar compositions and the thermal properties will be strongly depressed for compositions with a low comonomer content. In the isodimorphic case, where the comonomer structures are sufficiently similar, the copolymers are capable of crystallizing in the complete composition range, but the final properties are correlated with the amount of included co-units.[13, 25] For isodimorphic copolymers with compositions close to the pseudo-eutectic range, most often around equimolar compositions, both co-units are capable of forming their own separate crystallites. The amount of included co-units in copolymers can also be tuned by changing the thermal history of the copolymer, by e.g. non-isothermal and isothermal crystallization from the melt.[26] Another class of polymer system is represented by comb-like polymers with long side-chains attached to the backbone chain. These polymers, which are neither branched nor linear, often have stiff backbones with ring-like units which tend to form stacks, resulting in a layered, nanophase-separated structure, where the long side chains (often methylene sequences) aggregate and form nanodomains.[17, 48] One differentiates between four different nanophase-separated systems [49] which are shown schematically in Figure 1.3; if both main- and side-chains are crystalline one speaks of a fully crystalline (FC) system, as for example in modification B in the polymorphic system PPAOT [50]. Model systems where either the side-chains or the

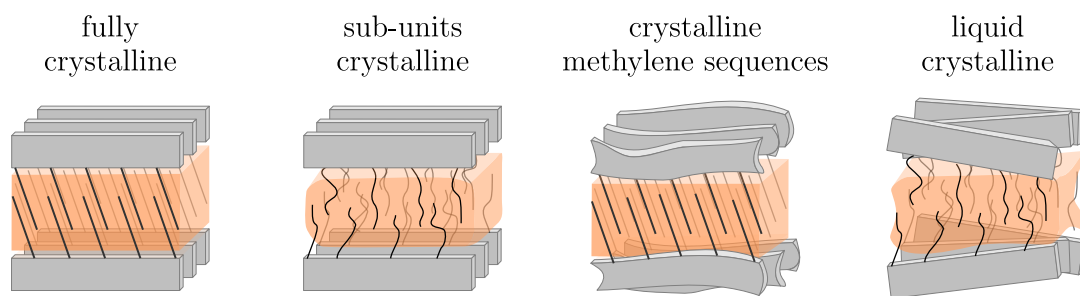


Figure 1.3: Schematic representation of comb-like polymers in the four known model systems: Fully crystalline, sub-units crystalline, crystalline methylene sequences and liquid crystalline. Redrawn from reference [49].

ring-like sub units of the main-chains are in a disordered state are referred to as sub-unit crystalline (SUC) and crystalline methylene sequences (MC), respectively. The liquid-crystalline state (LC) is characterized by a long-range order of the nanophase-separated layers, but without any crystalline order.[49] The formation of these model systems depends on the chemical structure of the rigid backbone [51], the side chain length [17, 22, 52, 53], the molecular weight [54] and the thermal history in polymorphic systems [17, 50].

1.2 Structural and dynamical analysis

Nuclear magnetic resonance (NMR) spectroscopy utilizes the intrinsic property of a *spin* which most atomic nuclei possess. Isotopes are NMR active if they have a nonzero ground state nuclear spin. Atoms with a nuclear spin of $1/2$, such as hydrogen, phosphorus and the rare carbon isotope ^{13}C are of major relevance in the investigation of organic materials. NMR spectroscopy allows to obtain information about the chemical structure as well as constraints and molecular or segmental dynamic processes of the samples. The range of available NMR methods is a wide field with different experimental approaches for solutions as well as solid-state materials. In solid-state materials dynamical processes with correlation times in the range from nanoseconds to seconds can be analyzed. To investigate the amplitude of reorientations, the number of interchanging sites and the correlation function of motion, anisotropic NMR interactions such as dipole-dipole interactions or anisotropic chemical shifts are utilized.[55] However, the dipole-dipole couplings in solid-state materials also cause a loss of one major advantage of NMR: the chemical selectivity and thus also molecular resolution. Therefore, it is advisable to additionally detect information of organic solids with regard to their structure with high-resolution obtained under magic-angle spinning (MAS).[56]

In semicrystalline polymers the investigation of the two-phase system with a rigid and mobile phase, as well as the coiled entangled structure in the melt or the liquid-

crystalline state in comb-like polymers, requires the combination of solid-state as well as solution-state NMR experiments. With dynamical filters the rigid and mobile phases can be selectively detected and analyzed. Solution-state NMR experiments allows for the detection of highly mobile dynamics by taking advantage of the J -coupling. The possibility to selectively analyze the structure and dynamics in solid as well as solution states, with a dynamical range that spans more than 10 orders of magnitude, makes NMR spectroscopy a powerful tool. It allows to analyze microscopic properties of polymers on a molecular level which is otherwise inaccessible by any other current method for the given combination.[55] Additional information regarding the dynamics of crystallization are obtained via optical polarization microscopy, small- and wide-angle X-ray scattering and differential scanning calorimetry (DSC).

1.3 Aim and outline

The aim of the work presented in this thesis is to deepen the understanding of the dynamics in the polymer systems, the structure formation and crystallization—especially for flexible, semicrystalline polymers. A strong focus lies on the effect of entanglements and the accompanying topological restrictions, both in the melt and amorphous phase of semicrystalline homopolymers with and without intracrystalline dynamics. Furthermore, this research also focuses also on the heterogeneity along the polymer chain and the influence of the thermal history on structure formation. In the second chapter the basic concepts of the relevant polymer physics with focus on the crystallization theories and the role of entanglements are presented. The chapter starts with a description of a single polymer chain, followed by the dynamics and relaxation mechanism in an entangled, multi-chain ensemble in a polymer melt. The complex crystallization process of a supercooled polymer melt and its competing dynamics during nucleation and crystal growth, focusing also on the underestimated role of entanglements which are rarely taken into account in standard crystallization models, are discussed. Another focus lies on more complex polymeric systems with a bimodal M_w -distribution and the crystallization of statistical copolymers. In both cases the presence of another possible crystallizable cunit has a strong influence on the final morphology. The influence of heterogeneity along the chain is further highlighted on comb-like polymers. By changing the main and/or side chain microstructure, the final morphology can be adjusted. Chapter 3 explains the basic solid-state NMR concepts in time-domain and ^{13}C structural MAS NMR as well as the complementary methodological concept. The publications and experimental results are summarized in chapter 4, followed by the discussion and summary in chapter 5. Paper I presents the role of entanglements on the semicrystalline structure formation in the model crystal-mobile polymer poly(ethylene oxide) (PEO). The

influence of the entanglement density in the melt and amorphous phase is investigated by the addition of short, noncrystallizable chains of the same species prior to crystallization. The dilution in its own oligomer reduces the entanglement density in the melt and allows to analyze the topological restrictions of entanglements and the influence of the intracrystalline dynamics on the structure formation, while all other parameters are kept constant. Thus far unpublished work on the crystallization of temperature-dependent simultaneous and co-crystallization in oligomer-diluted poly(ϵ -caprolactone) (PCL) is presented in the appendix. The second paper focuses on isodimorphic random butanediol–succinate/adipate copolymers (PBSAs) and the asymmetric incorporation of monomers of the minority component into the crystals of the majority component. The main investigation centers on two PBSA copolymers with compositions on either side of the pseudo-eutectic range by utilizing several dynamical ^{13}C NMR filter experiments. Furthermore, additional results demonstrate the influence of the thermal history on the two-step melting behavior for PBSA copolymers in the pseudo-eutectic range. These results can be found in the appendix. The third publication reports on the dynamics and polymorphic structure formation of the stiff comb-like polymer PPDOT into a nanophase-separated layered morphology with long-range order. It is shown that a layered morphology exists for all polymorphs, but the conformational statistic as well as backbone structure and the side-chain dynamic differs for all modifications.

2 | Scientific Background

In the following the formation of a semicrystalline morphology of polymers crystallized from an entangled melt and the relevant parameters for crystallization are discussed. The crystallization from the melt is described on a system consisting of homopolymers. After a brief description of the polymer chain, its possible conformations and models of an ideal or real chain are explained, as well as the dynamics in an entangled polymer system. These motions are relevant for the relaxation processes of polymers in the melt prior to crystallization and also influence the structure of the amorphous phase once the polymer is crystallized. The crystallization of homopolymers from the melt is subdivided into chapters focusing on nucleation of polymer crystallites, crystal growth and the formation of the semicrystalline structure. The effect of topological constraints on the final morphology is discussed separately and is followed by a summary, which brings the relevant parameters influencing the semicrystalline morphology into context. The structure formation of bimodal M_w -distributed systems, copolymers and comb-like polymers are discussed in more detail in separate chapters, as they are subject to the experimental findings presented in this thesis.

2.1 Description of a polymer chain

Polymers are long-chain molecules which are built of numerous covalently bonded monomers [1]. The chain length is characterized by the number of monomers in the chain N and their monomer molar mass M_{mon} in units of g/mol. The molecular weight $M_N = N \cdot M_{mon}$ is used to refer to the length of a polymer chain. In a polymer sample, the molecular weights of the chains are usually not completely uniform but show a certain polydispersity PDI , which describes the distribution of molecular weights in the sample.[15] The PDI is calculated via [15]

$$PDI = \frac{M_n}{M_w} \quad (2.1)$$

with the number and weight average molecular weight, $M_n = \sum_N n_N \cdot M_N$ and $M_w = \sum_N w_N \cdot M_N$, respectively. n_N and $w_N = n_N \cdot N / \sum_N (n_N \cdot N)$ are the number and weight fractions of polymer chains, having a certain molar mass M_N . An ensemble

of polymer chains with a high distribution of molecular weight is characterized by a high polydispersity, whereas a monodisperse sample has a $PDI = 1$. [15]

In thermal equilibrium the polymer chains can acquire different chain conformations, which are described by the the torsion angle φ and the bond angle θ between neighboring chains. The torsion angle, which is the angle between the bond vectors \vec{r}_i and \vec{r}_{i+2} of the successive atoms in the chain, has three energetic minima for sp^3 -hybridized carbons. The lowest energy state is the trans-conformation (t) for $\varphi = 0^\circ$ where \vec{r}_i and \vec{r}_{i+2} are parallel. Two other local minima are the gauche-plus (g^+) and gauche-minus (g^-) state at $\varphi = \pm 120^\circ$. The end-to-end distance of a polymer chain, with n main chain bonds of length l , reaches its maximal value $R_{max} = n \cdot l \cdot \cos(\theta/2)$ for an all-trans conformation. Additional gauche-conformations along the chain lead to a higher flexibility, since they break the rod-like all-trans chain into smaller sections. A measure for the stiffness of a polymer is the so-called Kuhn length b . It is a theoretical concept where the polymer chain is subdivided into N_s stiff segments, also called Kuhn segments, of length $b = R_{max}/N_s$. On length scales larger than the Kuhn length, the polymer is regarded as flexible, for smaller length scales the chain is best described as a rigid rod. In this approach the simplest model for an ideal polymer, the freely jointed chain model, is used. It assumes a random walk of N_s segments, which become independent of each other when separated by a sufficiently high number of bonds. [15]

Other models describing an ideal chain take the chemical structure of a polymer into account and consider fixed bond angles or assume an energy potential which hinders the torsion angle rotation. Nonetheless, all ideal chain models neglect the monomer-monomer interaction and assume that the polymer chains can overlap with each other. In real chains, the polymer chain can not simultaneously occupy the same space, resulting in a reduction of the conformational probabilities. This excluded volume interaction v can be divided into three subgroups, depending on whether the monomer-monomer interaction is attractive with $v > 0$, repulsive $v < 0$ or balanced $v = 0$. There is no energetic net penalty if the excluded volume is zero and no monomer-monomer interactions are present. In a good or athermal solvent ($v > 0$), the polymer coil is expanded. In a poor or non-solvent the excluded volume interaction is negative and the chain collapses. At a specific temperature, the so-called θ -temperature, the excluded volume interaction is zero and the chain can be described by a nearly ideal conformation. [15] In the absence of a solvent and above the glass and melting temperature an ensemble of polymer chains form a polymer melt, which can be described by an ideal chain with the root mean-square end-to-end distance $R_0 = b \cdot N^{0.5}$ [18].

2.2 Dynamics in an entangled polymer systems

Several theories and models are used to describe the dynamics and the relaxation of a polymer melt. One common model to characterize the dynamics in an unentangled polymer melt is the Rouse model. It assumes beads connected by harmonic springs to represent the dynamics and interactions along the chain without excluded volume effects. The model also neglects hydrodynamic interactions between the beads.[15] An important characteristic parameter is the Rouse time τ_R [15]

$$\tau_R = \frac{R^2}{D_R} \approx \frac{R^2}{kT} N \cdot \xi \quad (2.2)$$

defining the time the chain needs to diffuse over a distance in the order of its own size R , with the diffusion coefficient of the Rouse chain $D_R = kT/\xi$ and the friction coefficient ξ for N beads. The dynamic response of the polymer chain is dependent on the relevant time scale. Elastic behavior is observed for time scales shorter than the Kuhn monomer relaxation time $\tau_0 \approx \xi \cdot b^2/kT$. For $\tau_0 < t < \tau_R$ the chain exhibits a viscoelastic behavior. On time scales longer than the Rouse time the chain dynamics is described by a viscous motion.[15]

If the polymer chain exceeds a certain entanglement molecular weight M_e , it becomes subject to topological constraints caused by the surrounding chains, the so-called entanglements. In a concentrated solution or in a polymer melt the restrictions can be described by the popular Edwards tube model (schematically depicted in Figure 2.1). The molecules surrounding a certain segment of another polymer restrict the transverse fluctuations of the chain in question into a virtual tube with the diameter $a = b \cdot N_e^{0.5}$, with the entanglement strand end-to-end distance N_e . The fluctuating thermal motions within this tube are unhindered and independent of the topological restrictions, but the chain remains close to its primitive path $\langle L \rangle$, which is the shortest connection between the chain ends along the tube. On length scales smaller than the tube diameter the dynamics of the chains are described by the Rouse model of an unentangled polymer chain. The time the polymer chain needs to diffuse along its primitive path to leave its tube is defined by the reptation time τ_{rep} . [15]

The reptation model was first proposed by de Gennes [57] in 1971 using a mean-field approach, describing the motion of long polymer chains in a network, assuming that all chains behave similar to the observed chain in its tube. A further development of the model allows to describe the diffusive motion of polymer chains in an entangled melt. The reptation is predicted to be proportional to the cube of the molecular weight. Though, the experimentally observed exponent is 3.4.[58, 59] This stronger dependence of the molecular weight is caused by additional relaxation mechanisms [60],

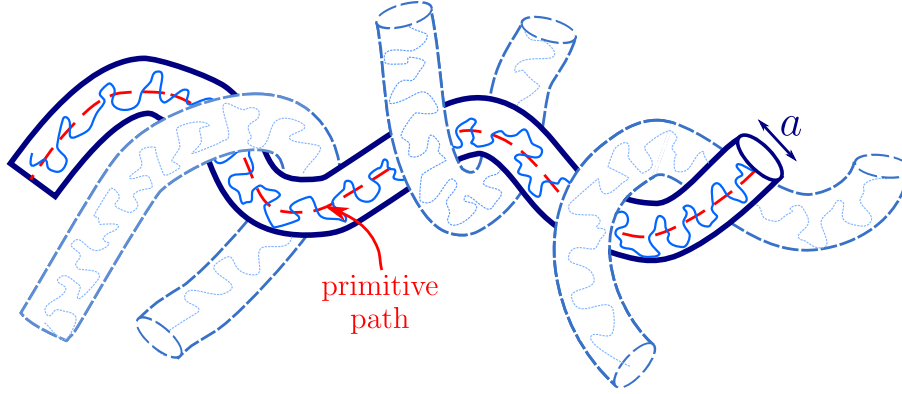


Figure 2.1: Schematic representation of the Edwards tube model: A polymer chain with topological restriction caused by entanglements induced by surrounding chains is represented by confined motion in a tube. The dynamics are restricted to a virtual tube with diameter a along a primitive part of the tube. Adapted from reference [15].

caused by primitive path or contour length fluctuations (CLF) of a single polymer chain and was first introduced by Doi [58, 59] as a modification of de Gennes reptation model. These fluctuating motions of a polymer chain at the tube end cause a reduction of the contour length $\langle L \rangle$ by a distance $\langle \Delta L \rangle$ [15]. According to Doi [58, 59] the time a chain needs to reptate along the reduced contour length is likewise reduced, resulting in a higher molecular weight dependency of the reptation time τ_{rep} for medium sized chains with $M_w/M_e < 100$. The correction factor for the contour length fluctuation is inversely proportional to the square root of the number of entanglements in the melt. Therefore, the dynamics in an entangled melt of long chains is in better agreement with the reptation model, since the effects of CLF are reduced.[15]

In an entangled polymer melt composed of shorter chains the constraint release, a many-body problem, becomes relevant. In the reptation model it is assumed that all tubes behave similarly. Therefore, not only the tube under observation is in motion, but also the surrounding chains, which causes topological constraints on the observed tube. While moving, the constraints imposed on the observed tube are partially lifted and fluctuate with time, allowing the observed chain to undergo large scale motions resulting in modifications of the confining tube for a given polymer chain.[15, 61] The effect of constraint release is relevant for branched polymers [62] and for long chains within a matrix of short chains [15]. For very long polymers the chain relaxes via constraint release before it can diffuse with the reptation time τ_{rep} . If the chains within the matrix become shorter the reptation is the faster process and defines the terminal relaxation. In polymer melts or in concentrated solutions the latter is the dominating process.[15]

In a linear entangled polymer melt the time dependence of the mean square monomer displacement $\langle [r(\vec{t}) - r(\vec{0})]^2 \rangle$ can be subdivided into three regimes with different relaxation time dependencies [15]:

$$\langle [r(\vec{t}) - r(\vec{0})]^2 \rangle \approx$$

$$\text{Regime I:} \quad \left(\frac{t}{\tau_0} \right)^{1/2} \quad \text{for } \tau_0 < t < \tau_e \quad (\text{free Rouse}) \quad (2.3)$$

$$\text{Regime II:} \quad \left(\frac{t}{\tau_e} \right)^{1/4} \quad \text{for } \tau_e < t < \tau_R \quad (\text{constrained Rouse}) \quad (2.4)$$

$$\text{Regime III:} \quad \left(\frac{t}{\tau_R} \right)^{1/2} \quad \text{for } \tau_R < t < \tau_{rep} \quad (\text{reptation}) \quad (2.5)$$

$$\text{Regime IV:} \quad \left(\frac{t}{\tau_{rep}} \right)^1 \quad \text{for } \tau_{rep} < t \quad (\text{free diffusion}) \quad (2.6)$$

On time scales shorter than the relaxation time of an entanglement strand τ_e , polymer segments exhibit coherent Rouse-like motions on a length scale shorter than an entanglement strand. This relaxation time dependence is classified by regime I as free Rouse motion. Constrained Rouse motion is observed on time scales between τ_e and the Rouse time τ_R . Here the motion is restricted by the topological constraints of the surrounding chains. The theoretically predicted $1/4$ power law is a characteristic value describing a constrained chain undergoing Rouse motion within a tube.[15] Reptation is observed on time scales above the Rouse time and below τ_{rep} , above which the polymer chains undergo free diffusion [62].

2.3 Crystallization of semicrystalline polymers from the melt

2.3.1 Nucleation of polymer crystallites

Polymer crystals grow from a nucleation point when crystallizable polymers, composed of chains with long sequences of monomeric units, which have a regularity in their chemical constitution, are cooled from the melt below their melting temperature T_m . [63] During the nucleation process molecules are attached and detached from the surface of the nuclei. According to classical nucleation theory, the nucleation formation rate I , which is given by [63]:

$$I = I_0 \cdot \exp\left(\frac{-\Delta G^*}{kT_c}\right) \quad (2.7)$$

is an activated process with a free energy barrier ΔG^* at the crystallization temperature T_c and describes the number of nucleating events per volume and time.[63] The prefactor I_0 is dependent on the probability that stable nuclei with a critical size are formed, as well as on the diffusive process of the monomers and the related attachment on the nucleus-melt surface. Nuclei with or below the critical size can

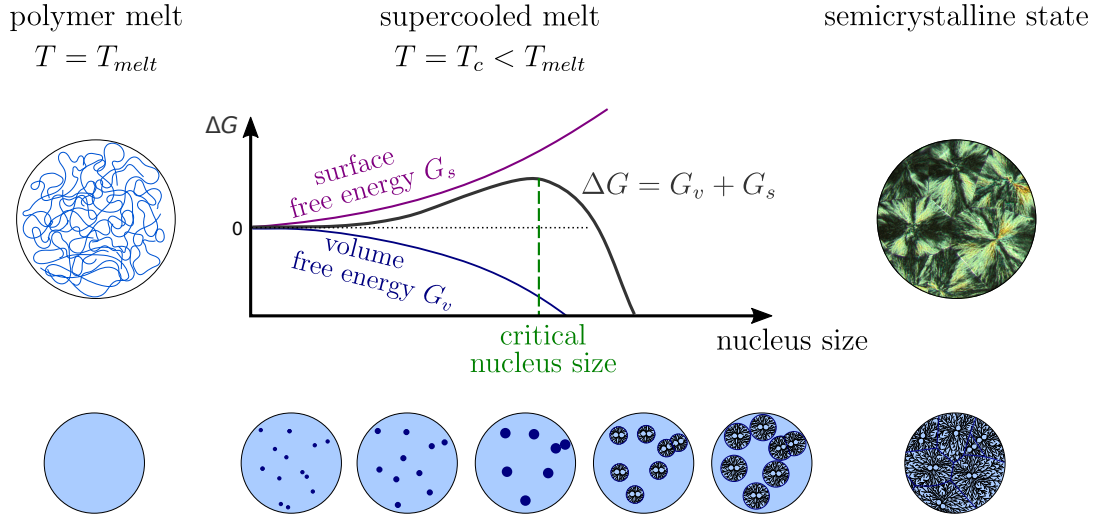


Figure 2.2: Schematic representation of the nucleation process of an entangled melt cooled from the melting temperature, T_{melt} , to the crystallization temperature T_c at which crystallization and crystal growth takes place. The nucleation process is described by the change in the free energy ΔG with its opposing contributions of the surface and volume free energy. Once the nuclei exceed a critical size the spherulites grow radially until the volume is filled and the primary crystallization is completed. Central diagram adapted from reference [63].

either lose attached monomers and dissolve or become a stable growing nucleus. One differentiates between heterogeneous and homogeneous nucleation. In the latter case small crystalline phases are formed directly in the supercooled melt without the formation being triggered by any foreign particles (impurities) as in the case of heterogeneous nucleation. The formation of nuclei without any impurities present only occurs for very strong supercooling, a situation that can be studied by confining the melt to small droplets that can not contain any impurities or thin films. The majority of nucleation processes are initiated by impurities in the supercooled polymer melt.[63]

Nonetheless, in both cases the formation of stable nuclei depends on changes of the free energy ΔG upon crystallization, with a positive contribution arising from the surface free energy G_s , which is opposed by the volume free energy G_v [64]

$$\Delta G = G_v + G_s = -V_n \Delta G_{melt} + \sum_i A_i \sigma_i \quad (2.8)$$

The volume free energy G_v is given by the product of the volume of the nucleus V_n and the difference of the free energy in the molten and crystallized state $\Delta G_{melt} = G_{melt} - G_{crystal} = \Delta H_{melt} - T \Delta S_{melt}$. ΔH_{melt} and ΔS_{melt} are the changes in enthalpy and entropy, respectively. The surface free energy G_s is calculated by the product of the lateral surface free energy σ_i , and the corresponding surface area A_i . [64]

Figure 2.2 illustrates the nucleation process from an entangled polymer melt at a

crystallization temperature T_c . For small nuclei the energy penalty for the surface exceeds the energy gain from the ordered crystalline structure and a part of the already formed nuclei will dissolve again. Nuclei above a critical size which have overcome the energy barrier ΔG^* , given by the maximum of the free energy ΔG , grow radially to spherulites, where they impinge upon each other until the complete volume is filled and the primary crystallization process is completed. The change in free energy, which needs to be overcome in order to attach a secondary nucleus to the surface of the primary crystals, is lower due to the reduced surface free energy G_s . Thus, the process of secondary nucleation is easier than the formation of a new nuclei.[63, 64]

The growth rate of isothermally crystallized spherulites depends on the crystallization temperature and is assumed to be constant at a given temperature. Its temperature-dependence can be described by a bell-shaped curve with a maximum between the glass (T_g) and melting (T_{melt}) temperatures. During the secondary crystallization the overall crystallinity of the system can increase further. This increase is associated with an insertion of smaller crystalline lamellae into the already existing amorphous-crystalline two-phase system or also with lamellae thickening.[64] The formation of the semicrystalline morphology, together with the description of selected crystallization theories, will be discussed in chapter 2.3.2.

2.3.2 Crystal growth and structure formation

The primary step for the structure formation of a semicrystalline morphology is either the homogeneous or heterogeneous crystal nucleation, as described in chapter 2.3.1, followed by the growth of the crystals with a specific rate. Several models try to explain the growth kinetics and structure formation of a specific semicrystalline morphology. The established surface nucleation theory of Hoffman and Lauritzen [27], the Sadler-Gilmer [28] and the intramolecular nucleation [29] models derive growth rate equations that are all based on the counterbalance of the driving force for the crystal formation and another entropic or enthalpic barrier term associated with secondary nucleation.[30] Other models assume that crystal reorganization processes during the growth are responsible for the formation of a certain lamellae thickness d_c [31–37]. An additional factor relevant for the growth rate of the crystals is the reptation motion of the entangled chain in the polymer melt, which is the only way to dissolve topological constraints that limits crystal formation. Consequently the growth rate is also dependent on the molecular weight M_w . [64]

The final semicrystalline morphology is described by a nanoscopic two-phase structure composed of stacked crystalline lamellae which are separated by disordered amorphous regions. The crystalline lamellae, with a certain thickness d_c , are composed of parallel

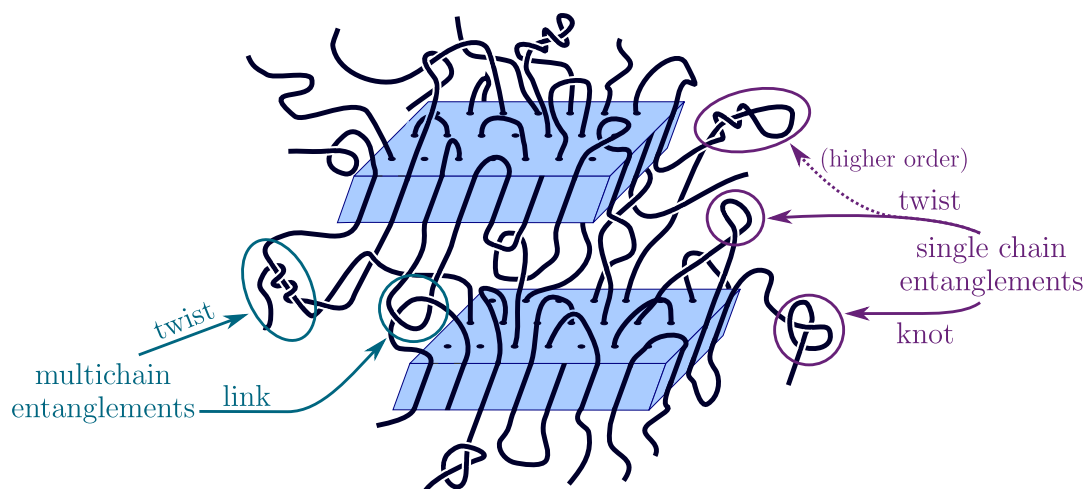


Figure 2.3: Schematic representation of a lamellae stack, separated by a disordered, entangled amorphous layer, displaying also the different types of topological constraints. Knots and twists of higher order or between two chains are harder to resolve than a simple twist of single chain. Linked chains which are already incorporated into the crystalline lamellae cannot be resolved. Adapted from reference [63].

chains in a helical conformation, the simplest being a 2_1 -helix for an all-trans conformation.[18]

Fritzsching et al. [65] proposed a modification of the structural textbook model picture: in order to minimize a potential density anomaly at the crystalline-amorphous interphase the polymer chains should exhibit a certain chain tilt in the crystallites, as reported for PE as early as the 1980s [66–69]. Furthermore, a reasonable amount of chains need to terminate at the crystal surface. Both modifications are necessary to obtain a semicrystalline morphology with adjacent reentry, which does not contain any density anomalies [65]. Sequences of the polymer chains which can not be incorporated into the crystalline lamellae during the crystallization process, e.g. entanglements, are shifted to the amorphous phase [70]. A sufficiently long polymer chain can pass through several neighboring lamellae, and as a consequence, generates tie chains which also become part of the amorphous phase [18, 64]. Figure 2.3 shows a schematic representation of two lamellae stacks separated by an amorphous layer. Additionally, different classes of entanglements, which will be discussed in chapter 2.3.3, are highlighted.

It is assumed, that the semicrystalline morphology is a nonequilibrium structure, obtaining a minimal crystalline thickness at a given crystallization temperature T_c . Smaller crystallites have a lower thermal stability. The Gibbs-Thomson equation describes this melting point depression for a certain crystalline thickness formed at a specific T_c . [18, 44, 46] In polymers with intracrystalline dynamics and a related crystalline-amorphous large-scale diffusion, such as poly(ethylene oxide) (PEO) or polyethylene (PE), the crystals can reorganize during the growth process, which

results in a lamellae thickening during primary crystallization [44, 71]. The absence or existence of intracrystalline dynamics allows for the classification semicrystalline polymers into crystal-fixed or crystal-mobile, respectively [16]. Boyd [45] reported that the crystallinity in crystal-mobile polymers is in generally higher.

In a comparison of the model crystal-mobile polymer poly(ethylene oxide) (PEO) and the crystal-fixed polymer poly(ϵ -caprolactone) (PCL), Schulz et al. [44] stated, that the final semicrystalline morphology differs in both cases and is thus strongly affected by the presence of the so-called α_c -relaxation. The intracrystalline dynamics in PEO allows a thickening of the crystalline lamellae during the growth until a minimum amorphous layer thickness is reached, since both processes—growth and reorganization—happen on a similar timescale. The resulting morphology is characterized by a wide variation in lamellae thickness and a well-defined amorphous thickness. It is assumed that the amorphous phase in crystal-mobile polymers is a crucial parameter for the final morphology. The morphology of PCL follows the more classical view of polymer crystallization, where a certain, well-defined crystalline thickness is selected. The amorphous thickness in PCL displays a wider distribution. In contrast to PEO, the crystalline lamellae of poly(ϵ -caprolactone) are only marginally stable and reorganize during heating.[44, 46]

In both model polymers the topological constraints in the melt and amorphous phase seem to play an important role in the structure formation, but the effect of entanglements are often not considered. The experimental findings presented by Kurz et al. [72] suggest that the entanglements in the melt and amorphous phase control the thickness of the amorphous layer in the crystal-fixed polymer PCL, and, thus, the final semicrystalline morphology.

The important role of entanglements on the nucleation and subsequent structure formation, both in the amorphous phase and, prior to the crystallization, in the melt, will be discussed in the following chapter.

2.3.3 Role of entanglements

The topological constraints imposed by the entanglements in the molten state and after crystallization in the amorphous phase influence not only the structure formation [34, 38, 40] of the semicrystalline polymer, but are another factor determining the nucleation rate of a supercooled entangled melt. This impact is not accounted for in the classical nucleation theory. The topological constraints can act as a “pinning” effect, limiting or preventing the formation and growth of a nuclei.[63]

Once the polymers are in the molten state topological constraints of different complexity will form—provided that the molecular weight is high enough—even if the sample is completely disentangled prior to melting. The complexity of the topological

constraints depend on the form and the number of involved chains. One may distinguish between twists, knots or links, which are multichain knots (see Figure 2.3). A twist of a single chain is one of the simplest entanglements and requires little time and topological movement to form or to resolve again. Higher order or multichain twists are more complicated and take longer times to develop. Twists can form at any point within the chain, independent of their complexity. In contrast, a chain end or a tip of a loop is required for the formation of knots, which are characterized by a chain end that passed through a loop of the same chain. In general, the higher the complexity the more time and larger topological movements are required to form or resolve the entanglements again.[63] As a consequence, the entanglements, especially complicated multichain entanglements, will suppress the nucleation and crystal growth since they can only be incorporated into the crystal if they resolve on a timescale faster than the crystal growth [31, 73].

The comparison of these timescale allows to divide the crystallization into a fast and a slow regime, as suggested by Robelin-Souffaché, and Rault [32]: to resolve a topological constraint such as a knot during crystallization, a topological movement along the polymer chain is needed, which requires a comparably long time. In the regime of slow crystallization the chains can relax on a timescale shorter than the crystal growth and the entanglements can dissolve completely or at least partially. In the fast regime the crystallization is too fast to allow for relaxation of entangled chains. The time it takes for an entangled chain to reptate and disentangle is dependent on the molecular weight.[32, 63]

Anwar et al. [74] find, from molecular dynamics simulation on short polymer chains slightly above and below the entanglement length, that the nucleation rate is not affected by the entangled chains. In contrast, experimental findings on highly entangled chains reveal that an increasing entanglement density results in a decreased nucleation rate [63]. This indicates that the nucleation rate of an entangled polymer melt is also dependent on the molecular weight.

Entanglements in the amorphous phase and melt are also suspected to be a limiting reason for the detected crystallinity, the lamellae thickness and to influence the final semicrystalline morphology, i.e. by chain folding [34, 38, 40, 67, 70, 75–79]. In 1967, Fischer [76] found that the thickness of the amorphous phase is temperature-dependent and increases with increasing temperature. Later, this temperature-dependence of the amorphous thickness d_a and consequently also of the crystallinity X_c was associated with the presence of entanglements [70, 77–79].

A recent simulation series on a coarse-grained model of the crystal-mobile polymer PVA using molecular dynamics simulations with a primitive path analysis, performed by Luo and Sommer [39, 41, 42, 80–82] showed, that the entanglement length directly influences the thickness selection of a crystalline lamellae. The authors conclude that

entanglements are an important factor for the crystallization process which affect the nucleation in the early stages of crystallization and the growth rate: In regions with a lower entanglement density the crystallization is faster and thicker crystalline lamellae are formed. The temperature-dependence of d_c is suspected to be correlated with the temperature-dependence of the entanglement length.

A molecular weight dependent investigation of entanglement effects in the crystal-fixed polymer PCL, performed by Kurz et al. [72], revealed that not the crystalline lamellae, but the amorphous layer thickness increases for increasing molecular weights and higher crystallization temperatures. A difference arising from the two crystallization regimes is only detected as a slightly steeper increase of d_a for the lower molecular weights. The authors find a two-fold enhancement of the entanglement density in the amorphous phase in comparison to the melt state and assume that the entanglement density determines the final amorphous, but not the lamellae thickness. The findings are explained by the hypothesis that a growing lamellae stops or limits the unknotting of entanglements, which are then accumulated in the amorphous phase close to the lamellae.[72] This effect was also invoked by Mandelkern [67] who proposed that a chain trapped in a growing crystal hinders or prevents its entanglements from unknotting, which ultimately limits the crystallinity. The enhanced entanglement density around the growing lamellae acts as a entropic barrier for a second lamella, which therefore can only grow within a certain distance such that a critical, temperature-dependent entanglement density is not exceeded. This latter model also allows for the growth of secondary lamellae as insertion within the already existing ones, once the temperature and thus the entropy barrier is lowered.[72]

2.3.4 Parameters influencing the semicrystalline morphology

All polymer crystallization models strive to explain the formation of a semicrystalline structure with certain crystalline and amorphous layer thicknesses and their thickness distributions, as well as the overall crystallinity. Often the experimental findings cannot be explained by the standard models. Other approaches describe the structure formation of a specific polymer or polymer class, e.g. crystal-mobile polymers, rather well, but fail to explain the morphology of others.

Important parameters for the structure formation that recurrently appear in crystallization models or explanations of certain experimental findings are the competing polymer-dynamic processes during crystallization at a specific crystallization temperature T_c . Entanglements that cannot be resolved may hinder the crystallization and are thus related to the limitation or the stop of the crystal growth. Disentanglement is described by reptation or also arm retraction processes and is therefore molecular weight dependent.[57, 61] Depending on the crystallization temperature and hence on

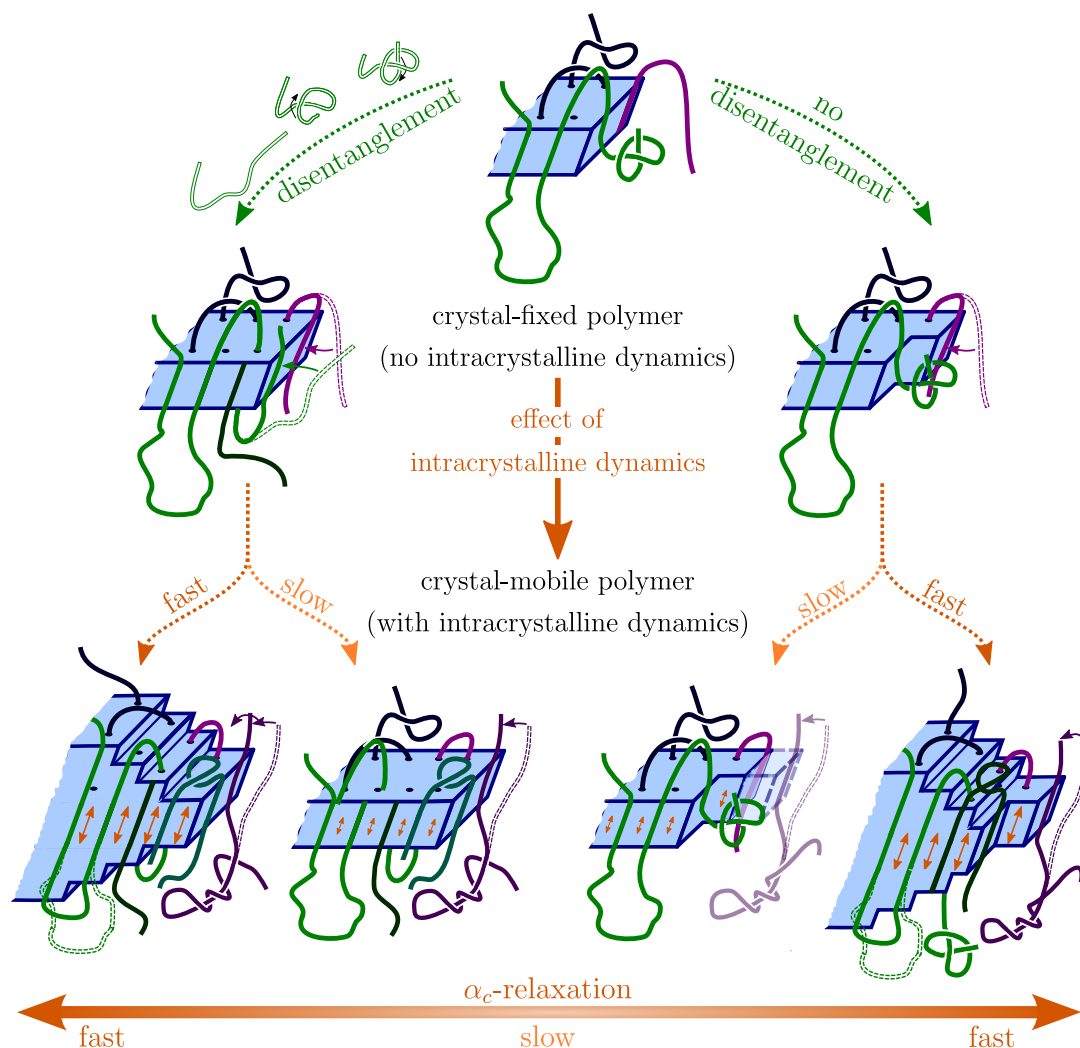


Figure 2.4: Schematic illustration of the competing dynamics during crystallization. For clarity the polymer chains are only partially shown. *Top*: Growing nuclei above the critical size which grows with a certain, temperature-dependent rate I . The purple chain can align at the growth front without any problems, whereas the green chain is knotted and needs to be disentangled in order to contribute to the crystallization by adding another layer to the lamellae. If disentanglement occurs on the same timescale or faster than the lamellae growth, another layer is added to the crystal (slow crystallization; *left column*). If the unknotting is too slow in comparison to the growth rate, only partial growth is possible and the crystal may not be thermally stable (fast crystallization; *right column*). If α_c -relaxation is present, sliding diffusion processes allow for crystal thickening directly at the growth front, provided that the intracrystalline dynamics are fast enough. In case of slow crystallization (*left column*), where disentanglement is possible, the lamellae thickening is not hindered by the entangled chains (*bottom, outer left*). In case of fast crystallization (*right column*), the α_c -relaxation may allow the lamellae to grow even if disentanglement does not occur or is too slow, as shown by the green entangled chain (*bottom, outer right*). For low crystallization temperatures the intracrystalline dynamics is too slow and the structure formation is similar to the crystal-fixed case, with competing dynamics of crystal growth and disentanglement (*bottom, middle left and right*).

the crystallization rate, the entanglements can resolve faster, on a similar timescale or slower than the growth of another lamellae stem [44]. In the absence of intracrystalline dynamics the competing dynamics of both processes influence the structure formation. The morphology is characterized by a well-defined crystalline thickness and a distributed amorphous layer thickness, which is assumed to be governed by the entanglement density. In crystal-mobile polymers the additional thermally activated α_c -relaxation and the associated “sliding diffusion” process in the crystals allows the crystalline lamellae to thicken directly at the growth front until a critical amorphous thickness or entanglement density in the amorphous phase is reached. This, of course, takes into account, that the relevant dynamics, which are dependent on the crystallization temperature T_c , act on a similar timescale. For rather low crystallization temperatures, a crystal-mobile polymer such as PEO can form a morphology that is similar to one observed in crystal-fixed polymers. This is a consequence of the strong dependence of the intracrystalline dynamics on temperature.[44, 72]

Concluding from all the findings discussed above, the competing dynamics of crystal growth, disentanglement and intracrystalline dynamics at the growth front of one crystalline lamellae is schematically illustrated in Figure 2.4.

Changes in the structure of a semicrystalline morphology, formed at a certain crystallization temperature, upon heating depend strongly on the prevailing isothermally crystallized morphology. In a crystal-mobile morphology with extended crystalline lamella and a minimized amorphous thickness, the crystalline lamellae are stable upon heating. In contrast, structures formed in the crystal-mobile polymer PEO at low T_c and in the crystal-fixed polymer PCL, have marginally stable crystallites which undergo continuous melting and recrystallization during heating.[46] This independent finding lends strong support to the scheme presented in Figure 2.4.

In both polymer classes the crystalline thickness is dependent on the crystallization temperature, but the underlying process governing how the specific lamellae thickness are formed, is still under discussion.

2.4 Structure formation in bimodal M_w -distributed systems

In polymer blends the structure formation depends strongly on the miscibility, which describes the phase behavior of both polymers in a mixture. The free energy of mixing for binary polymer systems is the thermodynamic parameter which describes the temperature and volume fraction dependence of the entropy and enthalpy change, respectively, associated with mixing. In a miscible blend, both components form one single phase and the properties describing this phase are often a combination of the pure polymer components.[83]

Bimodal molecular weight distributed systems, which are polymer blends where both

components have the same monomer units but have a different molecular weight, are supposed to be miscible, as shown by experimental and molecular dynamics simulation results [84–87]. An important parameter in the bimodal M_w -distributed systems is the molecular weight of the short chains. If the length of the short chain polymer exceeds the entanglement length both components contribute to the entangled system. In cases with short chain polymers with a molecular weight smaller than M_e one could speak of a oligomer-diluted polymer matrix, where the entangled structure is given by the long chain polymers and the oligomers (short chains) act as solvent. Both the reptation time τ_{rep} and the entanglement time τ_e depend on the concentration of the long chain polymers Φ . [15] The reptation time decreases, while the entanglement time increases with decreasing amount of long chain polymers according to [15]:

$$\tau_{rep}(\Phi) \approx \tau_0 \cdot \frac{N^3}{N_e(\Phi = 1)} \begin{cases} \Phi^{1.62} & \text{good solvent} \\ \Phi^{7/3} & \theta \text{ solvent} \end{cases} \quad (2.9)$$

$$\tau_e(\Phi) \approx \tau_0 \cdot N_e^2(\Phi = 1) \begin{cases} \Phi^{-2.31} & \text{good solvent} \\ \Phi^{-5/3} & \theta \text{ solvent} \end{cases} \quad (2.10)$$

with the entanglement strand end-to-end distance $N_e(\Phi = 1)$ of the pure long chain polymer. The entanglement strand end-to-end distance decreases for higher oligomer dilutions with $N_e(\Phi) \sim \sqrt{\tau_e(\Phi)}$ and thus also the entanglement density is reduced, which may affect the nucleation, crystallization, lamellar thickness and in general the complete semicrystalline morphology, once the oligomer-diluted polymer system is cooled to its crystallization temperature. [15]

Two systems have to be distinguished, dependent on whether the short chain polymers can crystallize in the relevant temperature range or not. In the latter case one speaks of a crystalline/amorphous blend, where the oligomers would decrease the entanglement density in the melt prior to crystallization, but do not contribute in the crystallization and are thus either incorporated into the amorphous phase of the semicrystalline polymer or a partial phase separation occurs during the lamellae formation. The resulting semicrystalline phase consists of amorphous layers of oligomers in a polymer-matrix and a potential, phase separated phase that only contains the low molecular weight chains. In crystalline/crystalline blends, both polymer and oligomer can crystallize at the relevant temperature. It can be distinguished between separate, simultaneous and co-crystallization. In separate and simultaneous crystallization both components form their own crystals either time-separated or simultaneously. In co-crystallization both components have a isomorphic behavior and are capable of forming one single crystal phase that contains contributions from both high and low molecular weight chains. [83]

According to molecular dynamics simulations performed by Zhai et al. [87], the nucleation in long chain polymers is intermolecular, meaning that tight loops are formed. In contrast, short-chain polymers nucleate as extended chains without loops. In mixtures of long and short chains, the ratio of tight loops and tie segments increases with increasing amount of long chains. Thus, additionally to the effect of a decreased entanglement density in the melt, the structure formation in mixtures of long and short chain polymers differs, is ratio-dependent and also influences the final topological features of the amorphous phase.[87]

These considerations are the basis of the findings discussed in chapter 4.1, which revealed that the semicrystalline structure changes only little if long-chain poly(ethylene oxide) is diluted with its non-crystallizable oligomer. Upon dilution faster intracrystalline dynamics and slightly smaller crystalline lamellae are detected. The findings are in good agreement with the dependence of the correlation time on the lamellae thickness, reported by Kurz et al. [72], and indicate only little changes in the fold surface for higher oligomer-dilutions. In this so far unpublished work, the oligomer-dilution of the crystal-fixed polymer PCL is investigated, focusing on the simultaneous and co-crystallization of oligomer and long-chain polymer. These findings are presented in the appendix A.2.

2.5 Crystallization of statistical copolymers

Two or more chemically distinct monomers which are covalently joined to form one polymer chain are called copolymers [12]. The composition mixture and sequence distribution are essential for the final semicrystalline structure. Both comonomer units can be joined to form either block or random statistical copolymers [13, 14]. In the following the focus lies on the description of statistical copolymers, where the sequence distribution is Markovian [47]. Similar to polymer blends one distinguishes between copolymers with two crystallizable or one amorphous and one crystallizable comonomer [88]. The random comonomer distribution usually interferes with the structure formation of extended crystalline lamellae and often results in a decreased lamellae thickness, reduced crystallinity and a melting point depression of the copolymeric material in comparison to the homopolymer [47].

Copolymers can form organized spherulitic superstructures, which was experimentally proven on ethylene- and propylene-based copolymers. However, the ordering within the spherulites worsens with increasing co-unit content and molecular weight.[88] Additionally, a reduction of the final lamellae thickness and a unit cell expansion is observed with increasing concentration of co-units. Changes in the unit cell are associated either with co-unit inclusion or with surface stresses which are caused by the reduced lamellae thickness and the associated increase of the surface-to-volume

ratio. The effect of the first can be reduced by slow crystallization.[89, 90]

The first model to describe the crystallization in statistical copolymers with one crystallizable unit was proposed by Flory [91]. The observed melting point depression is explained by an additional entropy gain during melting, once A units of the crystallite melt into an A/B mixture of both comonomers. Experimental data is in qualitative agreement with the expected trend, but the melting point depression observed in experiment is lower than the values predicted from Flory's equilibrium model. This is a consequence of the assumption that thick crystallites are formed and no B comonomers can be included into the A crystals. Other empirical or theoretical models, which assume a finite crystal thickness and allow for inclusion of co-units, describe the experimental findings better than Flory's model.[88, 91]

In the special case that both comonomers are crystallizable, the resulting semicrystalline morphology depends strongly on whether or not both monomers can form a joint crystalline phase over the complete crystallization range, if co-unit inclusion is possible or if one monomer is completely excluded from the crystalline phase of the second. The rare first case is known as isomorphism. For the occurrence of co-crystallization of both monomer units along the chain, strict molecular requirements of both monomers, such as a similar volume, shape and chain conformation, total miscibility and similar crystallization rate of the homopolymers, must be fulfilled. The resulting semicrystalline properties, such as the crystallinity or melting point, depend on the composition and can be linearly extrapolated between the properties of both homopolymers, as shown in Figure 2.5. The crystallites and the amorphous phase are composed of both comonomers.[13, 14, 25, 92]

A very common case for the crystallization of random copolymers is the complete exclusion of one comonomer from the crystal of the second co-unit. A crystalline structure is only formed for low comonomer concentration, where only the majority component contributes to the crystalline phase. For more symmetric mixtures the copolymer will not form a crystalline structure and remains completely amorphous. A special case is the isodimorphic behavior of copolymers which occurs if both monomers do not fulfill the strict molecular requirements for isomorphism, but still have similar repeating units. The formation of a semicrystalline morphology is possible over the complete composition range. Depending on the amount of included co-units in the crystalline phase of the second comonomer (usually the majority component), the behavior is either closer to isomorphic, with a high amount of included co-units, or, for a small fraction of included or completely excluded comonomers, closer to complete exclusion. The pseudoeutectic range, which occurs most often at equimolar mixtures, describes a composition range where both comonomers form their own crystallites, each with a distinct melting temperature.[25]

The crystallization of statistical copolymers is subject of chapter 4.2, where it is show

that the co-unit inclusion in the random isodimorphic copolymer, poly(butanediol-succinate/adipate) (PBSA), is asymmetric. For PBA-rich compositions, the minority BS-units are included in the crystalline structure of BA-bulk crystal, whereas for PBS-rich compositions a complete exclusion of the minority component is observed. The effect of the crystallization condition on the structure formation of PBSA copolymer in the pseudoeutectic range are discussed in the appendix A.3.

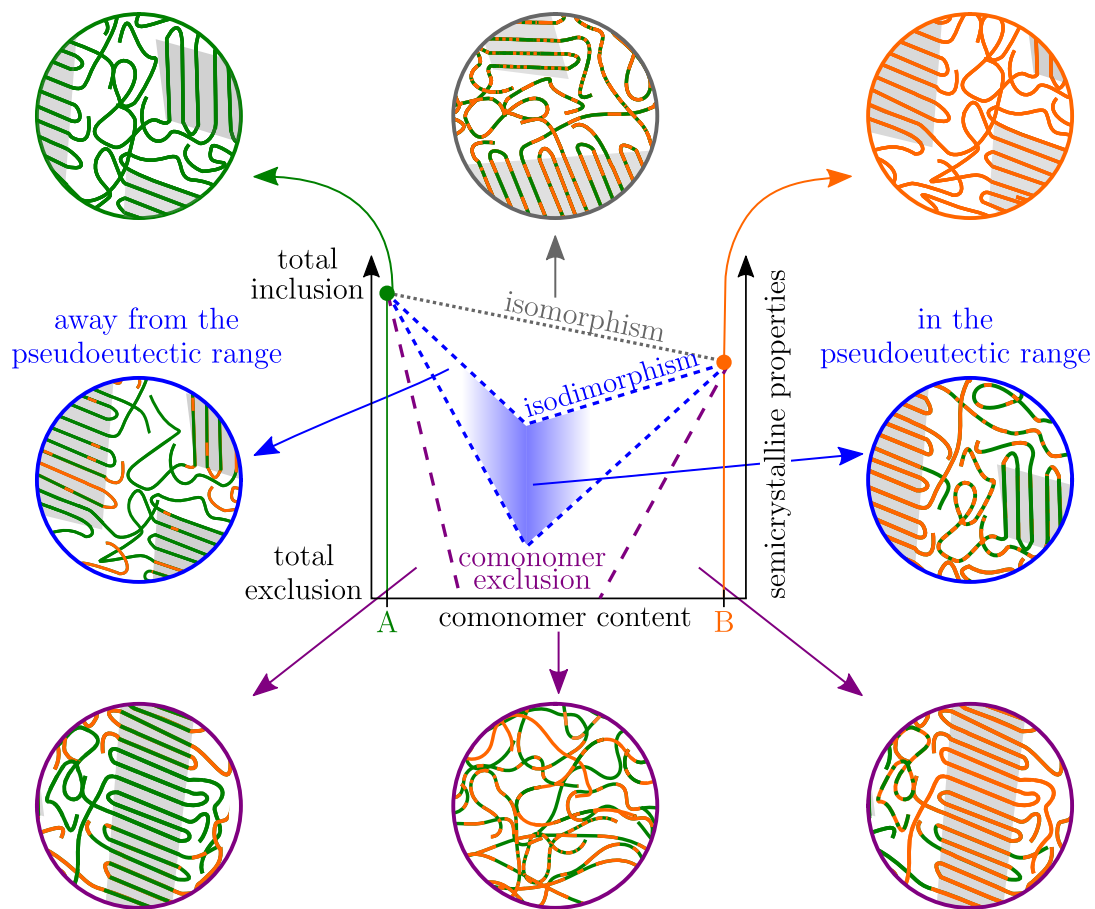


Figure 2.5: Schematic representation of the possible semicrystalline morphologies of statistical copolymers with two crystallizable units. In the upper left and right corner the semicrystalline structures of the homopolymers A and B are shown. The morphology in case of an isomorphous behavior is centered at the top with an approximately symmetric comonomer content. The isodimorphic behavior is represented in the central row. On the left, an exemplary morphology of A-rich composition away from the pseudoeutectic region is shown. In the majority A crystal B comonomeric units are incorporated. In the pseudoeutectic range (central row, right), often at approximately equimolar composition, A as well as B crystals are formed. The morphology in case of complete exclusion (lower left and right) with a A-rich and B-rich crystal, respectively, and a completely amorphous phase for higher comonomer contents in the middle. The central diagram is partially adapted from reference [25].

2.6 Structure formation of comb-like polymers

Polymers which are built from monomeric units having linear aromatic ester groups are often described as “rods”. This class of aromatic polyesters is characterized by a very high melting temperature, often above 400 °C, and the formation of a liquid crystalline phase in the melt, which was first described in the late 1970s. The late discovery can be attributed to the high melting temperature, limiting both experimental research and possible applications of this polymer class. In order to reduce the melting temperature several modifications of the structure, e.g. the attachment of substituents on the mesogenic units, or flexible spacers as well as the copolymerization with either another mesogenic or non-mesogenic unit, were proposed.[93] The addition of lateral substituents results in a considerable reduction of the melting temperature [94].

In a series of studies conducted by Ballauff et al. [17, 22, 95–100] the structure formation of rigid-rod polymers (in the following also called main chain or backbone) with flexible side chains was investigated. The focus laid on the influence of the length of the side chains, the chemical structure, the position of the side on the main chain and the temperature-dependence: above a certain length of the side chains the rigid-rod polymers form a layered mesophase. The long side chains, which are often methylene sequences, aggregate and form nanodomains. The distance between the layers, composed of the rigid-rod polymers, increases proportionally to the length of the side chains. Depending on the side chain length, thermal history and preparation of the sample, additional structural modifications can be found, which differ in the packing of the side chains in the nanophases and the layer spacings. The length of the side chains, which is necessary to form a layered mesophase, depends on the position and amount of the side chains that are attached to the backbone and also on the microstructure of the main chains.

For comb-like polymers with aromatic backbones the formation of a layered structure is a common feature [96]. Several experimental studies, e.g. on polyester PPTE-16, polyimide PPPI-16 or polyamide PPA-16 [51], were performed to better understand the final morphology of the layered morphology and the side chain packing in the nanodomains. The influence on temperature and side chain length will now be considered in more detail on the example of poly(1,4-phenylene-2,5-*n*-dialkyloxy terephthalate)s (PPAOTs) with *n* alkyl carbon atoms per side chain. For side chains having six or more carbon atoms, a layered nanophase separated morphology is observed. Depending on the side chain length and preparation method two polymorphic structures develop. Polymorph A is produced by either melt cooling for side chains with $n \geq 6$ or for solution crystallized samples with side chains having $n \leq 8$ carbon atoms. A sample crystallized from solution with ten or more carbons per side chains results in

modification B. PPAOT in modification B undergoes a solid-solid phase transition to modification A during heating. Once the sample is in modification A the structure will slowly convert back into polymorph B under ambient conditions, indicating that B is the thermodynamically more stable phase at lower temperatures, while modification A is stable at higher temperatures.[50] For PPAOTs with 10 carbon atoms per side chain a second transition from modification A to liquid crystalline state is reported before the final melting [49]. The spacing between the layers is larger in modification A and increases for both polymorphs with the number of side chain carbons, whereas the distance between the $\pi - \pi$ -stacks is larger in B and changes only little with the side chain length. Overall the volume density of each CH_2 group is lower in modification B, suggesting crystalline packing in the nanophases, whereas for A a disordered packing is assumed.[50] The four model systems for comb-like polymers, as suggested by Danke et al. [49], are shown in the introductory chapter in Figure 1.3: modification B of PPAOTs can be described by a fully crystalline system, while modification A can be referred to a model with crystalline sub-units. For PPAOTs with 10 carbon atoms per side chain a liquid crystalline state is detected. The fourth model with a disordered main chain and crystalline side chains is not found for PPAOTs.[49]

The structure and dynamics of the polymorphs in PPAOTs with 10 carbons per side chain (PPDOT) are discussed in chapter 4.3 of this thesis. The well-ordered backbones in $\pi - \pi$ -stacks in both modifications differ in their conformation, but in both polymorphs no indication of a backbone-amorphous phase is detected, which suggests a complete ordering of the sample in a layered morphology. The observed liquid-crystalline phase, which acts as a precursor to the crystal phase formation, is suspected to minimize the formation of a backbone-amorphous phase.

3 | Experimental Methods

In this chapter the experimental methods, primarily the nuclear magnetic resonance (NMR) spectroscopy, will be discussed. At first an introduction to the basic concepts of NMR, the nuclear spin and its interactions in a multispin system, as well as the resulting effects of coupled (interacting) spins on the detected signal is given. This is followed by the description of the important influence of external and internal motions within the sample, which can vary over a wide range of timescales, and the related relaxation effects. Afterwards the utilization of the spin-spin interactions, such as the direct dipole-dipole coupling and the chemical shift anisotropy, is described for several NMR pulse sequences. These interactions can be used for the structural and dynamical characterization of the polymer systems that are presented in this thesis. The complementary method, polarization optical microscopy, was used to study the growth rate of spherulites and will also be briefly addressed in this chapter. Much of the following explanations and theoretical descriptions of fundamental NMR concepts are based on the book of M. Levitt [55], unless otherwise stated.

3.1 Fundamentals of nuclear magnetic resonance (NMR)

3.1.1 Nuclear spin

The spin of a nucleus can be understood as a form of (spin) angular momentum and is an intrinsic property of each material. Nuclear magnetic resonance (NMR) spectroscopy utilizes this intrinsic property of a nuclear spin, which has the nuclear spin quantum number I_s , as well as the resulting nuclear magnetism. The ground state nuclear spin I has the lowest energy state and can be regarded as an empirical property of each nucleus. In general, the energy difference between the ground and excited spin states is large and therefore the excited states will be ignored in the following discussions.

Once the material is brought into a magnetic field, the degeneracy of the ground state nuclear spin is broken. The resulting splitting of the energy level is referred to as nuclear Zeeman splitting and increases with increasing magnetic field strength, but is still much smaller than the thermal energy at ambient temperatures. NMR spectroscopy is based on the Zeeman splitting of the ground state nuclear spin I in

the presence of a magnetic field and therefore cannot be applied to atoms or isotopes having a ground state $I = 0$, such as the common carbon isotope ^{12}C in organic matter. Representatives for spin- $1/2$ nuclei, that are relevant for the investigation of organic matter, are the most common hydrogen isotope ^1H and the rare ^{13}C isotope. In this work the focus lies solely on the investigation of spin- $1/2$ nuclei.

In quantum mechanics the wavefunction describing the spin state under the influence of a time-dependent interaction is given by the solution of the time dependent Schrödinger equation [101]

$$\frac{d}{dt} |\psi\rangle (t) = -i\hat{\mathcal{H}} |\psi\rangle (t) \quad (3.1)$$

The Hamiltonian of an unperturbed spin- $1/2$ nuclei in an external magnetic field B , is $\hat{\mathcal{H}} = \mu \cdot B$ with the magnetic moment μ , which is closely linked to the nuclear spin angular momentum I via $\hat{\mu} = \gamma\hat{I}$, where γ is the gyromagnetic ratio of the nuclei.[101] With the assumption that the external magnetic field is aligned along the z -direction, the Hamiltonian of an unperturbed spin- $1/2$ nuclei is [101]

$$\hat{\mathcal{H}} = \mu \cdot B = \gamma\hbar\hat{I}_z B \quad (3.2)$$

with the energy eigenstates $|\alpha\rangle = \begin{pmatrix} 0 \\ 1 \end{pmatrix}$ and $|\beta\rangle = \begin{pmatrix} 1 \\ 0 \end{pmatrix}$, which are both eigenstates of the operator \hat{I}_z and have the eigenvalues $\pm 0.5\gamma B_0$. B_0 is the magnetic field at the site of the nuclei. The energy difference between both states is equal to the Zeeman splitting and to the so-called Larmor frequency $\omega_0 = -\gamma B_0$. [101]

The population of the eigenstates are given by the Boltzmann distribution for an ensemble of noninteracting spins- $1/2$ in thermal equilibrium. At a given temperature T the lower energy state $|\alpha\rangle$ is more populated than the higher-energy eigenstate $|\beta\rangle$, resulting in a net polarization along the external magnetic field. The net polarization can be represented as a magnetization vector \vec{M} , that points along the z -axis as shown in Figure 3.1. This magnetization can be manipulated by an irradiation with a radio frequency (RF) pulse, which oscillates with the Larmor frequency ω_0 and is therefore on-resonance with the precession of the spins. Thus, the oscillating field B_{RF} , generated by the RF-pulse, can change the spin polarization, even though the field is many magnitudes smaller than the static magnetic field. Once a RF-field is applied to the magnetization is rotated by an angle

$$\beta_\phi = \omega_{nut}\tau = \left| \frac{1}{2}\gamma B_{RF} \right| \tau \quad (3.3)$$

The flip angle depends on the so-called nutation frequency ω_{nut} , which is proportional to the strength of the applied RF-field $B_{RF} \sim \cos(\omega_0\tau + \phi_O)$ and its duration τ . The

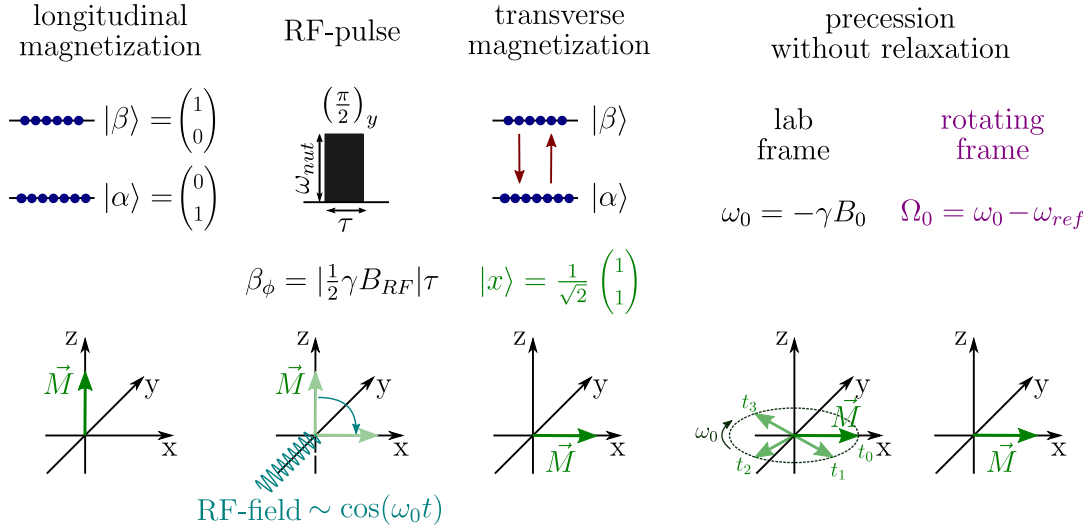


Figure 3.1: *First column:* An ensemble of noninteracting spin- $1/2$ in a strong, static magnetic field, which reached a state of thermal equilibrium, has a longitudinal magnetization \vec{M} arising from the population difference of the energy eigenstates $|\alpha\rangle$ and $|\beta\rangle$. The magnetization can be represented as a vector pointing along the direction of the external magnetic field z . *Second column:* A $(\pi/2)_y$ -pulse flips the magnetization \vec{M} along the x -axis in the transverse plane and thus, generates transverse magnetization. *Third column:* The spin state $|x\rangle$ is described by a superposition of $|\alpha\rangle$ and $|\beta\rangle$. The arrows represent quantum coherence. *Fourth column:* The transverse magnetization precesses in the lab frame with the Larmor frequency ω_0 . In the rotating frame the magnetization is static if $\omega_0 \simeq \omega_{ref}$. Adapted from reference [55].

phase ϕ_0 describes the axis $(\pm x, \pm y)$ at which the RF-pulse is applied. A $(\pi/2)_y$ -pulse flips the magnetization by an angle of $(\pi/2)$, or 90° , to the x -axis into the transverse x - y plane, as shown in Figure 3.1. The magnetization in the transverse plane, pointing along x , can be described by a superposition state $|x\rangle = 1/\sqrt{2}|\alpha\rangle + 1/\sqrt{2}|\beta\rangle$. Arrows between the states $|\alpha\rangle$ and $|\beta\rangle$ represent the presence of quantum coherences, or in other words the presence of transverse magnetization. The transverse magnetization is time-dependent and precesses with the Larmor frequency ω_0 around the axis of the external magnetic field. In order to spare the unnecessary time dependence of the magnetization in theory and also for illustrations in the vector model, one uses the framework of a so-called rotating frame. An observer rotates with a reference frequency ω_{ref} which is similar to ω_0 and therefore the magnetization appears to be static. Not all spins in real systems have the exact same or theoretical predicted Larmor frequency and thus an offset frequency $\Omega_0 = \omega_0 - \omega_{ref}$ is needed to describe the system. The effects of the offset and the related chemical shift are further described in chapter 3.1.2.

One of the simplest NMR experiments is called a free induction decay (FID) and consists of one $\pi/2$ -pulse (in Figure 3.2 applied along the y -axis). The detection of the transverse magnetization starts, with a short delay, directly after applying the pulse.

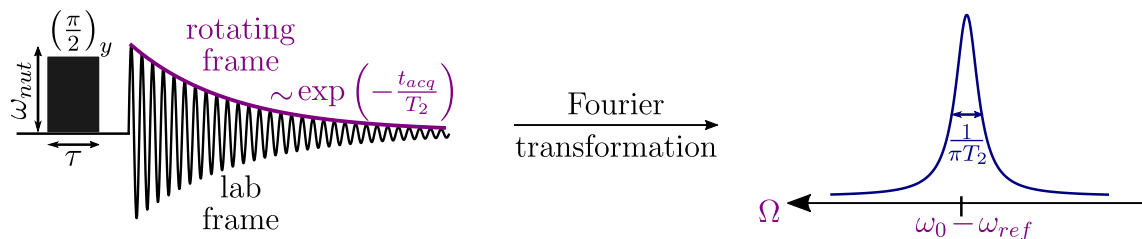


Figure 3.2: A $(\pi/2)_y$ -pulse is applied to an ensemble of noninteracting spins in a static magnetic field and generates transverse magnetization. The FID intensity decays exponentially with the transverse relaxation time T_2 . In the lab frame the signal also oscillates with the Larmor frequency ω_0 . The Fourier transformation of an exponential decaying function yields a Lorentzian peak with the peak width at half height equal to $1/\pi T_2$. Adapted from reference [55].

This delay, which is called dead time, is caused by the time needed to turn the receiver on after the end of the strong RF-pulse. The NMR signal is detected, utilizing the same coil that is used to apply the RF-pulse, for a specific acquisition time t_{acq} and decays proportional to $\exp(-t_{acq}/T_2)$, where T_2 is the transverse relaxation time. In the lab frame the decaying signal oscillates with the Larmor frequency ω_0 , whereas in the rotating frame the signal can be described by an exponential decay that oscillates with Ω_0 . For a pulse that is applied exactly on-resonance, Ω_0 is equal to zero. A Fourier transformation of the time-dependent signal yields a Lorentzian peak with the center frequency ω_0 in the lab frame or $\Omega_0 = \omega_0 - \omega_{ref}$ in the rotating frame. The peakwidth at half height is equal to $1/\pi T_2$. A fast exponential decay in the time-domain is characterized by a low T_2 -value, resulting in a broad peak in the frequency domain and vice versa. Note, that the described signal shown in Figure 3.2 arises from the model case of an ensemble of noninteracting spins, which all have the exact same Larmor frequency. The detection of an FID in a multiphase system with coupled spins will be discussed in chapter 3.2.1. Spin interactions and the concept of relaxation will be discussed in the following chapters.

3.1.2 Spin interactions

The solution of the time-dependent Schrödinger equation yields the description of all interactions in the sample. In order to simplify and solve the equation, the contributions of the electrons in the system are neglected and only the nuclear spin states appear in the Hamiltonian $\hat{\mathcal{H}}_{spin}$. The time-dependent Schrödinger equation is then given by

$$\frac{d}{dt} |\psi_{spin}\rangle(t) = -i\hat{\mathcal{H}}_{spin} |\psi_{spin}\rangle(t) \quad (3.4)$$

with the wave function $|\psi_{spin}\rangle(t)$, describing the spin state of a nucleus. The nuclear

spin Hamiltonian $\hat{\mathcal{H}}_{spin}$ includes contributions of external and internal spin interactions. External interactions are caused by the interaction of the nucleus with external electric or magnetic fields. A spin- $1/2$ nuclei has a spherically symmetric charge distribution and therefore does not interact with the electronic environment, resulting in an electron spin Hamiltonian $\hat{\mathcal{H}}_{el}$ equal to zero. The magnetic spin Hamiltonian $\hat{\mathcal{H}}_{mag}$ is composed of three contributions. The homogeneous, strong, static magnetic field, the radio-frequency (RF) field generated by a RF pulse and a gradient field, which is used in diffusion experiments. Internal interactions are caused by electric or magnetic fields that originate from the nuclei and its surrounding electrons. The internal spin interactions will now be discussed in the following paragraphs.

Chemical shift and chemical shift anisotropy The magnetic field at the site of the nuclei B_0 is given by the sum of the static magnetic field B and a comparably small local field B_{loc} . The local field experienced by two nuclei differs, if their electronic environment or also the conformation in a polymer chain is different, e.g. for a CH-group in comparison to a CH₂-group or an all-trans chain compared to a gauche-rich conformation. These local fields are caused by the static magnetic field, which induces currents in the electrons clouds. These currents also generate a small magnetic field that is—for protons—three to five orders of magnitude smaller than the static field. The superposition of the static and the induced (local) field yields the field at the site of a nuclei B_0 . The difference in the experienced field B_0 is described by the chemical shift δ in **parts per million** (ppm) and is calculated via

$$\delta = \frac{\Omega_0}{\omega_{ref}} = \frac{\omega_0 - \omega_{ref}}{\omega_{ref}} \quad (3.5)$$

with the apparent Larmor frequency of a nuclei $\omega_0 = \gamma \cdot B_0$ and a reference frequency ω_{ref} . The chemical shift is a universal parameter in NMR, since it is independent of the strength of the static magnetic field. The induced field in a molecule can often be described as anisotropic, since the electronic environment around the nuclei is—in most cases—not spherical. The experienced field B_0 and consequently also the chemical shifts are anisotropic and depend on the orientation of the molecule with respect to the static magnetic field. One speaks of chemical shift anisotropy (CSA). In isotropic liquids, the fast molecular motions average the anisotropy and one observes NMR spectra with one sharp peak at the isotropic chemical shift ω_{iso} . In a solid powder sample the molecules exhibit all possible orientations in respect to the static magnetic field. All crystal orientations have a distinct Larmor frequency and thus, a distinct chemical shift that depends on the alignment towards the static field. The observed spectra, so-called powder patterns, are a superposition of all individual peaks arising from each crystal in its orientation. The broadening effect of

the CSA on the spectra is an example for inhomogenous broadening. In such spectra, the peak width at half-height exceeds the expected value of $1/\pi T_2$ and consequently the corresponding transverse relaxation time T_2 is apparently shortened.

Direct dipole-dipole coupling The direct dipole-dipole coupling (DD-coupling) is a through space interaction of a spin with the magnetic field that is generated by another spin and vice versa. The magnitude of the DD-coupling constant D is inversely proportional to the cube of the spin-spin-distance r_{jk}^3 ; it is given by

$$D = -\frac{\mu_0}{4\pi} \cdot \frac{\gamma_j \gamma_k \hbar}{r_{jk}^3} \quad (3.6)$$

where μ_0 is the magnetic constant and γ the gyromagnetic ratio of the spins j and k . In the presence of the large external magnetic field some internal spin interactions are masked by the strong interaction of the spins with the external field. Thus, one can use the secular approximation of the internal spin Hamiltonian. The secular dipole-dipole Hamiltonian describing the DD-coupling of two spins j and k for the homonuclear or heteronuclear cases are,

$$\hat{\mathcal{H}}_{jk}^{DD} = d_{jk}(3\hat{I}_{jz}\hat{I}_{kz} - \hat{\mathbf{I}}_j \cdot \hat{\mathbf{I}}_k) \quad (\text{homonuclear case}) \quad (3.7)$$

$$\hat{\mathcal{H}}_{jk}^{DD} = 2d_{jk}\hat{I}_{jz}\hat{I}_{kz} \quad (\text{heteronuclear case}) \quad (3.8)$$

$$\text{with } d_{jk} = D \cdot P_2(\cos(\theta_{jk})) \quad (\text{secular DD-coupling}) \quad (3.9)$$

$$\text{and } \hat{\mathbf{I}}_j \cdot \hat{\mathbf{I}}_k = \hat{I}_{jx} \cdot \hat{I}_{kx} + \hat{I}_{jy} \cdot \hat{I}_{ky} + \hat{I}_{jz} \cdot \hat{I}_{kz} \quad (3.10)$$

where $\hat{\mathbf{I}}_j \cdot \hat{\mathbf{I}}_k$ is the product of the spin angular momentums $\hat{\mathbf{I}}_j$ and $\hat{\mathbf{I}}_k$, with its three components; \hat{I}_x , \hat{I}_y and \hat{I}_z . $P_2(\cos(\theta_{jk})) = 0.5(3\cos^2(\theta_{jk}) - 1)$ is the second Legendre polynomial. θ_{jk} describes the angle between the static magnetic field and the connecting vector of the spins j and k . Therefore, the secular DD-coupling constant d_{jk} and consequently both dipolar couplings are dependent on the molecular orientation. At the magic angle $\theta_{MA} = \arctan(\sqrt{2})$ the secular dipolar coupling is zero. In an isotropic liquid intramolecular and short-range intermolecular dipole-dipole couplings average to zero, whereas long-range intermolecular couplings remain, but are often very small and may be ignored. In a solid sample one spin is coupled to every other spin in the immediate vicinity and both inter- and intramolecular dipole-dipole couplings can be present.

J -coupling The indirect spin-spin coupling or J -coupling arises from the interaction of the nuclei with the surrounding electrons of the second spin, with which they are chemically bonded. The detected chemical shift allows to investigate the local

environment in an isotropic liquid where the direct dipole-dipole coupling is—to a good approximation—averaged to zero. The J -coupling is present in a solid, but is often overpowered by the much larger DD-coupling and is therefore often ignored.

Spin-rotation The positive and negative electric charges of the molecule, caused by the nuclei and the electrons respectively, are in motion if the molecule rotates or tumbles. These motions of the electric charges and therefore of their electric currents result in a fluctuating magnetic field, which can interact with the spin magnetic moment. For spin- $1/2$ nuclei, this interaction is much smaller than the dipole-dipole coupling and the chemical shift anisotropy and is only important for small molecules.

Quadrupole coupling A nuclei with $I > 1/2$ has an electric quadrupole moment which interacts with the electric field gradient that is generated by the surrounding electron clouds. The investigated nuclei in this work are solely spin- $1/2$ nuclei and thus the quadrupolar coupling is not discussed further.

Coupled spin- $1/2$ pair In a spin- $1/2$ -pair the interactions can either be homonuclear or heteronuclear. In both cases, the spin state of a coupled spin pair is described by

$$|\psi\rangle = c_{\alpha\alpha} |\alpha\alpha\rangle + c_{\alpha\beta} |\alpha\beta\rangle + c_{\beta\alpha} |\beta\alpha\rangle + c_{\beta\beta} |\beta\beta\rangle \quad (3.11)$$

$$\text{with } 1 = |c_{\alpha\alpha}|^2 + |c_{\alpha\beta}|^2 + |c_{\beta\alpha}|^2 + |c_{\beta\beta}|^2$$

with the so-called Zeeman products states of the coupled spin- $1/2$ -pair, $|\alpha\alpha\rangle$, $|\alpha\beta\rangle$, $|\beta\alpha\rangle$ and $|\beta\beta\rangle$. The secular spin Hamiltonian of a spin- $1/2$ -pair describing the internal spin interactions is given by

$$\hat{\mathcal{H}}_{int} = \omega_{0,j} \hat{I}_{1z} + \omega_{0,k} \hat{I}_{2z} + \hat{\mathcal{H}}_{jk}^J + \hat{\mathcal{H}}_{jk}^{DD} \quad (3.12)$$

$\omega_{0,j}$ and $\omega_{0,k}$ are the Larmor frequencies of the spin j and k . $\hat{\mathcal{H}}_{jk}^J$ and $\hat{\mathcal{H}}_{jk}^{DD}$ are the Hamilton operators for the J- and DD-coupling, respectively, which can be both either homo- or heteronuclear. The dipolar Hamiltonians are given in equation 3.7 and 3.8. The quadrupolar coupling is zero for spin- $1/2$ nuclei and therefore not taken into account.

3.1.3 Relaxation

Relaxation describes the behavior of the spins in a static, strong external magnetic field once they have been disturbed, e.g. by a radio-frequency pulse. The time-dependent decay of the coherences in the x - y plane is called spin-spin relaxation, described by the transverse relaxation time T_2 . The spin-lattice relaxation time

constant T_1 is proportional to the time, which is necessary to reach their thermal equilibrium in the external magnetic field. The time between subsequent scans, the recycle delay, is given by $\sim 5 \cdot T_1$. In spin- $1/2$ nuclei, the relaxations are a consequence of fluctuating magnetic fields experienced by the nuclei and are caused by thermal motions, dipole-dipole couplings and chemical shift anisotropy. In solid state the effect of spin rotations can be neglected.

Random field relaxation The transverse magnetization $B_{x,y}$ of an ensemble of non-interacting spins in a static, strong external magnetic, which has been generated by an $\pi/2$ -pulse, fluctuates with time. These fluctuations arise independent of spin interactions or orientation dependence and their time-average is zero. A description takes place through an autocorrelation function,

$$G(\tau) = \langle B_{x,y}(t)B_{x,y}(t + \tau) \rangle \stackrel{\text{assumption}}{\approx} \langle B_{x,y}^2 \rangle \cdot \exp(-\tau/\tau_c) \quad (3.13)$$

that describes the fluctuating field at a time t compared to a later time $t + \tau$. For long times τ , $G(\tau)$ decays to zero. The decay is often assumed to be a single exponential function, with the correlation time τ_c . Rapid fluctuations cause a fast decay of the autocorrelation function and have a small τ_c -value, and vice versa. A related quantity is the spectral density $J(\omega)$, which is defined as the Fourier transform of $G(\tau)$ multiplied by two. Hence, $J(\omega)$ is proportional to an absorptive Lorentzian

$$J(\omega) = 2 \cdot \int_0^\infty G(\tau) \exp(i\omega\tau) d\tau = 2\langle B_{x,y}^2 \rangle \frac{\tau_c}{1 + \omega^2\tau_c^2} \quad (3.14)$$

Slow fluctuations of $B_{x,y}$ result in a long correlation time and a narrow spectral density. The longitudinal relaxation in an ensemble of noninteracting spins depends on the transition probabilities between the eigenstates $|\alpha\rangle$ and $|\beta\rangle$. The eigenstates underlie the Boltzmann distribution, as shown in Figure 3.1. The transition probability from state $|\alpha\rangle$ to $|\beta\rangle$, W_- , and $|\beta\rangle$ to $|\alpha\rangle$, W_+ , can be calculated via

$$W_\pm = W \left(1 \pm \frac{1}{2} \frac{\hbar\gamma B}{k_B T} \right) \quad \text{with } W = 0.5 \gamma^2 \langle B_{x,y}^2 \rangle J(\omega_0) \quad (3.15)$$

with the Boltzmann constant k_B , the temperature T and the spectral density at the Larmor frequency $J(\omega_0)$. The magnetization M_z along the external magnetic field in thermal equilibrium is given by the difference of the spin state populations. Once the system has been perturbed, e.g. by an RF-pulse, the magnetization along z at a time point t is given by

$$M_z(t) = M_0^\infty \cdot (1 - \exp(-t/T_1)) \quad (3.16)$$

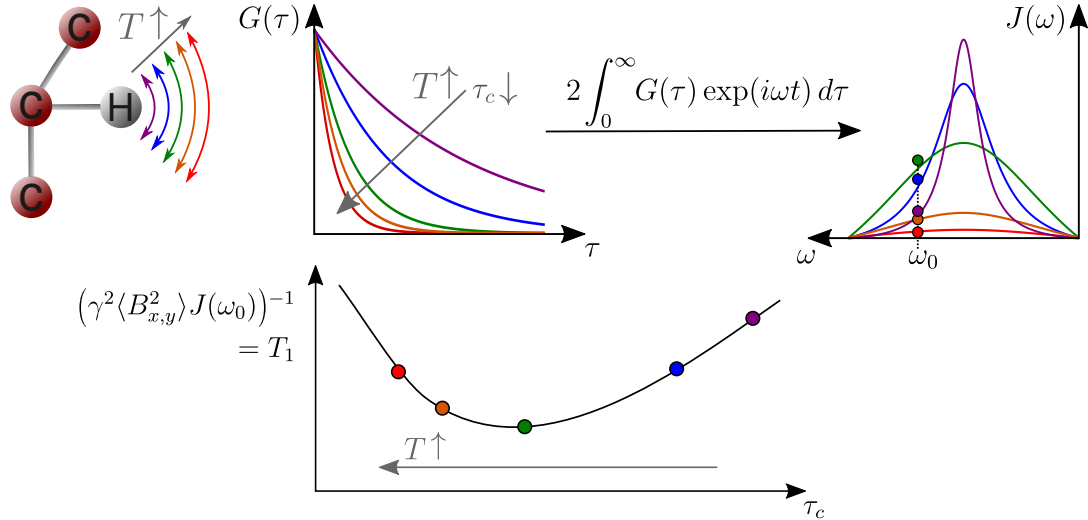


Figure 3.3: The motions of a fluctuating hydrogen atom are increasing with higher temperatures T , resulting in a decreasing correlation time τ_c . Accordingly, the auto-correlation function $G(\tau)$ decays faster at higher temperatures. For small correlation times the spectral density $J(\omega)$ is very broad. With increasing τ_c the spectra becomes more narrow. The value of the spectral density at the Larmor frequency $J(\omega_0)$ is highlighted with the colored circles in the upper right graph. The dependence of the longitudinal relaxation time T_1 on τ_c and T is shown below. The inverse proportionality of T_1 on spectral density at the Larmor frequency results in a first decrease of T_1 with increasing correlation times until a minimum value is reached and is then followed by an increase. Adapted from reference [55].

with the spin-lattice relaxation time $T_1 = (2W)^{-1} = (\gamma^2 \langle B_{x,y}^2 \rangle J(\omega_0))^{-1}$. Thus, the longitudinal relaxation time depends on the correlation time of motion, according to equation 3.14, and reaches a minimum value at a specific τ_c .

In Figure 3.3 the change of the correlation times with increasing temperatures are shown exemplarily on a fluctuation hydrogen atom. For increasing temperatures T the correlation time of motion τ_c decreases, which results in a faster decay of the autocorrelation function $G(\tau)$. The spectral density, calculated according to equation 3.14, is broad for small correlation times (high T) and becomes narrower for larger values of τ_c . Thus, for fast motions the spectral density at the Larmor frequency $J(\omega_0)$ is small. With increasing values of τ_c (decrease of T) the spectral density becomes more narrow and the value of $J(\omega_0)$ rises and reaches a maximum at a specific correlation time. For even slower motions $J(\omega_0)$ decreases again. The longitudinal relaxation time T_1 is inversely proportional to $J(\omega_0)$, resulting in a T_1 minimum.

Dipole-dipole relaxation In a real sample, the interaction between spins influences the relaxation behavior. In a solid sample the direct dipole-dipole coupling is the strongest interaction between two $1/2$ -spins. The transition probabilities and thus also the longitudinal relaxation time are strongly influenced by these interac-

tions. Two homonuclear coupled spin- $1/2$ have twelve transitions between the four eigenstates; with two zero, eight single and two double quantum transitions. The transition probabilities are given by

$$\underbrace{W_0 = \frac{1}{10}D^2J(0)}_{\text{zero quantum coherence}} \quad \underbrace{W_1 = \frac{3}{20}D^2J(\omega_0)}_{\text{single quantum coherence}} \quad \underbrace{W_2 = \frac{3}{5}D^2J(2\omega_0)}_{\text{double quantum coherence}} \quad (3.17)$$

Thus, the influence of the dipole-dipole coupling on the transition probabilities depends on the internuclear distance ($D \sim r_{jk}^{-3}$) with an inverse power of six. The spin-lattice relaxation for the intramolecular dipole-dipole relaxation of a two-spin system can be calculated to

$$T_1 = \left[\frac{3}{10}D^2 (J(\omega_0) + 4J(2\omega_0)) \right]^{-1} \quad (3.18)$$

and its T_1 - τ_c -dependence is qualitative similar to the one for random field fluctuations shown in Figure 3.3. The transverse relaxation time T_2 describes the decay of the coherences in a spin ensemble and is caused by the *loss* of synchronization of the precessing spins. The fluctuating fields that are experienced by each spins vary over time and this results in a gradual loss of the coherences. The transverse relaxation time T_2 of intramolecular dipolar coupled spins is given by

$$T_2 = \left[\frac{3}{20} \cdot D^2 (3J(0) + 5J(\omega_0) + 2J(2\omega_0)) \right]^{-1} \quad (3.19)$$

A larger dipolar coupling constant D results in a faster decay of the coherences. The differences in the transverse relaxation times can be used to differentiate between mobile and rigid regions in a two-phase system and allows to quantify the volume fractions in a given system in terms of the amplitude of the relaxation contributions. A T_2 -filter can be used to selectively polarize the mobile phase in a sample. These applications are further described in chapter 3.2.1 and 3.3.4. The effect of motions on relaxation is subject of the following section.

$T_{1,\rho}$ relaxation The transverse magnetization, obtained by a $\pi/2$ -pulse, can be “locked” at a specific direction in the rotating frame by applying a resonant RF field, a so-called “spin-locking” pulse, along this direction. The transverse magnetization cannot precess if the spin-lock pulse is strong enough and thus the free evolution of the transverse magnetization is suppressed. The spin-locked magnetization will decay to zero with the characteristic $T_{1,\rho}$ relaxation time, the longitudinal relaxation in the rotating frame. This methods allows to study slow molecular dynamics.

3.1.4 Motions

Motional processes Internal or external motions can strongly influence the detected NMR spectra. An external motion can be applied to the sample by magic-angle spinning, where the complete sample is mechanically rotated at the magic angle $\theta_{MA} = \arctan(\sqrt{2})$. The fast rotation averages anisotropic spin interactions, such as the chemical shift anisotropy and dipole-dipole interactions (see chapter 3.3). Internal motions in the sample can be probed by NMR spectroscopy over a wide range of timescales. The detection is possible once the molecular motions have changed the nuclear spin Hamiltonian. The characteristic time-scales of motions in NMR are the Larmor timescale in the range of nanoseconds, defined by: $\tau_0 \sim \omega_0^{-1}$; the spectral timescale τ_{spec} in the range of micro to milliseconds: $\sim |\omega_{0,1} - \omega_{0,2}|^{-1}$ and the relaxation timescale given by the spin-lattice relaxation time T_1 . Molecular vibrations of light atoms, such as hydrogen, and often also local rotations, for example of a methyl group, are very fast motions in the range of femto to picoseconds and are thus faster than the Larmor timescale. Molecular motions, e.g. rotations, in a liquid and also segmental motions in a polymer are often in the same time range as the inverse Larmor frequency. Chemical exchange, which influences the chemical shift and the J -coupling, can vary from nanoseconds to seconds. The effect of the exchange rate k on the NMR lineshape is discussed below. Macroscopic diffusion and flow are also in the range of seconds and can change the nuclear spin interactions in an inhomogeneous magnetic field. This effect is utilized in diffusion experiments.

Motional effects Motions with different timescales influence the nuclear spin dynamics differently and the effects can be seen in changes of relaxation processes or in the NMR lineshape. Motions that are faster than the Larmor timescale will average the nuclear spin Hamiltonian before the secular approximation. This non-secular Hamiltonian will strongly affect relaxation processes, whereas the secular Hamiltonian influences the NMR lineshape. Motions described by the inverse Larmor frequency are responsible for and influence the spin-lattice relaxation. Processes at the spectral timescale have a strong influence on the form of the NMR spectrum. These effects are further discussed below. Slower motions normally do not influence the NMR lineshape or relaxation processes, but can be detected with e.g. exchange experiments.[102]

Motional Lineshapes Motions in the range of the spectral lineshape have a strong influence on the appearance of the NMR spectra and thus, may also affect the transverse relaxation time T_2 . According to equation 3.19, T_2 decreases with increasing correlation times. Thus, for intermediate towards faster motions a motional narrowing of the spectra takes place, resulting in an increase of T_2 . However, as opposed to equation 3.19, the T_2 measured in an echo experiment, where the main interaction

is refocused, displays a minimum and increases again towards slower motions. This effect is exemplarily shown in Figure 3.4 on a symmetric two-site exchange of an isolated spin, that exchanges between two chemical sites. The Larmor frequencies at each site differ and are given by $\omega_{0,1}$ and $\omega_{0,2}$. The comparison of the exchange rate k with the chemical shift difference of both sides allows to distinguish between two regimes: slow intermediate motions characterized by a slow exchange rate with $k < 0.5 \cdot |\omega_{0,1} - \omega_{0,2}|$ and a high exchange rate with $k > 0.5|\omega_{0,1} - \omega_{0,2}|$. Even though the exchange rate may vary, the transitions between both sites are extremely fast. For a slow exchange rate two distinct resonances at $\omega_{0,1}$ and $\omega_{0,2}$ are detected. The narrow peaks correspond to a long spin-spin relaxation time T_2 . For faster exchange rates the peaks coalesce, resulting in a broadening of the peak and consequently in a decrease of T_2 . However, even faster motions yield one sharp, single resonance at an averaged chemical shift $\bar{\omega}$ and one speaks of motional narrowing. Since a narrow peak is synonymous to a long transverse relaxation time, one detects an increase of T_2 .

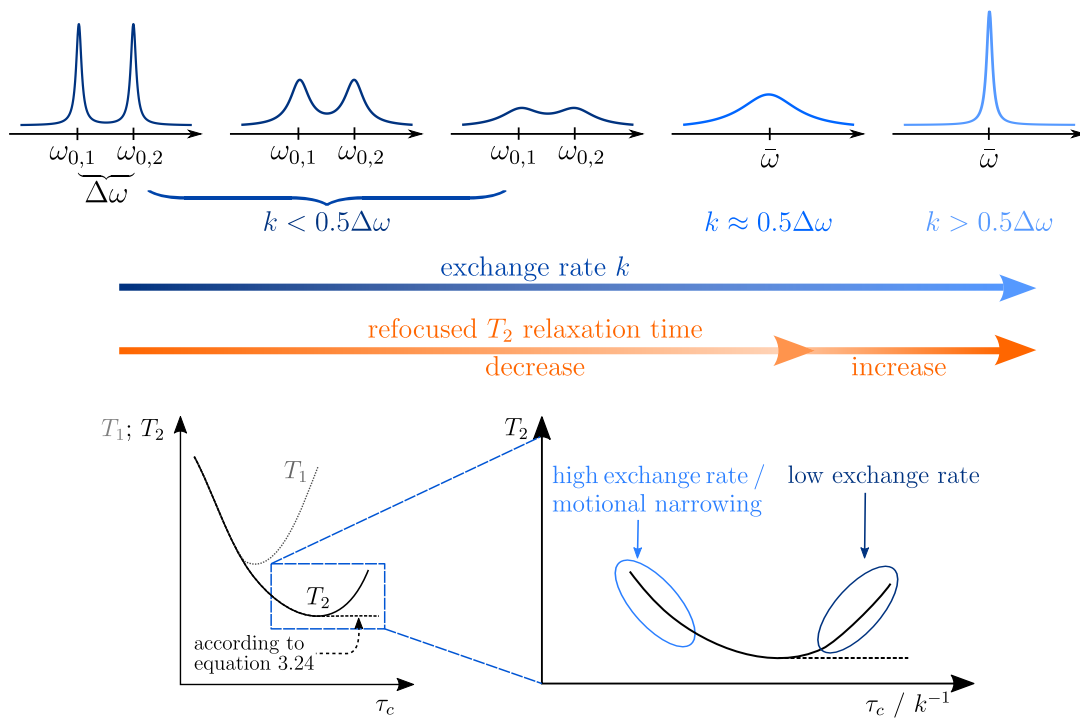


Figure 3.4: Schematic NMR spectra for a two-site exchange of a non-interacting spin. For exchange rates $k < 0.5 \cdot |\omega_{0,1} - \omega_{0,2}| = 0.5\Delta\omega$ two resonances with the chemical shifts at each site, $\omega_{0,1}$ and $\omega_{0,2}$, are detected. Increasing motions (higher exchange rate) will at first results in a coalesce of the two peaks and finally in a motional narrowed peaks for $k > 0.5 \cdot |\omega_{0,1} - \omega_{0,2}|$. The transverse relaxation time will at first decrease until the peaks are coalesced. Once the peak, at the average chemical shift $\bar{\omega}$, becomes narrow, the transverse relaxation time increases again. In the bottom plot the correlation time dependence of the longitudinal relaxation time T_1 , the transverse relaxation time T_2 according to equation 3.19 and the effect of intermediate motions are shown. Adapted from reference [55].

3.2 Static ^1H time-domain NMR

3.2.1 FID experiment in a multi-phase system

A proton (^1H) free induction decay of a multi-phase system, for example a semicrystalline polymer with a rigid and mobile phase, allows to quantify the molar fractions of each phase. The different dipole-dipole couplings in the amorphous and rigid phase of a semicrystalline polymer result in a different transverse relaxation time T_2 for regions with a different mobility. A high DD-coupling causes a faster loss of coherence, characterized by a fast relaxation, whereas T_2 is long in regions with faster motions having lower residual dipolar couplings. In Figure 3.5 a FID and the contributions of its amorphous, intermediate and crystalline fractions are shown. A deconvolution in the frequency domain is impractical for a static powder sample, since the corresponding peaks of the crystalline and intermediate (rigid-amorphous) phase are broad and all three signal contributions overlap, which inhibits a deconvolution.[103] For the analysis of the detected FID the following equation is used [103]

$$I_{FID} = \underbrace{f_a \cdot e^{-(t_{acq}/T_{2,a}^*)^{\nu_a}}}_{\text{amorphous}} + \underbrace{f_i \cdot e^{-(t_{acq}/T_{2,i}^*)^{\nu_i}}}_{\text{intermediate}} + \underbrace{f_c \cdot e^{-(a^2 t_{acq}^2/2)} \cdot \sin(b \cdot t_{acq}) / (b \cdot t_{acq})}_{\text{crystalline}} \quad (3.20)$$

The amorphous and intermediate components are fitted with a stretched exponential function, where $T_{2,a}^*$ and $T_{2,i}^*$ are the apparent transverse relaxation times and the shape parameters ν_a and ν_i . In regions with a higher mobility the exponents ν are in the range of 0.8 and 2. In the crystalline phase a Gaussian distribution with $\nu = 2$, is assumed. The signal arising from the crystalline phase can be described by an Abragam function. The second moment M_2 , a measure for the dipolar coupling of the crystalline phase, can be calculated from the parameters a and b via $M_2 = a^2 + b^2/3 = 9/20 \cdot D^2$. The prefactors f_a , f_i and f_c yield the molar fractions of each phase.[103, 104]

MAPE-filter The **magic and polarization echo** is a dipolar filter, which is able to selectively detect the mobile component of the investigated system and is applied before the FID pulse sequence. This filter experiment utilizes the different mobilities in the rigid and mobile components of the sample. For sufficiently long filter times, the coherences of regions with a high dipolar coupling cannot be refocused, which allows to solely detect the signal arising from the mobile region. The detected signal can be fitted with a stretched exponential function, yielding the parameters $T_{2,a}^*$ and ν_a . These parameters are used in equation 3.20 to stabilize the fit.[103, 105]

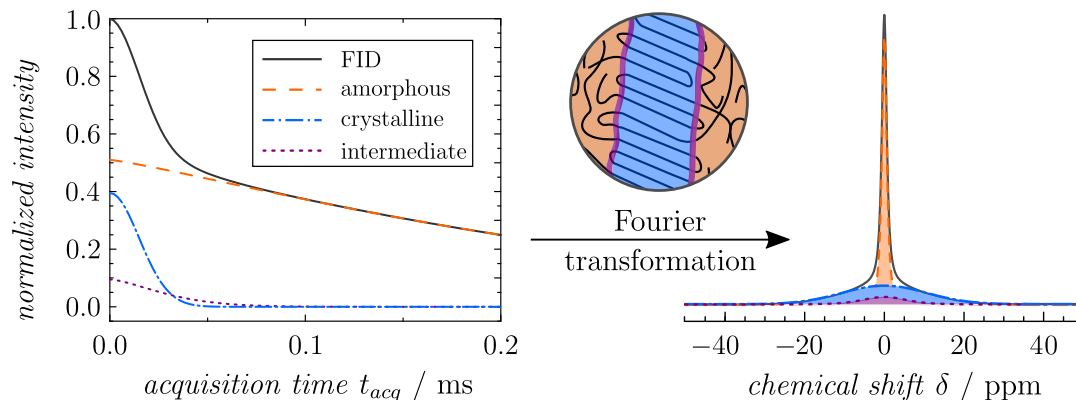


Figure 3.5: The free induction decay in the time domain (solid gray line) and its three components: amorphous (dashed orange), intermediate (dotted purple) and crystalline (blue dash-dotted). The analysis in the frequency domain would be more complicated since the signals of all three phases overlap and no good analytical approximation is available for the spectral shapes.

Anderson-Weiss approximation The broad spectral width of the rigid components in a semicrystalline polymer is caused by the orientation dependence of the homonuclear dipolar interactions. Fast intracrystalline dynamics in crystal-mobile polymers can cause a spectral narrowing, which corresponds to an increase of the transverse relaxation time and a decrease of the linewidth. Dynamics with correlation times faster or on the same timescale as t_{acq} are detectable with ^1H FIDs. The Anderson-Weiss approximation is used to analyze the motions responsible for motional narrowing, assuming a Gaussian distribution of the varying (Larmor) frequencies and an exponential decay of the autocorrelation function $G(t)$ with the correlation time τ_c . [106, 107] The approximation for the dipolar FID is given by [106, 107]

$$I_{FID}^{AW}(t_{acq}) = \exp \left[-\Delta M_2 \cdot \tau_c^2 \left(\frac{t_{acq}}{\tau_c} - 1 + e^{t_{acq}/\tau_c} \right) \right] \cdot e^{-0.5 M_2^{stat} S^2 t_{acq}^2} \quad (3.21)$$

$$\text{with } \Delta M_2 = M_2^{stat} (1 - S^2) = M_2^{stat} - M_2^{dyn}$$

with the static and dynamic second moment, M_2^{stat} and M_2^{dyn} , and the order parameter $S = \sqrt{M_2^{dyn}/M_2^{stat}}$. [106, 107] The intracrystalline dynamics (also referred to as “ α_c -relaxation”), e.g. in PEO, are temperature-dependent and the corresponding correlation time of motion decreases with higher temperatures. Figure 3.6 shows the temperature-dependence of the second moment M_2 in a PEO sample. The static second moment is detected for low temperatures. For high enough temperatures, and thus faster intracrystalline dynamics, the calculated second moment decreases and reaches M_2^{dyn} . The normalized crystalline FID signal contributions of a PEO sample display an increase of the transverse relaxation times with increasing temperatures. The correlation time of the intracrystalline dynamic τ_c and the order parameter S

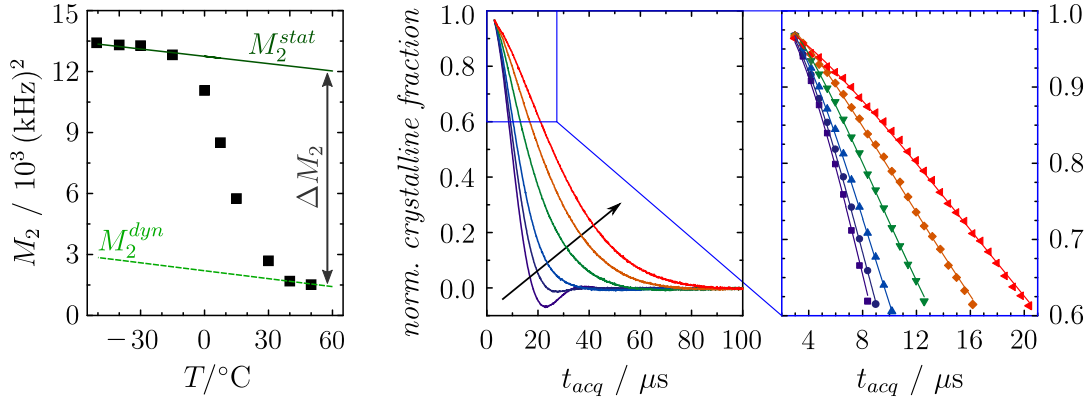


Figure 3.6: *Left*: the temperature-dependence of the calculated second moment M_2 of a isothermally crystallized PEO sample. For low temperatures and thus slow intracrystalline dynamics the second moment has its static value M_2^{stat} . Increasing the temperature gradually decreases the second moment to M_2^{dyn} . *Right*: normalized crystalline FID signal contribution for various temperatures. The increase of the transverse relaxation time is caused by the thermally activated α_c -relaxation. The first 40% of the signal can be fitted using equation 3.21, yielding the correlation time τ_c and the order parameter S .

can be derived by a simultaneous fit of the first 40% of the temperature-dependent crystalline FID signals with equation 3.21.[72, 106, 107]

The correlation time τ_c of the reorientation process, related with the intracrystalline dynamics, is given by an Arrhenius temperature-dependence [72]

$$\tau_c = \tau_0 \cdot \exp\left(\frac{E_a}{kT}\right) \quad (3.22)$$

with the activation energy E_a and the prefactor τ_0 [72]. The proton FID analysis together with the Anderson-Weiss approximation was used to determine the temperature-dependent amorphous, intermediate and crystalline fractions and to quantify the intracrystalline dynamics in oligomer-diluted poly(ethylene oxide). The results are presented in chapter 4.1. Additionally, the ^1H FID experiment was used for the signal fraction analysis in PBSA copolymers, presented in chapter 4.2 and oligomer-diluted poly(ϵ -caprolactone) (chapter A.2). The obtained signal fractions yield only a average value over all components in the mixtures and the copolymer. Therefore other additional methods may be used to analyze the systems.

3.2.2 Saturation recovery

One method to detect the longitudinal relaxation time T_1 is the saturation recovery pulse sequence, shown in Figure 3.7. A first $\pi/2$ -pulse generates transverse magnetization \vec{M}_{xy} . Directly after the pulse the longitudinal magnetization \vec{M}_z is zero. During a waiting time τ longitudinal magnetization is gradually built up with the

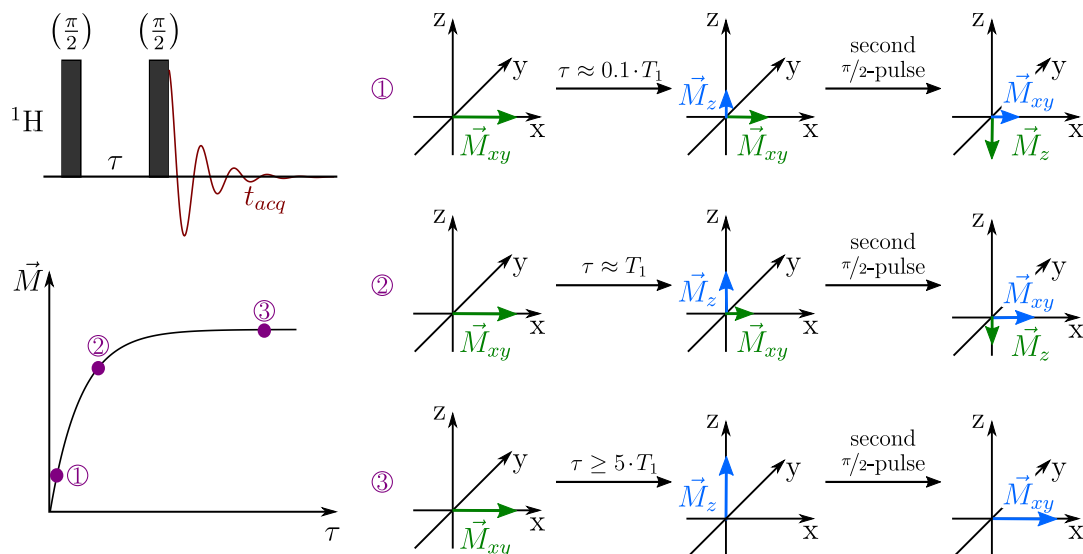


Figure 3.7: The saturation recovery sequence is an arrayed experiment, with an FID detection after increasing waiting times τ between the two $\pi/2$ -pulses. The first pulse generates transverse magnetization \vec{M}_{xy} . During the waiting time τ a certain amount of the z -magnetization \vec{M}_z is build-up again. The second $\pi/2$ -pulse is used to “read-out” this build-up z -magnetization. After a waiting time of $\tau = 5 \cdot T_1$ the complete longitudinal magnetization is restored after the perturbation with the first $\pi/2$ -pulse.

characteristic relaxation time T_1 . To detect this longitudinal magnetization a second $\pi/2$ -pulse is used to rotate \vec{M}_z into the transverse plane. The saturation recovery is an arrayed experiment, where the pulse sequence is repeated for several time points τ . The intensity build up curve can be fitted with equation 3.16.[55] After a perturbation, for example by an radio-frequency pulse, the spin system needs at least five times T_1 to reach equilibrium. This time interval, also called recycle delay, defines the waiting time between subsequent scans.[55] The saturation recovery experiment was used in all NMR experiments to determine the necessary recycle delay.

3.2.3 Proton multiple quantum (MQ) NMR

The proton dipolar coupling depends, according to equation 3.9, on the angle of the internuclear axis with respect to the external magnetic field θ_{jk} . Fast segmental dynamics can change the angle θ_{jk} resulting in an averaging of dipolar coupling if the motions are on the timescale of the inverse residual dipolar coupling constant. The time-averaged dipolar coupling in liquids or in samples with isotropic dynamics is zero. In an entangled melt or amorphous phase the segmental dynamics are weakly anisotropic due to the presence of topological constraints and yield a residual dipole-dipole coupling D_{res} .[108]

The dynamic order parameter S_b , given by time-average of the second Legendre

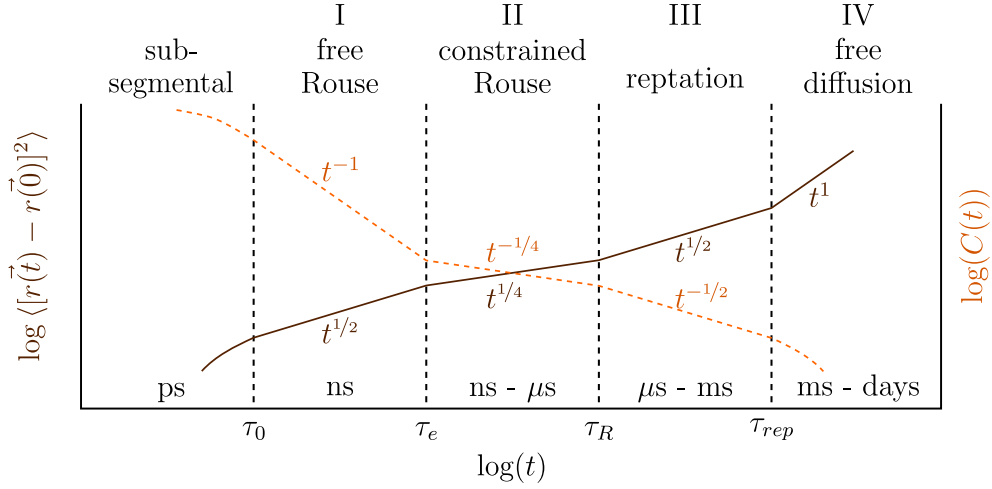


Figure 3.8: Schematic representation of the time dependence of the mean square displacement $\langle [r(\vec{t}) - r(\vec{0})]^2 \rangle$ (solid brown line) and the orientation autocorrelation function $C(t)$ (dashed orange line) according to the tube/reptation model. The regime boarders are given by the monomer relaxation time τ_0 , the entanglement time τ_e , the Rouse time τ_R and the reptation time τ_{rep} . [15, 61] Adapted from reference [111].

polynomial, can also be calculated from the ratio of the residual and static dipolar coupling (D_{res}/D_{stat}) multiplied with a prefactor k , which represents the averaging of fast motions within the segments. The value of S_b depends on the ratio of the end-to-end vector r between the chains segments and the entanglement strand end-to-end distance N_e . This allows to analyze the entanglement density in an amorphous phase or polymer melt as well as the crosslinks in an elastomer [108]

$$S_b = \langle P_2(\cos(\theta_{jk})) \rangle_t = k \frac{D_{res}}{D_{stat}} = \frac{3}{5} \frac{r^2}{N_e} \quad (3.23)$$

The MQ NMR enables the measurement of weak residual dipolar couplings also allows to access the intermediate motional regime. The motion of the segments of a polymer chain are described in terms of the orientation autocorrelation function (OACF) of the second Legendre polynomial [109, 110]

$$C(t) \sim \langle P_2(\cos \theta(t + \tau)) P_2(\cos \theta(\tau)) \rangle_\tau \sim t^{-\kappa} \quad (3.24)$$

which can be assumed to follow a power law, with the time-scaling exponent κ . The dynamic regimes of $C(t)$ are in agreement with the regimes of the tube/reptation model discussed in chapter 2.2 [109]. Figure 3.8 shows the time-dependence of the dynamic regimes for the mean square displacement $\langle [r(\vec{t}) - r(\vec{0})]^2 \rangle$ and the OACF. For the analysis of the polymer systems in this work, an optimized Baum-Pines sequence, as shown in Figure 3.9 A, was used. The sequence is based on the evolution of a spin pair under a dipolar Hamiltonian and involves the excitation of multiple

quantum (MQ) coherences. Double quantum (DQ) and also MQ coherences cannot be directly detected, but are accessed by an excitation and a reconversion pulse block into detectable (transverse) magnetization. Both the excitation and reconversion block are built up from several $\pi/2$ - and π -pulses (for details see Figure 3.9 A). The filter time τ_{DQ} can be varied by changing the cycle time t_c and/or the cycle number n_c . The intensity of the DQ quantum coherences I_{DQ} are dependent on the filter time τ_{DQ} and can be detected by using the carrier phase ϕ_0 in the excitation block and $\phi_0 + \Delta\phi$ for the reconversion. $\Delta\phi$ underlies a four step phase cycle of $\Delta\phi = x, y, -x, -y$. Together with the receiver phase $\phi_{DQ} = x, -x, -x, x$ the DQ intensity can be detected. A change of the receiver phase to $\phi_{ref} = x, x, x, x$ allows to detect the reference intensity I_{ref} , which includes all magnetization that has not been excited to MQ coherences.[111, 112] The addition of the DQ and reference intensity yields the sum intensity $I_{\Sigma MQ}$: [111, 112]

$$I_{\Sigma MQ} = \underbrace{\langle \sin \phi_1 \sin \phi_2 \rangle}_{I_{DQ}} + \underbrace{\langle \cos \phi_1 \cos \phi_2 \rangle}_{I_{ref}} \quad (3.25)$$

$$\text{with } \phi_1 = D_{stat}/k \int_0^{\tau_{DQ}} P_2(\cos \theta(t)) dt \quad \text{and} \quad \phi_2 = D_{stat}/k \int_{\tau_{DQ}}^{2\tau_{DQ}} P_2(\cos \theta(t)) dt$$

The reference, sum and DQ signal intensities of an entangled polymer in the melt are shown in Figure 3.9 B. The intensity of I_{ref} arises from the entangled chains, as well as from dangling chain (ends), solvent or oligomers, which often display an isotropic motion without any remaining DD-coupling. These signal contributions, so-called “defects”, are detected in the reference experiment as a slowly decaying exponential function (“tail”), which has to be subtracted before the subsequent analysis.[108] An analytical fitting approach, based on the power-law model of the OACF (equation 3.24), allows to determine the effective power-law scaling exponent κ and the amplitude of the OACF. Hereby, the DQ intensity, I_{DQ} , and the sum intensity with subtracted tail, $I_{\Sigma MQ} - tail$, are simultaneously fitted with [113]

$$I_{\Sigma MQ} - tail = e^{-2\tau_{DQ}/T_2} \cdot e^{[-a \cdot ((\kappa - \kappa^2)t_0^2 + (2\kappa^2 - 4\kappa)\tau_{DQ}t_0 + 2\tau_{DQ}^{2-\kappa}t_0^\kappa)]} \cdot \sinh [0.5a \cdot ((\kappa^2 - \kappa)t_0^2 + (2^{3-\kappa} - 4)\tau_{DQ}^{2-\kappa}t_0^\kappa)] \quad (3.26)$$

$$I_{ref} = e^{-2\tau_{DQ}/T_2} \cdot e^{[-a \cdot (1.5(\kappa - \kappa^2)t_0^2 + (2\kappa^2 - 4\kappa)\tau_{DQ}t_0 + (4 - 2^{2-\kappa})\tau_{DQ}^{2-\kappa}t_0^\kappa)]} \quad (3.27)$$

with $a = 0.2 \cdot D_{res}^2 \cdot [(\kappa - 2)(\kappa - 1)]^{-1}$ and $\kappa > 0$ as well as $\kappa \neq 1, 2$. The fit is performed in the time interval ranging from the first data point t_0 until the time point, which corresponds to the maximum value of the build-up curve of I_{DQ} . The residual dipolar coupling D_{res} describes the plateau of the OACF for time points up to t_0 . The fitting

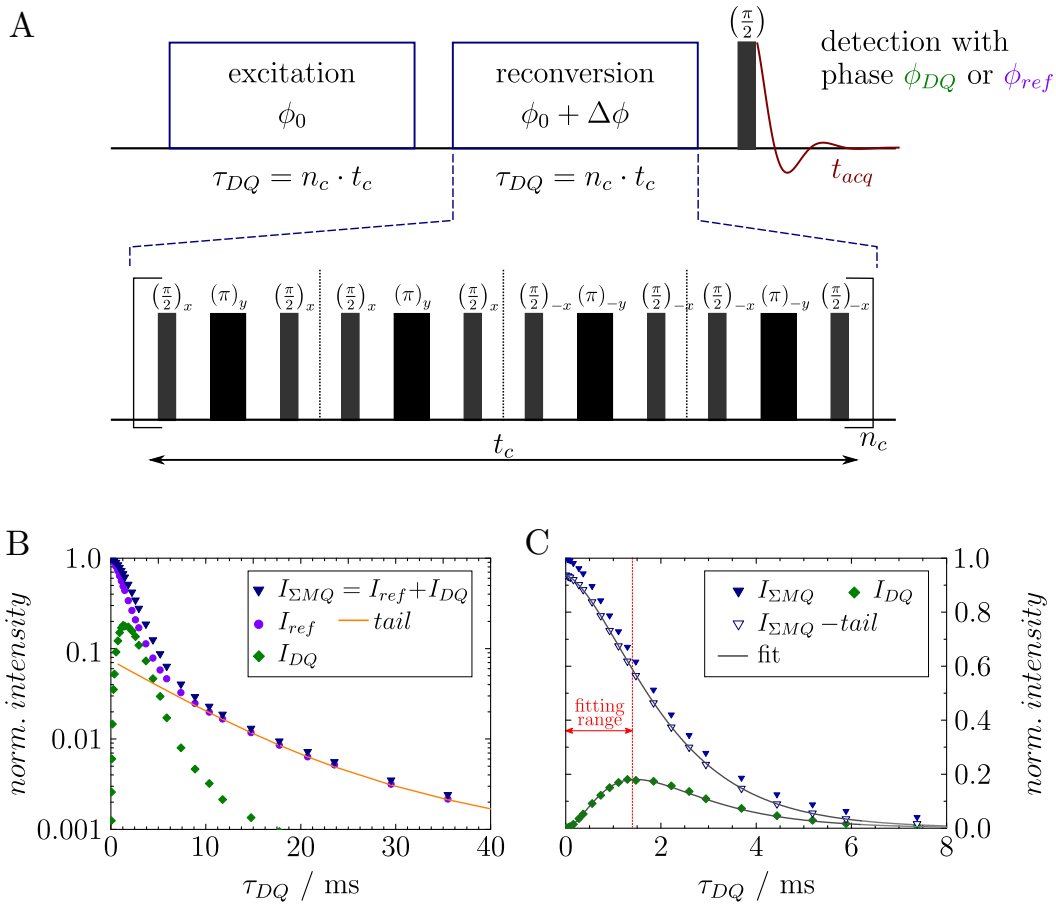


Figure 3.9: A) Optimized Baum-Pines sequence with excitation and reconversion pulse block. Each block consists of several $\pi/2$ (gray narrow rectangles) and π -pulses (black broad rectangles). In the reconversion block the carrier phase ϕ_0 is shifted by an four-phase cycle with $\Delta\phi = x, y, -x, -y$. The DQ and reference signals can be detected using different phase cycles. Adapted from reference [111]. B) Detected DQ (I_{DQ} , green diamonds) and reference signal (I_{ref} , purple circles) with tail (orange fit) and sum intensity ($I_{\Sigma MQ}$, blue upside down triangle). C) Simultaneous fit of I_{DQ} and $I_{\Sigma MQ} - tail$ (blue, open upside down triangle) until the maximum I_{DQ} -value.

approach also considers fast molecular motions with correlation times less than t_0 by adding the term $\exp(-2\tau_{DQ}/T_2)$. T_2 describes the transverse relaxation of these fast motions. In Figure 3.9C the fitting range and the corresponding fit of $I_{\Sigma MQ} - tail$ and I_{ref} are shown.[113, 114]

The Baum-Pines sequence was used to analyze the effect of the entanglement density on the semicrystalline structure of oligomer-diluted poly (ϵ -caprolactone) (PCL). The so far unpublished results are presented in chapter A.2 in the Appendix, Additionally, DQ-results of high- M_w PCL melts were used for a back-extrapolation of the OACF to obtain an universal reference residual dipolar coupling at the entanglement time τ_e . Details are given in chapter A.1 in the appendix.

3.3 ^{13}C structural NMR

The orientation dependent spin interactions in a static sample cause an inhomogeneously broadened spectrum, as explained in chapter 3.1.2. In a magic angle spinning (MAS) experiment the sample is within a cylindrical rotor, which is spun rapidly around its own axis. The angle between the spinning axis and the static magnetic field, the so-called magic angle, is $\theta_{MA} = \arctan(\sqrt{2}) \approx 54.74^\circ$. Under MAS the orientation dependence of the chemical shift frequency is time averaged, resulting in a narrow resonance at the isotropic chemical shift ω_{iso} . The fast rotation removes the broadening effect caused by anisotropic interactions, e.g. chemical shift anisotropy, and can also assist to remove the effect of dipolar couplings, provided that the spinning frequencies are fast in comparison to the DD-coupling. If this condition cannot be fulfilled, decoupling sequences can be used to remove the effect of homo- or heteronuclear dipolar coupling.[115] One of the first NMR pulse programs for homonuclear decoupling was proposed by Lee and Goldburg [116] in 1965 and is based on the removal of the dipolar coupling of the average Hamiltonian to the zeroth order. Other homonuclear decoupling sequences are variations of the Lee-Goldburg decoupling experiment or are based on solid echo pulse trains, magic-echo sandwich pulses or numerically optimized pulse schemes. The frequency-switched and phase modulated Lee-Goldburg sequences are most commonly used.[117] The detection of the weak signal of dilute spins, for example ^{13}C , is additionally complicated by the broadening effect of heteronuclear coupling. The removal of the ^1H - ^{13}C coupling can be achieved by applying a high power radio frequency (RF) pulse with the proton Larmor frequency during the ^{13}C signal acquisition.[115]

3.3.1 Polarization transfer

One advantage of NMR is the analysis of structural information via the chemical shift. However, the spectra of protons in a solid-state sample are often too unselective. Molecular resolution can be obtained in spectra of other, often dilute nuclei, for example ^{13}C . The detection of the signal of a dilute spin system X often results in a very low signal-to-noise ratio even under magic angle spinning and with high power decoupling during detection. An additional problem arises from the long T_1 -relaxation time that is caused by the absence of homonuclear coupling. Thus, the detection of a spectrum of X nuclei with a decent signal-to-noise ratio would require a large amount of scans separated by a long recycle delay. A solution to this problem is the polarization transfer via cross polarization (CP) or by insensitive nuclei enhanced by polarization transfer (INEPT). In both techniques, the dilute spins receive polarization from abundant spins (e.g. ^1H), which also have a faster

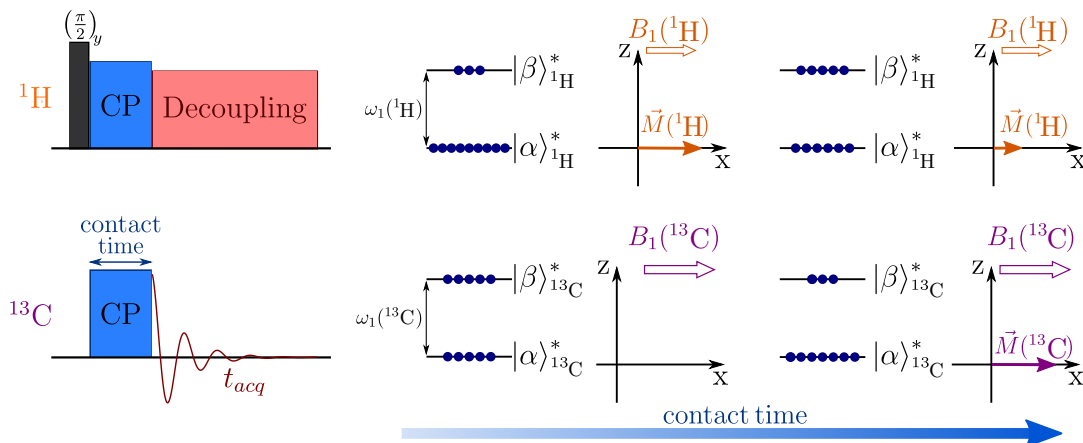


Figure 3.10: Schematic representation of the cross polarization (CP) pulse sequence for a polarization transfer from ^1H to ^{13}C . Transverse polarization of ^1H is obtained after the application of a $(\pi/2)_y$ -pulse. The ^{13}C channel has no transverse magnetization at the beginning of the CP experiment. The polarization transfer from the proton to carbon channel occurs during the application of an on-resonance spin lock pulse on each channel. The spin lock fields, $B_1(^1\text{H})$ and $B_1(^{13}\text{C})$, have to be equal (Hartmann-Hahn match) and ^1H and ^{13}C must be coupled. During the experiment the net energy and polarization of the spin system have to be conserved. Thus, transitions from the rotating frame spin states $|\alpha\rangle_{^1\text{H}}^*$ to $|\beta\rangle_{^1\text{H}}^*$ during the contact time are compensated by transitions from $|\beta\rangle_{^{13}\text{C}}^*$ to $|\alpha\rangle_{^{13}\text{C}}^*$. For long enough contact times a transverse magnetization in the carbon channel is generated. Adapted from reference [115].

T_1 -relaxation. The dipolar and J -couplings between the abundant and dilute nuclei is mandatory for the polarization transfer. In the following explanations ^{13}C is used for the X and ^1H for the abundant nuclei.[115]

Cross polarization The pulse sequence for the cross polarization (CP) experiment is shown in Figure 3.10. In the vector model a rotating frame for both channels is assumed. The spin states in the rotating frames are denoted as $|\alpha\rangle_{^1\text{H}}^*$ and $|\beta\rangle_{^1\text{H}}^*$ as well as $|\alpha\rangle_{^{13}\text{C}}^*$ and $|\beta\rangle_{^{13}\text{C}}^*$, respectively.

In the CP sequence a $(\pi/2)_y$ -pulse on the proton channel generates transverse magnetization along the x -axis. An on-resonance contact pulse along x locks this transverse magnetization. The effect of the external magnetic field vanishes during the application of the spin lock field $B_1(^1\text{H})$, since the field is applied on-resonance and parallel to the magnetization. Simultaneously, an on-resonance spin lock field $B_1(^{13}\text{C})$ is applied on the ^{13}C channel. For the occurrence of a polarization transfer, the proton and ^{13}C nuclei must be coupled and the so-called Hartmann-Hahn match [115]

$$\underbrace{\gamma_{^{13}\text{C}} \cdot B_1(^{13}\text{C})}_{=\omega_1(^{13}\text{C})} = \underbrace{\gamma_{^1\text{H}} \cdot B_1(^1\text{H})}_{=\omega_1(^1\text{H})} \quad (3.28)$$

needs to be fulfilled. The Hamilton operator describing the heteronuclear dipolar

coupling (equation 3.8) contains only operators along z , whereas the ^1H and ^{13}C spin states are aligned in the transverse x - y -plane. Thus, the net energy and angular momentum of the spin system cannot be affected by the dipolar Hamiltonian. Nonetheless, both properties must be conserved. Therefore, a redistribution of the energy between both nuclei is possible, provided that the Hartmann-Hahn condition is fulfilled: the proton spin states at the beginning of the contact pulses cannot be sustained during the contact, due to the much smaller spin lock field $B_1(^1\text{H})$, (small in comparison to the static magnetic field). The resulting transitions from $|\alpha\rangle_{^1\text{H}}^*$ to $|\beta\rangle_{^1\text{H}}^*$ are compensated by transition from $|\beta\rangle_{^{13}\text{C}}^*$ to $|\alpha\rangle_{^{13}\text{C}}^*$, resulting in a polarization of ^{13}C nuclei. The polarization transfer depends on the contact time. In case of a short contact only the closest protons can transfer their polarization. Additionally, the polarization transfer rate increases for stronger dipolar couplings. The spin-locked polarization relaxes with the $T_{1\rho}$ -relaxation time, as described in chapter 3.1.3. Fast molecular motions, which average the dipolar coupling in the system, also reduce the CP efficiency. Additionally, the averaging of the dipolar coupling under magic-angle spinning results in a further reduction of the CP efficiency: the Hartmann-Hahn match is dependent on the MAS frequency ω_R if the spinning rates are on the order of the dipolar coupling. The matching condition under MAS is given by $\omega_1(^{13}\text{C}) - \omega_1(^1\text{H}) = \pm\omega_R$. In order to maintain a suitable matching condition during the experiment a ramped-amplitude CP (RAMP) is used. In this pulse sequence the spin lock field strength of either the ^1H or the X channel is changed linearly while the second field strength is kept constant.[115, 118] CP is often used for the signal enhancement of dilute nuclei. But the intensities of the obtained spectra are not quantitative due to the dependence of the polarization transfer on the dipolar coupling, contact time and the matching of the Hartmann-Hahn condition.[115]

The cross polarization technique was used to detect ^{13}C spectra in the comb-like polymer PPDOT and the copolymer PBSA. Additionally, CP is used in nearly all NMR experiments with ^{13}C detection (Torchia, DIPSHIFT and Spin Diffusion) for signal enhancement. All measurements were performed under magic-angle spinning to obtain narrow resonances.

Insensitive nuclei enhanced by polarization transfer INEPT is a technique to enhance the intensity of dilute nuclei. In contrast to CP, the INEPT pulse sequence utilizes the heteronuclear J -coupling between an abundant and dilute spin and can thus also be applied to highly mobile systems, where the dipole-dipole coupling is averaged to zero. Transverse proton magnetization evolves under J -coupling with the longitudinal ^{13}C magnetization and is manipulated by a spin echo to transfer the refocused transverse magnetization to the ^{13}C nuclei.[119] This technique is used in this work to analyze the liquid-crystalline state of PPDOT, as shown in chapter 4.3.

3.3.2 Torchia method for T_1 measurement

In dilute spin systems the absence of homonuclear decoupling results in a very long T_1 relaxation time. This and the low-signal to noise ratio makes the saturation recovery sequence, as explained in chapter 3.2.2, not feasible. Nonetheless, the ^{13}C T_1 relaxation time is an important parameter since it yields information about the molecular motions. The pulse sequence introduced by Torchia allows the measurement of the ^{13}C longitudinal relaxation time utilizing the cross polarization transfer from protons to carbons with the advantages of an enhanced signal-to-noise ratio and a short ^1H recycle delay [115].

The Torchia pulse sequence (shown in Figure 3.11) consists of two nearly identical pulse sequences, which differ only in the phase of the first $(\pi/2)$ -pulse. After an initial $(\pi/2)_y$ -pulse on the proton channel the transverse magnetization is transferred to the carbon via a CP contact pulse. Once enough polarization has been transferred, the transverse ^{13}C magnetization M_{CP} is rotated along the z -axes by applying a $(\pi/2)_{-y}$ -pulse. The “stored” magnetization relaxes exponentially with the ^{13}C relaxation time T_1 to M_0 , the Boltzmann value of the ^{13}C spin states in a static magnetic field at a given temperature T . After a waiting time τ the remaining magnetization is rotated into the $x - y$ -plane in order to detect the FID. The second step of the phase cycle differs in the phase of the first $(\pi/2)$ -pulse applied to the carbon channel. The phase (y) is chosen such that the transferred magnetization M_{CP} is then aligned along $-z$. [120] The waiting time-dependencies of M_{-y} and M_y are given by [120]:

$$M_{-y}(\tau) = (M_{CP} - M_0) \cdot \exp(-\tau/T_1) + M_0 \quad (3.29)$$

$$M_y(\tau) = (-M_{CP} - M_0) \cdot \exp(-\tau/T_1) + M_0 \quad (3.30)$$

The subtraction of the detected magnetization of both phase cycle steps yields an exponential function, which decays to zero with the ^{13}C T_1 relaxation time [120]:

$$M_{torchia}(\tau) = M_{-y}(\tau) - M_y(\tau) = 2M_{CP} \cdot \exp(-\tau/T_1) \quad (3.31)$$

With an arrayed experiment, the τ -dependence of the magnetization and thus the relaxation time can be detected. The τ -dependent signals are shown on the right in Figure 3.11. In a multiphase system, the Torchia pulse sequence can be used as a filter experiment. With a fixed τ_0 value, mobile signals with $5 \cdot T_{1, mobile} < \tau_0$ can be completely filtered and only the rigid phase will be detected. [120]

The longitudinal relaxation times of carbons can be used to analyze and selectively detect immobilized polymer segments. This was used in the experimental distinction between crystalline and immobilized regions in both components of the copolymer PBSA. The results are shown in chapter 4.2 and in the appendix chapter A.3

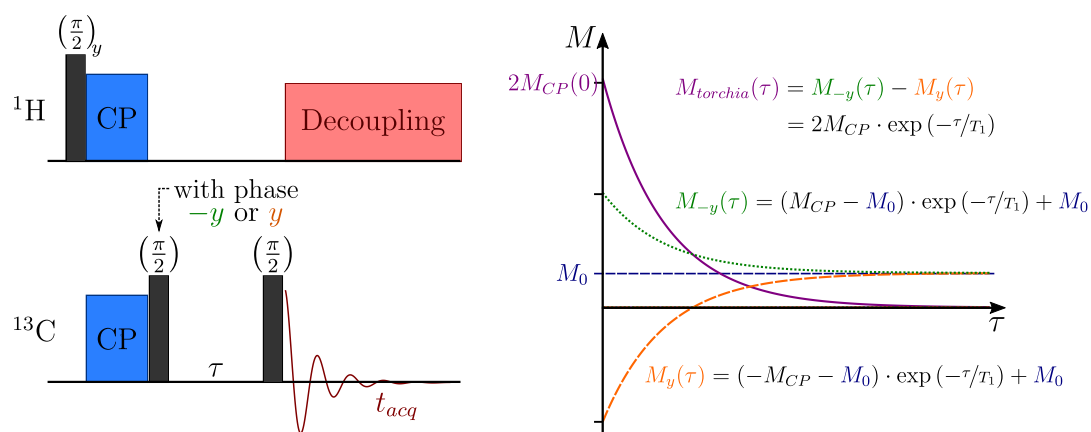


Figure 3.11: *Left*: schematic illustration of the Torchia experiment. It consists of two sequences, that differ in the phase ($-y$ and y) of the first $\pi/2$ -pulse applied to the carbon channel. Adapted from reference [120] *Right*: τ -dependent signals detected for the two pulse sequences M_{-y} (green, dotted line) and M_y (orange, dashed line). The subtraction of M_y from M_{-y} yields a magnetization $M_{torchia}(\tau)$ (purple, solid line) described by an exponential decay that is proportional to T_1 .

3.3.3 DIPSHIFT

The **dipolar chemical shift** correlation sequence (DIPSHIFT), as shown in Figure 3.12, is a MAS 2D experiment which separates the structural information given by the chemical shift in the form of a 1D spectra, from the dynamic information (the ^{13}C - ^1H dipolar coupling) in the indirect dimension. The technique allows to measure the motionally averaged ^{13}C - ^1H heteronuclear dipolar coupling. After the polarization transfer from ^1H to ^{13}C and an optional **rotor-directed exchange of orientations** (RODEO) part can be implemented. It removes anisotropic effects which arise under short CP times.[121, 122]. In either way, the magnetization evolves under heteronuclear coupling (using homonuclear dipolar decoupling on protons for cleaner evolution) for a duration t_1 ranging from zero to the time necessary for one rotor period τ_R . The remaining part of the rotor period is completed under heteronuclear dipolar decoupling. After on complete rotor period a π -pulse on the ^{13}C is applied. This allows the detection of a chemical shift refocused signal under heteronuclear decoupling after another rotor period.[123, 124]

Intensity modulation curves in the indirect dimension are detected, by incrementing the duration of the homonuclear dipolar decoupling. The modulation curves are periodic with the MAS period, with a pronounced reduction of the intensity value for $t_1 = 0.5\tau_R$. The reduction of the intensity is more pronounced for stronger couplings. A fit of the modulation curves yields the residual dipolar coupling. The order parameter S is given by ratio of the fitted value and the static reference dipolar coupling [121]. In Figure 3.12 spectra of an alanin-glycin blend detected for various t_1 increments are shown. The intensity modulation curves are highlighted with a

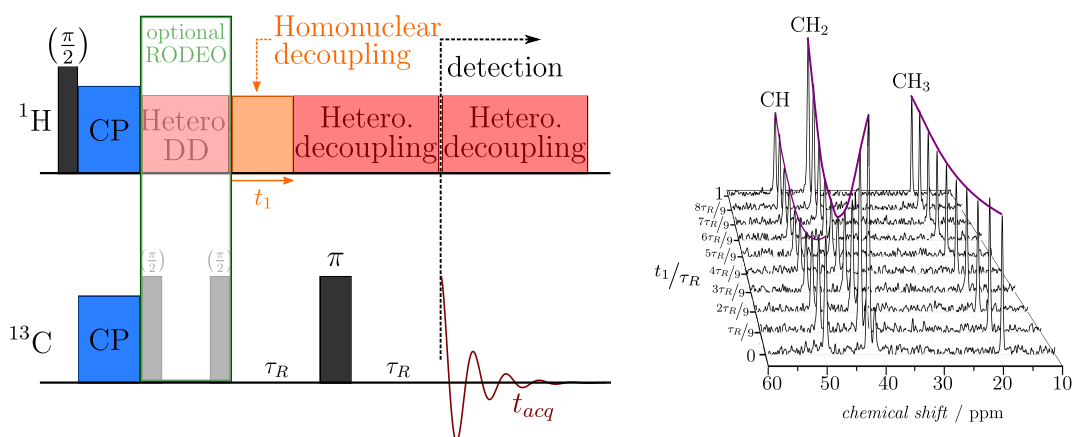


Figure 3.12: *Left*: schematic illustration of the DIPSHIFT pulse sequence with the optional RODEO part. The incrementation of the homonuclear dipolar decoupling with $0 < t_1 < \tau_R$ results in intensity modulation curves, shown on the right. Adapted from reference [122]. *Right*: 2D DIPSHIFT results of a alanin-glycin blend with focus on the CH, CH₂ and CH₃ resonance. The t_1 incrementation lies in the indirect dimension. The intensity loss at $t_1 = 0.5 \cdot \tau_R$ depends on the dipolar coupling strength and is less pronounced for the methyl group due to its higher mobility.

solid purple line in the indirect dimension. For slow and fast molecular motions with correlation times either much slower or larger than the inverse dipolar coupling constant, the intensity of the resonances detected for $t_1 = 0$ and $t_1 = \tau_R$ are equal. In the intermediate motion regime, defined by correlation times that are in the range of the inverse dipolar coupling constant, a signal loss for $t_1 = \tau_R$ is detected. In this regime, the spin pairs lose their orientation correlation during the experiment, resulting in a loss of intensity, which allows to estimate the rate constant of the molecular motion.[124, 125]

The DIPSHIFT pulse sequence was used to analyze the ^1H - ^{13}C dipolar coupling of the side chains and the backbone of the comb-like polymer PPDOT in its two polymorphs. The results are shown in chapter 4.3.

3.3.4 Spin Diffusion

Spin diffusion describes the quasi-random exchange of polarization, which attains a diffusive character in a large spin system. This effect is used to study domain sizes and heterogeneities in (co-)polymer samples. The diffusion of magnetization takes place for abundant spins, e.g. ^1H , which are dipolar coupled. The elementary step of spin diffusion is a flip-flop process, where a spin pair with opposite spin orientation changes the spin state simultaneously, whereby the net magnetization of the spin system is conserved. In a multispin system this process can be repeated with the same pair or one spin of the original pair together with a new spin. This results in a diffusive process of the polarization.[126]

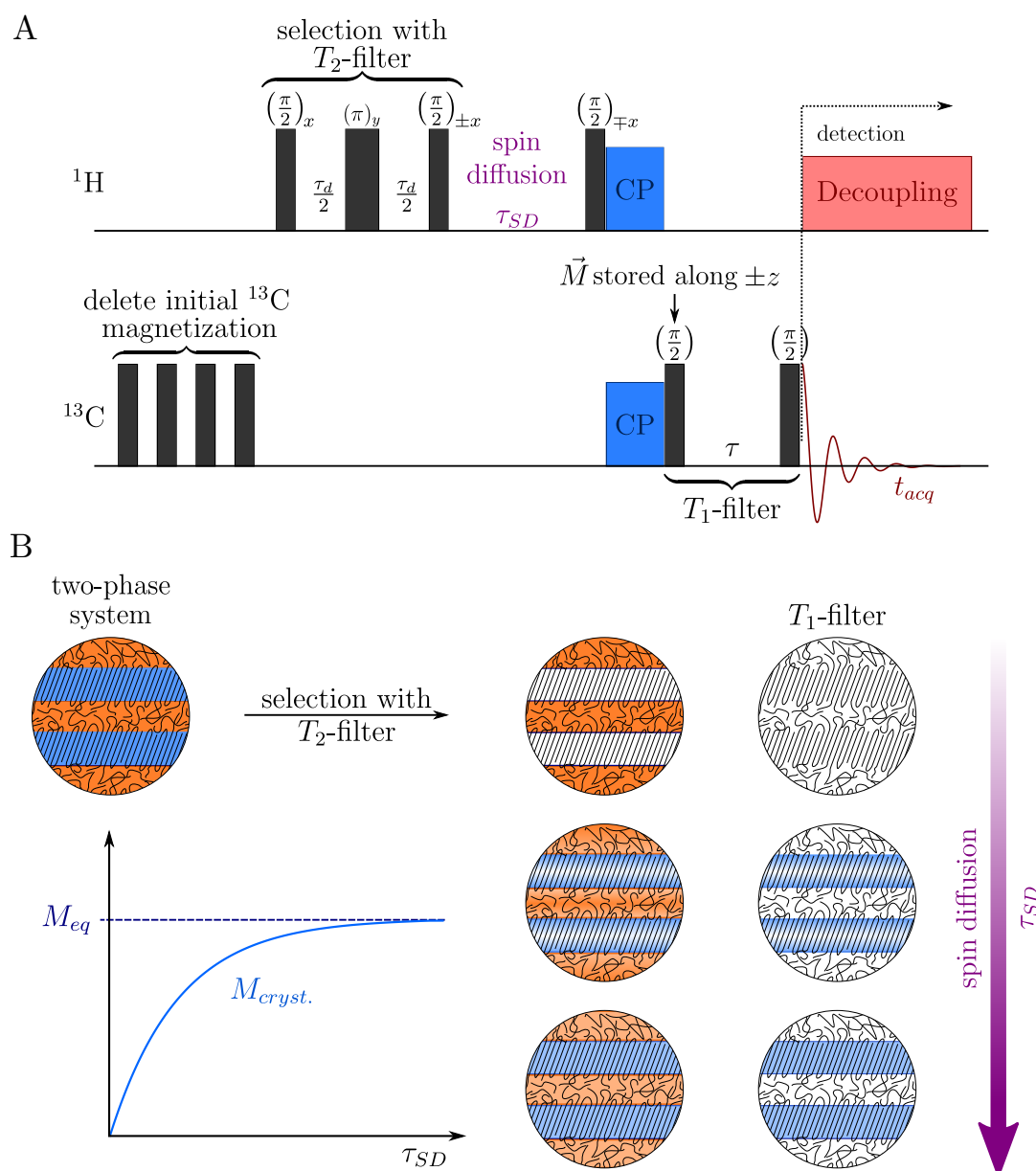


Figure 3.13: A) Schematic illustration of a pulse sequence with proton spin diffusion and a ^{13}C detection. Several $\pi/2$ -pulses on the ^{13}C channel delete the initial carbon polarization. A T_2 -filter (with filter time τ_d) is used for the selection of the proton magnetization. A π -pulse after $\tau_d/2$ refocuses chemical shift and field inhomogeneities. After the spin diffusion time τ_{SD} , the magnetization is transferred to the carbon channel via cross polarization. Signal detection occurs after an optional T_1 -filter. B) Illustration of the selection, spin diffusion and T_1 -filtering of the spin diffusion pulse sequence with ^{13}C detection on a two-phase system: a semicrystalline polymer with a mobile (orange) and rigid (blue) phase. The T_2 -filter selects the signals of the mobile regions. Thus, the crystalline phase is shown colorless after the selection. During τ_{SD} polarization diffused from the mobile to the rigid regions, here represented with a color gradient. The optional T_1 -filter removes all signals arising from the mobile regions. The detected crystalline signal M_{cryst} shows an increase for higher τ_{SD} until the diffusion process equilibrates the polarization in both phases.

The spin diffusion experiment is based on the Goldman-Shen dipolar filter experiment. After a first $\pi/2$ -pulse the magnetization is selected, based on their transverse relaxation, during the time interval τ_d . A second 90° pulse, applied after τ_d , stores the magnetization along z for the spin diffusion time τ_{SD} , followed by a third $\pi/2$ -pulse with subsequent detection of the proton signal.[127] The pulse sequence shown in Figure 3.13 A is based on the Goldman-Shen experiment, but with a ^{13}C signal acquisition, which has the advantage of spectral resolution. As a first step the initial ^{13}C magnetization is deleted with several $\pi/2$ -pulses. The proton magnetization is selected with a T_2 -filter, an additional π -pulse refocuses the chemical shift and possible field inhomogeneities. The selected magnetization is stored along z and undergoes spin diffusion for a time period τ_{SD} . After a rotation to the $x - y$ -plane the magnetization is transferred to the carbon channel with cross polarization. After CP it is possible to apply a T_1 -filter in order to only detect the rigid regions of a multiphase system. This is advisable if mobile and rigid resonances overlap.[128]

In Figure 3.13 B the signal selection for the different filters of the spin diffusion experiment are schematically shown for a two-phase system, represented by a semicrystalline polymer with an amorphous (orange) and rigid (blue) phase. After the selection with a T_2 -filter, only the mobile amorphous regions have a detectable coherent magnetization. For short spin diffusion times, $\tau_{SD} \simeq 0$, no or only very little magnetization diffused into the rigid, crystalline regions and after CP and subsequent T_1 -filter no signal would be detected. With increasing spin diffusion times the detected crystalline signal after CP and T_1 -filter increases with τ_{SD} until an equilibrium value M_{eq} is reached. Even longer spin diffusion times would not lead to an additional increase in the diffused magnetization. Typical times for τ_{SD} are in the range from $100 \mu\text{s}$ to a few 100 ms. The time dependence of the build-up curve yields information about the domain sizes and the shape of the domain. Spin diffusion experiments are also often applied to analyze the semicrystalline morphology of the different phases in copolymers.[126]

In this work spin diffusion experiments were performed on PBSA copolymers to prove the exclusion of BA units from the crystalline structure of the second monomer. Additionally, the location of BA-units in pocket-like structures at the crystalline BS-surface was proven. The complete results are presented in chapter 4.2.

3.4 Polarized optical microscopy

Polarized optical microscopy is used to investigate the semicrystalline morphology by using visible, polarized light. Similar to an optical microscope the sample is enlarged using two lenses. The objective lens creates an inverted, magnified image, which is viewed by the second lens. In a polarized optical microscope, the visible but

unpolarized light is additionally filtered with two polarization filters, the so-called polarizer and analyzer. Only light that is polarized parallel to the polarization axis of the filter can pass through, other polarization planes are blocked. This creates linearly polarized light. If the polarization axis of polarizer and analyzer are perpendicular to each other no light will be transmitted and the observed image is dark. The insertion of a birefringent medium, e.g. a semicrystalline polymer, can change the polarization axis of the light and some light can pass through the analyzer. If the medium is an amorphous polymer or melt, the observed images is also dark, since the sample is optically isotropic. Birefringence in a semicrystalline polymer is caused by the difference in the refractive index parallel and perpendicular to the crystallographic axes of the lamellae. If the long axis of the lamellae is parallel or perpendicular to the polarization planes of the first filter no change of the polarization axis of the light will occur and the corresponding area of the image will be dark. A change of the polarization axis of the light will occur in regions where the polarized light and the

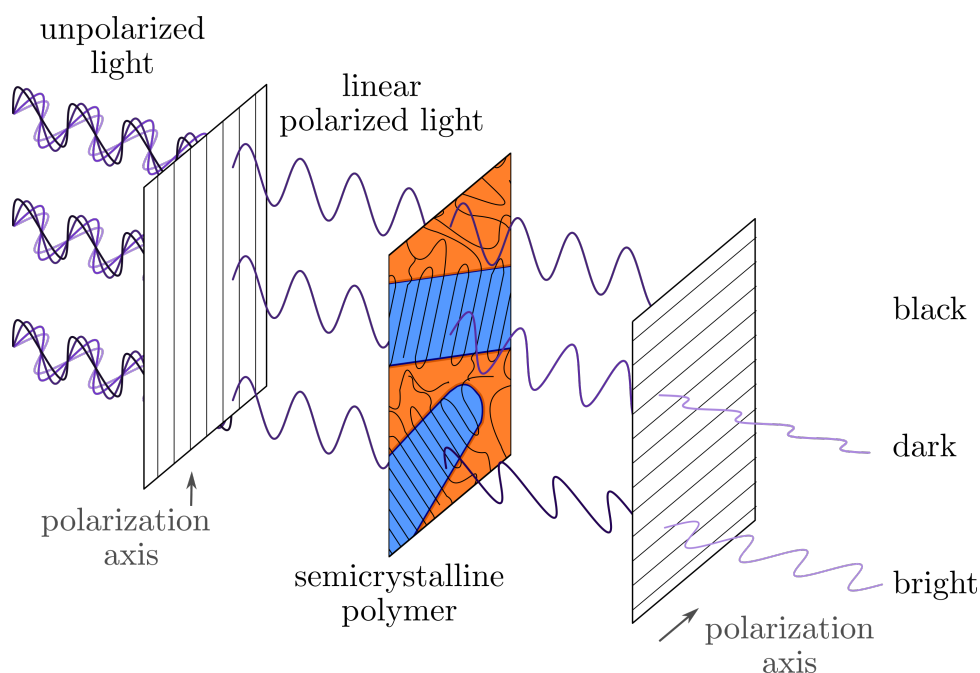


Figure 3.14: Schematic illustration of the two polarization filters and a semicrystalline polymer as medium in a polarized optical microscope. Unpolarized light passes through a polarization filter, and linearly polarized light, parallel to the polarization axis of the filter, is generated. The orientation of the light, once it passed through the semicrystalline polymer, depends on the phase (crystalline or amorphous) and the orientation of the chains within the crystalline lamellae. An isotropic medium, such as the amorphous phase, does not change the axis of the polarized light. Here, the second axis polarization filter is perpendicular to the first, thus the light which passed through the amorphous phase is completely absorbed and the images appears dark. The amount of transmitted light that passed through a crystal depends on the crystal orientation. Crystal chains with an angle of 45° towards the filter axes yield the brightest image.

long axis of the lamellae are neither parallel nor perpendicular, resulting in a brighter image. The effect of different aligned crystals on the transmitted light are shown in Figure 3.14. If the semicrystalline polymer forms a spherulite, the resulting image of an polarized optical microscope is the “Maltese-cross” with dark regions where the polarized light is parallel or perpendicular to the crystallographic axis.[18, 129]

This technique was used to analyze the growth velocity of spherulites in oligomer-diluted PEO. The results were used in the publication presented in chapter 4.1.

4 | Results

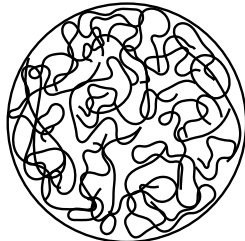
The underlying parameters responsible for the formation of a semicrystalline morphology with distinct properties are not yet fully understood. The published as well as so far unpublished results are presented in this chapter and the Appendix A. The research aims to deepen the understanding of the structure formation and crystallization with a focus on the correlated molecular or segmental dynamics. The investigated polymer systems are diverse and consist of samples with flexible and stiff chains, having either a homo- or heterogeneity along the chain, or also of bimodal polymer blends. This broad range allows to correlate the morphology of different semicrystalline polymer systems with the effect of an investigated property, e.g. co-crystallization. The graphical overview in Figure 4.1 summarizes the investigated systems and properties as well as changes of the external conditions.

In bimodal M_w -distributed systems effects of a reduced entanglement density on the structure formation in a crystal-fixed (PCL) and crystal-mobile (PEO) polymer can be compared. Additionally, the variation of the crystallization temperature and its effect on co-crystallization, in case of PCL, and the intracrystalline dynamics in PEO is considered. The published results of oligomer-diluted PEO are presented in chapter 4.1, the results on oligomer-diluted poly(ϵ -caprolactone) are not yet published and can be found in the Appendix A.2. The random copolymer poly(butanediol-succinate/butanediol-adipate) (PBSA) has a flexible chain, similar to PEO and PCL. Depending on the composition, the formed semicrystalline morphology is strongly influenced by a possible co-unit inclusion of the minority component into the crystalline structure of the second monomer (co-crystallization) and/or the formation of two separated crystalline structures, one for each comonomer crystallization. The asymmetric co-unit inclusion in PBSA copolymers is discussed in the published results presented in chapter 4.2. The dependence of the separate crystallization of BA- and BS-crystals in copolymers in the pseudoeutectic range on the thermal history is summarized in the Appendix A.3. The comb-like polymer poly(1,4-phenylene-2,5- n -didecyloxy terephthalate), with 10 carbon atoms in the flexible alkyl side chains (PPDOT), is investigated in respect to its polymorphism and the correlated phase transitions. By changing the thermal history of the sample different modifications are formed. The results are presented in chapter 4.3.

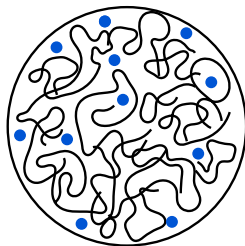
bimodal
 M_w -distribution

- ▲ chapter 4.1
- △ chapter A.2

entangled
polymer melt



oligomer
dilution

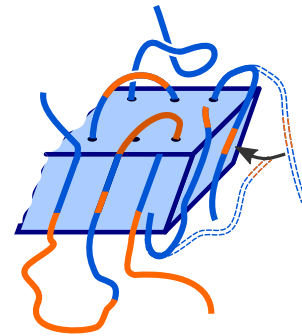


<u>investigated system</u>
flexible chain ▲ △ ■ □ ●
stiff chain ●
homopolymer ▲ △
heterogeneity along the chain ■ □ ●
blend ▲ △
polymorphism □ ●
<u>investigated properties</u>
entanglements ▲ △
intracrystalline dynamics ▲
phase transition ●
polymorphism ●
co-crystallization ▲ ■ □
simultaneous/ separate crystallization ▲ □
<u>external condition</u>
thermal history ● □
crystallization temperature ▲ △

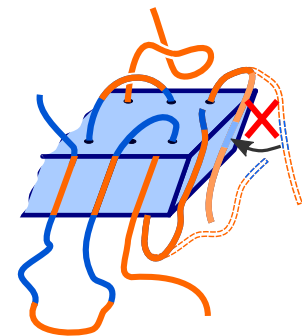
copolymer: PBSA

- chapter 4.2
- chapter A.3

inclusion possible

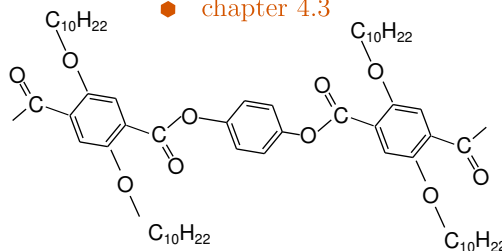


no inclusion

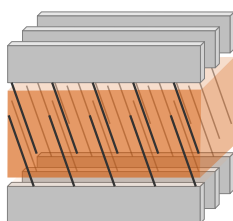


comb-like polymer: PPDOT

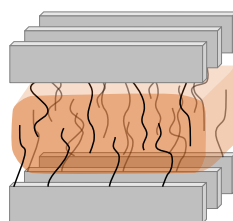
- chapter 4.3



modification B



modification A



liquid crystalline

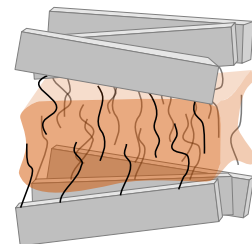


Figure 4.1: Overview of the studied crystallizable polymeric systems.

4.1 Paper I

Intracrystalline dynamics in oligomer-diluted poly(ethylene oxide)¹

The presence of intracrystalline dynamics—a defect-driven helical jump process—has a strong influence on the semicrystalline morphology [44]. In a collaborative publication [130] we could show that the defect-driven jumps along the 7_2 -helix in poly(ethylene oxide) (PEO) are generated at the crystalline-amorphous fold surface. The correlation time of these diffusing defects are distributed over a decade and depend approximately linearly on the lamellae thickness.

Schulz et al. [44] report, that the reorganization due to the intracrystalline dynamics results in a crystal thickening during the growth of the lamellae if the defect diffusion and the crystal growth are on the same timescale, as it is the case in PEO. Furthermore, it is assumed that the amorphous phase, characterized by a certain entanglement density, is a limiting factor for the final crystalline thickness. Recent experimental and theoretical studies revealed that the entanglement density in the melt and amorphous phase influences the final semicrystalline morphology [34, 38, 39, 41, 42, 80–82]. Thus, changes in the morphology imposed by variations in the entanglement density may also affect the fold surface where the diffusive defects are generated.

In the following publication, high- M_w PEO was diluted with oligo(ethylene oxide) in the melt prior to crystallization. The oligomer-dilution allows to modify the properties of the melt and amorphous phase, while all other parameters of the high- M_w PEO are kept constant. Thereby, the influence of a reduced entanglement density in the melt on the lamellae thickness, crystal growth and the defect generation in the crystalline-amorphous interface were studied by analyzing the results of the ^1H FID experiment with the Anderson-Weiss approximation as well as complementary DSC, small angle X-ray scattering studies and polarization microscopy.

The author contributions of the following article are: M. Schäfer and K. S. designed research. M. Schäfer and partially N. W. (in the scope of a Bachelor thesis and with help from M. Schäfer) performed the NMR measurements and analyzed the NMR data. M. S. performed and analyzed the DSC and SAXS measurements. M. Schäfer, N. S., M. S. T. T.-A. and K. S. discussed the results. M. Schäfer and, in minor parts, K. S. wrote the paper with refinements by M. S., T. T.-A. and K. S.

¹The following article [M. Schaefer et al., *Macromol. Chem. Phys.*, **221**, 1900393 (2020)] has been published under the terms of the Creative Commons Attribution 4.0 International License (CC BY 4.0) that permits unrestricted use, distribution and reproduction in any medium under specification of the authors (Mareen Schäfer, Niklas Wallstein, Martha Schulz, Thomas Thurn-Albrecht und Kay Saalwächter) and the source (*Macromol. Chem. Phys.*; DOI: 10.1002/macp.201900393). The link to the article on the publishers website is: <https://onlinelibrary.wiley.com/doi/full/10.1002/macp.201900393>. No changes were made.



Intracrystalline Dynamics in Oligomer-Diluted Poly(Ethylene Oxide)

Mareen Schäfer,* Niklas Wallstein, Martha Schulz, Thomas Thurn-Albrecht, and Kay Saalwächter*

Solid-state creep, ductility, and drawability are relevant mechanical properties of “crystal-mobile” polymers, related to a large-scale chain transport through the crystal, which is in turn mediated by intracrystalline monomer jumps. Here, high- M_w poly(ethylene oxide) is used as a well-controlled model system, modulating the properties of the amorphous phase by diluting with a non-crystallized oligomer. Faster intracrystalline motions are found upon oligomer addition, indicating little changes in the fold surface and a dominant influence of the somewhat reduced lamellar thickness.

1. Introduction

In defending^[1] his “macromolecular hypothesis,” Hermann Staudinger realized early on the relevance of the possibility that long chain molecules may be able to crystallize.^[2] Reflecting on the present-day use of polymers, thermoplastic polymers based upon semicrystalline homopolymers in fact make up the largest fraction of polymer materials produced industrially.^[3] Their mechanical properties can be tuned over wide ranges, thanks to molecular-scale control parameters such as tacticity, low degrees of branching, or the molecular weight (M_w) distribution.^[4] Controlling and varying the properties of simple homopolymers is a cornerstone of improving the polymers’ recyclability, toward a circular and thus more sustainable plastics economy.^[5]

Semicrystalline polymers can be subdivided into two major classes, namely crystal-fixed and crystal-mobile polymers. Diffusive chain mobility within and through the crystalline lamellae enables high crystallinity,^[6,7] and is the molecular basis of the deformability of polymer crystals, explaining important

mechanical properties such as creep^[8] and ultradrawability.^[9] Also the process of reversible surface melting and crystallization, and the correlated changes in the crystalline-amorphous interphase, which is reported for crystal-mobile polymers such as poly(ethylene oxide) (PEO),^[10] is only feasible due to the intracrystalline dynamics in this polymer class. There is some evidence that jump-like monomer motions (“helical jumps”) are mediated by localized and traveling conformational

defects,^[11–16] which are thus the elementary process of the intracrystalline chain diffusion.

Although it is likely that such conformational defects originate in the amorphous phase,^[17] direct evidence is hard to attain because the said defects are a rare and dynamic species.^[16] In fact, molecular methods detecting intracrystalline jump motions do not detect the moving conformational defect, but just the timescale on which monomers become translated by one “raster” as a result of the defect passing by. This holds for dielectric spectroscopy focusing on rotations of intracrystalline carbonyl defects in case of polyolefins,^[6] as well as for many different NMR methods.^[14,16] NMR studies by Yao *et al.* focusing on the larger-scale chain exchange between amorphous and crystalline regions have emphasized the relevance of the fold surface,^[18] where it was found that, somewhat curiously, solution-grown PE crystals dominated by adjacent re-entry lead to much faster chain motion as in the melt-crystallized state. This was rationalized by a reduced entropic barrier.

Since large-scale chain transport is also dependent on constraints in the amorphous phase,^[19,20] it is beneficial to focus on the local back-and-forth jump process.^[21,22] Using proton-based low-field proton NMR methods that require comparably little experimental time, we could previously confirm the findings of Yao *et al.* for different morphologies of PE.^[23] Moreover, using a multitude of PEO, samples providing a well-controlled model system, we were able to delineate a near-linear crystal-thickness dependence of the intracrystalline jump rate, which is in phenomenological agreement with the diffusion of conformational defects originating in the fold surface or the amorphous phase.^[16]

Here, we build upon this earlier work^[16] and attempt to modify the properties of the amorphous phase by adding a low- M_w PEO diluent, which as we show does not crystallize under the studied conditions and the relevant temperature range. In this way, we can test whether the polymer crystallizes more slowly and exhibits thicker lamellae in comparison to pure samples. Such changes were recently found in computer simulations

M. Schäfer, N. Wallstein, Prof. K. Saalwächter
Institut für Physik - NMR
Martin-Luther Universität Halle-Wittenberg
Betty-Heimann-Str. 7., D-06120 Halle (Saale), Germany
E-mail: mareen.schaefer@physik.uni-halle.de;
kay.saalwaechter@physik.uni-halle.de

M. Schulz, Prof. T. Thurn-Albrecht
Institut für Physik - Polymerphysik
Martin-Luther Universität Halle-Wittenberg
Betty-Heimann-Str. 7., D-06120 Halle (Saale), Germany

The ORCID identification number(s) for the author(s) of this article can be found under <https://doi.org/10.1002/macp.201900393>.

© 2019 The Authors. Published by WILEY-VCH Verlag GmbH & Co. KGaA, Weinheim. This is an open access article under the terms of the Creative Commons Attribution License, which permits use, distribution and reproduction in any medium, provided the original work is properly cited.

DOI: 10.1002/macp.201900393

performed by ref. [24], and were explained by a reduction of the entanglement density and likewise the topological constraints in the melt prior to crystallization. Experimental studies on crystal-fixed poly(ethylene-co-octene) performed by ref. [25] reveal that the growth of thicker crystals upon dilution is affected by the chosen diluent and might arise from the different solvent qualities. Neglecting end group effects, our low- M_w PEO diluent can be regarded as an athermal solvent. We apply differential scanning calorimetry (DSC), polarization microscopy and small-angle X-ray scattering (SAXS) to characterize the samples, and use the mentioned proton low-field NMR method to extract the timescale of monomer jumps. We find a weak decrease in crystallite thickness and a correspondingly weak enhancement of intracrystalline dynamics upon adding the diluent. We find a constant or slightly decreased crystalline thickness in contrast to the results of the simulation. Observed changes in intracrystalline dynamics can be traced back to changes in crystal thickness.

2. Experimental Section

2.1. Materials

PEO samples from Polymer Standard Service with $M_w = 52.9$ kDa with a PDI=1.19 and $M_w = 187$ kDa with a PDI=1.16 were used as polymer samples, referred to as PEO53 and PEO187, respectively. As oligomer a PEO sample from Sigma-Aldrich with $M_n = 0.3$ kDa, well below the critical molecular weight ($M_c=5.9$ kDa^[26]), was used. With its six monomer units, a corresponding crystalline 7_2 helix would measure 1.7 nm. The high- M_w polymers were diluted with different mass fractions Φ of oligo(ethylene oxide). The oligomer was liquid at room temperature and supposed to mix homogeneously with the polymer in the molten state. Here mixtures with up to $\Phi = 0.5$ oligomer fraction for both molecular weights that are crystallized at $T_c = 30$ and 54 °C (excluding the PEO53 with $\Phi = 0.5$ at the latter T_c , due to the long crystallization time) were investigated.

Polarization microscopy experiments were performed on an Olympus BX51 equipped with a Linkam hot stage to determine the speed of the spherulite growth front and assess the nucleation density.

Differential scanning calorimetry (DSC) measurements were performed on a UNIX DSC7 from Perkin Elmer. For all PEO mixtures and both molecular weights a cooling and heating DSC scan with 10 K min^{-1} were performed (see **Figure 1**). In all samples a crystallization peak between 35 and 50 °C can be observed during cooling. For higher mixtures the crystallization of the polymer component starts at lower temperatures and the crystallinity is reduced roughly by the dilution factor. This indicates that the oligomer does not co-crystallize in this temperature range. For mixtures with $\Phi \geq 0.3$ a second crystallization peak is observed for temperatures below -10 °C. This additional peak is interpreted as the crystallization of the oligomer, but does not change the interpretation of the NMR and SAXS results since the oligomer crystals melt below 0 °C, where the relevant NMR temperature range starts. SAXS measurements were performed at 30 and 54 °C, right after the crystallization at these temperatures. Furthermore a melting point depression of the polymer crystals is observed for all dilutions.

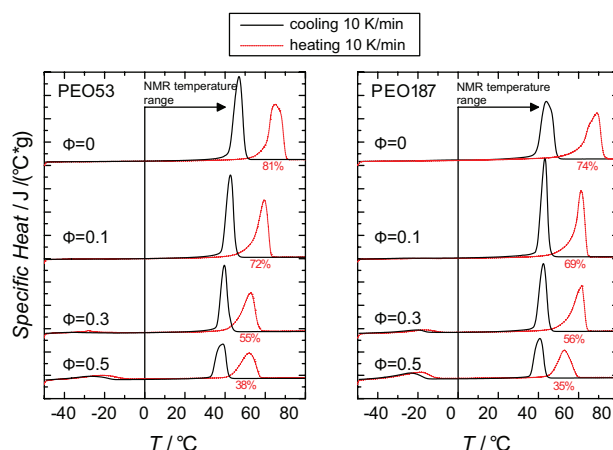


Figure 1. DSC cooling and heating scans with 10 K min^{-1} for PEO53 (left) and PEO187 (right). Φ is the oligomer mass fraction.

SAXS measurements on a Kratky compact camera from Anton-Paar GmbH equipped with a focusing X-ray optics from AXO Dresden GmbH and with the 1D detector Mythen2 R 1K from Dectris. A temperature-controlled sample holder were employed to determine the long period L and the sizes of the crystalline (d_c) and amorphous (d_a) domains. The latter were obtained from a newly developed analysis approach of the interface distribution function. See refs. [7,27] for details, which also provide information on the distribution of these quantities in terms of standard deviation σ ($\sigma = 1.2$ nm) of an assumed Gaussian distribution.

2.2. ^1H NMR FID Analysis and Crystalline Signal

^1H time domain signals (free induction decays, FIDs) were acquired on a 200 MHz Bruker Avance III Spectrometer, using a static probe head with a short dead time of only 2.5 μs . The temperature accuracy of all measurements is ± 1 K with a temperature gradient in sample of ± 0.5 K. Regular as well as MAPE-filtered FIDs (the latter acquiring only the most mobile components) were measured stepwise from -50 °C to T_{melt} . The differences in dipole–dipole couplings in the amorphous and crystalline regions allow a clear distinction of the signal contributions. In the crystalline phase with comparably low mobility, the overall strong dipolar coupling leads to a fast decay of the time-domain signal. The decay in the amorphous phase is much slower due to large-scale motions far above T_g , leading to an averaging of the dipolar couplings once the segmental relaxation time is faster than the inverse average dipole–dipole coupling, that is, about 10 μs . The FIDs were decomposed into three signal fractions (see **Figure 2a**),^[28–30] the highly dipole–dipole-coupled crystalline fraction f_c , the intermediate phase f_i and the amorphous fraction f_a using the following three component fit

$$\begin{aligned} \text{FID}^{\text{norm}}(t) &= f_a(t) + f_i(t) + f_c(t) \\ &= f_a \cdot \exp\left(-\left(t/T_{2,a}^*\right)^{v_a}\right) + f_i \cdot \exp\left(-\left(t/T_{2,i}^*\right)^{v_i}\right) \\ &\quad + f_c \cdot \exp\left(-0.5(at)^2\right) \cdot \sin(bt) / bt \end{aligned} \quad (1)$$

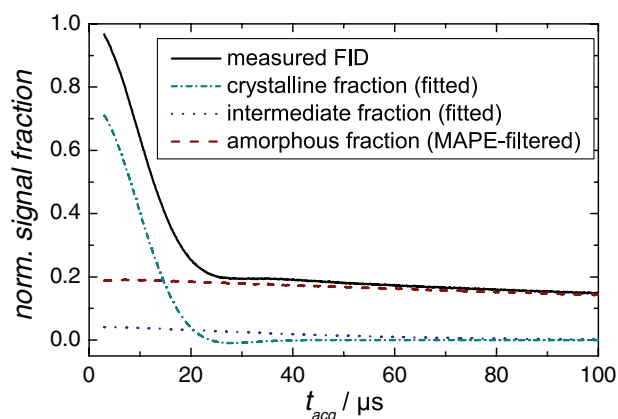


Figure 2. FID deconvolution into amorphous (dashed), intermediate (dotted) and crystalline (dashed-dotted) signal fractions. The acquired FID signal is shown in black.

wherein the fit parameters of the mobile phase are known from the additional measurement of a MAPE-filtered FID with a filter duration of $0.6 \mu\text{s}$ for the pure and $\Phi = 0.1$ samples and $0.45 \mu\text{s}$ for the samples with $\Phi \geq 0.3$.^[30,31] The crystalline fraction $f_c(t)$ is described by the so-called Abragam function, which describes a strongly coupled FID. The transverse relaxation times $T_{2,i}^*$ and $T_{2,a}^*$ are in the range of a few to several hundreds of microseconds. From the fit parameters a and b , the dipolar second spectral second moment can be calculated via $M_2 = a^2 + b^2/3$; this parameter is proportional to the static limit dipolar coupling: $M_2 = 9/20 \cdot D_{\text{stat}}^2$.

2.3. Anderson–Weiss-Analysis for Intracrystalline Dynamics

The decomposition of the FIDs allows to access the response of the pure crystalline component by subtraction of the intermediate and amorphous signal components. The normalized crystalline signal components are shown in **Figure 3a**. It becomes apparent that the fast helical jump motions in the crystalline lamellae of PEO, which can be described by a 7_2 -helix, have a strong effect on the signal decay of the crystalline FID. This temperature-dependent motional averaging, caused by fast reorientations of the ^1H - ^1H -dipole-dipole coupling tensor of the CH_2 -groups, enables a direct analysis of the intracrystalline dynamics in PEO for a range of correlation times covering about 2 decades centered around $10 \mu\text{s}$. On the basis of Anderson–Weiss (AW) theory^[32–35] the first 40% of the crystalline FID signals are used for the fitting procedure (see **Figure 3b**), which is explained in detail in ref. [16] on our previous study on PEO. In short, we perform a simultaneous fit on data taken at different temperatures, assuming that the temperature-dependent correlation times of the helical jump motions are described by an Arrhenius temperature dependence,

$$\tau_c = \tau_0 \cdot \exp(E_A / (R \cdot T)) \quad (2)$$

with the final AW-fit parameters τ_0 , the activation energy E_A , as well as a dimensionless distribution width σ_τ assuming a log-normal distribution of correlation times. The recalculated

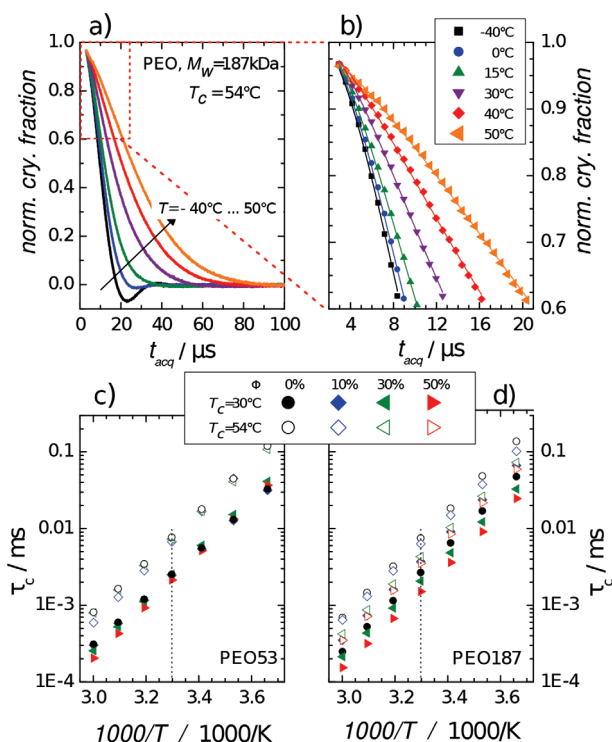


Figure 3. Panel a) displays the normalized crystalline signal fractions. The first 40% of the signal are used for the Anderson-Weiss-fit in b). The resulting Arrhenius temperature dependencies for PEO53 and PEO187 are shown in c) and d).

Arrhenius plots of all measured samples are shown in **Figure 3c,d**. All samples have a similar activation energy (similar slope in the Arrhenius plot) of approximately 65 kJ mol^{-1} , and feature a distribution width σ_τ in the range of about 0.7 to 1.8 decades with wider distributions for higher diluted samples and higher crystallization temperatures. The undiluted samples have distribution widths of 0.7 to 1.15, well in line with our previous findings on bulk PEO.^[16]

3. Results and Discussion

3.1. Crystalline Growth

In **Figure 4** the microscopy-based crystallization speeds for all mixtures depending on the crystallization temperature T_c are shown. For both molecular weights the same behavior of a decreasing crystallization speed with either increase of the oligomer content or higher crystallization temperatures is observed. The lower molecular weight PEO53 crystallizes faster and the effect of the oligomer content is not as pronounced as in PEO187. The optical micrographs of all samples and mixtures do not show any sign of heterogeneity or areas of non-crystallizable oligomers. The results thus suggest that oligomer and polymer are indeed in a mixed state without large-scale demixing before crystallization. However, an at least partial phase separation on the lamellar scale or a heterogeneous mixture in the semicrystalline state (which may arise from the effect of endgroups, especially in the 50% oligomer mixtures),

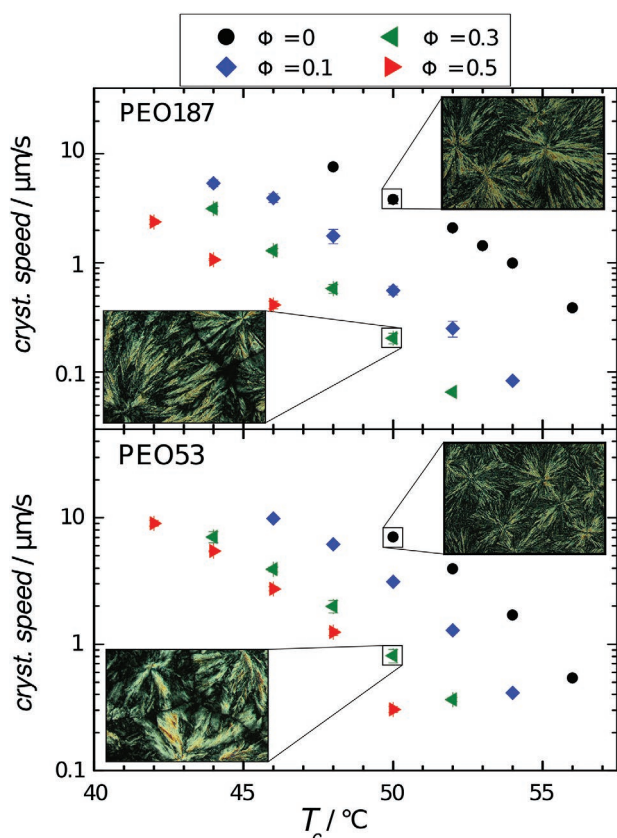


Figure 4. Crystallization speed for PEO53 (left) and PEO187 (right) with different amount of oligomer crystallized at different temperatures. The inserts show polarization micrographs with dimensions of 1.3×0.9 mm.

cannot be fully excluded. For both polymers an increase in the spherulite size for increasing oligomer content is observed (see the micrographs shown as insets), indicating a reduced nucleation density upon increasing Φ and explaining the much reduced bulk crystallization rates of the mixtures.

3.2. Structural Parameters and Crystallinity

In the upper panel of **Figure 5** the amorphous and crystalline thicknesses (d_a and d_c) obtained from SAXS measurements are shown. The “error bars” indicate the distribution width of the corresponding structural parameter.^[27] For PEO187 the crystalline thickness decreases for an increasing oligomer content at the low crystallization temperature and displays no significant trend for higher crystallization temperatures (the 50% mixture is again missing due to slow crystallization). The lower molecular weight polymer, PEO53, does not show any considerable changes in the structural parameters with increasing oligomer content. The 50% mixtures are also missing due to the slow crystallization. An increase of the lamellae thickness d_c in oligomer-diluted polymer systems, as inferred from computer simulations,^[24] can therefore not be confirmed.

The lower panel of **Figure 5** shows the crystallinity measured via ^1H NMR FID analysis,^[29] and in comparison also the calculated SAXS crystallinities are shown. For low oligomer con-

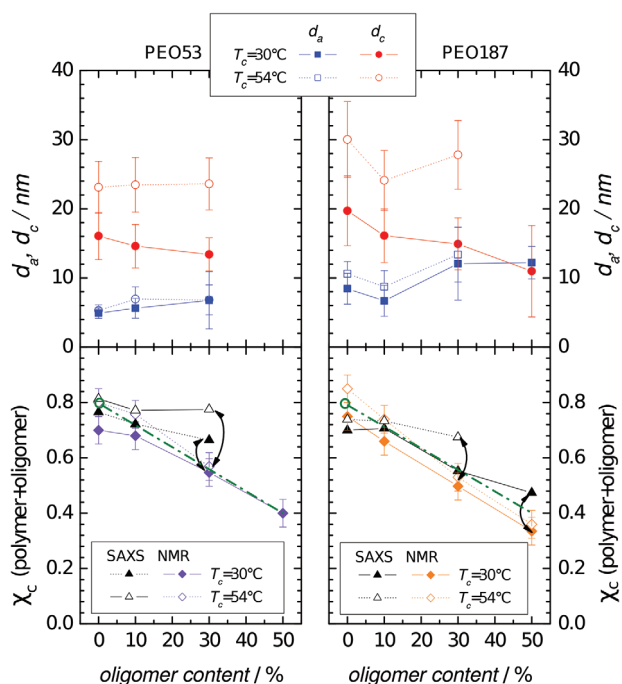


Figure 5. Upper panel: Dependence of the amorphous d_a and crystalline d_c thickness of PEO53 (left) and PEO187 (right) for two crystallization temperatures on the oligomer content. Lower panel: Linear crystallinity (SAXS) vs. crystallinity of complete sample (NMR). The dash-dotted lines starting in the circles indicate the trend expected when the crystallinity of the high- M_w component is constant at 80%, coexisting with non-crystallized oligomer.

trations, $\Phi < 0.1$ both SAXS and NMR crystallinity are in rather good agreement; only for higher oligomer contents the calculated SAXS crystallinities are clearly higher by 10 to 20%. The differences in the obtained crystallinities are shown by the black arrows in **Figure 5**. This indicates again – at least – a partial phase separation of the oligomer and polymer for high-oligomer mixtures in the semicrystalline state, where some of the oligomer leaves the stacked structure. In the ^1H NMR analysis the signals of both oligomer and polymer are measured. Thus, the obtained polymer crystallinity would also be reduced by the factor of Φ if a complete phase separation would be present. Taken together, upon diluting the sample with its oligomer, a slight decrease rather than an increase in d_c or crystallinity is obtained. These results are in contradiction to the computer simulation results of ref. [24].

In this context, it should be noted that our previous studies^[7] indicate that the final crystalline thickness in PEO results from reorganizations in the lamellae, caused by the helical jump motions which are fast in comparison to the lateral growth. Thus, the observed almost unchanged crystalline thickness of the long-chain PEO at the given reduced growth velocity suggests that the crystalline thickness is not the one that is initially kinetically selected.

3.3. Intracrystalline Dynamics

Figure 6a shows the dependence of the average correlation time τ_c at 30 °C on the oligomer content. The solid and dotted lines

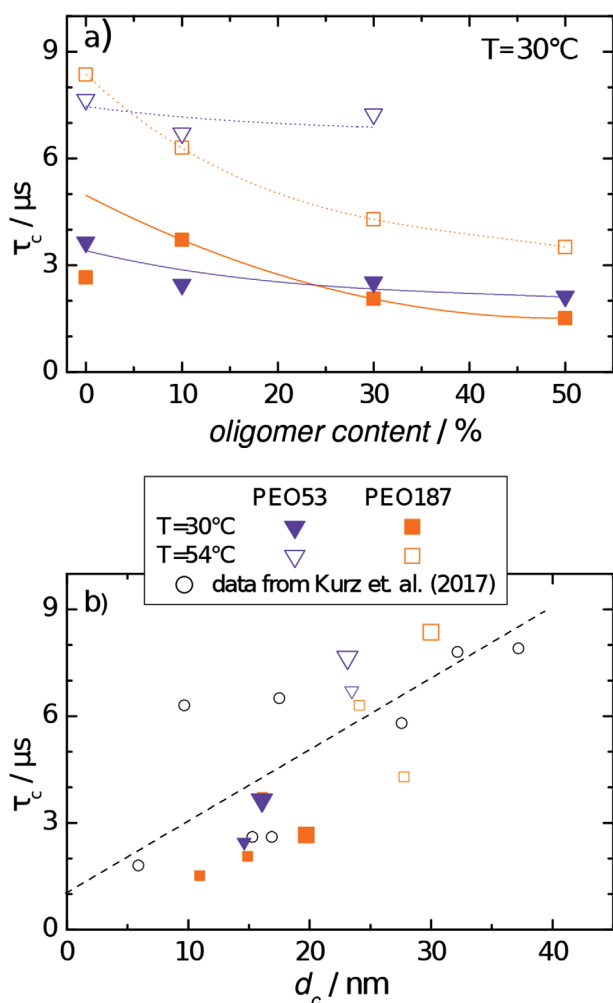


Figure 6. a) The dependence of the average correlation time τ_c at 30°C for PEO53 and PEO187. Closed and open symbols represent the lower and higher crystallization temperature, respectively. The dashed line in b) is a prediction from a model assuming a constant defect generation rate in the fold surface.^[16] The larger symbols denote the undiluted samples.

are a guide to the eye. In PEO187 the average correlation times at 30°C are decreasing for increasing oligomer content. The intracrystalline dynamics in PEO53 changes only little for the different mixtures. Both high- M_w polymers display a slower intracrystalline motion for higher crystallization temperatures, where thicker crystalline lamellae are formed. This observation is in agreement with our earlier studies on the dependence of the intracrystalline jump motion in PEO on the lamellar thickness.^[16] The dependence of $\tau_c(30^\circ\text{C})$, around which it is determined most accurately, on d_c is shown in Figure 6b. The open, black circles are the re-plotted correlation times from ref. [16], the small rectangle and triangles denote the corresponding results of the diluted PEO187 and PEO53, respectively. The enlarged symbols represent the pure polymer samples. The trend of higher correlation times for thicker crystals is also observed for the new data points. Therefore, no trend to a higher or lower probability for the defect generation in the fold surface and the resulting change in the d_c -dependence can be seen.

4. Summary and Conclusion

We used a combination of small angle X-ray scattering and NMR to investigate the effect of dilution of PEO with short noncrystallizable oligo(ethylene oxide) prior to the crystallization on the semicrystalline morphology of the high- M_w PEO. DSC measurements revealed that the oligomer does not crystallize in the relevant temperature range. With increasing oligomer content a melting point depression and a decrease in crystallinity is observed for both high M_w -PEO samples. The comparison of SAXS and NMR crystallinities revealed a partial phase separation occurs upon crystallization for high-oligomer mixtures. The morphology differences upon dilution are not very significant; only a marginally significant trend toward thinner crystalline lamellae for higher oligomer mixtures is observed. Given that the lateral growth velocity of the crystalline lamellae is significantly reduced, we hypothesize that the observed crystalline thickness is not the one that is kinetically selected initially, but is a result of a thickening process enabled by the intracrystalline dynamics. The intracrystalline jump motions are faster for thinner crystals, and no trend toward an enhanced or limited defect generation in the fold surface can be detected. The partial phase separation and the corresponding small changes in the fold surface might be the reason for the insignificant changes in the helical jump motions.

Acknowledgements

Financial support within the framework of Deutsche Forschungsgemeinschaft (DFG, German Research Foundation)—project number 189853844—TRR 102 “Polymers under multiple constraints” (project A01) is highly appreciated.

Conflict of Interest

The authors declare no conflict of interest.

Keywords

intracrystalline dynamics, oligomer-dilution, poly(ethylene oxide), semicrystalline polymers

Received: September 16, 2019
Revised: November 5, 2019
Published online: November 26, 2019

- [1] H. Staudinger, *Naturwissenschaften* **1934**, 22, 65.
- [2] G. Mie, J. Hengstenberg, H. Staudinger, H. Johner, M. Lüthy, R. Signer, *Naturwissenschaften* **1927**, 15, 379.
- [3] S. M. Al-Salem, P. Lettieri, J. Baeyens, *Waste Manage* **2009**, 29, 2625.
- [4] R. Mülhaupt, B. Rieger, *Chimia* **1995**, 49, 486.
- [5] T. Hees, F. Zhong, M. Stürzel, R. Mülhaupt, *Macromol. Rapid Commun.* **2019**, 40, 1800608.
- [6] R. H. Boyd, *Polymer* **1985**, 26, 323.
- [7] M. Schulz, R. Kurz, A. Seidlitz, R. Bärenwald, A. Petzold, K. Saalwächter, *Macromolecules* **2018**, 51, 8377.



- [8] I. M. Ward, M. A. Wilding, *J. Polym. Sci. B Polym. Phys.* **1984**, 22, 561.
- [9] W.-G. Hu, K. Schmidt-Rohr, *Acta Polym.* **1999**, 50, 271.
- [10] T. Albrecht, S. Armbruster, S. Keller, G. Strobl, *Eur. Phys. J. E* **2001**, 6, 237.
- [11] D. H. Reneker, B. M. Fanconi, J. Mazur, *J. Pol. Science* **1962**, 59, 39.
- [12] D. H. Reneker, B. M. Fanconi, J. Mazur, *J. Appl. Phys.* **1977**, 48, 4032.
- [13] B. Ewen, G. Strobl, T. Richter, *Faraday Discuss. Chem. Soc.* **1980**, 69, 19.
- [14] K. Schmidt-Rohr, H. W. Spiess, *Multidimensional Solid-State NMR and Polymers*, Academic Press, London **1994**.
- [15] S. W. Mowry, G. C. Rutledge, *Macromolecules* **2002**, 35, 4539.
- [16] R. Kurz, A. Achilles, W. Chen, M. Schäfer, A. Seidlitz, Y. Golitsyn, J. Kressler, W. Paul, G. Hempel, T. Miyoshi, T. Thurn-Albrecht, *Macromolecules* **2017**, 50, 3890.
- [17] For all-trans polyethylene, it is the only possible place, as it is not possible to form a pair of defects within the crystal without “drawing-in” additional monomers.
- [18] Y. F. Yao, R. Graf, H. W. Spiess, D. R. Lippits, S. Rastogi, *Phys. Ref. E* **2007**, 76, 060801.
- [19] K. Schmidt-Rohr, H. W. Spiess, *Macromolecules* **1991**, 24, 5288.
- [20] Y. F. Yao, R. Graf, H. W. Spiess, S. Rastogi, *Macromol. Rapid Commun.* **2009**, 30, 1123.
- [21] T. Miyoshi, In *Modern Magnetic Resonance*, (Ed: G. A. Webb), Springer, Netherlands, Dodrecht **2008**, pp. 615–619.
- [22] T. Miyoshi, A. Mamun, W. Hu, *J. Phys. Chem. B* **2010**, 114, 92.
- [23] R. Bärenwald, S. Goerlitz, R. Godehardt, A. Osichow, Q. Tong, M. Krumova, S. Mecking, K. Saalwächter, *Macromolecules* **2014**, 47, 5163; Correction: *Macromolecules* **2014**, 47, 7677.
- [24] C. Luo, M. Kröger, J.-U. Sommer, *Macromolecules* **2016**, 49, 9017.
- [25] B. Heck, G. Strobl, M. Grasmuck, *Eur. Phys. J. E* **2003**, 11, 117.
- [26] J. E. Mark, *Physical Properties of Polymers Handbook*, Springer, New York **2007**.
- [27] A. Seidlitz, T. Thurn-Albrecht, In *Polymer Morphology*, (Ed: Q. Guo), Wiley, Hoboken, New Jersey **2016**, pp. 151–164.
- [28] E. W. Hansen, P. E. Kristiansen, B. Pedersen, *J. Phys. Chem. B* **1998**, 102, 5444.
- [29] K. Schärer, A. Achilles, R. Bärenwald, C. Hackel, K. Saalwächter, *Macromolecules* **2013**, 46, 7818.
- [30] K. Schärer, M. Roos, P. Micke, Y. Golitsyn, A. Seidlitz, T. Thurn-Albrecht, H. Schneider, G. Hempel, K. Saalwächter, *Solid State Nucl. Magn. Reson.* **2015**, 72, 50.
- [31] T. Hees, F. Zhong, M. Stürzel, R. Mülhaupt, *J. Magn. Reson.* **1972**, 6, 157.
- [32] P. W. Anderson, P. R. Weiss, *Rev. Mod. Phys.* **1953**, 25, 269.
- [33] A. Abragam, *The Principles of Nuclear Magnetism*, Oxford University Press, Oxford **1961**.
- [34] V. D. Fedotov, V. M. Chernov, T. N. Khazanovich, *Polym. Sci. U. S. S. R.* **1978**, 20, 1037.
- [35] R. Kimmich, *NMR Tomography, Diffusometry, Relaxometry*, Springer, Berlin **1997**.

4.2 Paper II

Asymmetric co-unit inclusion in statistical copolyesters²

In copolymers a change of the comonomer composition allows to manipulate the semicrystalline structure and thus the properties of the material. In this material class the investigative focus lies on changes of the morphology imposed by this externally controllable parameter, rather than the effect of internal properties, such as the entanglement density or a possible intracrystalline dynamic. In random isodimorphic copolymers both comonomers can crystallize within the pseudoeutectic range (a material specific composition range). On either side of this range, the majority component crystallizes with a possible incorporation of co-units from the second monomer. The lamellae thickness, melting point, crystallinity and other parameters describing the semicrystalline morphology depend on whether or not co-unit inclusion of one comonomer in the crystals of the second component is possible, and if yes, to which extent.[47]

In the following publication the random copolymer butanediol-succinate/butanediol-adipate (PBSA) is investigated with regards to its asymmetric co-unit inclusion on either side of the pseudoeutectic range. ¹H FID analysis, DSC and small and wide-angle X-ray scattering was used to characterize PBSA copolymers over the complete compositional range with respect to the signal fractions, thermal behavior and the semicrystalline structure. ¹³C MAS NMR relaxation studies as well as spin diffusion was used to investigate and quantify the asymmetric co-unit inclusion in the copolymers PBSA 20/80 and 60/40 (BS/BA content).

The author contributions of the following article are: M. Schäfer and K. S.-R. designed research. A. J. M. provided the copolyester samples. M. Schäfer performed, analyzed and interpreted the ¹H FID NMR experiments. M. Schäfer, S. Y. and K. S.-R. performed the ¹³C NMR measurements. M. Schäfer analyzed and interpreted the NMR data with the help of K. S.-R.. R. A. P.-C. and A. J. M. performed and interpreted the DSC results. R. A. P.-C. and A. P. performed and A. P. together with T. T.-A. interpreted the X-ray scattering experiments. M. Schäfer wrote the first draft of the paper. M. Schäfer wrote the paper in the final form with refinements by K. S.-R. and A. P. and all co-authors.

²The following article is reprinted (adapted) with permission from (Asymmetric Co-unit Inclusion in Statistical Copolyesters; Mareen Schäfer, Shichen Yuan, Albrecht Petzold, Ricardo A. Pérez-Camargo, Alejandro J. Müller, Thomas Thurn-Albrecht, Kay Saalwächter, and Klaus Schmidt-Rohr. *Macromolecules* **54** (2), 835-845 (2021) DOI: 10.1021/acs.macromol.0c01965). Copyright (2021) American Chemical Society. The link to the article on the publishers website is: <https://pubs.acs.org/doi/abs/10.1021/acs.macromol.0c01965>. No changes were made

Asymmetric Co-unit Inclusion in Statistical Copolyesters

Mareen Schäfer,* Shichen Yuan, Albrecht Petzold, Ricardo A. Pérez-Camargo, Alejandro J. Müller, Thomas Thurn-Albrecht, Kay Saalwächter, and Klaus Schmidt-Rohr*



Cite This: *Macromolecules* 2021, 54, 835–845



Read Online

ACCESS |



Metrics & More

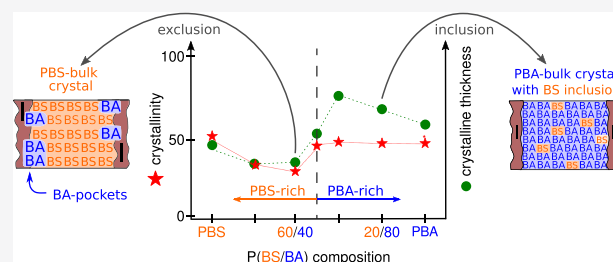


Article Recommendations



Supporting Information

ABSTRACT: The biodegradation of isodimorphic random butanediol-succinate/adipate copolymers (PBSAs) can be affected by a change in the semicrystalline morphology. A crucial point for the final semicrystalline structure is the incorporation of monomers of the minority component into the crystals of the majority component. We use proton time-domain NMR and wide-angle X-ray scattering to characterize the copolymers across their complete composition range and analyze the possible inclusion of minority comonomers in the PBA-rich 20/80 and the PBS-rich 60/40 composition by applying different solid-state ^{13}C NMR experiments. For the PBA-rich copolymers, we find a nearly constant volumetric crystallinity of 50% up to the 50/50 composition combined with an increase of the crystalline lamella thickness. NMR has detected the BS units incorporated into the BA crystalline structure, where on average every tenth monomer is a BS comonomer. In PBS-rich crystals, the crystallinity and crystallite thickness decrease from neat PBS to PBSA 60/40 by 37% and ~20%, respectively. We also find evidence that the BA units are excluded from the bulk crystal but accumulate at the crystallite surface. The amount of BA units in these pocket-like structures can be estimated to be 7–9% of the BA comonomer content.



INTRODUCTION

Several synthetic polymers combine good mechanical properties with biodegradability and therefore find widespread use in biomedical and environmentally sensitive applications and also as conventional materials. In particular, aliphatic polyesters are an important material class due to their good biodegradability and related controllable degradation.^{1–3} These properties can be modified by tuning the semicrystalline morphology since they depend not solely on the chemical structure of the polymer but also correlate with the chain conformation, the final crystallinity, and the crystal surface structure.^{3,4}

Copolymers are macromolecules where two or more chemically distinct monomer units are covalently joined to form one polymer chain,⁵ making it possible to change the semicrystalline structure significantly. The final solid-state morphology is strongly influenced by the composition mixture and sequence distribution.^{6,7} A random polymerization of both monomeric units usually interferes with the formation of extended crystalline lamellae and in general results in an increased biodegradation rate as well as reduced crystallinity, melting point, and tensile strength of the copolymeric material in comparison to the homopolymer.⁸ Additionally, the semicrystalline properties of these random copolymers depend on whether the two monomers are capable of forming one joint crystal structure if only a small amount of co-units can be included or whether the minority component is completely excluded from the crystalline lamellae of the majority

comonomer. According to these conditions, one distinguishes between isomorphism, isodimorphism, or total exclusion.

In the first case, both monomers produce a solid-state morphology with one shared crystalline structure over the complete composition range. To obtain this isomorphic behavior, strict molecular requirements of both comonomers, namely, similar and compatible chain conformations, lattice symmetry, unit cell parameters, total miscibility in the melt, and a similar rate of crystallization, need to be fulfilled. The resulting properties of the various copolymer compositions (such as crystallinity and melting point) can be described by a linear interpolation of the neat homopolymer properties.^{6,7,9}

Isodimorphic behavior is characterized by the formation of a distinct crystalline phase of one co-unit. In the so-called pseudo-eutectic range, often for equimolar compositions, i.e., near 50/50, both components crystallize each in their own crystalline structure. The formation of a semicrystalline morphology occurs over the complete composition range.¹⁰ Isodimorphism exists in cases where both comonomers do not fulfill the strict molecular requirements,^{6,10} but the structures are sufficiently similar such that partial comonomer inclusion

Received: August 25, 2020

Revised: November 17, 2020

Published: January 4, 2021

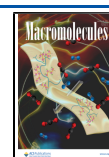


Table 1. Melting Temperature T_m , Average Plateau Signal Fractions of the Rigid (f_r), Intermediate (f_i), and Highly Mobile (f_m) Phases Derived from the Proton FID Analysis and Long Period L Derived from Small Angle X-ray Scattering^b

P(BS-BA)	T_m (°C)	f_r^a	f_i^a	f_m^a	L (nm)	$\Delta d_{c, \text{NMR}}$ (nm)	L_c (nm)
0/100	59.1	0.48	0.14	0.38	12.56	6.03–7.79	3.3 ± 1.3
20/80	47.9	0.49	0.13	0.38	14.45	7.08–8.96	4.9 ± 1.0
40/60	28.5/43.2	0.50	0.13	0.37	15.84	7.92–9.98	
50/50	17.8/52.4	0.47	0.18	0.35	11.15	5.24–7.25	
60/40	70.2	0.33	0.13	0.54	10.58	3.49–4.86	1.5 ± 0.4
80/20	92.6	0.38	0.12	0.50	9.33	3.54–4.67	3.0 ± 0.6
100/0	113.5	0.52	0.17	0.31	8.52	4.43–5.88	3.2 ± 0.4

^aError approximately 5% of the given value. ^bCalculated lamellar thickness range from NMR parameters $\Delta d_{c, \text{NMR}}$ with the lower limit $d_{c, \text{min}} = L \cdot f_r$ and the upper limit $d_{c, \text{max}} = L \cdot (f_r + f_i)$, and the correlation length L_c .

into the crystal lattice of the second co-unit is possible. The resulting semicrystalline structure depends on the amount of the partially included co-unit. The structural and thermal properties are in general depressed at intermediate compositions. The higher the amount of the included comonomer, the closer is the behavior to the isomorphous case. In the case of nearly complete exclusion, the parameters defining the structure are closer to the case of complete exclusion, where the co-units are rejected from the crystalline lamellae of the dominant comonomer. The resulting crystals are relatively thin because pure crystallizable segments are limited in length by the occurrence of noncrystallizable comonomers. As a result, thermal properties are strongly depressed and a region exists (around nearly equimolar mixtures) where the copolymer does not crystallize.¹⁰ Generally, the copolymer properties and biodegradability are strongly dependent on how severely the crystal formation is hindered by the occurrence of the randomly distributed co-units and their possible inclusion into the crystal.

In this work, we investigate biodegradable random poly-(butanediol-succinate-*ran*-butanediol-adipate) (PBSA) copolymers, which display isomorphous behavior,¹¹ with strong focus on the 60/40 and 20/80 compositions. The semicrystalline properties of this copolymer have been analyzed quite extensively, with regard to their biodegradability,^{12–15} melt,¹⁶ thermal properties,^{11,17,18} and crystallization kinetics.^{19,20} Both homopolymers are polymorphous and develop so-called α and β forms. The α -form of PBS is characterized by a monoclinic unit cell with lattice parameters $a = 5.232 \text{ \AA}$, $b = 9.125 \text{ \AA}$, $c = 10.90 \text{ \AA}$, and $\beta = 123.9^\circ$, with an all-trans conformation of the succinate and a TGT \bar{G} T conformation of the butanediol units^{21,22} and forms when crystallized from the melt or solution.³ The β -form, which develops under stretching, has a monoclinic unit cell with lattice parameters $a = 5.84 \text{ \AA}$, $b = 8.32 \text{ \AA}$, $c = 11.86 \text{ \AA}$, and $\beta = 131.6^\circ$ with an all-trans chain conformation.²¹ The thermodynamically more stable α -form of PBA³ has a monoclinic unit cell with $a = 6.776 \text{ \AA}$, $b = 7.904 \text{ \AA}$, $c = 14.42 \text{ \AA}$, and $\beta = 135.6^\circ$ with slight deviations from an all-trans conformation in the ester moiety.^{23,24} The β -form is characterized by an all-trans conformation²⁴ and an orthorhombic unit cell with $a = 5.06 \text{ \AA}$, $b = 7.35 \text{ \AA}$, and $c = 14.67 \text{ \AA}$.^{25,26} Pérez-Camargo et al.¹¹ have reported a change from the α -PBA unit cell in the homopolymer to the β -form in PBA-rich PBSA-copolymers for slow cooling and also for neat PBA in the case of fast cooling. Neat PBS and PBS-rich compositions remain in the α -form, but the d -spacings increase with increasing the PBA amount.

Based on the changes in d -spacing and the change from α - to β -PBA, Pérez-Camargo et al.¹¹ suggested that a partial

inclusion of the minority component into the crystal structure of the second comonomer occurs over the complete composition range. On the other hand, Ren et al.¹⁹ report that no partial inclusion of the minority component occurs for the 80/20 composition since X-ray scattering experiments show that PBS and PBSA 80/20 have the same unit cell. This is supported by the results of ¹³C T_1 NMR experiments performed by Kuwabara et al.²⁷ on PBS and the PBSA 80/20 copolymer, which indicate that the minority BA units are solely in the amorphous phase and are completely excluded from the BS crystals. The inclusion of minority components is also affected by the crystallization condition. Pérez-Camargo and co-workers²⁰ reported that, for BS-rich crystals, the inclusion of the BA comonomer is limited to the case of slow crystallization, while for BA-rich crystals, the inclusion is independent of the cooling conditions.

We use ¹³C solid-state NMR experiments to answer the question of minority comonomer inclusion on two samples, namely, the 20/80 and 60/40 compositions, which are on either side of the pseudo-eutectic range. With additional time-domain proton free induction decay (FID) analysis and X-ray scattering, the changes in signal fractions of the rigid and mobile phases and structural parameters are investigated for the complete composition range.

EXPERIMENTAL SECTION

Materials. Neat PBA and PBS as well as all copolymers investigated in this work were produced by organometallic synthesis.¹¹ The synthesis and chemical characterization of the copolyesters has been reported previously.^{11,28,29} The chemical structure characterization of PBSA copolymers can be found elsewhere.¹¹ In this work, we will refer to the various copolymers according to their succinate/adipate molar composition ratios.

Time-domain NMR experiments (¹H FID analysis) and X-ray scattering were performed over the complete composition range, while the focus of the additional investigations with ¹³C NMR filter experiments lies on the 20/80 and 60/40 compositions and for reference on neat PBS and PBA. Prior to the experiments all samples were held in the melt state at approximately 30 °C above their melting temperature (see Table 1) for 5 min and subsequently cooled at 5 K/min to –50 °C followed by stepwise heating at 10 K/min to the desired experimental temperature. An exception were the ¹³C-filter NMR experiments on the 60/40 sample, which was isothermally crystallized at 35 °C for 21 h and afterward cooled with liquid nitrogen. A comparison of the results of NMR studies of the 60/40 sample with both thermal histories is given in section A in the Supporting Information and reveals only little difference with respect to the characteristic NMR features.

Small-Angle and Wide-Angle X-ray Scattering. X-ray scattering experiments were performed using a Retro-F laboratory setup (SAXSLAB, Massachusetts) equipped with a microfocus X-ray

source (AXO Dresden GmbH, Germany) with an ASTIX multilayer X-ray optics (AXO Dresden GmbH, Germany) as monochromator for Cu $K\alpha$ radiation ($\lambda = 0.154$ nm). The instrument was used in transmission mode. As sample holders, aluminum discs with a central hole of 2 mm in diameter were used. Measurements were recorded in vacuum using a PILATUS3 R 300 K detector (Dectris Ltd., Switzerland). The measurements were performed at two samples-to-detector distances to cover a larger q -range ranging from 0.02 \AA^{-1} up to about 3.1 \AA^{-1} ($s = 0.03$ to 7 nm^{-1}). We used a measurement time of 60 s for the small-angle X-ray scattering (SAXS) range and 300 s for the wide-angle X-ray scattering (WAXS) range.

For the measurement, the samples were heated to the corresponding temperatures, using a hotstage with a TMS 94 temperature controller (Linkam, United Kingdom) and a LNP liquid nitrogen controller (Linkam, United Kingdom). Prior to the scattering measurement, the samples were heated to $150 \text{ }^\circ\text{C}$ and cooled to $-40 \text{ }^\circ\text{C}$ with a cooling rate of 5 K/min and subsequently heated to the measurement temperature of $21 \text{ }^\circ\text{C}$. The intensity was normalized to the scattering of the density fluctuations at $q = 0.5 \text{ nm}^{-1}$ in order to account for different amounts of material in the X-ray beam.

^1H NMR FID Analysis. The ^1H FID (free induction decay) experiments were performed on a Bruker Avance III spectrometer with a proton Larmor frequency of 200 MHz and a short dead time of $2.5 \mu\text{s}$. All data sets were acquired under stepwise heating from $-50 \text{ }^\circ\text{C}$ to T_{melt} with a temperature accuracy of $\pm 1 \text{ K}$ and a temperature gradient of $\pm 0.5 \text{ K}$ within the sample. The time between scans was sufficiently long to allow the magnetization to return to its equilibrium state.

^{13}C Cross-Polarization. The ^{13}C NMR experiments were performed on a Bruker Neo 400WB NMR spectrometer at a ^{13}C resonance frequency of 100 MHz. Most of the measurements were conducted using a Bruker double resonance magic-angle spinning (MAS) probe head with 4 mm zirconia rotors. While the PBSA 60/40 sample was placed into a Kel-F insert first, all other samples were loaded directly into the rotors. The typical B_1 field strength used in cross-polarization was 58 kHz, and the radio-frequency field strength was $\gamma \cdot B_1/2\pi = 69$ and 63 kHz for ^1H and ^{13}C pulses, respectively. SPINAL-64³⁰ with a field strength of 95 kHz and two pulse phase modulation (TPPM)³¹ with a field strength of 85 kHz were used for dipolar decoupling during the echo and acquisition periods, respectively. The typical contact time in cross-polarization (CP) experiments was 1.1 ms, with an amplitude ramp from 86 to 100% on the ^1H channel, and the number of scans ranged from 512 to 4096. ^{13}C chemical shifts were referenced to the glycine ^{13}COO resonance at 176.46 ppm. The ^{13}C NMR spectra were acquired at $\sim 300 \text{ K}$ unless otherwise noted. The MAS frequency used in most of the experiments was 5 kHz, except for ^1H DQ experiments, where 8 kHz was used.

^{13}C Direct Polarization. In ^{13}C direct polarization (DP) NMR experiments for the detection of mobile CH_2 groups in all the samples, recycle delays were set to 1 s with 4096 scans.³² For ^{13}C T_1 measurements of the mobile components during a z -filter with alternating storage of the magnetization along $+z$ and $-z$ and corresponding receiver inversion, the recycle delay was set to 2 s, with up to 2048 scans.

$T_{1,C}$ Filter. After cross-polarization from ^1H to ^{13}C , a phase-cycled z -filter³³ of up to 10 s was applied to study the ^{13}C spin–lattice relaxation behavior in the crystalline phases, with a 0.1 ms CP time and 4096 scans. The total measurement time for a series of spectra for each sample was up to 44 h.

^1H Double Quantum Filter at 8 kHz. For ^1H double quantum (DQ) filtering with ^{13}C detection, half a rotation period ($63 \mu\text{s}$) bracketed by 90° pulses for DQ generation and the same duration for reconversion were applied to the rotating sample with a MAS frequency of 8 kHz. The intermediate DQ generation time maximizes the polarization of components of intermediate mobility, while the DQ coherence in the crystalline components is destroyed by multi-spin effects and that of the amorphous components does not get excited due to the weak dipolar couplings. After cross-polarization from ^1H to ^{13}C , the ^{13}C signal of the intermediate components was

observed. The ^{13}C T_1 relaxation of the intermediate-mobility components selected by this DQ filter was measured up to 1 s.

$T_{1,p}$ Filter. A ^1H spin-lock field up to 5 ms with a field strength of 54 kHz on the ^1H channel was applied after the ^1H excitation, allowing for spin–lattice relaxation of spins in the rotating frame. After cross-polarization from ^1H to ^{13}C , the ^{13}C signal of the remaining components was observed. A 0.1 ms CP time and a 1 s $T_{1,C}$ filter was used to suppress the amorphous signals. Up to 1024 scans were acquired for the spectra presented.

$T_{2,H}$ Filter and Spin Diffusion. Experiments with ^1H spin diffusion after $T_{2,H}$ filtering followed by cross-polarization to ^{13}C were used to detect the location of immobilized segments. During the $T_{2,H}$ filter of 0.4 ms duration, the ^{13}C – ^1H dipolar interaction was decoupled by irradiation at the ^{13}C frequency with a field strength of 51 kHz. The mixing time for ^1H spin diffusion (after the $T_{2,H}$ filter and before CP) ranged up to 1 s. After cross-polarization from ^1H to ^{13}C , the ^{13}C signal of the ^1H -polarized crystalline components was observed via suppression of the noncrystalline components by a 1 s $T_{1,C}$ filter. The total measurement time for a series of spin diffusion data was up to 21 h.

RESULTS AND DISCUSSION

Sample Characterization. Thermal Behavior. The thermal behavior for all PBSA copolymers was previously studied by us.^{11,20} To summarize the results, the heating scans at 20 K/min for all PBSA copolymers and both homopolymers are shown in Figure 1. The samples were cooled from the melt

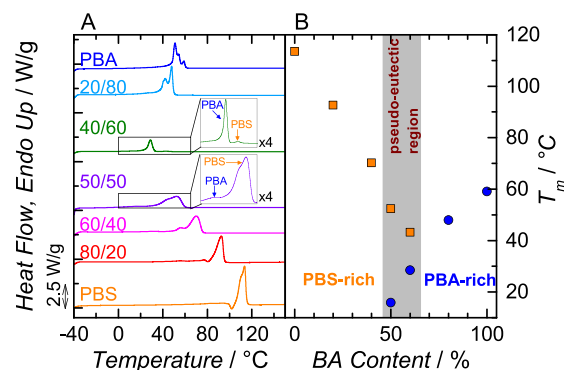


Figure 1. (A) DSC thermograms (second heating at 20 K/min after previously cooling at 5 K/min), with enlarged traces showing the two-step melting of neat PBA and PBS crystal in PBSA 40/60 and PBSA 50/50. (B) Melting temperature values T_m , taken from (A), as a function of BA content. The shadowed region indicates the pseudo-eutectic region. Data taken from ref 11.

at 5 K/min until $-40 \text{ }^\circ\text{C}$. In this way, all the thermal transitions (including those below room temperature) are registered in the subsequent heating. With increasing comonomer content, the melting temperature decreases for both PBS- and PBA-rich copolymers. In the so-called pseudo-eutectic region (i.e., PBSA 40/60 and PBSA 50/50 copolymers), BA- and BS-rich crystals coexist and a two-step melting process can be detected (similar changes are also observed for the crystallization behavior during the non-isothermal test as well as other variables or parameters related to other crystallization conditions^{11,20}). BA-rich crystals have a melting temperature approximately 10 – $15 \text{ }^\circ\text{C}$ lower than BS-rich crystals. The melting behavior of all other samples is defined by one melting temperature (see Table 1), indicating only one type of crystals. It is worth noting that the coexistence of BA- and BS-rich crystals and the two-step melting process,

in the 40/60 and 50/50 compositions, had been proven by WAXS measurements performed at $-40\text{ }^{\circ}\text{C}$, in our previous work.¹¹ In the present work, the WAXS patterns were taken at $21\text{ }^{\circ}\text{C}$ to facilitate their analysis; therefore, the coexistence of BA- and BS-rich crystals is not reflected in Figure 4.

¹H NMR FID Analysis and Rigid Signal. The free induction decay (FID) describes the time evolution of the transverse magnetization decay after a $90^{\circ}\frac{\pi}{2}$ pulse. The differences in the time-averaged dipole–dipole couplings in rigid, intermediate, and mobile regions enable the distinction and quantification of the signal contributions of each phase. The rigid phase has strong dipole–dipole couplings, resulting in a fast signal decay. In the mobile phase, a slower decay is caused by the large-scale motions far above T_g and was also selectively detected in MAPE-filtered FIDs with filter times between 0.55 and 0.70 ms (see Figure 2A). The acquired full FIDs can be decomposed

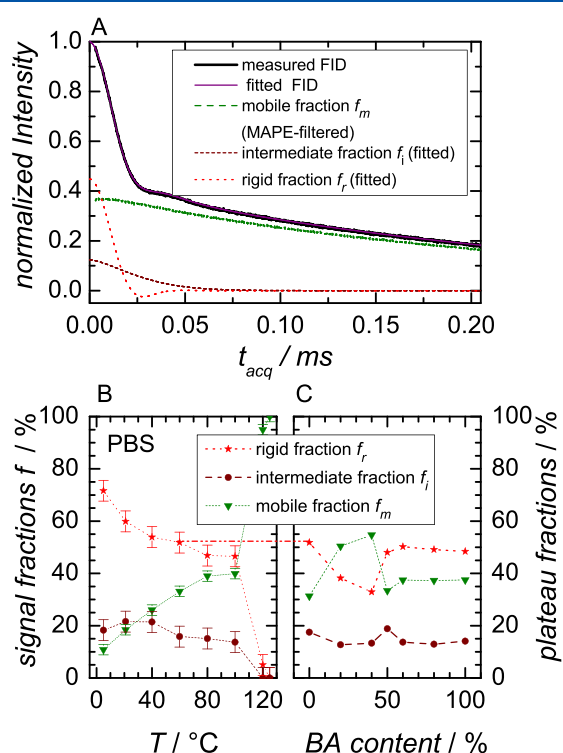


Figure 2. ¹H FID analysis. (A) Deconvolution into the rigid (short-dashed), intermediate (dashed), and highly mobile (short-dotted) fraction of PBS at $80\text{ }^{\circ}\text{C}$. The acquired and fitted FIDs are plotted as thick black and purple solid lines, respectively. (B) Temperature-dependent signal fractions of PBS. (C) Average signal fractions given for the complete composition range. The average is calculated for the plateau-like temperature range, starting at $40\text{ }^{\circ}\text{C}$ for PBS, at $21\text{ }^{\circ}\text{C}$ for BA content between 20 and 50%, and at $0\text{ }^{\circ}\text{C}$ for a BA content of $\geq 50\%$ and ending at $15\text{--}20\text{ }^{\circ}\text{C}$ before the final or first partial melting (see Table 1).

into three signal fractions,^{34–36} the rigid (f_r), intermediate (f_i), and highly mobile (f_m) phases, by using the fit function

$$I_{\text{norm}}(t) = f_m(t) + f_i(t) + f_r(t) \\ = f_m \cdot \exp(-t/T_{2,m}^*) + f_i \cdot \exp(-t/T_{2,i}^*) \\ + f_r \cdot \exp(-0.5(at)^2) \cdot \sin(bt)/bt$$

with the transverse relaxation times $T_{2,i}^*$ and $T_{2,m}^*$, which are in the range of tens and hundreds of microseconds, respectively. The fit parameters of the mobile amorphous phase are known from the MAPE-filtered FID and are used to stabilize the three-component fit of the FID. The rigid fraction $f_r(t)$ is described by a so-called Abragam function, with parameters a and b , yielding the static second moment via $M_2 = \frac{9}{20}D_{\text{eff}}^2 = a^2 + \frac{b^2}{3}$, where D_{eff} is the effective (average) dipole–dipole coupling constant.

In Figure 2B, the temperature dependence of the three signal contributions of PBS is shown. At low temperatures, close to T_g , the segmental motions in the amorphous phase are too slow to be detected as a mobile contribution. The glass transition temperatures of PBSA copolymers and neat homopolymers range from $-35.2\text{ }^{\circ}\text{C}$ for neat PBS to $-59.2\text{ }^{\circ}\text{C}$ for neat PBA.¹¹ For increasing temperatures starting at $40\text{ }^{\circ}\text{C}$, far above the corresponding T_g , a plateau-like temperature range for the rigid fraction of PBS develops before the start of the melting process. This behavior is observed for all samples, with the exception of the 50/50 and 40/60 composition, where a two-step melting process, caused by the separate PBA and PBS crystals, is observed. The temperature-dependent signal fractions of the copolymers and PBA are shown in Figure S.3 in the Supporting Information. A plot of the plateau fractions defined as the average fractions for the plateau-like temperature range, defined by the temperature-dependent rigid fractions (for PBS the range from 40 to $100\text{ }^{\circ}\text{C}$), is shown in Figure 2C. For PBSA 40/60 and PBSA 50/50, close to the pseudo-eutectic range, the plateau fractions are determined before the melting of pure BA crystals in order to give an average for the crystallinities of both comonomers. Note that the plateau-like temperature range shows a stronger temperature dependence for the copolymers, which can be explained by the melting of small secondary lamellae.^{35,37} For the sake of comparability, the average values for the indicated temperature ranges rather than the specific values at a given temperature are shown in Figure 2. The constant rigid fraction with decreasing BA content down to the 50/50 composition and its sudden decrease for samples with majority BS content suggests an inclusion of minority BS units into BA crystals but an exclusion or very limited inclusion of the minority BA units into BA crystals.

X-ray Scattering (WAXS/SAXS). The semicrystalline structure of PBSA was investigated by SAXS, for which the results are shown in Figure S.4 in the Supporting Information. A quantitative analysis of the SAXS data is difficult as strictly speaking a treatment as a two-phase system might not be justified over the full range of compositions. However, well-defined values of the long period can be determined for all compositions from the peak maxima of the Lorentz-corrected SAXS patterns, which are displayed in Figure 3.

An average crystal thickness $d_{c,\text{NMR}}$ was estimated using the long period L and the signal fractions obtained from ¹H FID analysis. The range of $d_{c,\text{NMR}}$ is determined by the rigid fraction f_r and the intermediate fraction f_i

$$L \cdot f_r \leq d_{c,\text{NMR}} \leq L \cdot (f_r + f_i) \quad (1)$$

depending on whether or not the intermediate fraction is also attributed to the crystalline phase. The calculated values for the lamellar thickness range obtained from NMR $d_{c,\text{NMR}}$ as well as the long period L are given in Table 1.

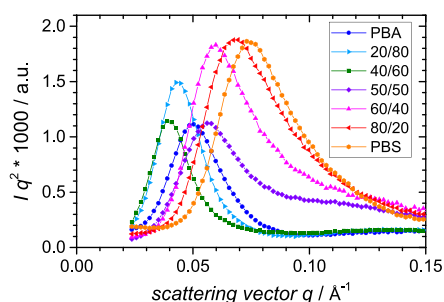


Figure 3. Lorentz-corrected SAXS intensities for all sample compositions.

Accompanying WAXS data for all samples at room temperature are shown in Figure 4. The reflections for the

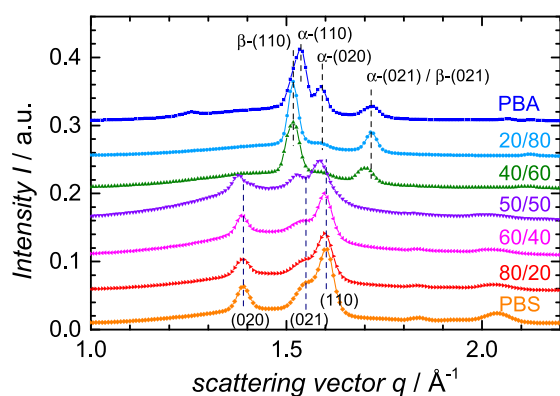


Figure 4. WAXS diffractograms for all sample compositions taken at room temperature. Data shifted vertically by 0.05 each for clarity.

pure components were indexed using the monoclinic unit cells for PBS²¹ and α -PBA,¹⁸ respectively. Similar to the results by Perez-Camargo et al.,¹¹ a change from the α -form in neat PBA to the β -form for PBA-rich copolymers was found and indexed according to the orthorhombic unit cell of β -PBA.²⁵ For the 40/60 composition, the reflections of the minority fraction of PBS crystallites were difficult to discern, but they could be confirmed in a diffractogram taken above the melting temperature of PBA.¹¹ In PBSA 50/50, the PBA crystallites had melted already at room temperature, and therefore only reflections corresponding to the PBS crystallites were detected. The corresponding d -spacings are shown in Figure S.4 in the Supporting Information.

While qualitatively the observations are similar to previous results,¹¹ the effects are in fact smaller in these measurements taken at room temperature and especially for the PBA-rich compositions superimposed by a change in crystal structure. (Previous WAXS measurements were performed at -40 °C.) More detailed information about the possible inclusion or exclusion of comonomers in crystalline PBSA by NMR could therefore offer new interesting insights.

WAXS measurements also serve as a cross-check for the relative change in lamellar thickness of the different copolymers. Therefore, the correlation length along the crystallographic c -axis, L_c was determined from the width of the (021) reflection using the Scherrer equation and a projection onto the c -axis

$$L_c = L_{(021)} \sin(\alpha) \approx \frac{2\pi}{\Delta q} \sin(\alpha) \quad (2)$$

with the full width at half-maximum Δq and the projection angle α along the c -axis. The projection angle was determined from the unit cell parameters b and c by $\tan(\alpha) = \frac{b}{2c}$.

Assuming a constant chain tilt angle between the crystallographic c -axis and the lamellar normal for all compositions, changes in L_c should resemble the relative changes in lamellar thickness. Figure 5 depicts the lamellar thickness range

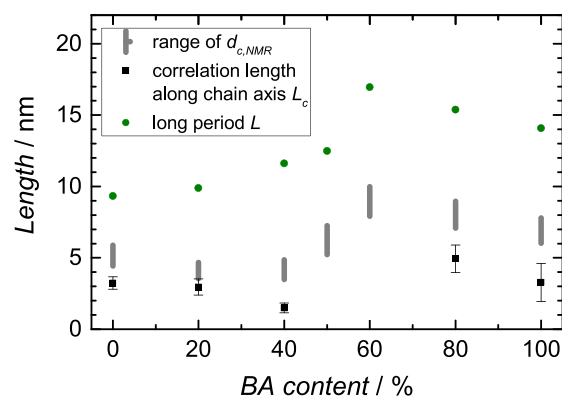


Figure 5. Long period L from SAXS, lamellar thickness range estimated from NMR $d_{c,NMR}$ using eq 1, and correlation length along the c -axis L_c using eq 2 for all sample compositions. Error bars reflect the fitting uncertainty.

determined by NMR $d_{c,NMR}$ as well as the correlation length along the direction of the chain (crystallographic c -axis) L_c . The absolute values of L_c and $d_{c,NMR}$ differ from each other as expected because a possible chain tilt is not accounted for in L_c . Nevertheless, for BS-rich and BA-rich copolymers, L_c follows the change in $d_{c,NMR}$ nicely. The values of L_c are also in good agreement with the lamellar thickness of PBSA copolymers determined by Pérez-Camargo et al.²⁰ The values for copolymers in the pseudo-eutectic range, PBSA 50/50 and PBSA 40/60, are not given since the peak positions of these compositions in Figure 4 deviate considerably from those of the pure components, indicating an additional change in crystal structure for the midpoint compositions. The changes in the crystal structure can be attributed to the proximity to the pseudo-eutectic range and the associated formation of neat PBA and PBS crystals. Note that in PBSA 50/50, the neat PBA crystals are already molten at room temperature.

Within the framework of these estimations, the crystallite thickness for neat PBS is rather limited with $d_c < 6$ nm and therefore the crystalline structure contains fewer than 10 monomeric units even if chain tilt is assumed. For PBS-rich copolymers, the crystallite thickness reduces further with increasing BA fraction. An inclusion of minority BA units in a BS crystal phase seems unlikely since such small crystalline lamellae might become rather unstable by the inclusion of a gauche-containing defect. In contrast, the neat PBA crystals are thicker than PBS crystals and an increase of the crystallite thickness for increasing BS units in BA-rich samples is detected. Even though PBSA 40/60 and PBSA 50/50 are special cases, due to their closeness to the pseudo-eutectic range, the steady increase of the long period L from neat PBA to PBSA 50/50 with more or less constant volumetric

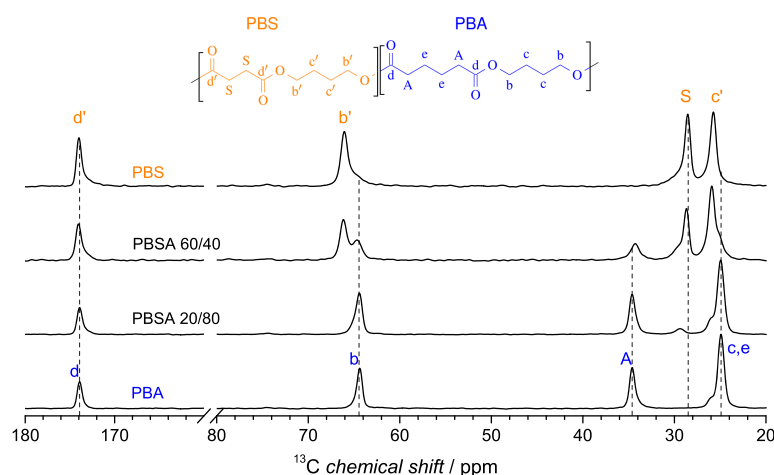


Figure 6. ^{13}C CP MAS spectra of PBS, PBA, PBSA 20/80, and PBSA 60/40 with a 1.1 ms contact time. The numbering scheme of the PBSA copolymer is shown at the top.

crystallinity indicates an increase of the lamellar thickness and a possible inclusion of minority BS units, in agreement with expectations based on crystallinity mentioned above.

To detect and quantify a possible inclusion of the minority components, samples on either side but away from the pseudo-eutectic range and with the maximum possible minority comonomer content, namely, PBSA 20/80 and PBSA 60/40, were chosen to be analyzed in more detail using various ^{13}C NMR experiments.

^{13}C MAS NMR Experiments on PBSA 20/80 and PBSA 60/40. ^{13}C CP MAS Spectra. In Figure 6, the ^{13}C 1.1 ms CP spectra of the homopolymers and the copolymers 20/80 and 60/40 are shown together with their corresponding numbering scheme. The resonances labeled with A and S can be used to analyze the BA and BS units in the copolymers separately, while all other resonances overlap. The difference in the chemical shifts of the butanediol b and b' resonances of PBA and PBS, respectively, is explained by a different chain conformation. According to Ichikawa et al.,^{21,22} PBS adopts a $T_6GT\bar{G}T$ conformation, whereas PBA exhibits a slight deviation from an all-trans conformation with different reported values for the $\text{CH}_2\text{--O}$ torsion angle in the ester group.^{23,24}

Relaxation-Filtered MAS ^{13}C NMR Spectra. Immobilization of segments, including minority components, in the crystal or at the crystal surface can be identified in NMR through spin-lattice relaxation filtering. In CP ^{13}C spectra, resonances of the crystalline, intermediate, and highly mobile amorphous phases of both comonomers are simultaneously detected, and these signals may overlap. Crystalline segments are identified by their long ^{13}C spin lattice relaxation times ($T_{1,C} > 10$ s). They also show less inhomogeneous line broadening than the disordered intermediate and much less motional averaging of dipolar couplings than the amorphous segments. To selectively detect signals of the different phases in the copolymers 20/80 and 60/40, with a focus on the S and A resonances, various ^{13}C -filtered spectra were recorded and analyzed. Direct polarization (DP) excitation with a short recycle delay of 1 s selectively excited the resonances of the highly mobile, amorphous components. Conversely, a short contact time of 0.1 ms in CP NMR strongly suppressed the signals of these isotropically mobile segments with their weak C–H couplings. Meanwhile, a 0.1 ms CP time polarizes not only the crystalline but also

partially the intermediate phase, and their signals can be separated based on the different $T_{1,C}$ relaxation times of the phases. Chain segments with intermediate-amplitude dynamics undergo faster ^{13}C spin–lattice relaxation than crystalline components.

The intensity decay of $T_{1,C}$ -filtered CP MAS spectra with a 0.1 ms contact time of PBSA 20/80 and PBSA 60/40 for the S resonance at 29.5 ppm, the A resonance at 34.5 ppm, and the mixed A+S resonance (resonances c/c' and e in Figure 6) at 25 ppm is shown in Figure 7, with the initial intensities normalized to 1. The intensity decay, which is sensitive to

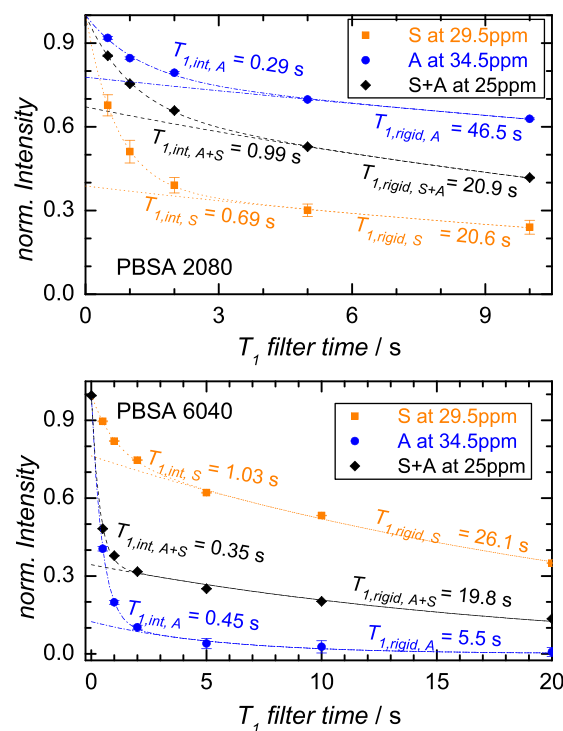


Figure 7. Intensity decay of T_1 -filtered CP MAS spectra with a 0.1 ms contact time of PBSA 20/80 (top) and PBSA 60/40 (bottom). The intensities are normalized to 1. The dotted and dashed lines are the corresponding fits.

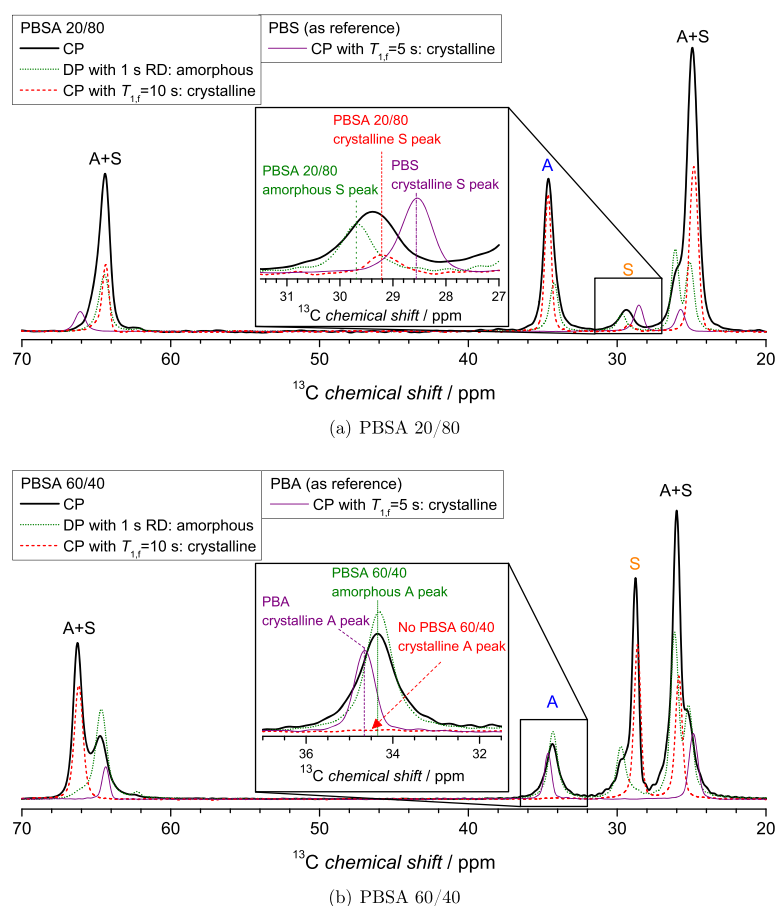


Figure 8. Comparison of selective ^{13}C spectra of (a) PBSA 20/80 and (b) PBSA 60/40: ^{13}C CP MAS spectrum with a 1.1 ms contact time (black) displays both rigid and mobile amorphous components. A direct polarization (DP) spectrum (green) with a 1 s recycle delay displays only the mobile amorphous resonances, while a $\tau = 10$ s T_1 -filtered CP spectrum with a 0.1 ms contact time (red) shows the signals corresponding to the crystalline phase. A T_1 -filtered CP spectrum of the neat majority component (purple) is shown as a reference of the crystalline peak positions of the minority resonance. In the insets, the comparison of all four spectra of the minority resonances is highlighted.

motions on the timescale of the inverse Larmor frequency ($\sim 0.01 \mu\text{s}$), of the S, A, and S+A resonances of PBSA 20/80 can be separated into intermediate and crystalline signal fractions, with $T_{1,\text{int}} \lesssim 1$ s and $T_{1,\text{rigid}} > 20$ s, respectively. The long relaxation time of $T_{1,\text{rigid},\text{S}} = 20.6$ s indicates a crystalline environment of the minority BS units.

In Figure 8a, a comparison of the PBSA 20/80 spectra selective for the phases of different segmental mobilities, with focus on the S resonance of the minority component, is shown. In the regular CP spectra (thick black line), the crystalline and amorphous signal contributions cannot be separated in the S resonance. The mobile amorphous (green dotted line) and rigid crystalline (red dashed line) signals, which have different chemical shifts, are detected separately after 1 s DP excitation and CP NMR with a ^{13}C 10 s T_1 filter, respectively; the intermediate components have not yet relaxed or have already relaxed away, respectively. The difference in chemical shift of the PBSA 20/80 S resonance with the reference crystalline peak of neat PBS (thin purple solid line), detected in a 5 s T_1 -filtered 0.1 ms CP spectrum, reveals that the crystalline BS units in PBSA 20/80 do not form pure PBS crystals but exist in a different crystalline environment, apparently incorporated into the BA crystalline structure. This is important direct evidence of mixed crystals in PBSA 20/80.

In the unselective CP ^{13}C spectrum of PBSA 60/40 (black line in Figure 8b), only one broad A peak is observed. The mobile resonance (green dotted line), detected after DP with a 1 s recycle delay, has the same peak position as the CP resonance. The ^{13}C T_1 relaxation of PBSA 60/40 in CP spectra can also be deconvolved into contributions from intermediate-amplitude and nearly immobilized segments. While the intermediate component of the A resonance decays on a similar timescale as the intermediate S component, the slowest relaxing A signal, associated with nearly immobilized minority BA units, decays still 4 to 5 times faster than the crystalline signals of the S and the mixed A+S resonance.

After a 10 s T_1 filter, no signal of the A resonance remains (red dashed line), indicating that the sample contains no crystalline minority component. For reference, the neat PBA crystalline peak (thin purple line) is also shown. The comparison of the filtered ^{13}C spectra as well as the fast ^{13}C T_1 decay leads to the conclusion that no significant fraction of BA units is included into the crystalline BS structure.

Potentially, the faster signal decay of the A resonance of PBSA 60/40 could be a consequence of local motions with rates near the inverse Larmor frequency driving ^{13}C T_1 relaxation, caused by the presence of gauche conformers due to a potential inclusion of BA units, where each monomer has

two CH₂ groups more than the BS comonomer, into the BS crystal. To exclude this hypothesis, ¹H $T_{1\rho}$ experiments with ¹³C detection were performed on PBSA 60/40 as well as the mixed crystals in PBSA 20/80.

With a $T_{1\rho}$ filter, relaxation of spin-locked magnetization is probed, with ¹H spin diffusion averaging the relaxation on the scale of a few nanometers. If both BA and BS units are in the same crystal, the intensity decay after a certain sufficiently long $T_{1\rho}$ filter time must be very similar.

A 5 ms $T_{1\rho}$ filter was applied before a 0.1 ms CP time, yielding signals mainly of the rigid and some of the intermediate component. In Figure 9, the $T_{1\rho}$ -filtered spectrum

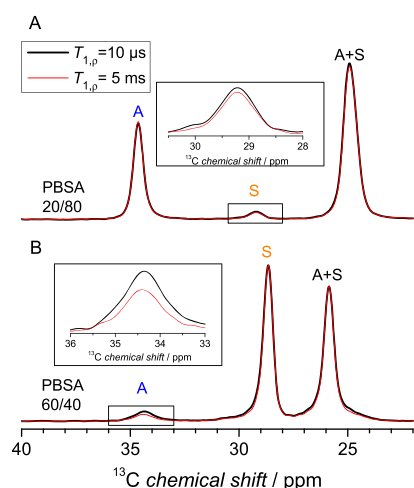


Figure 9. Comparison of relative peak intensities in $T_{1\rho}$ -filtered ¹³C CP MAS spectra after spin locks of 10 μ s and 5 ms duration followed by 0.1 ms cross-polarization and an additional 1 s T_1 filter to select the immobilized components. The intensities for the different $T_{1\rho}$ -filtered spectra are scaled in (A) to match the PBA resonance at 34.5 ppm for PBSA 20/80 and in (B) to match the PBS resonance at 28.5 ppm for PBSA 60/40.

is compared with a spectrum after a negligible spin lock of 10 μ s duration. The intensities are scaled such as to match the crystalline A resonances for PBSA 60/40 and the crystalline S resonances for PBSA 20/80. For PBSA 20/80, the reference system with mixed crystals, the signal decays of all three shown resonances are quite similar: a slightly faster decay of the A resonance shows that not all but the majority of the rigid BS units share the crystalline $T_{1\rho}$ because they are incorporated into the BA crystalline structure. The amount of the included minority BS units in the BA crystalline structure of PBSA 20/80 can be estimated by comparing the integrals of the A and S resonances in all T_1 -filtered spectra. It follows that 1 out of 10 crystallized monomers in PBSA 20/80 is a BA unit. Taking into account also the different lengths and the related difference in volume occupied in the crystal, the crystalline fraction of BA units in the BS crystal can be estimated to be 9%.

In contrast, the intensity decay of the small crystalline A resonance in PBSA 60/40 displays a more pronounced signal loss than the majority crystalline S resonance. These results together with the fast T_1 relaxation reveal that the majority BA and minority BS units do not form the same bulk crystal. Thus, spin diffusion experiments are used to determine the location

of these rigid BA units within the semicrystalline structure of the PBS 60/40 copolymer.

¹H Spin Diffusion: Location of the Rigid-Intermediate Fraction in PBSA 60/40. The relatively long 5.5 s T_1 relaxation time of the least mobile but noncrystalline A component indicates that BA units exist in a more restricted environment than the intermediate phase with its shorter relaxation time $T_1 \approx 1$ s. The location of crystalline and interfacial minority components across the structural period of the morphology can be probed by ¹H spin diffusion. For such an experiment, the magnetization of the mobile component is selected by a proton T_2 filter. After a certain mixing or ¹H spin diffusion time and cross-polarization to ¹³C, a 1 s T_1 filter on the ¹³C channel was employed to suppress the signal of the core amorphous component. Therefore, only the signal of the part of the crystallite polarized by spin diffusion will be detected. The measurement scheme is schematically shown in Figure 10A. With the minimal mixing time, no signal will be detected since the amorphous and intermediate signals are suppressed effectively by the T_{1C} filter and the crystalline phase is not yet polarized. For longer mixing times, polarization diffuses into the crystalline phases and a rigid component can be detected.

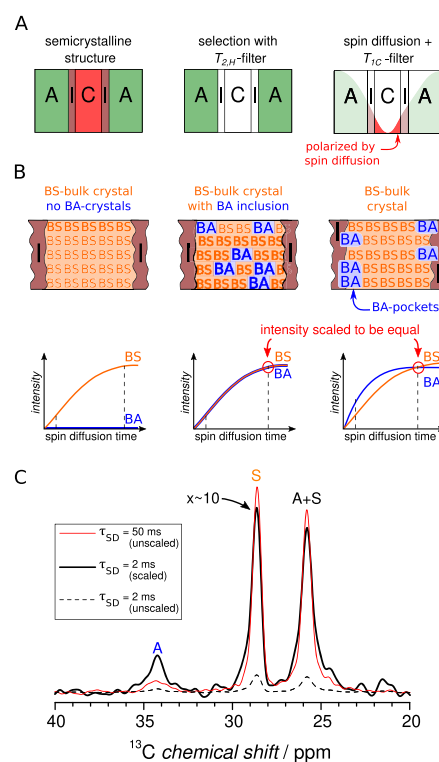


Figure 10. (A) Schematic representation of the ¹H spin-diffusion experiment with ¹³C detection. With a 0.4 ms ¹H T_2 filter, the mobile component magnetization is selected. After spin diffusion, CP, and a 1 s T_1 filter, the polarized crystalline part can be detected selectively. (B) Schematic intensity build-up curves of the A and S resonances for pure BS crystal, inclusion of BA units in a BS crystal, and with BA units in pocket-like structures at the crystalline-intermediate interface. (C) Comparison of relative peak intensities in ¹³C spectra of PBSA 60/40 after 2 ms (thick black trace) and 50 ms (thin red trace) of ¹H spin diffusion. The 2 ms spectrum (thick black trace) was scaled such that the integral of the S resonance is the same for both spin diffusion times. The unscaled 2 ms spectrum is shown at the bottom (dashed black trace).

A further increase of the spin diffusion time eventually leads to equilibration of the rigid signal intensity.

In Figure 10B, the expected intensity build-up curves of BA and BS units for three crystalline structures are presented. In the case of complete exclusion of BA units from the BS crystal or its surface, no A resonance signal would be detected, not even for a long spin diffusion time. In the case of inclusion of BA units, the signals of the A and S resonance would build up with the same rate, i.e., proportionally. Comparison of PBSA 60/40 spectra, scaled such that the integral of the S resonance is the same for the spectra, detected after 2 and 50 ms of spin diffusion time (see Figure 10C), makes it apparent that neither a pure BS crystal nor BA inclusions describe the crystalline structure of PBSA 60/40. The full spin diffusion build-up curves of PBSA 60/40 are shown in Figure S.6 in the Supporting Information. The presence of pure BS crystals without associated BA units is excluded due to the detection of an immobilized-A signal. With a mixed crystal, the A resonance would have the same intensity in both spectra since the intensities in the given spectra are scaled such that the integral of the S resonance is identical for both spin diffusion times. The observed intensity of the minority component is relatively higher for the shorter mixing time, implying that the BA units are polarized earlier than the bulk of the BS crystal. With increasing mixing time, the BS crystal becomes more strongly polarized, and therefore the intensity of the S relative to the A resonance for 50 ms of spin diffusion will be significantly higher than at 2 ms. This intensity scaling can only be explained by the location of the BA units at the crystallite surface, presumably in pocket-like structures as shown in Figure 10B. The occurrence of the randomly distributed BA units at the crystal edges suggests that they cannot be incorporated into the crystalline structure. This provides a simple explanation for the reduced lamellar thickness in comparison to neat PBS.

Quantification of Immobilized Minority Components with $T_{1,C}$ Filters. By a quantitative DP saturation recovery experiment without distortion by heteronuclear Overhauser enhancement, the different morphological components of BA units can be quantified. Phases with different mobilities relax with different spin–lattice relaxation times. Therefore, this experiment can be used to quantify the amount of BA units in the pocket-like structures as well as in the intermediate and mobile phases. The ranges of the fitting parameters for all three phases were determined by the signal decays of the A resonance after various $T_{1,C}$ filters (see Figure 11A). The intensity decay of the intermediate phase is analyzed in a ^1H DQ-filtered 0.4 ms CP experiment and yields $T_{1,\text{int}} = 0.355$ s. A $T_{1,C}$ filter applied after a DP ^{13}C NMR experiment with a 2 s recycle delay allows the quantification of the mobile relaxation time $T_{1,\text{mobile}}$ to 0.237 s. The relaxation time $T_{1,\text{rigid}} = 5.5$ s of the pocket-like structures, together with $T_{1,\text{int}} = 0.45$ s of the intermediate phase, was already determined by the intensity decay in T_1 -filtered 0.1 ms CP spectra, as shown in Figure 7. The different relaxation times for the mobile and intermediate phase can be explained by a gradient in mobility (mostly the motional amplitude) within the noncrystalline layers. These fitting parameters were used to stabilize the three-component fit of the saturation recovery data of the A resonance (plotted as a decay, 1 - normalized intensity), shown in Figure 11B, revealing that approximately 7–9% of BA units are in pocket-like structures at the crystallite surface.

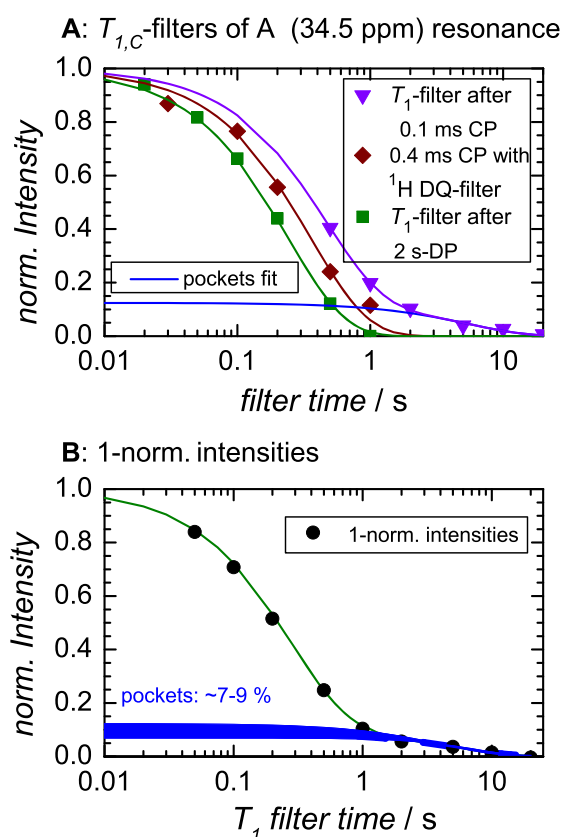


Figure 11. (A) T_1 relaxation of the A resonance of PBSA 60/40 at 34.5 ppm after three applied filter sequences. (B) Deconvolution of $T_{1,C}$ relaxation of the full A resonance of PBSA 60/40 into mobile, intermediate, and pocket fractions; data were obtained by saturation recovery but plotted inversely, as a decay, to match the curves in (A).

SUMMARY AND CONCLUSIONS

We have used a combination of time-domain ^1H NMR and ^{13}C NMR spectroscopy with relaxation time filters as well as WAXS to analyze the possible inclusion of the minority component into the crystallites in random PBSA copolymers. ^1H FID and WAXS measurements were used to characterize the complete composition range, while ^{13}C T_1 filters and ^{13}C -detected ^1H spin diffusion experiments answered the question of inclusion for the PBS-rich sample with a 60/40 composition and PBA-rich sample with a 20/80 composition, i.e., on either side of the pseudo-eutectic range.

Our data conclusively demonstrate crystal inclusion of the minority BS component in PBA-rich but not that of BA in PBS-rich samples. The long period and the calculated crystallite thickness d_c from SAXS and NMR increase from PBA to PBSA 40/60 by ~ 25 –30%. The volumetric crystallinity remains constant at 50% in PBA-rich samples down to PBSA 50/50. These observations imply the inclusion of the minority BS units into the BA crystal. The dependence of the crystallinity of PBA-rich samples on the comonomer content is therefore closer to the isomorphous case than to complete exclusion. Solid-state ^{13}C NMR with relaxation time editing directly detects the crystalline BS comonomers in BA crystals, with a characteristic long $T_{1,C}$, small line width and a distinct ^{13}C chemical shift that shows that they do not form

separate PBS crystallites. The amount of the included BS units can be estimated to be 9%.

In combination with the crystallinity from the FID analysis, this shows that ~22% of BS and ~55% of BA units are in a crystalline environment. The remaining BA and BS units form the intermediate and amorphous phases. In contrast, the crystallite thickness and crystallinity of PBS-rich copolymers (PBA, PBSA 80/20, and PBSA 60/40) decrease with increasing comonomer content by ~20% and ~37%, respectively, indicating that crystallites cannot extend beyond BA segments terminating sequences of pure BS. The observed slight increase of the long period is caused by a higher amorphous fraction, not by thicker crystalline lamellae, which contain only very few monomer units. ^{13}C NMR experiments reveal that the BA units in PBSA 60/40 are excluded from all crystals. The least mobile BA component, with a $T_{1\rho}$ five-fold shorter than in the crystallites, accounts for 7–9% of the total BA fraction. It can be assigned to BA segments terminating crystallizable sequences of BS segments and therefore located at the crystallite surfaces in pocket-like structures. The analyzed ^{13}C NMR results of PBSA 60/40 were detected on an isothermally crystallized sample. This thermal treatment differs from the preparation method used for the other samples and techniques. However, the comparison of FID and ^{13}C T_1 -filtered CP spectra reveals only slight differences in the overall signal fractions and melting behavior. The exclusion of BA units from the BS crystals is similar for both preparation methods.

The crystal inclusion of the minority component for PBA-rich but not for PBS-rich samples established here is in agreement with the more indirect conclusions of Ren et al.,¹⁹ Kuwabara et al.,²⁷ and Pérez-Camargo et al.²⁰ The advantage of our combination of ^{13}C MAS NMR experiments is that it reveals not only the asymmetric co-unit inclusion but also allows us to quantify the included minority units in PBSA 20/80 as well as the localization and quantification of the rigid-intermediate minority BA units in PBSA 60/40.

A change in thermal treatment of PBSA copolymers and a potential related change in the BA inclusion, as reported by Pérez-Camargo et al.,²⁰ could tackle the question if the randomly occurring BA units are the limiting factor for the crystallite thickness. Similarly, a higher amount of crystal-incorporated minority BS units could cause a further increase of the lamellar thickness in PBA-rich copolymers.

The dependence of the included minority components and the related crystallinity and crystallite thickness on the thermal treatment of the copolymers will be investigated in further studies.

■ ASSOCIATED CONTENT

Supporting Information

The Supporting Information is available free of charge at <https://pubs.acs.org/doi/10.1021/acs.macromol.0c01965>.

NMR results on samples with different thermal histories, FID analyses results for the complete composition range, additional X-ray scattering results, and NMR spin-diffusion build-up curves (PDF)

■ AUTHOR INFORMATION

Corresponding Authors

Mareen Schäfer – *Institut für Physik - NMR, Martin-Luther Universität Halle-Wittenberg, 06120 Halle (Saale)*,

Germany; orcid.org/0000-0001-6589-2087;

Email: mareen.schaefer@physik.uni-halle.de

Klaus Schmidt-Rohr – *Department of Chemistry, Brandeis University, Waltham, Massachusetts 02453, United States*;

orcid.org/0000-0002-3188-4828; Email: srohr@brandeis.edu

Authors

Shichen Yuan – *Department of Chemistry, Brandeis University, Waltham, Massachusetts 02453, United States*

Albrecht Petzold – *Institut für Physik - Polymerphysik, Martin-Luther Universität Halle-Wittenberg, 06120 Halle (Saale), Germany*; orcid.org/0000-0002-2920-7019

Ricardo A. Pérez-Camargo – *Beijing National Laboratory for Molecular Sciences, CAS Key Laboratory of Engineering Plastics, CAS Research/Education Center for Excellence in Molecular Sciences, Institute of Chemistry, Chinese Academy of Sciences, Beijing 100190, China*; orcid.org/0000-0003-4500-530X

Alejandro J. Müller – *POLYMAT and Polymer Science and Technology Department, Faculty of Chemistry, University of the Basque Country UPV/EHU, 20018 Donostia-San Sebastian, Spain*; IKERBASQUE, Basque Foundation for Science, Bilbao, Spain; orcid.org/0000-0001-7009-7715

Thomas Thurn-Albrecht – *Institut für Physik - Polymerphysik, Martin-Luther Universität Halle-Wittenberg, 06120 Halle (Saale), Germany*; orcid.org/0000-0002-7618-0218

Kay Saalwächter – *Institut für Physik - NMR, Martin-Luther Universität Halle-Wittenberg, 06120 Halle (Saale), Germany*; orcid.org/0000-0002-6246-4770

Complete contact information is available at: <https://pubs.acs.org/10.1021/acs.macromol.0c01965>

Notes

The authors declare no competing financial interest.

■ ACKNOWLEDGMENTS

Financial support within the framework of Deutsche Forschungsgemeinschaft (DFG, German Research Foundation) - project number 189853844 - TRR 102 "Polymers under multiple constraints" (project A01) is highly appreciated. The solid-state NMR spectrometer used for the ^{13}C MAS NMR experiments in this work was funded by the NSF MRI program (award no. 1726346). A.J.M. acknowledges funding from the Basque Government through grant IT1309-19. R.A.P.-C. is supported by the National Key R&D Program of China (2017YFE0117800) and by PIFI of the Chinese Academy of Science for international postdoctoral researchers (2019PE0004).

■ REFERENCES

- (1) Ikada, Y.; Tsuji, H. Biodegradable polyesters for medical and ecological applications. *Macromol. Rapid Commun.* **2000**, *21*, 117–132.
- (2) Nair, L. S.; Laurencin, C. T. Biodegradable polymers as biomaterials. *Prog. Polym. Sci.* **2007**, *32*, 762–798.
- (3) Pan, P.; Inoue, Y. Polymorphism and isomorphism in biodegradable polyesters. *Prog. Polym. Sci.* **2009**, *34*, 605–640.
- (4) Iwata, T.; Doi, Y. Crystal structure and biodegradation of aliphatic polyester crystals. *Macromol. Chem. Phys.* **1999**, *200*, 2429–2442.

- (5) Bovey, F. A.; Winslow, F. H. In *Macromolecules, an Introduction to Polymer Science*; Bovey, F. A., Winslow, F. H., Eds.; Academic Press: New York, 1979; Chapter 1.
- (6) Allegra, G.; Bassi, I. W. Isomorphism in Synthetic Macromolecular Systems. *Adv. Polymer Sci.* **1969**, *6*, 549–574.
- (7) Natta, G.; Corradini, P.; Sianesi, D.; Morero, D. Isomorphism Phenomena in Macromolecules. *J. Polym. Sci.* **1961**, *51*, 527–539.
- (8) Sisti, L.; Totaro, G.; Marchese, P. In *Biodegradable and Biobased Polymers for Environmental and Biomedical Applications*; Kalia, S., Avérous, L., Eds.; Scrivener Publishing & John Wiley and Sons: Hoboken, 2016; Chapter 7.
- (9) Basterretxea, A.; Gabirondo, E.; Flores, I.; Etxeberria, A.; Gonzalez, A.; Müller, A. J.; Mecerreyes, D.; Coulembier, O.; Sardon, H. *Macromolecules* **2019**, *52*, 3506–3515.
- (10) Pérez-Camargo, R. A.; Arandia, I.; Safari, M.; Cavallo, D.; Lotti, N.; Soccio, M.; Müller, A. J. Crystallization of isodimorphic aliphatic random copolyesters: Pseudo-eutectic behavior and double-crystalline materials. *Eur. Polym. J.* **2018**, *101*, 233–247.
- (11) Pérez-Camargo, R. A.; Fernández-d'Arlas, B.; Cavallo, D.; Debuissy, T.; Pollet, E.; Avérous, L.; Müller, A. J. Tailoring the structure, morphology, and crystallization of isodimorphic poly-(butylene succinate-*ran*-butylene adipate) random copolymers by changing Composition and thermal history. *Macromolecules* **2017**, *50*, 597–608.
- (12) Tserki, V.; Matzinos, P.; Pavlidou, E.; Vachliotis, D.; Panayiotou, C. Biodegradable aliphatic polyesters. Part I. Properties and biodegradation of poly(butylene succinate-co-butylene adipate). *Polym. Degrad. Stab.* **2006**, *91*, 367–376.
- (13) Rizzarelli, P.; Puglisi, C.; Montaudo, G. Soil burial and enzymatic degradation in solution of aliphatic co-polyesters. *Polym. Degrad. Stab.* **2004**, *85*, 855–863.
- (14) Zhao, J. H.; Wang, X. Q.; Zeng, J.; Yang, G.; Shi, F. H.; Yan, Q. Biodegradation of poly(butylene succinate-co-butylene adipate) by *Aspergillus versicolor*. *Polym. Degrad. Stab.* **2005**, *90*, 173–179.
- (15) Tomita, K.; Kuroki, Y.; Hayashi, N.; Komukai, Y. Isolation of a thermophile degrading poly(butylene succinate-co-butylene adipate). *J. Biosci. Bioeng.* **2000**, *90*, 350–352.
- (16) Eslami, H.; Grmela, M.; Dubois, C.; Lafleur, P. Melt rheology of biodegradable poly[(butylene succinate)-co-adipate]: Experimental and model predictions. *J. Polym. Sci., Part B Polym. Phys.* **2010**, *48*, 832–839.
- (17) Wang, Y.; Bhattacharya, M.; Mano, J. F. Thermal analysis of the multiple melting behavior of poly(butylene succinate-co-adipate). *J. Polym. Sci., Part B Polym. Phys.* **2005**, *43*, 3077–3082.
- (18) Nikolic, M. S.; Djonlagic, J. Synthesis and characterization of biodegradable poly(butylene succinate-co-butylene adipate)s. *Polym. Degrad. Stab.* **2001**, *74*, 263–270.
- (19) Ren, M.; Song, J.; Song, C.; Zhang, H.; Sun, X.; Chen, Q.; Zhang, H.; Mo, Z. Crystallization kinetics and morphology of poly(butylene succinate-co-adipate). *J. Polym. Sci., Part B Polym. Phys.* **2005**, *43*, 3231–3241.
- (20) Pérez-Camargo, R. A.; Liu, G.; Cavallo, D.; Wang, D.; Müller, A. J. Effect of the crystallization conditions on the exclusion/inclusion balance in biodegradable poly(butylene succinate-*ran*-butylene adipate) copolymers. *Biomacromolecules* **2020**, *21*, 3420–3435.
- (21) Ichikawa, Y.; Kondo, H.; Igarashi, Y.; Noguchi, K.; Okuyama, K.; Washiyama, J. Crystal structures of α and β forms of poly(tetramethylene succinate). *Polymer* **2000**, *41*, 4719–4727.
- (22) Ichikawa, Y.; Suzuki, J.; Washiyama, J.; Moteki, Y.; Noguchi, K.; Okuyama, K. Strain-induced crystal modification in poly-(tetramethylene succinate). *Polymer* **1994**, *35*, 3338–3339.
- (23) Noguchi, K.; Kondo, H.; Ichikawa, Y.; Okuyama, K.; Washiyama, J. Molecular and crystal structure of poly(tetramethylene adipate) α form based on synchrotron X-ray fiber diffraction. *Polymer* **2005**, *46*, 10823–10830.
- (24) Pouget, E.; Almontassir, A.; Casas, M. T.; Puiggali, J. On the crystalline structures of poly(tetramethylene adipate). *Macromolecules* **2003**, *36*, 698–705.
- (25) Minke, R.; Blackwell, J. Polymorphic Structures of Poly(tetramethylene Adipate). *J. Macromol. Sci., Part B* **1979**, *16*, 407–417.
- (26) Minke, R.; Blackwell, J. Single Crystals of Poly(tetramethylene Adipate). *J. Macromol. Sci., Part B* **1980**, *18*, 233–255.
- (27) Kuwabara, K.; Gan, Z.; Nakamura, T.; Abe, H.; Doi, Y. Molecular mobility and phase structure of biodegradable poly-(butylene succinate) and poly(butylene succinate-co-butylene adipate). *Biomacromolecules* **2002**, *3*, 1095–1100.
- (28) Debuissy, T.; Pollet, E.; Avérous, L. Synthesis of potentially biobased copolyesters based on adipic acid and butanediols: Kinetic study between 1,4- and 2,3-butanediol and their influence on crystallization and thermal properties. *Polymer* **2016**, *99*, 204–213.
- (29) Debuissy, T.; Pollet, E.; Avérous, L. Synthesis and characterization of biobased poly(butylene succinate-*ran*-butylene adipate). Analysis of the composition-dependent physicochemical properties. *Eur. Polym. J.* **2017**, *87*, 84–98.
- (30) Fung, B. M.; Khittrin, A. K.; Ermolaev, K. An improved broadband decoupling sequence for liquid crystals and solids. *J. Magn. Reson.* **2000**, *142*, 97–101.
- (31) Bennett, A. E.; Rienstra, C. M.; Auger, M.; Lakshmi, K. V.; Griffin, R. G. Heteronuclear Decoupling in Rotating Solids. *J. Chem. Phys.* **1995**, *103*, 6951–6958.
- (32) Mowery, D. M.; Harris, D. J.; Schmidt-Rohr, K. Characterization of a Major Fraction of Disordered All-trans Chains in Cold-Drawn High-Density Polyethylene by Solid-State NMR. *Macromolecules* **2006**, *39*, 2856–2865.
- (33) Torchia, D. A. The measurement of proton-enhanced carbon-13 T1 values by a method which suppresses artifacts. *J. Magn. Reson.* **1987**, *30*, 613.
- (34) Hansen, E. W.; Kristiansen, P. E.; Pedersen, B. Crystallinity of Polyethylene Derived from Solid-State Proton NMR Free Induction Decay. *J. Phys. Chem. B* **1998**, *102*, 5444–5450.
- (35) Schäler, K.; Achilles, A.; Bärenwald, R.; Hackel, C.; Saalwächter, K. Dynamics in Crystallites of Poly(ϵ -caprolactone) As Investigated by Solid-State NMR. *Macromolecules* **2013**, *46*, 7818–7825.
- (36) Schäler, K.; Roos, M.; Micke, P.; Golitsyn, Y.; Seidtlitz, A.; Thurn-Albrecht, T.; Schneider, H.; Hempel, G.; Saalwächter, K. Basic principles of static proton low-resolution spin diffusion NMR in nanophase-separated materials with mobility contrast. *Solid State Nucl. Magn. Reson.* **2015**, *72*, 50–63.
- (37) Kurz, R.; Schulz, M.; Scheliga, F.; Men, Y.; Seidtlitz, A.; Thurn-Albrecht, T.; Saalwächter, K. Interplay between Crystallization and Entanglements in the Amorphous Phase of the Crystal-Fixed Polymer Poly(ϵ -caprolactone). *Macromolecules* **2018**, *51*, 5831–5841.

4.3 Paper III

Structure and dynamics in a polymorphic nanophase-separated stiff comblike polymer³

Heterogeneity along the polymer chain cannot only be manufactured by copolymerization, but also by the addition of flexible side chains to stiff aromatic polyesters. These comb-like polymers can also form a semicrystalline structure, provided that the side chains are long enough. In this case the structure is characterized by a long-ranged ordered layered morphology with well-ordered backbones, which are separated by nanodomains built from flexible side chains. This class of material gained more and more industrial importance, as many semiconducting polymers can be described by a similar layered morphology. Polymorphism and phase transitions are two relevant factors that may influence the properties of these materials.

In the following publication the polymorphism and temperature dependent phase transitions of the comb-like polymer poly(1,4-phenylene-2,5-*n*-didecyloxy terephthalate), with $n = 10$ carbons per side chain (PPDOT), are studied with focus on the molecular motions and dynamics of the side and main chains.¹³C MAS CP spectra, DSC and wide-angle X-ray scattering (WAXS) were used to observe the solid-solid phase transition from modification B to A and the phase transition between modification A and a liquid crystalline phase upon heating. The transition from the liquid-crystalline state to modification A was also detected during cooling. The temperature-dependent main and side chain mobility in modification A and B were studied with the DIPSHIFT technique. An investigation of the liquid-crystalline phase was accomplished with the comparison of ¹³C CP MAS and INEPT spectra.

The author contributions of the following article are: M. Schäfer, V. D., M. B. and K. S. designed research. M. B. provided the samples. M. Schäfer performed the NMR experiments and analyzed and interpreted the NMR data. V. D. performed and analyzed the DSC and WAXS experiments. V. D. and M. B. interpreted the DSC and WAXS results. M. Schäfer, V. D., M. B. and K. S. discussed the results. M. Schäfer wrote the first draft of the paper. M. Schäfer and, in minor parts, V. D. wrote the paper with refinements by all co-authors.

³The following article [V. Danke et al., *Macromolecules*, **52**, 6943-6952 (2019)] is an open access article published under an ACS AuthorChoice License, which permits copying and redistribution of the article or any adaptations for non-commercial purposes. The link to the article on the publishers website is: <https://pubs.acs.org/doi/abs/10.1021/acs.macromol.9b00951>. No changes were made.

Structure and Dynamics in a Polymorphic Nanophase-Separated Stiff Comblike Polymer

Varun Danke,^{†,‡} Mario Beiner,^{‡,⊥} Kay Saalwächter,^{§,⊥} and Maren Schäfer^{*,§,⊥}

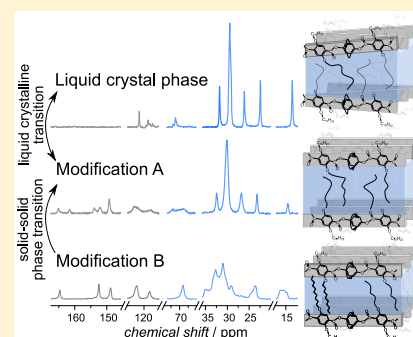
[†]Naturwissenschaftliche Fakultät II, Martin-Luther-Universität Halle-Wittenberg, Heinrich-Damerow-Str. 4, D-06120 Halle (Saale), Germany

[‡]Fraunhofer Institut für Mikrostruktur von Werkstoffen und Systemen IMWS, Walter-Hülse-Str. 1, D-06120 Halle (Saale), Germany

[§]Institut für Physik - NMR, Martin-Luther Universität Halle-Wittenberg, Betty-Heimann-Str. 7. D-06120 Halle (Saale), Germany

[⊥]Naturwissenschaftliche Fakultät II, Martin-Luther-Universität Halle-Wittenberg, Heinrich-Damerow-Straße-4, D-06120 Halle (Saale), Germany

ABSTRACT: We have investigated the structure and molecular motions of the side and main chains in the comblike polymer poly(1,4-phenylene-2,5-*n*-didecyloxy terephthalate) with 10 carbons in the alkyl side chain (PPDOT) with respect to its two polymorphic states by means of ¹³C magic-angle spinning (MAS) NMR spectroscopy. Structure and polymorphism of such stiff-chain systems are relevant for many semiconducting polymers. Both modifications, called A and B, exhibit a layered morphology with well-ordered backbones forming π - π stacks separated by nanodomains of methylene sequences and are connected by a B-A solid-solid phase transition in the range 70–110 °C during heating. At ambient temperature, the polymorph A slowly converts back to the thermodynamically more stable modification B. We use ¹³C CP MAS spectra to observe the structural changes during the phase transition and the structural differences in both modifications. In ¹³C DIPSHIFT experiments, which inform about motionally averaged ¹H-¹³C dipole-dipole couplings, we do not see any indication of a backbone-amorphous phase, and therefore we emphasize that the entire sample exhibits well-ordered π - π stacking for $T < 180$ °C. The polymorphs differ in the conformational statistics and dynamics of the side chains as well as in the structural conformation of the backbone. Above 180 °C we detect the formation of a liquid-crystalline phase, characterized by the loss of the π - π stacking and molecular motions of the side chains with correlation times $\tau_c < 0.01$ μ s.



1. INTRODUCTION

Comblike polymers containing flexible alkyl side chains attached to rigid backbones are a class of functional materials, primarily of interest due to their applications in the field of organic photovoltaics,^{1,2} organic semiconductors,³ fiber-reinforced composites for lightweight components,^{4,5} and organic fuel cells.⁶ Although the primary objective of introducing flexible side chains is to improve the processability of high-performance materials,^{7,8} it also results in interesting structural and morphological changes. Formation of a layered morphology on the nanoscale is observed in almost all cases.^{9–13} The packing of the side chains is often influenced by the nature of the backbone acting as a constraint,^{11,14,15} molecular weight,^{16,17} position of the side chain,^{18,19} length of the side chain,²⁰ and thermal history.^{21,22} It is a well-known fact that rigid backbones containing aromatic groups often exhibit π - π interactions and tend to form stacks. On the other hand, side chains, when long enough, may crystallize despite the steric constraints posed by the backbone.^{9,20,23,24} Based on the different packing behavior of the side chains, structural modifications or polymorphs are reported for comblike polymers such as alkoxyated polyamides,^{19,25} polyimides,¹⁹ polyesters,²² and poly(3-alkylthiophenes).^{16,17} Additionally,

the coupling between the packing of the rigid backbones and flexible side chains may lead to competing effects which play a role during structure formation.^{26–28}

Alkoxyated polyesters having side chains of different lengths have been extensively studied in the past^{7,10,12,19,29} and are known to exist in at least two layered structural modifications: A and B.^{13,27,30} Solid-state NMR studies on poly[1,4-phenylene 2,5-bis(hexadecyloxy)terephthalate] reveal that backbone modifications have an influence on the conformational behavior of the side chains.³¹ A conformational disorder of the backbone is associated with mobile side chains in gauche-rich conformations, whereas a uniform backbone structure allows to form additional ordered crystalline side chain regions.²⁸ Recent work of our group has addressed detailed temperature-dependent changes in spacings of Bragg planes during heating a pristine sample of poly(1,4-phenylene 2,5-*n*-didecyloxy terephthalate) (PPDOT) having 10 alkyl carbons in the side chain. We found that a steplike increase in the interlayer spacing due to side chain melting during a solid-

Received: May 8, 2019

Revised: August 22, 2019

Published: September 5, 2019

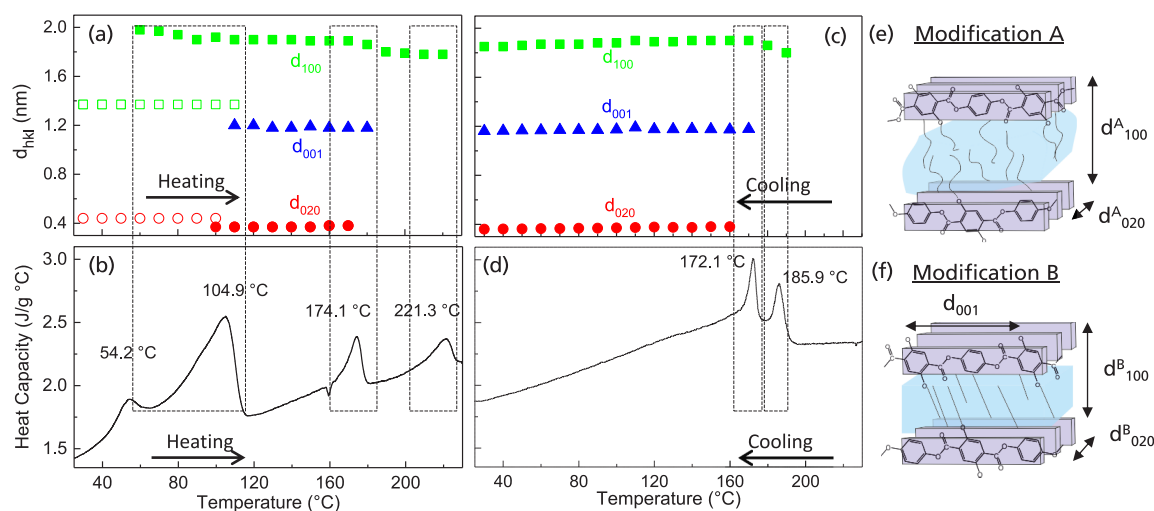


Figure 1. Interplanar spacings calculated for (100), (001), and (020) planes plotted as a function of temperature in the first heating (a) and the corresponding DSC heating curve (b) showing multiple endothermic phase transitions. Open symbols denote spacings for modification B, and closed symbols denote spacings for modification A. The corresponding Bragg spacings during cooling are shown in panel c. The DSC cooling curve (d) shows the two high-temperature transitions from the melt to liquid-crystalline and from liquid-crystalline to modification A. Panels (e) and (f) show the schematic for modification A and B, respectively. Data reproduced from ref 27 with permission from Elsevier.

solid phase transition from modification B to modification A^{22,27} is accompanied by an $\approx 18\%$ smaller π - π stacking distance. This implies that change along one dimension of the orthorhombic unit cell²² is accompanied by a contraction along the other direction, thereby highlighting the effect of interrelations between main and side chains on the overall packing state. Further details are briefly discussed in the first part of the **Results and Discussion** section.

In this study we primarily focus on the packing states of the backbone and side chains in PPDOT-A and PPDOT-B of poly(1,4-phenylene-2,5-*n*-didecyloxy terephthalate) (PPDOT) having $n = 10$ alkyl carbons in the side chain. We employ advanced solid-state NMR spectroscopic methods to study conformational order as well as molecular mobility, in particular side chain mobility to understand the packing behavior of the side chains. In addition, insights into molecular ordering of the backbone in the different structural modifications are gained to comment on the interplay and interdependencies of the packing tendencies of the rigid backbone and flexible side chains. Notably, we find no indication for a backbone-amorphous phase that is typically present in semicrystalline polymers.

2. EXPERIMENTAL SECTION

2.1. Materials. Poly(1,4-phenylene-2,5-*n*-didecyloxy terephthalate) with 10 alkyl carbons in the side chain and M_w of 95 kg/mol was used as a model system. The detailed synthesis route is described elsewhere.³² A pristine sample showing pure modification B (PPDOT-B) and a sample cooled after heating above the solid–solid transition temperature range (120 °C) containing pure modification A (PPDOT-A) were used for NMR investigations.

2.2. X-ray Diffraction (XRD). Temperature-dependent XRD measurements were performed in reflection mode using an Empyrean diffractometer (PANalytical) equipped with the temperature chamber TTK 450 (Anton Paar). The heating and cooling rate was kept at 10 K/min. The emitted Cu $K\alpha$ radiation is parallelized and monochromatized using a parallel beam mirror ($\lambda = 1.54$ Å). The scattered beam passes a parallel plate collimator (0.27°) and is detected by a Pixel 3D detector with 19 channels of 0.055 μm size combined to be used as a receiving slit. The scan range with the

magnitude of scattering vector q ($q = 4\pi \sin \theta/\lambda$) was $1.5 \text{ nm}^{-1} \leq q \leq 20.0 \text{ nm}^{-1}$, with a step size of 0.05° and counting time of 1 s per step.

2.3. Differential Scanning Calorimetry (DSC). The DSC measurements on PPDOT were performed with the help of a power-compensated PerkinElmer DSC 7. The samples were cooled to -60 °C prior to measuring. The heating and cooling rates were 10 K/min. Samples with a mass of 5–8 mg were used.

2.4. Solid-State Nuclear Magnetic Resonance (NMR). ^{13}C NMR measurements were performed on a Bruker Avance III spectrometer with ^{13}C Larmor frequency of 100.06 MHz with 4 mm double- and triple-resonance magic-angle spinning (MAS) probes at a spinning frequency of 7 kHz. The samples were packed in 4 mm ZrO_2 MAS rotors. The 90° pulse lengths for ^1H and ^{13}C were set to 3.0 and 3.3 μs , respectively. The contact times for ^1H - ^{13}C cross-polarization (CP) were chosen to be 2 ms. For the heteronuclear decoupling the SPINAL64 sequences was applied with at a ^1H decoupling frequency of 83.3 kHz. The t_1 increments under homonuclear decoupling were acquired by using continuous-wave Lee–Goldburg irradiation.

3. RESULTS AND DISCUSSION

3.1. Structure and Thermal Behavior. Temperature-dependent X-ray diffraction studies have shown a jump in the interlayer spacing d_{100} from 13.6 to 19 Å within the transition range from 60 to 120 °C during heating (see Figure 1a). A recently published X-ray diffraction pattern²⁷ shows clearly that this feature corresponds to a solid–solid transition from modification B to modification A. On the basis of detailed crystallographic analysis and calculation of the volume occupied per CH_2 unit of the side chain for each modification, it was inferred that the side chains in modification A are amorphous (Figure 1e) while in modification B they are crystalline (Figure 1f). The crystallographic state of the polymer is characterized by a long-range ordered layered structure and an orthorhombic unit cell, which differs in its dimension, also along the π - π stacking direction, for both polymorphs.²² Above 170 °C the π stacking between the backbones is completely lost although the layered morphology still persists even above this temperature. It was concluded that the polymer at this stage is in a liquid-crystalline state.^{21,30}

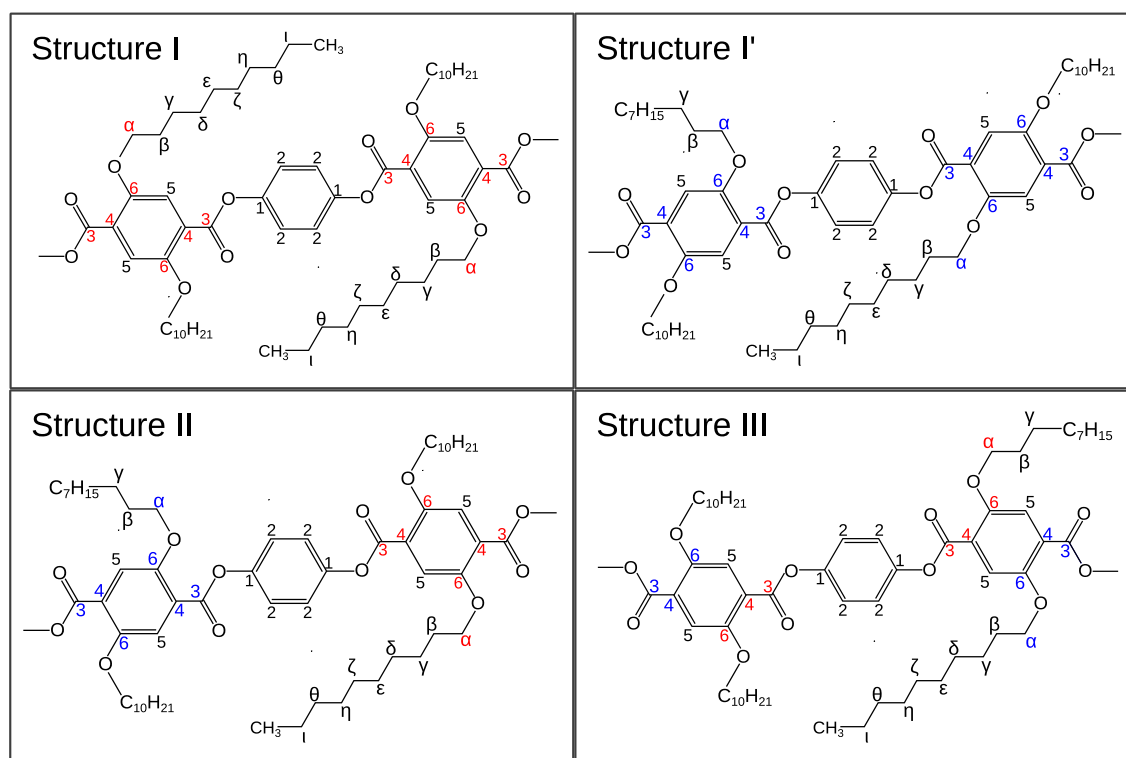


Figure 2. Schematic illustration of possible backbone structures (adapted from ref 37) and the numbering scheme for the peak assignment in the NMR spectra. The symmetry and the *cis/trans* states of the ester group lead to diverse chemical environments of some backbone carbons and might also influence the first side chain carbons. The difference in the possible backbone structures depends on whether the C3=O bond is parallel to the C6–O to the side chain bond (highlighted with red numbers) or not parallel (highlighted with blue numbers).

Multiple phase transitions are also seen in a DSC first heating scan as shown in Figure 1b. The endothermic event in the form of a bimodal peak in the range 60–110 °C is indicative of the solid–solid transition from modification B to modification A due to melting of the side chains. The modification A–liquid-crystalline transition is seen in the range 160–180 °C, followed by the transition to the melt state above 220 °C represented by a final melting peak. During cooling, the DSC cooling curve shows an exothermic transition from the melt to the liquid-crystalline state between 190 and 180 °C (Figure 1d) accompanied by the first appearance of the (100) reflection (Figure 1c). Another exothermic transition at 172 °C and the first appearance of the (020) reflection at 160 °C indicate a transition from the liquid-crystalline state to modification A. The solid–solid transition from modification A to modification B is not seen in the cooling scan. The polymer first forms a semioordered liquid-crystalline state wherein a long-range ordered morphology exists, but the backbones exhibit no discernible π stacking prior to forming modification A. The stiff backbones most likely pack first during cooling, and the side chains remain disordered forming modification A. However, it is interesting to note that over time modification A partially converts to modification B at ambient conditions, indicating that modification B is thermodynamically preferred at room temperature.²²

3.2. Phase Transitions and Structural Modifications in PPDOT. 1D ¹³C spectra recorded under magic-angle spinning (MAS) yield information about the structure, dynamics, and conformation of the investigated polymer. The so-called γ -gauche effect describes the conformation-dependent ¹³C

chemical shift for a certain CH_n group. Chains in an *all-trans* conformation usually have slightly higher chemical shifts than segments in the *gauche*-containing regions.^{33,34}

Two different techniques are used to record ¹³C MAS spectra. With direct polarization (DP) the peak integrals reflect the true phase compositions, but the acquisition of the spectra takes usually very long due to the lower ¹³C equilibrium polarization and the rather long ¹³C relaxation time T₁. Qualitative and time-efficient spectra can be recorded with the cross-polarization (CP) sequence, which transfers the high polarization of protons to the less polarized carbons atoms. The efficiency of the polarization transfer depends on the mobility of the different phases (amorphous and crystalline), resulting in nonquantitative spectra. Generally, the recorded spectra reflect a time-average over several milliseconds in the conformational states of the sample.

Figure 3 shows temperature-dependent ¹³C CP spectra recorded at 7 kHz under stepwise heating of modification B from 40 °C (top) to 180 °C and subsequent cooling to 40 °C (bottom). The corresponding signal assignment^{28,35,36} for possible backbone conformations and the side chains is shown in Figure 2. The aromatic backbone carbons resonate between 114 and 170 ppm. The ¹³C CP MAS spectrum of PPDOT-B at T = 40 °C displays distinct, well-resolved peaks, indicating a well-ordered π - π stacking of the backbones with only one chemical shift for each carbon. Therefore, the backbone carbons in modification B are all located in a similar chemical environment, resulting in the same chemical shift. Thus, we assume that the conformation can best be described by either structure I or I' (see Figure 2), which are characterized by *trans*

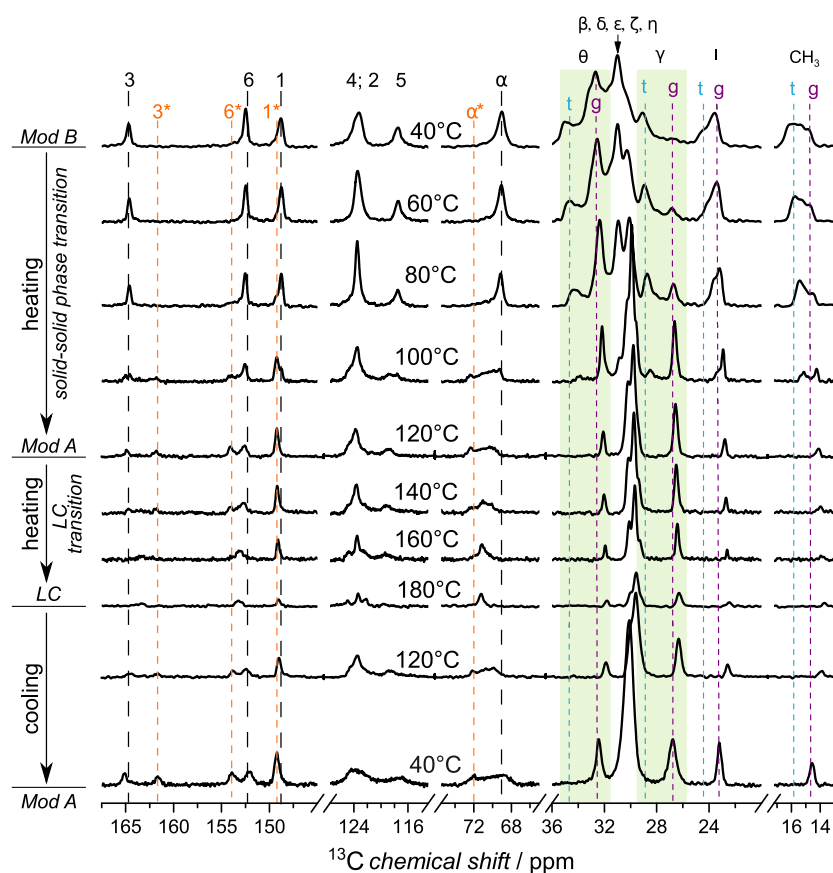


Figure 3. Temperature-dependent ^{13}C CP MAS spectra of PPDOT in modification B (top) at 40 °C, with the solid–solid phase transition in the range 80–120 °C and the transformation to the liquid-crystalline state at 180 °C. During cooling to 40 °C the structure remains in modification A. The green shaded regions highlight the change in the structure of the alkyl chains from a mix of segments in *trans*-rich and *gauche*-rich regions in PPDOT-B (top) to *gauche*-containing chains in PPDOT-A (bottom). All spectra are recorded at a spinning frequency of 7 kHz and a contact time of 2 ms at the indicated temperatures. In Figure 2 the numbering scheme for the repeat unit with various backbone structures of PPDOT is shown.

states about the central ring and has a point symmetry with regard to the substituted phenyl rings. The C3=O bonds in both structures are either all parallel (I) or not parallel (I') to the side chain C6–O bond connecting to the side chains. For $T \geq 100$ °C additional peaks for carbons “3” and “6” as well as a change of the “1” resonance to slightly higher chemical shifts appear. The additional as well as the changed peak positions in Figure 3 are labeled with an extra “*”. Furthermore, a broadening of the resonances for carbons “4” and “5” is detected. As reported by Tonelli,³⁸ the chemical shift is influenced by conformational changes, especially if these changes involve a variation of the local π -packing,³⁹ as happened in PPDOT during the solid–solid phase transition. Therefore, we attribute the experimentally found shift in peak position and/or the detection of additional resonances to a conformational change of the backbone during the phase transition from modification B (structures I or I') to A (likely related to structure II or III in Figure 2). The transition from structure I or I' to II during heating seems very unlikely to us, since the DSC scans reveal a very fast transition between modification B to A, and this structural change would involve a 180° flip of the substituted rings whereby the side chains would also have to change position. Thus, we hypothesize that the conformational changes in the backbone can be described by a change of the ester groups at the substituted rings from

trans to *cis* (structure III). Depending on the conformation of modification B, the additional resonances (labeled with an extra “*” in Figure 3) describe the change from a conformation with all C=O bonds parallel to the closest C–O bond (structure I to III) or from a nonparallel conformation (structure I' to III) to a mixed state. Integrating the area underneath the resonances reveals that approximately half of C=O groups change their conformation during the phase transition. Note that there are other transitions scenarios requiring a 180° flip of the substituted ring which seem also unlikely and hence have not been considered here.

Increasing the temperature to 180 °C results in the second phase transition to the liquid-crystalline phase. The signal intensities at this temperature are too low to resolve the “3(*)” resonances. For carbons “1(*)” and “6(*)” the chemical shifts attain an average value between both backbone conformations, which can be explained by the high backbone mobility in this phase (see separate discussion below). Upon cooling the sample from 180 to 40 °C the changes in backbone resonances remain in modification A, and there is no transformation back to modification B.

The carbon atoms in the alkyl chain resonate between 13 and 76 ppm. Prior to the thermal treatment, the spectrum at 40 °C shows a well-resolved peak for the α -carbons (69.1 ppm), which are closest to the backbone. The γ -, ι -CH₂ and the

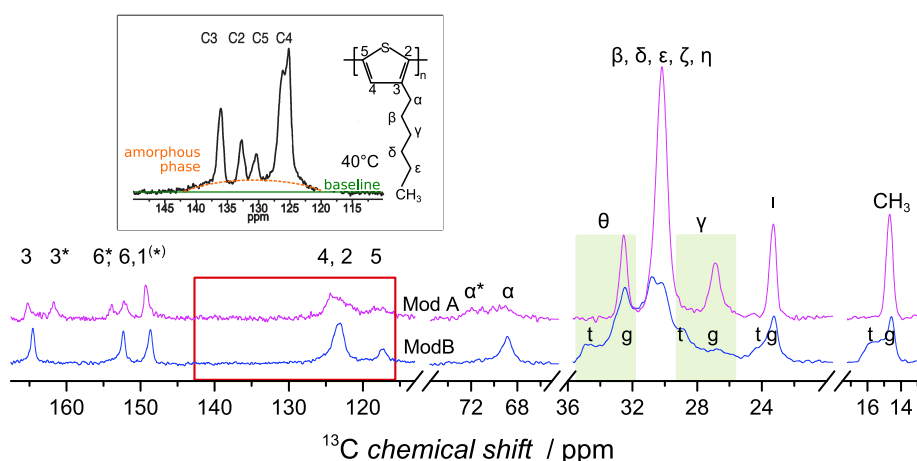


Figure 4. Comparison of ^{13}C DP MAS spectra for Mod A (top) and Mod B (bottom) at 40 °C. The recycle delay between each scan was chosen such that a quantitative spectrum of the alkyl chains was detected. The green, filled rectangles highlight the most distinct differences in alkyl chains of both modifications; the red box underlines the absence of a backbone-amorphous phase as shown exemplarily via a spectrum of P3HT¹⁷ in the inset. The broad amorphous phase signal of P3HT is highlighted by the dotted orange line.

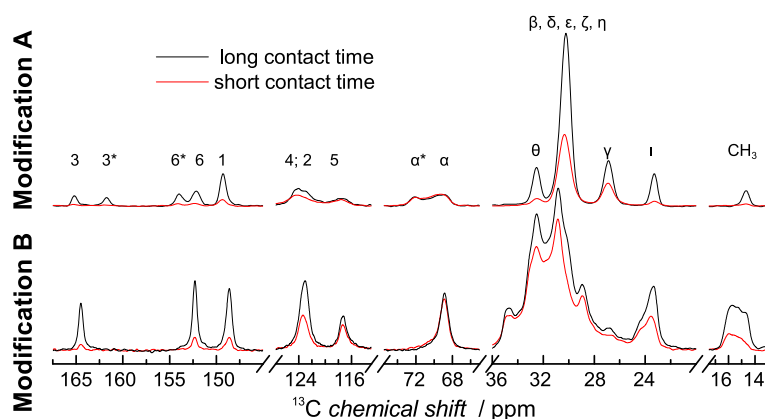


Figure 5. Comparison of ^{13}C CP MAS spectra with short and long contact time for both modifications. A small difference in intensity refers to strong ^1H – ^{13}C dipolar coupling and high rigidity for the corresponding carbons.

methyl group each exhibit two overlapping peaks, indicating that the alkyl chains exist in *trans*-rich (t) and *gauche*-rich (g) environments, with a downfield shift of 1–2.5 ppm for the resonance of the *trans*-rich conformation.³⁸ The broad signal between 29 and 36 ppm is associated with overlapping resonances of the β , δ to θ -CH₂ groups. Only the peak at 35 ppm can be correlated to the θ -carbons in *trans*-rich conformation, while the remaining resonances cannot be separated.

With increasing temperature, the fraction of *trans*-rich conformers decreases whereas the fraction of carbons in a *gauche*-rich conformation increases. This temperature-dependent transformation is most distinct for the γ - and θ -carbons, highlighted by the green, filled regions in Figure 3. At 40 °C the *trans*-rich resonance of both carbons can be seen clearly whereas the *gauche*-rich one is only visible via a small shoulder for the γ -carbons and not resolvable for the θ -CH₂ groups. With increasing temperature the *trans*-rich fractions decrease and vanish completely at 120 °C, whereas the peak associated with the *gauche*-rich conformation increases in intensity and in the case of the θ -carbons becomes distinguishable from the upfield resonances. The same temperature dependence is observed for all carbons of the side chain in the *trans*-rich

conformation. Above 100 °C an additional resonance for the α -carbons is detected. This resonance correlates with the changes in the backbone conformation, which also influences the chemical shift of the α -carbons due to their spatial proximity to the backbone. A further influence on the chemical environment and therefore the chemical shift along the side chain can be excluded for the γ -carbons and toward the chain end since no shift of resonance or additional peaks are detected. An influence on the β -carbons can be neither confirmed nor excluded due to the overlapping resonances with the inner CH₂ groups.

For the liquid-crystalline phase at 180 °C, we observe a signal intensity drop, indicating a high side chain mobility. The $\alpha^{(*)}$ -carbons resonance shifts to an average chemical shift, which can also be explained by the fast motions of both backbone and side chains. In general, a shift to lower ppm values for higher temperatures is observed for all side chain resonances. During cooling to 40 °C the side chains remain in the noncrystalline *gauche*-rich conformation; only the α -carbons resonate at two distinguishable chemical shifts arising from the conformational differences of the backbone.

The differences in structure and conformation in both modifications become even clearer with a direct comparison of

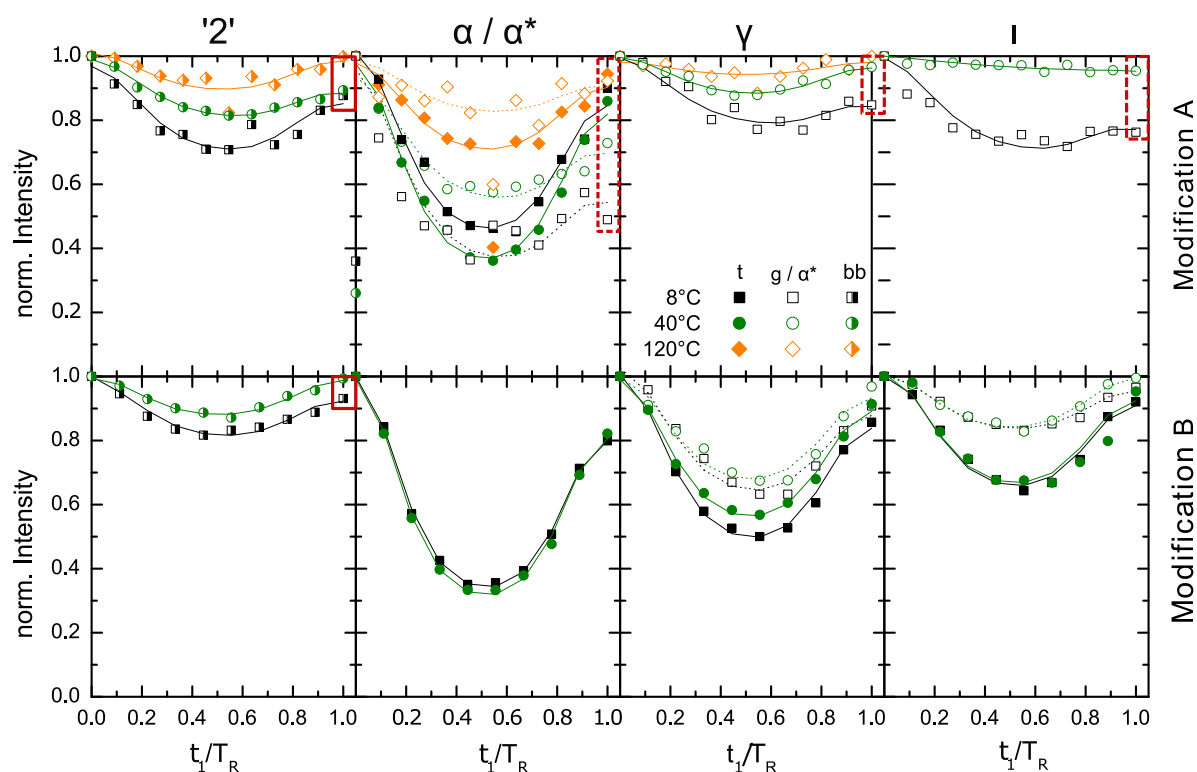


Figure 6. DIPSIFT modulations curves recorded on both modifications of PPDOT at 7 kHz. The boxes mark T_2 -related intensity losses at $t = t_1/T_R = 1$. Open symbols and dashed boxes represent *gauche*-rich or the α^* -carbons; closed symbols represent *trans*-rich and half-filled backbone carbons (both solid red boxes).

^{13}C DP spectra at 40 °C in Figure 4. The ^{13}C T_1 relaxation time was chosen long enough to detect the quantitative phase composition for the alkyl chains. The green, filled rectangles in Figure 4 highlight the main differences of the alkyl chains in either modification. Both the γ - and θ - CH_2 groups in modification A show resonances that are associated with chains in a *gauche*-rich region, whereas modification B displays resonances for both conformations. The structural differences in the backbone are identifiable by the additional resonances of the α -, “3”, and “6”-carbons in modification A as well as the different chemical shift of carbons “1” and the broadening of the signals “4” and “5”.

In contrast to similar polymers such as P3HT,¹⁷ no broad amorphous background signal is detected. The inset in Figure 4 shows exemplarily the well-defined backbone resonances and the broad amorphous phase signal (orange line) of P3HT.¹⁷ In the spectra of our system no indication for a backbone-amorphous phase in both modifications is detected, as highlighted by the red box. Therefore, we emphasize that the main chains of the whole sample appear to be well-ordered up to 160 °C, even though they exhibit different backbone structures in both polymorphs.

3.3. Main- and Side-Chain Mobility at Ambient Temperature. By changing the duration of the polarization transfer in a ^{13}C CP experiment, we enabled a first qualitative analysis of the mobility differences. For short contact times the components with a strong ^1H – ^{13}C dipolar coupling are emphasized. Only for longer contact times are also the more mobile components detected. A small intensity difference of resonances detected with short and long contact times can be taken as evidence for strong coupling and thus a rigid

environment. This comparison holds only for carbons with attached hydrogen atoms; hence, the comparison is only applicable for the side chains and the “2” and “5” carbons. In Figure 5, the comparison of short- and long-contact ^{13}C CP MAS spectra of both modifications is shown. The intensity differences for CP spectra with short and long contact times are relatively small for all resonances of the alkyl chain in modification B. The intensities of α - CH_2 resonances are similar, but the intensity differences become more pronounced toward the chain end, indicating a mobility gradient along the side chain. In PPDOT-A a more pronounced intensity difference for short and long contact time is observed. The $\alpha^{(*)}$ -carbons have a high rigidity since the intensity difference is insignificant. Along the side chain the mobility increases strongly with almost no detectable signal of the methyl group for the spectra with a short contact time. Small intensity differences for the backbones resonances of the “5” carbons in both modifications imply a strong rigidity of the main chain originating from the π – π stacking. The “2” resonances display a higher difference in intensity; thus, the phenyl ring without the attached side chain has a higher mobility, caused for example by uniaxial rotation or a two-site jump.^{40,41}

For a more quantitative analysis of the coupling constants and an estimation on the amplitude of molecular motions the 2D DIPSIFT (dipolar chemical shift correlation) sequence is used.^{42–44} This method enables the measurement of the motionally averaged carbon–proton dipolar couplings D_{res} provided that the rate of motion exceeds the static-limit coupling constant ($D_{\text{CH}}/2\pi \approx 21$ kHz for a CH). The influence of the dipolar coupling and chemical shift is probed by the intensity modulations of ^{13}C CP MAS spectra, which

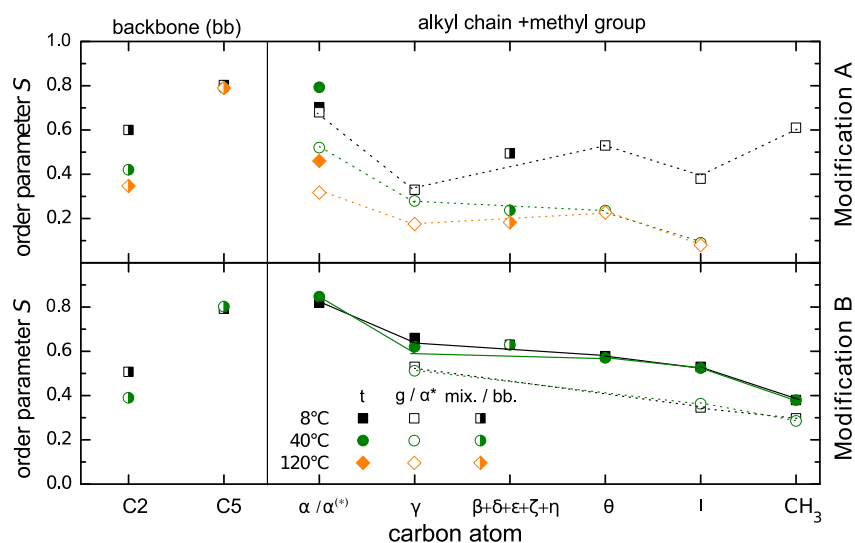


Figure 7. Temperature-dependent order parameters of the protonated backbone carbons (half-filled symbols), *trans*-rich (closed symbols), and *gauche*-rich (open symbols) conformations of the alkyl chains in both modifications.

depends on an evolution time t_1 ranging from 0 to the time of one rotor period T_R and has a minimum at $T_R/2$. With these modulation curves, residual dipolar couplings of the order of 10 kHz can be determined. The depth is less pronounced for weaker couplings. For very fast molecular dynamics, with correlation times τ_c that are much smaller than the inverse dipolar frequency $1/D_{CH} \sim 10 \mu s$, the intensities at $t_1 = 0$ and $t_1 = T_R$ will be equal. For intermediate dynamics with $\tau_c \approx 1/D_{CH}$, the spins will lose their phase correlation during the experiment, resulting in the T_2 relaxation effect, and thus the dipolar signal at $t_1 = T_R$ will be lower in intensity, allowing an estimation of the rate constant of the corresponding molecular motions.^{45,46}

The DIPSHIFT curves in Figure 6 compare the temperature dependence and molecular motions in both modifications for the “2”-, $\alpha^{(*)}$ -, γ -, and l -carbons. Both modifications show an intensity loss due to intermediate motions of the “2”-carbons (highlighted by the red boxes in Figure 6), whereby the loss of intensity is less pronounced in modification B (bottom line). By use of the Anderson–Weiss approximation,^{45,46} the correlation times τ_c of these intermediate dynamics can be estimated. The unsubstituted rings in modification A have motions in the slow regime at 8 °C. Increasing temperatures result in a higher mobility in the intermediate regime at 40 °C, and subsequently fast molecular dynamics with $\tau_c \ll 1 \mu s$ at 120 °C are reached. In PPDOT-B the fast motion regime for the “2”-carbons is approached at 40 °C. The alkyl chains in modification A have molecular motions with correlation times of several 100 μs at 8 °C. During heating τ_c reduces to several 10 μs at 40 °C and approaches the intermediate regime above 40 °C with $\tau_c \approx 10 \mu s$. The α^* -CH₂ groups have for all temperatures faster molecular dynamics than the α -carbons. The DIPSHIFT curves of the l -CH₂ groups at 120 °C could not be analyzed due to the intensity loss of the resonance in the high-temperature phase (see discussion below). The molecular motions of the alkyl chains in B depend only to a small extent on temperature and on the conformational environment.

Order Parameters. The ratio D_{stat}/D_{CH}^a is equal to the order parameter S , ranging from 0 (isotropic movement) to 1

(static). Temperature-dependent results for both modifications are plotted in Figure 7. In modification B the apparent order parameter of the alkyl chain decreases toward the chain end. The mobility differences in *trans*- and *gauche*-rich conformations are confirmed by the slightly higher order parameter for the *trans*-rich carbons, reaching from $S \sim 0.66$ (t)/ $S \sim 0.51$ (g) for the γ -carbons to $S \sim 0.38$ (t)/ $S \sim 0.29$ (g) for the methyl group. The resonances for the β -, δ -to- η -carbons are overlapping; therefore, averaged order parameters for these CH₂ are given. The α -carbons have a relatively high order parameter of $S \sim 0.83$, caused by the spatial proximity to the backbone and the corresponding mobility constraints of the phenyl rings, which is similar to the order parameter of the “5” carbons ($S \sim 0.80$). No apparent temperature dependence for the alkyl chains and the “5” carbons is detected; only the “2” carbons show a decrease of the order parameter from $S \sim 0.51$ at 8 °C to $S \sim 0.39$ at 40 °C and thus an increase in mobility for a higher temperature. For the motional process of the phenyl ring without side chains we assume π -flips with additional vibrations, since the expected order parameter of a two-site jump is ~ 0.6 , and for a uniaxial rotation one would expect a very low value.^{40,41}

In modification A the order parameter of the “2”-carbons varies from ~ 0.60 at 8 °C to ~ 0.35 at 120 °C. This leads to the reasonable interpretation that the unsubstituted rings are more hindered in their mobility in modification A than in modification B. This is in agreement with the structural parameters of PPDOT published by Gupta et al.,²² reporting that the distance between neighboring π - π stacks is smaller in modification A and might also be a result of the differences in the backbone conformation. The high order parameter of $S \sim 0.80$ of the “5”-carbons shows that the well-ordered π - π stacks remain rigid even at temperatures up to 120 °C. In modification A, the change in backbone conformation results in two different chemical environments for the α -carbons. The ones with a parallel ester group to the “6”-carbons (structure I) have a lower order parameter than the α^* -carbons (open symbols) over the complete temperature range. In backbone structure II or III no C=O bond is in direct vicinity to the α^* -CH₂ groups, which could supposedly increase the mobility of

these carbons. At low and ambient temperatures the order parameter of the α -carbons, which are in a similar chemical environment as those in modification B, are also comparable to the ones in B. In contrast to that, the mobility of the $\alpha^{(*)}$ -carbons increases strongly for $T = 120$ °C, and the order parameter reduces to $S(\alpha) \sim 0.46$ ($S(\alpha^*) \sim 0.32$).

The higher mobility of the side chains in A, as indicated by the comparison of ^{13}C CP MAS spectra with different contact times, can be confirmed by the order parameters of the *gauche*-rich domains. Although at 8 °C the order parameters of the alkyl side chains in modification A and B have comparable values, the side chain dynamics in modification A have a stronger temperature dependence. At 40 °C the order parameters along the alkyl chain (~ 0.28 for γ -carbons and ~ 0.08 for ι -carbons) have less than half of the value as in modification B. An increase of the temperature to 120 °C leads to a further reduction of the order parameter.

For fast molecular motions at high temperatures (above 120 °C) an intensity loss of the corresponding resonances of the alkyl chain occurs. Therefore, only the more strongly coupled CH pairs will be detected in the ^{13}C CP MAS spectra recorded during the DIPSHIFT experiment. To analyze this bias effect, we compare long-contact ^{13}C CP MAS spectra (that measure both mobile and rigid components) with INEPT (insensitive nuclei enhanced by polarization transfer) spectra, which detect only resonances with order parameters lower than $S < 0.3$ and dynamics with a correlation time $\tau_c < 0.01$ μs .⁴⁷ In contrast to CP experiments, where the polarization is transferred by the dipole–dipole coupling, the J -coupling between a carbon–proton pair is used in the INEPT technique. From the comparison of CP and INEPT intensities one can draw conclusions about the site-resolved dynamics.⁴⁷

The comparison of INEPT and CP spectra at 120 °C is plotted in Figure 8 (top). The INEPT intensities of the alkyl chain end (θ , ι , and CH_3) are many times larger than the CP intensities; additionally, a slight chemical shift difference is detected. This indicates the coexistence of two phases in alkyl chain, one with an order parameter from 0.23 to 0.08 (θ to ι), measured with the DIPSHIFT sequence, and another phase with an order parameter $S \sim 0$. This second highly mobile side chain could be originated in the different chemical environments of the side chains and the correlated differences in mobility for the $\alpha^{(*)}$ -carbons, especially for high temperatures, detected by the DIPSHIFT experiment. The CH_2 groups

closer to the backbone have higher order parameters, and accordingly the INEPT intensities decrease and are lower than those measured with cross-polarization. The rigid $\alpha^{(*)}$ and backbone carbons give no INEPT signal.

In summary, modification A is defined by a well-ordered, rigid backbone, which we think is best described by structure III and has mobile alkyl chains in *gauche*-rich conformations. The dynamics of the side chain depend strongly on temperature. The order parameter decreases toward higher temperatures, and at 120 °C the molecular motions of the alkyl chain reach the intermediate motional regime; at this temperature a second coexisting phase appears that features an order parameters $S \sim 0$ along the side chains. The backbone remains rigid up to 120 °C. The flip motion of the phenyl ring without attached side chains varies from the slow limit at 8 °C to the fast regime at 120 °C. Modification B exhibits a rigid, well-ordered π – π stacking of the backbone, with a faster flip motion of the unsubstituted phenyl ring, reaching the fast limit already at 40 °C. The alkyl chains exist in *trans*- and *gauche*-rich regions with a weak temperature dependence, which may be assigned to side chain-crystalline and side chain-amorphous subphases, respectively. The mobility of the side chain is smaller than in modification A.

Liquid-Crystalline Phase. PPDOT exhibits a transition to a liquid-crystalline phase at around 174 °C during heating as seen in DSC scans (Figure 1b) as well as recently published fast scanning calorimetry results.⁴⁸ The comparison of CP and INEPT spectra in this phase is given in Figure 8 (bottom) and was detected at 180 °C.

In this phase the complete alkyl chain is highly mobile, with INEPT intensities which are equal to ($\alpha\text{-CH}_2$) or—for the rest of the alkyl chain—significantly higher than the CP intensities. The intensity difference in CP and INEPT for the “2”- and “5”-carbons implies a high mobility of both phenyl rings with and without attached side chains. These findings verify that a second phase transition to a liquid-crystalline phase with a high backbone mobility and fast dynamics of the entire side chains with $S \sim 0$ occurs. It should also be pointed out that the α -carbons only resonate at one averaged chemical shift α^{LC} ; therefore, the chemical environments for all α -carbons must be similar. This and the high mobility of the phenyl rings indicate a loss of the π – π stacking of the backbones. This is complemented by the disappearance of the (020) reflection corresponding to the π – π stacking of the backbones above 170 °C (Figure 1a). However, the layered morphology survives even above this temperature.

4. SUMMARY AND CONCLUSIONS

We used a combination of ^{13}C solid-state NMR techniques to probe the packing state of the backbone and side chains in PPDOT-B and PPDOT-A as well as in the liquid-crystalline phase at high temperatures. PPDOT-A and PPDOT-B have a well-ordered backbone in π – π stacks but with different conformations for each modification. Despite the structural differences, there is no indication of a backbone-amorphous phase in both polymorphs. In the liquid-crystalline phase, the π – π stacking of the backbones is no longer present, and well-defined backbone resonances again suggest a uniform backbone packing in the entire sample. We speculate that the existence of such a liquid-crystalline phase, being a precursor of a crystalline phase, may promote the minimization of a backbone-amorphous phase.^{49–51}

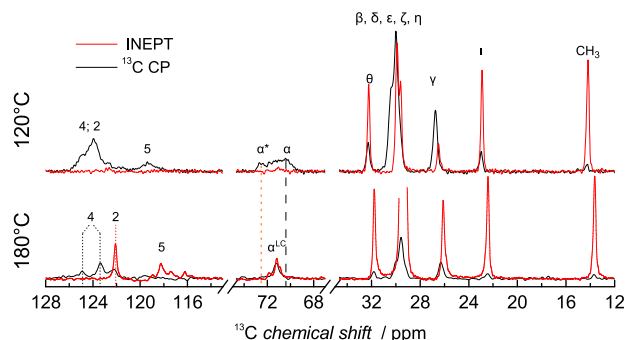


Figure 8. Comparison of ^{13}C CP MAS and INEPT spectra of PPDOT in modification A at 120 °C (top) and in the liquid-crystalline phase 180 °C (bottom). A large INEPT intensity indicates a low order parameter or dynamics with a correlation time $\tau_c < 0.01$ μs .

Differences in both modifications are found with regards to the packing states and the dynamics of the alkyl nanodomains. The side chains in PPDOT-A have molecular motions in the intermediate regime and are in an amorphous environment with *gauche*-rich conformers. The side chain CH₂ groups in modification B have a larger order parameter than modification A and coexist in *trans*- and *gauche*-rich conformations. Whether both conformations alternate on the molecular scale with one another or form separate phases on the nanometer scale or beyond is still under investigation.

It is an intriguing question whether such subtle differences in π - π stacking and local dynamics affect electronic properties in the case of semiconducting polymers, where polymorphic states are very common.^{10,17,26,29} Notably, many NMR crystallographic studies of such compounds have so far neglected the existence of—or found no evidence for—the presence of backbone-disordered phases.^{19,28,39} The corresponding implications for materials performance are yet to be worked out.

AUTHOR INFORMATION

Corresponding Author

*E-mail: mareen.schaefer@physik.uni-halle.de.

ORCID

Varun Danke: 0000-0001-9874-7935

Mario Beiner: 0000-0003-0459-323X

Kay Saalwächter: 0000-0002-6246-4770

Mareen Schäfer: 0000-0001-6589-2087

Notes

The authors declare no competing financial interest.

ACKNOWLEDGMENTS

Financial support within the framework of Deutsche Forschungsgemeinschaft (DFG, German Research Foundation), project number 189853844 - TRR 102 “Polymers under multiple constraints” (Projects A01 and B14), is highly appreciated. Insightful discussions with Gaurav Gupta and Tiago Mendes Ferreira are gratefully acknowledged. We also thank an anonymous reviewer for very insightful suggestions concerning the interpretation of some observations.

ADDITIONAL NOTE

⁴F₀₁ For CH₂ groups the effective D_{CH} is ≈ 19 kHz. For the determination of this reference coupling a mixture of alanin and glycin was used.

REFERENCES

- (1) Blom, P. W. M.; Vissenberg, M. C. J. M. Charge transport in poly(p-phenylene vinylene) light-emitting diodes. *Mater. Sci. Eng., R* **2000**, *27*, 53–94.
- (2) Liu, C.; Qiu, Z.; Li, F.; Meng, W.; Yue, W.; Zhang, F.; Qiao, Q.; Wang, M. From binary to multicomponent photoactive layer: A promising complementary strategy to efficient hybrid solar cells. *Nano Energy* **2015**, *12*, 686–697.
- (3) Lee, B. H.; Hsu, B. B. Y.; Patel, S. N.; Labram, J.; Luo, C.; Bazan, G. C.; Heeger, A. J. Flexible Organic Transistors with Controlled Nanomorphology. *Nano Lett.* **2016**, *16*, 314–319.
- (4) Jackson, W. Liquid crystal polymers. IV. Liquid crystalline aromatic polyesters. *Br. Polym. J.* **1980**, *12* (4), 154–162.
- (5) Ballauff, M. Stiff-chain polymers - Structure, phase-behavior, and properties. *Angew. Chem., Int. Ed. Engl.* **1989**, *28*, 253–267.
- (6) Yin, Y.; Du, Q.; Qin, Y.; Zhou, Y.; Okamoto, K.-i. Sulfonated polyimides with flexible aliphatic side chains for polymer electrolyte fuel cells. *J. Membr. Sci.* **2011**, *367*, 211–219.
- (7) Lenz, R. Balancing mesogenic and non-mesogenic groups in the design of thermotropic polyesters. *Faraday Discuss. Chem. Soc.* **1985**, *79*, 21–32.
- (8) Lenz, R. Synthesis and Properties of Thermotropic Liquid Crystal Polymers with Main Chain Mesogenic Units. *Polym. J.* **1985**, *17*, 105.
- (9) Pankaj, S.; Beiner, M. Long-term behavior and side chain crystallization of poly(3-alkyl thiophenes). *Soft Matter* **2010**, *6*, 3506–3516.
- (10) Damman, S. B.; Mercx, F. P. M.; Kootwijkdamman, C. M. Liquid-crystalline mainchain polymers with a poly(p-phenylene terephthalate) backbone. 1. Synthesis, characterization and rheology of polyesters with alkoxy side-chains. *Polymer* **1993**, *34*, 1891–1897.
- (11) Plate, N. A.; Shibaev, V. P. Comb-like polymers - Structure and properties. *Macromol. Rev.* **1974**, *8*, 117–253.
- (12) Schrauwen, C.; Pakula, T.; Wegner, G. Structure and mechanical properties of films of rigid-rod polymers having flexible side chains. *Makromol. Chem.* **1992**, *193*, 11–30.
- (13) Ballauff, M.; Schmidt, G. F. Rigid rod polymers with flexible side chains. 2. Observation of a novel type of layered mesophase. *Makromol. Chem., Rapid Commun.* **1987**, *8*, 93–97.
- (14) Pankaj, S.; Beiner, M. Confined dynamics and crystallization in self-assembled alkyl nanodomains. *J. Phys. Chem. B* **2010**, *114*, 15459–15465.
- (15) Shi, H.; Zhao, Y.; Dong, X.; Zhou, Y.; Wang, D. Frustrated crystallisation and hierarchical self-assembly behaviour of comb-like polymers. *Chem. Soc. Rev.* **2013**, *42*, 2075–2099.
- (16) Meille, S. V.; Romita, V.; Caronna, T.; Lovinger, A. J.; Catellani, M.; Belobrzekaja, L. Influence of Molecular Weight and Regioregularity on the Polymorphic Behavior of Poly(3-decylthiophenes). *Macromolecules* **1997**, *30*, 7898–7905.
- (17) Pascui, O. F.; Lohwasser, R.; Sommer, M.; Thelakkat, M.; Thurn-Albrecht, T.; Saalwächter, K. High Crystallinity and Nature of Crystal-Crystal Phase Transformations in Regioregular Poly(3-hexylthiophene). *Macromolecules* **2010**, *43*, 9401–9410.
- (18) Kakali, F.; Kallitsis, J.; Pakula, T.; Wegner, G. Synthesis and X-ray Characterization of Alkoxy-Substituted Aromatic Polyesters Containing Terphenyl or Quinquephenyl Units in the Main Chain. *Macromolecules* **1998**, *31*, 6190–6198.
- (19) Adam, A.; Spiess, H. W. On the packing behaviour of alkoxy-substituted stiff macromolecules. *Makromol. Chem., Rapid Commun.* **1990**, *11*, 249–259.
- (20) Watanabe, J.; Ono, H.; Uematsu, I.; Abe, A. Thermotropic polypeptides. 2. Molecular packing and thermotropic behavior of poly(L-glutamates) with long n-alkyl side chains. *Macromolecules* **1985**, *18*, 2141–2148.
- (21) Damman, S. B.; Mercx, F. P. M. Liquid-crystalline main-chain polymers with a poly(p-phenylene terephthalate) backbone. 2. Fiber spinning and mechanical properties of polyesters with alkoxy side-chains. *J. Polym. Sci., Part B: Polym. Phys.* **1993**, *31*, 1759–1767.
- (22) Gupta, G.; Danke, V.; Babur, T.; Beiner, M. Interrelations between side chain and main chain packing in different crystal modifications of alkoxyated polyesters. *J. Phys. Chem. B* **2017**, *121*, 4583–4591.
- (23) Shi, H.; Zhao, Y.; Zhang, X.; Zhou, Y.; Xu, Y.; Zhou, S.; Wang, D.; Han, C. C.; Xu, D. Packing mode and conformational transition of alkyl side chains in N-alkylated poly(p-benzamide) comb-like polymer. *Polymer* **2004**, *45*, 6299–6307.
- (24) Gonzalez De La Campa, J. I.; Barrales-Rienda, J. M.; Gonzalez Ramos, J. Side-chain crystallinity, heat of melting, and thermal transitions in poly[N-(10-n-alkyloxycarbonyl-n-decyl)maleimides] (PEMI). *J. Polym. Sci., Polym. Phys. Ed.* **1980**, *18*, 2197–2207.
- (25) Ebert, M.; Herrmann-Schönherr, O.; Wendorff, J. H.; Ringsdorf, H.; Tschirner, P. Sanidics: A new class of mesophases, displayed by highly substituted rigid-rod polyesters and polyamides. *Liq. Cryst.* **1990**, *7*, 63–79.

- (26) Shi, H.; Zhao, Y.; Jiang, S.; Rottstegge, J.; Xin, J. H.; Wang, D.; Xu, D. Effect of Main-Chain Rigidity on the Phase Transitional Behavior of Comblike Polymers. *Macromolecules* **2007**, *40*, 3198–3203.
- (27) Danke, V.; Gupta, G.; Reimann, S.; Binder, W. H.; Beiner, M. Structure formation in nanophase-separated systems with lamellar morphology: Comb-like vs. linear precision polymers. *Eur. Polym. J.* **2018**, *103*, 116–123.
- (28) Clauss, J.; Schmidt-Rohr, K.; Adam, A.; Boeffel, C.; Spiess, H. W. Stiff macromolecules with aliphatic side chains: side-chain mobility, conformation, and organization from 2D solid-state NMR spectroscopy. *Macromolecules* **1992**, *25*, 5208–5214.
- (29) Ballauff, M. Rigid rod polymers having flexible side chains. I. Thermotropic poly(1,4-phenylene 2,5-dialkoxyterephthalate)s. *Makromol. Chem., Rapid Commun.* **1986**, *7*, 407–414.
- (30) Damman, S. B.; Vroege, G. J. Liquid-crystalline main-chain polymers with a poly(p-phenylene terephthalate) backbone. X-ray-diffraction of the polyester with dodecyloxy side-chains. *Polymer* **1993**, *34*, 2732–2739.
- (31) Whittaker, A. K.; Falk, U.; Spiess, H. W. Solid-state ^{13}C nuclear magnetic resonance studies of side-group conformations in the rigid-rod polyester poly[1,4-phenylene 2,5-bis(hexadecyloxy)-terephthalate]. *Makromol. Chem.* **1989**, *190*, 1603–1612.
- (32) Babur, T.; Balko, J.; Budde, H.; Beiner, M. Confined relaxation dynamics in long range ordered polyesters with comb-like architecture. *Polymer* **2014**, *55*, 6844–6852.
- (33) Earl, W. L.; VanderHart, D. L. Observations in Solid Polyethylenes by Carbon-13 Nuclear Magnetic Resonance with Magic Angle Sample Spinning. *Macromolecules* **1979**, *12*, 762–767.
- (34) Tonelli, A. E. Calculated γ Effects on the ^{13}C -NMR Spectra of 3,5,7,9,11,13,15-Heptamethylheptadecane Stereoisomers and Their Implications for the Conformational Characteristics of Polyporpylene. *Macromolecules* **1978**, *11*, 565–567.
- (35) McElheny, D.; Grinshtein, J.; Frydman, V.; Frydman, L. Solid-State ^{13}C NMR of Liquid Crystalline Polyesters: Variations in Morphology, Alignment, and Dynamics within a Homologous Series. *Macromolecules* **2002**, *35*, 3544–3552.
- (36) Brandolini, A. J.; Hills, D. D. *NMR Spectra of Polymers and Polymer Additives*, 1st ed.; CRC Press: New York, 2000.
- (37) Červinka, L.; Ballauff, M. Rigid-rod polymers with flexible side chains 9. Wide-angle x-ray analysis of side-chain ordering in poly(1,4-phenylene-2,5-di-n-hexadecyloxyterephthalate). *Colloid Polym. Sci.* **1992**, *270*, 859–872.
- (38) Tonelli, A. E. In *The Conformational Connection Between the Microstructures of Polymers and Their NMR Spectra*; Webb, G., Ando, I., Eds.; Annual Reports on NMR Spectroscopy; Academic Press: 1997; Vol. 34, pp 185 – 229.
- (39) Dudenko, D.; Kiersnowski, A.; Shu, J.; Pisula, W.; Sebastiani, H. W.; Spiess, D.; Hansen, R. H. A Strategy for Revealing the Packing in Semicrystalline π -Conjugated Polymers: Crystal Structure of Bulk Poly-3-hexyl-thiophene (P3HT). *Angew. Chem., Int. Ed.* **2012**, *51*, 11068–11072.
- (40) Fedotov, V. D.; Schneider, H. In *Structure and Dynamics of Bulk Polymers by NMR Methods*; Diehl, P., Fluck, E., Günter, H., Kosfeld, R., Seelig, J., Eds.; Springer-Verlag: Berlin, 1989; Vol. 21.
- (41) Reichert, D.; Saalwächter, K. In *Dipolar Couplings: Molecular-Level Mobility*; Harris, R. K., Wasylchen, R. E., Duer, M., Eds.; John Wiley & Sons: Chichester, 2009.
- (42) Munowitz, M. G.; Griffin, R. G. Two-dimensional nuclear magnetic resonance in rotating solids: An analysis of line shapes in chemical shift-dipolar spectra. *J. Chem. Phys.* **1982**, *76*, 2848–2858.
- (43) Harris, R. K.; Jackson, P.; Merwin, L. H.; Say, B. J.; Hägele, G. Perspectives in High-resolution Solid-state Nuclear Magnetic Resonance, with Emphasis on Combined Rotation and Multiple-pulse Spectroscopy. *J. Chem. Soc., Faraday Trans. 1* **1988**, *84*, 3649–3672.
- (44) Hong, M.; Gross, J. D.; Griffin, R. G. Site-Resolved Determination of Peptide Torsion Angle φ from the Relative Orientations of Backbone N-N and C-H Bonds by Solid-State NMR. *J. Phys. Chem. B* **1997**, *101*, 5869–5874.
- (45) Hirschinger, J. A Simple Analytical Model to Describe Dynamic Magic-Angle Spinning Experiments. *Concepts Magn. Reson., Part A* **2006**, *28A*, 307–320.
- (46) de Azevedo, E. R.; Saalwächter, K.; Pascui, O.; de Souza, A.; Bonagamba, T. J.; Reichert, D. Intermediate motions as studied by solid-state separated local field NMR experiments. *J. Chem. Phys.* **2008**, *128*, 104505.
- (47) Nowacka, A.; Mohr, P. C.; Norrman, J.; Martin, R. W.; Topgaard, D. Polarization Transfer Solid-State NMR for Studying Surfactant Phase Behavior. *Langmuir* **2010**, *26*, 16848–16856.
- (48) Danke, V.; Gupta, G.; Huth, H.; Schawe, J.; Beiner, M. Polymorphic states and phase transitions in a comb-like polymer having a rigid polyester backbone and flexible side chains. *Thermochim. Acta* **2019**, *677*, 162–168.
- (49) McCulloch, I.; Heeney, M.; Bailey, C.; Genevicius, K.; MacDonald, I.; Shkunov, M.; Sparrowe, D.; Tierney, S.; Wagner, R.; Zhang, W.; Chabinyc, M. L.; Kline, R. J.; McGehee, M. D.; Toney, M. F. Liquid-crystalline semiconducting polymers with high chargecarrier mobility. *Nat. Mater.* **2006**, *5*, 328–333.
- (50) Kleinhenz, H.; Rosu, C.; Chatterjee, S.; Chang, M.; Nayani, K.; Xue, Z.; Kim, E.; Middlebrooks, J.; Russo, P. S.; Park, J. O.; Srinivasarao, M.; Reichmanis, E. Liquid Crystalline Poly(3-hexylthiophene) Solutions Revisited: Role of Time-Dependent Self-Assembly. *Chem. Mater.* **2015**, *27*, 2687–2694.
- (51) Xie, R.; Colby, R. H.; Gomez, E. D. Connecting the Mechanical and Conductive Properties of Conjugated Polymers. *Adv. Electron. Mater.* **2018**, *4*, 1700356.

5 | Summary, conclusions and outlook

Knowledge on how to influence and control the crystallization of semicrystalline polymers is of great interest for manufacturing materials with specific properties. Ongoing research strives to deepen the understanding on the structure formation of semicrystalline polymers. However, current research often focuses on either one particular influencing factor, e.g. entanglements, or a specific polymer material. Thus, a general model on the structure formation is not yet available and existing models may even contradict each other [27–29, 31–37]. Based upon recent studies on PCL, POM and PEO [44, 46, 72, 130, 131]¹, partially conducted in the framework of this thesis, it became apparent that the semicrystalline morphology is strongly influenced by the interdependency of crystal growth and reorganization during the crystallization. Additionally, the effect of entanglements in the amorphous phase and melt are expected to influence the final semicrystalline structure. If and how these findings can be applied to other homopolymers or also to more complex systems with a heterogeneity in their chemical structure is not yet clear.

This thesis is devoted to the study of the structure formation of polymer systems, that develop a semicrystalline morphology with rigid and mobile regions, using static proton and magic-angle spinning ¹³C NMR experiments. Depending on the investigated polymer system and the scientific question, different NMR techniques are necessary to allow for a comprehensive analysis of the dynamical or structural properties. Static proton NMR provides comparatively fast experiments with a high signal-to-noise ratio and yield quantitative spectra or time-domain signals. However, the acquired signals represent an average of the sample, therefore only regions with different mobilities can be distinguished using this technique. Thus, static ¹H pulse sequences are best suited for polymers systems without polymorphism or various contributions to either the rigid or amorphous phase. In the latter cases a selective chemical investigation is often necessary. A large variety of ¹³C MAS pulse sequences

¹[130]: R. Kurz, A. Achilles, W. Chen, **M. Schäfer**, A. Seidlitz, Y. Golitsyn, J. Kressler, W. Paul, G. Hempel, T. Miyoshi, T. Thurn-Albrecht and K. Saalwächter. Intracrystalline Jump Motion in Poly(ethylene oxide) Lamellae of Variable Thickness: A Comparison of NMR Methods. *Macromolecules* **50**, 3890-3902 (2017)

[131]: M. Schulz, **M. Schäfer**, K. Saalwächter and T. Thurn-Albrecht. Intracrystalline chain dynamics as the relevant factor governing lamellar thickness in semicrystalline polymers. submitted to *Macromolecules* (2021).

enables the determination of dynamical and/or structural information with molecular resolution. These measurements are often based on cross polarization (CP) in order to enhance the otherwise weak ^{13}C signal, but this has the unfortunate side-effect that the results yield a non-quantitative ratio of the amorphous and crystalline resonance intensities. Hence, the combination of quantitative proton and/or (several) chemical selective ^{13}C NMR experiments is often required for a thorough characterization of the complete sample. With complementary X-ray scattering, caloric experiments and/or optical microscopy the structural parameters, thermal behavior and crystalline growth dynamics are also accessible.

To build upon the knowledge, which was gained on the structure formation of the homopolymers PEO and PCL having a narrow, unimodal M_w -distribution, both polymers were diluted with their own oligomer prior to crystallization. This allowed to shift the research focus on the impact of the entanglement density in the melt and amorphous phase, while the conclusions drawn by the preceding investigations were still applicable. The experiments revealed that the fast intracrystalline dynamics in PEO seems to be the prevailing factor for the final semicrystalline morphology. The absence of the reorganization within the crystal during the crystallization of oligomer-diluted PCL results in a more pronounced change of the morphology upon dilution. An additional factor influencing the structure formation is the composition-dependent simultaneous crystallization and the formation of mixed polymer/oligomer crystals.

In random copolymers the final semicrystalline morphology is also governed by the comonomer composition as well as the composition-dependent separate crystallization and a possible co-crystallization. The distinction between isomorphism and isodimorphism—the former has a total, the latter a limited or no co-unit inclusion—stresses the relevance of the incorporation of co-units in the crystal structure of the second comonomer. In PBSA copolymers the asymmetric co-unit inclusion leads to a similar asymmetric dependence of the crystallinity and crystalline thickness on the BS/BA composition. An additional dependence of the separate crystallization and co-unit inclusion for compositions in the pseudoeutectic range on the thermal history was found. This could be correlated with the polymorphic behavior of the homopolymer PBA [26].

Changes in the thermal history allow to access the polymorphs of the comb-like polymer PPDOT. The combination of stiff and flexible chains results in a layered morphology which differs from the melt-crystallized semicrystalline structure. The polymorphs differ in the local dynamics of the side chain as well as the structural conformation of the backbone. A counterplay between the conformation and dynamics in side and main chain could be a relevant factor for the presence of the two modifications.

The presented results show that general models describing the structure formation of semicrystalline homopolymers are difficult to devise. Even for a rather simple system, e.g. a crystal-mobile polymer with a well-defined molecular weight, at least three competing dynamic processes are relevant for the final morphology. By changing external parameters, for example the crystallization and/or measurement temperature or by blending the polymer with its own oligomer, new parameters have to be taken into account. For polymer systems with a heterogeneity along the chain the situation becomes even more complex. For these polymers the structure formation is strongly influenced by their heterogeneous chemical structure. Furthermore, the mentioned dynamical parameters are potentially significant and interrelate with the given constraints imposed by the chain structure. Thus, a step-wise analysis, which successively focuses on all possible influencing factors, is necessary to gain a more comprehensive understanding on polymer crystallization.

Based on these findings a step-wise approach for further research on the presented polymer systems is outlined in the following.

Crystal-mobile in comparison to crystal-fixed bimodal M_w -blends

1. Co-crystallization/simultaneous crystallization

For a thorough comparison of semicrystalline structures formed by oligomer-diluted PEO and PCL, the effect of simultaneous crystallization and/or the formation of mixed crystals must be evaluated. This can be accomplished by increasing (decreasing) the molecular weight of the PEO (PCL) oligomer to enable (prevent) the simultaneous formation and/or co-crystallization in both blends. The upper limit of the PEO-oligomer chain length is given by the entanglement molecular weight $M_e = 1.73 - 2$ kDa [132]. An oligomer with a molecular weight of 2 kDa could only be incorporated in long-chain crystals with a maximum length of 13 nm. However, a detailed study on the M_w -dependence of the crystalline thickness of isothermally crystallized PEO revealed a minimum thickness of 14.6 nm [133]. Thus, the formation of mixed crystals is unlikely and a comparison to the presented results on oligomer-diluted PCL would not be possible. The reduction of the molecular weight of the PCL oligomer may prevent the formation of pure oligomer and oligomer/polymer crystals. This would also allow to investigate the amorphous phase of the semicrystalline structure and thus seems to be the better option. For shorter oligomer end groups effects may become relevant and have to be taken into account.

2. Entanglements

Without a simultaneous crystallization and co-crystallization, the effect of oligomer-dilution on the amorphous phase in PCL could be analyzed. In pure PEO samples the amorphous phase cannot be characterized [134] due to its small size, whereby confinement effects such as the constraints imposed by e.g. tie chains or loops become important. It would have to be examined if an analysis becomes feasible for a certain amount of oligomer-dilution. In either way, the entanglement density in the melt could be analyzed and compared for all possible oligomer-dilutions of both polymers.

Heterogeneous chemical structure

1. Co-crystallization/simultaneous crystallization

The results on the separate crystallization of BA and BS-rich crystals in random PBSA copolymers with compositions in the pseudoeutectic range and on mixed crystals for all PBSA compositions have to be completed. Thereby, the effect of cooling rates and structure formation at specific crystallization temperatures can be determined.

2. Entanglements

Once the amount of included minority components in PBSA copolymers and their dependence on the thermal history is derived, the effect on the amorphous phase can be analyzed. Here a selective chemical analysis is important, in order to evaluate the couplings of BA and BS-units in the amorphous phase separately.

3. Polymorphism

For PBSA copolymers the impact of the polymorphism of the homopolymer PBA can be studied with respect to the amount of included co-units and the formation of BA- and BS-rich crystals.

In PPDOT the presence of a polymorphic structure evoked by the mutual influencing dynamics of side and main-chain could be confirmed by ^{13}C NMR studies on comb-like structures with varying side chain lengths.

A | So far unpublished results

A.1 Estimation of a reference entanglement density for molten PCL by evaluating the amplitude of the OACF at τ_e

Double-quantum (DQ) NMR data sets are analyzed with the power-law ansatz (for details see chapter 3.2.3), whereby the DQ signal I_{DQ} and the corrected sum signal $I_{\Sigma MQ} - tail$ are simultaneously fitted, yielding the the time scaling exponent κ as well as the residual dipolar coupling $D_{res}(\tau_{DQ,min})/(2 \cdot \pi)$ averaged to a time corresponding roughly to the first experimental data point $2\tau_{DQ,min}$. Alternatively, the DQ NMR results allow to construct the segmental orientation autocorrelation function (OACF) $C(t) \sim \sqrt{D_{res}(t)}$, with

$$C(t) \sim \frac{I_{DQ}/(I_{\Sigma MQ} - tail)}{\tau_{DQ}^2} = \frac{I_{nDQ}}{\tau_{DQ}^2} \quad (\text{A.1})$$

In both approaches, a large part of the OACF $C(t)$ can be constructed by using the time-temperature superposition (TTS) principle.[109, 135, 136]

The amplitude of constructed OACF at the entanglement time τ_e , separating regime I and II, reflects the entanglement density of the system [109]. However, for certain samples, such as poly(ϵ -caprolactone) (PCL), the construction of the OACF covering the regimes I to IV is not possible, due to the limited temperature range in which the samples are in a molten state. In the given case of PCL the constructed OACF covers only regimes III and IV [72]. To access the entanglement density of the system, a back-extrapolation to the entanglement time τ_e , is performed. Figure A.1 schematically displays the linear back-extrapolation in a double-logarithmic plot showing the dependence of $C(t)$ on τ_{DQ} . Starting from the first experimental data point $t_0 = \tau_{DQ}$, a linear extrapolation towards the entanglement time with the time scaling exponent κ as slope is applied. Since regime II cannot be reached without crystallization of the sample, the appropriate time scaling exponent for $C(t)$ is given by the M_w -dependent universal values for κ published previously [109, 136]. The entanglement time τ_e can be calculated via

$$\tau_e = \tau_D \cdot Z^{3.4} \quad (\text{A.2})$$

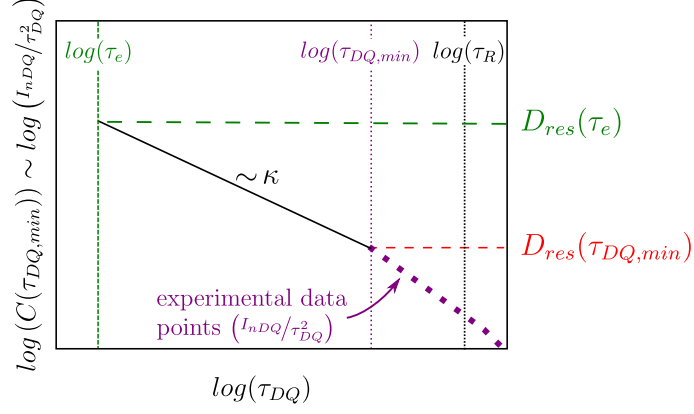


Figure A.1: Schematic representation of the linear back-extrapolation from $\log(C(\tau_{DQ,min}))$ to $\log(C(\tau_e))$ using an appropriate power-law for $C(t)$ in regime II, given by the time scaling exponent κ .

with $Z = M_w/M_e$ being the number of entangled strands of the sample with molecular weight M_w , and entanglement molecular weight M_e [136, 137]. The disentanglement time τ_D was obtained from rheology experiments. Additionally the transition from regime II to III at Rouse time $\tau_R = \tau_D/Z^{1.4}$ needs to be considered. The residual dipolar coupling value $D_{res}(\tau_e)$ at τ_e is calculated as follows

$$\log(C(\tau_e)) = -\kappa \cdot \log(\tau_e) + t \quad (\text{A.3})$$

$$\begin{aligned} \log(C(\tau_{DQ,min})) &= -\kappa \cdot \log(\tau_{DQ,min}) + t \\ \Leftrightarrow t &= \log(C(\tau_{DQ,min})) + \kappa \cdot \log(\tau_{DQ,min}) \end{aligned} \quad (\text{A.4})$$

$$\begin{aligned} \xrightarrow{\text{A.3+A.4}} \log(C(\tau_e)) &= -\kappa \cdot \log(\tau_e) + \kappa \cdot \log(\tau_{DQ,min}) + \log(C(\tau_{DQ,min})) \\ &= \log \left[\left(\frac{\tau_e}{\tau_{DQ,min}} \right)^{-\kappa} \cdot C(\tau_{DQ,min}) \right] \end{aligned} \quad (\text{A.5})$$

$$\Rightarrow C(\tau_e) = \left(\frac{\tau_e}{\tau_{DQ,min}} \right)^{-\kappa} \cdot C(\tau_{DQ,min}) \quad (\text{A.6})$$

$$\text{with } D_{res}(\tau_e) \sim \sqrt{C(\tau_e)} \text{ and } D_{res}(\tau_{DQ,min}) \sim \sqrt{C(\tau_{DQ,min})}$$

$$\Rightarrow D_{res}(\tau_e) = \sqrt{\left(\frac{\tau_e}{\tau_{DQ,min}} \right)^{-\kappa} \cdot D_{res}(\tau_{DQ,min})} \quad (\text{A.7})$$

The residual dipolar coupling at τ_e can be calculated using the entanglement time τ_e , the time of the first experimental data point $\tau_{DQ,min}$, the time scaling exponent κ and the residual dipolar coupling $D_{res}(\tau_{DQ,min})$. However, all parameters are subject to errors arising from fits and experimental uncertainties and in the case of κ one is bound to use the universal numbers which are valid for different flexible homopolymers. Minimizing the errors arising for the extrapolated D_{res} -value would

allow to find a universal reference value for the entanglement density of molten PCL. For a high- M_w sample, with $Z = 0.56 \cdot M_w \cdot \rho_s / M_e \gtrsim 500$, the predicted value of 0.25 for κ in regime II of tube-model [57, 138–140] can be used. This minimizes the error caused by a uncertain slope in the linear back-extrapolation. The experimentally observed values for such high M_w/M_e -fractions obtained with NMR are in the range of 0.25 to 0.28 [109, 136, 141]. Another advantage of high- M_w PCL samples, especially if the measurement is performed at a low temperature, is the reduced influence of the fraction of isotropically moving chain ends on the fitting parameter $D_{res}(\tau_{DQ,min})$. Uncertainties, regarding the first experimental data point $\tau_{DQ,min}$, arise from the experimental setup, but, as shown later, this will only contribute weakly to the overall error.

The main uncertainty originates from the calculated values of τ_e according to equation A.2. The calculated values, with disentanglement time τ_D (taken from reference [133]), assuming a relative error of 5 %, are shown in Figure A.2 A. The entanglement times for PCL are scattered between a upper and lower limit of $\tau_{e,max} = 14 \cdot 10^{-4}$ ms and $\tau_{e,min} = 1 \cdot 10^{-4}$ ms, respectively. The effect of the uncertainties of the starting ($\Delta\tau_{DQ,min}$) and end point ($\Delta\tau_e$) of the linear back-extrapolation on the extrapolated D_{res} -value is shown in Figure A.2 B. The range of $\Delta D_{res}(\tau_e)$ is mainly caused by the uncertainties in the entanglement time (range is shown in green); only a small fraction of this range is caused by the error of the starting point (shown in red). Note that the possible range for $\tau_{DQ,min}$ is exaggerated in comparison to $\Delta\tau_e$.

The fitted residual dipolar coupling values $D_{res}(\tau_{DQ,min})$ of high- M_w PCL samples, measured in the melt at 52 °C (taken from reference [72]), are used together with the time scaling exponent $\kappa = 0.25$, predicted by the tube-model for high- M_w samples, to calculate (using equation A.7) the upper and lower limits of the extrapolated value $D_{res,max}(\tau_e)$ and $D_{res,min}(\tau_e)$, respectively. The upper and lower limits for PCL with a molecular weight of 2000 and 4500 kDa, as well as the average value of both are given in Table A.1. The mean value of the given results is used to determine the reference residual dipolar coupling range to $D_{res}^{ref}(\tau_e)/(2 \cdot \pi) = 580 \pm 120$ Hz and can be used as a universal, reference value for the residual dipolar coupling of PCL at τ_e

Table A.1: Fitted $D_{res}(\tau_{DQ,min})$ -values for high- M_w PCL samples measured at 52 °C. For the back-extrapolation the time scaling exponent $\kappa = 0.25$ is used. The upper and lower limit of $D_{res}(\tau_e)$ are calculated using $\tau_{DQ,min} = 0.1$ ms and $\tau_e = 1 \cdot 10^{-4}$ ms as well as $\tau_{DQ,min} = 0.046$ ms and $\tau_e = 14 \cdot 10^{-4}$ ms, respectively.

molecular weight M_w / kDa	$D_{res}(\tau_{DQ,min})/(2\pi)$ / Hz	$D_{res}(\tau_e)/(2\pi)$ / Hz	
		upper limit	lower limit
2000	277	657	428
4500	316	749	488
\emptyset		703	459

A.2 Effects on crystallization and entanglement density caused by oligomer dilution of poly(ϵ -caprolactone)

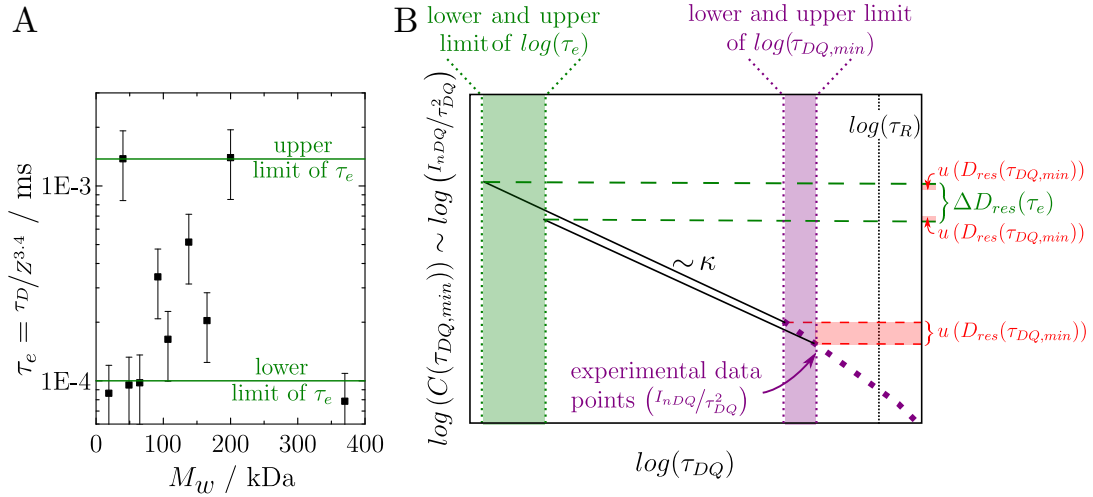


Figure A.2: A: Molecular weight dependence of calculated $\tau_e = \tau_D / Z^{3.4}$ of PCL. B: Schematic representation of the linear extrapolation in a log-log-Plot with the error range of $D_{res,ext}$ arising from the error margins of $\tau_{DQ,min}$ (red) and τ_e (green).

and thus for the entanglement density of PCL in the melt state. To minimize the error, a more precise determination of the entanglement time is necessary, since only 15% of the error for $\Delta D_{res}^{ref}(\tau_e)$ arise from the uncertainty of $\tau_{DQ,min}$.

The above described approach can also be applied for the back-extrapolation to obtain the entanglement density in the amorphous phase of the semicrystalline PCL which allows to calculate the entanglement enhancement factor ϵ .

$$\epsilon = \frac{D_{res}^{s.c.}(\tau_e)}{D_{res}^{ref}(\tau_e)} \quad (\text{A.8})$$

In the semicrystalline state, regime II can be reached and the thus the fit parameter κ from the power-law ansatz (see chapter 3.2.3) can be used for the back-extrapolation.

A.2 Effects on crystallization and entanglement density caused by oligomer dilution of poly(ϵ -caprolactone)

Recent studies indicate that the density of entanglements in the melt prior to crystallization influence the growth process [36] and morphology [34, 38, 72] of a semicrystalline polymer [39]. Additionally, these topological constraints are suspected to limit the final crystal thickness. In this work, high molecular weight poly(ϵ -caprolactone) (PCL) is diluted with its unentangled oligomer prior to crystallization. The oligomer-dilution results in a reduction of the entanglement density of the molten high- M_w PCL, while all other parameters are kept constant.

Materials

The polymer poly(ϵ -caprolactone) (PCL) used in this work has a molecular weight of $M_w = 200$ kDa and a polydispersity of 1.07. The oligomer sample has a molecular weight $M_w = 2.2$ kDa with a polydispersity of 1.05 and is therefore below the entanglement molecular weight $M_e = 2.3 - 3$ kDa [142]. Both samples were purchased from Scientific Polymer Products Inc. Oligomer and polymer mixtures were prepared with the mass fraction of the oligomer ($\Phi_{oligomer}$) ranging from 10% to 90%, by dissolving both samples with the desired mass fraction in chloroform for 2 h. Afterwards the solutions were placed in the fume hood for 4 days and vacuum oven for 24 h, respectively, in order to remove the residual solvent. In this work, the mixing ratios are given according to their polymer/oligomer weight fractions, i.e. PCL 80/20 consists of 80% polymer and 20% oligomer. The pure polymer and oligomer samples are referred to as PCL200 and PCL2.2, respectively. Prior to the NMR experiments the samples were held in the melt state for 15 min at approximately 30°C above their melting temperature and cooled to 53°C for measurements in the melt state or were rapidly cooled to the desired crystallization temperature T_c . The experiments were performed using step-wise heating.

Characterization of PCL oligomer and polymer

Prior to the investigation of the polymer/oligomer mixtures both pure samples were crystallized at several temperatures and investigated with ^1H FID and DQ experiments with focus on the semicrystalline three-phase structure and the constitution of the amorphous phase. A detailed analysis of the dynamics and entanglement density in the amorphous phase, using the residual dipolar couplings D_{res} obtained with ^1H DQ experiments, is presented together with the results of the mixtures.

Polymer PCL200 The pure polymer sample PCL 200 was crystallized at 35, 45 and 53°C, respectively. The temperature-dependent results of the signal fractions of the amorphous f_a , intermediate f_i and crystalline f_c phase are shown in the bottom row of Figure A.3. The intermediate fractions are similar for all samples and temperatures, whereas increasing the crystallization temperature results in a slight reduction of the crystallinity, which is most prominent at 53°C. However, the crystalline thickness d_c remains almost similar for all crystallization and measurement temperatures [143, 144].

The amount of defects in the sample φ can be calculated by multiplying the amorphous phase fraction with the amount of defects in the amorphous phase φ_{am} .

$$\varphi = \varphi_{am} \cdot f_a \quad (\text{A.9})$$

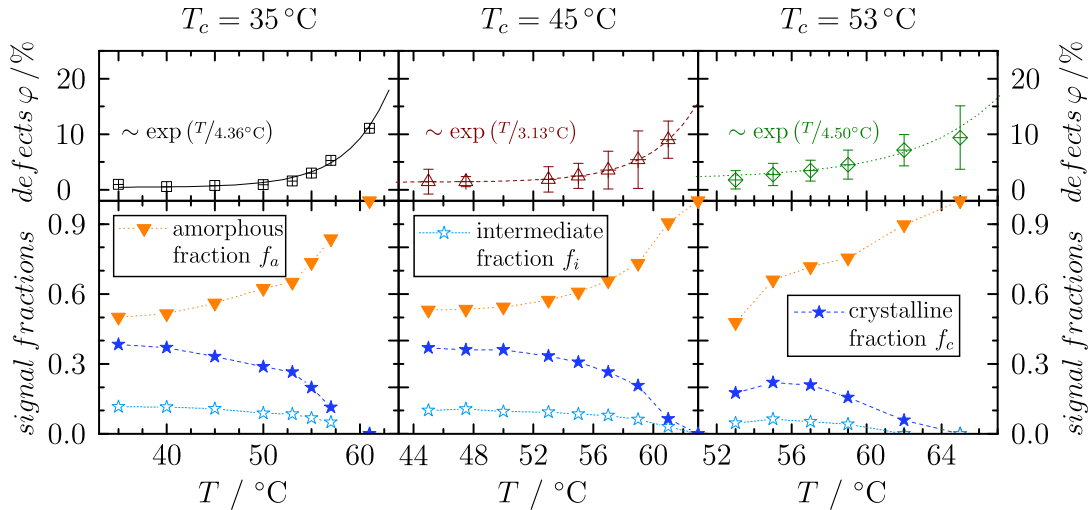


Figure A.3: Temperature-dependent amount of elastically inactive (isotropically mobile) defects φ in PCL samples crystallized at 35, 45 and 53 °C (top) and the volume fractions of the amorphous (orange, upside down triangle), intermediate (light blue, open star) and crystalline (blue, closed star) phase.

The amount of defects in the amorphous phase is derived from the tail-fit in the DQ analysis and is for most temperatures approximately 1-2%. The signal arises from the highly mobile chain ends terminating in the amorphous phase. Close to and above the final melting temperature the amount of defects increases exponentially. This is caused by the higher amount of molten chain ends which terminated in the now molten crystal or crystal surface as well as the increased thermal motion. The dotted and dashed lines in Figure A.3 are the corresponding fits.

Oligomer PCL2.2 The pure oligomer sample crystallized at 35 and 45 °C shows a similar behavior with decreasing crystallinity for increasing crystallization temperature. However, the crystallinity is 20% higher at 35°C than in the pure polymer PCL sample and $\sim 10\%$ higher at 45°C. The intermediate fraction has a similar value as in PCL200 of $\sim 10 - 13\%$. It is assumed that the lamellae formed by the oligomers consist of extended chains (without folds) having a chain tilt of approximately 43° and a defined crystal thickness [145] as shown in the schematic illustration in Figure A.4 B. Additionally, no entanglements are present in the amorphous phase, due to the low molecular weight. Thus, the amorphous phase consists of non-crystallized oligomer chains $X_{non}^{oligomer}$ and dangling chain ends $X_{dce}^{oligomer}$ from the partial crystalline oligomer chains.

$$f_a = X_{non}^{oligomer} + X_{dce}^{oligomer} \quad (\text{A.10})$$

The amount of non-crystallized oligomer chains $X_{non}^{oligomer}$ is equal to the measured amount of defects in the amorphous phase φ_{am} . The temperature-dependent signal

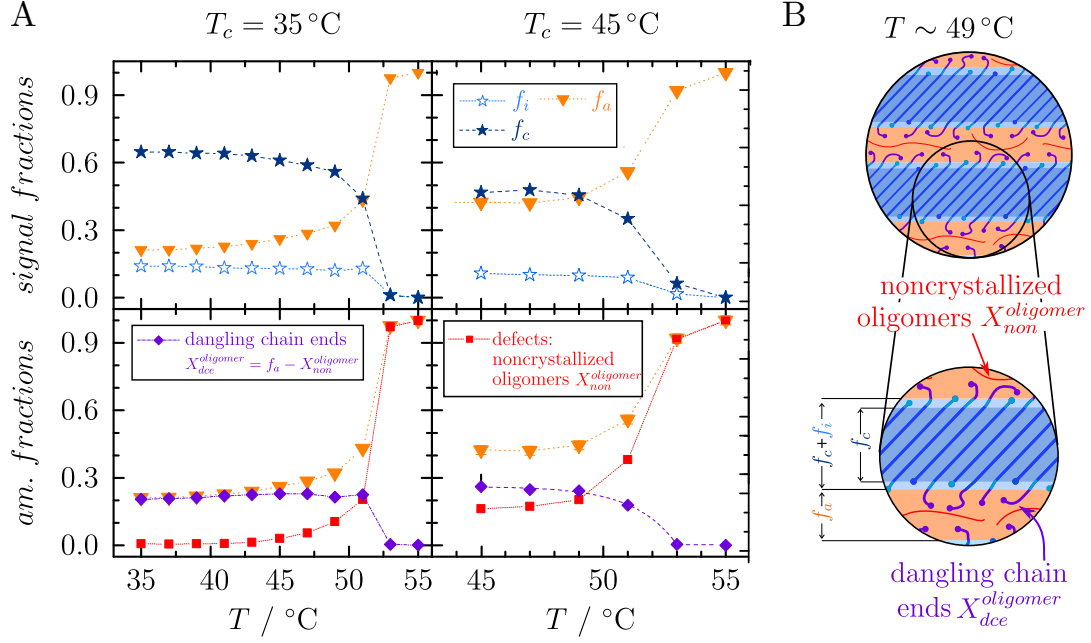


Figure A.4: A) *Top row*: temperature-dependent fractions of the amorphous (orange, upside down triangle), intermediate (light blue open star) and crystalline (blue, closed star) signal fraction of the pure oligomer crystallized at 35°C and 45°C (top). *Bottom row*: composition of the amorphous fraction, with non-crystallized oligomers (red squares) and dangling chain ends (purple diamonds). B) Schematic illustration of the crystalline-amorphous three-phase system at approximately 49°C , with an enlargement showing all five signal contributions.

fractions and the deconvolution of the amorphous phase fraction into non-crystallized oligomer and dangling chains ends are shown in Figure A.4 A. For higher crystallization temperatures the amount of non-crystallized oligomers is larger, resulting in an overall lower rigid (crystalline plus intermediate) fraction $f_{rigid}^{oligomer}$.

For a quantitative analysis, the volume fraction of oligomer chains within the crystalline lamellae, $f_{rigid}^{oligomer}$, is compared to the amount of chains that contribute to the crystalline structure. The latter describes the amount of constrained oligomer chains and is the sum of the rigid fraction and the dangling chain ends, with $X_{con.}^{oligomer} = f_{rigid}^{oligomer} + X_{dce}^{oligomer}$. The volume fraction of oligomers in the lamellae $\chi_{lamellae}^{oligomer}$ is given by

$$\chi_{lamellae}^{oligomer} = \frac{f_{rigid}^{oligomer}}{X_{con.}^{oligomer}} = \begin{cases} 77.5\% & \text{for } T_c = 35^\circ\text{C} \\ 70.0\% & \text{for } T_c = 45^\circ\text{C} \end{cases} \quad (\text{A.11})$$

The percentage of oligomer chains in the lamellae can be averaged to $74 \pm 4\%$.

Entanglement density in a oligomer-diluted PCL melt

Rheology experiments performed on oligomer/polymer mixtures [145] show that the dependence of the disentanglement time τ_D on the oligomer content $\Phi^{oligomer}$ fulfills the power law for a good solvent: $\tau_D \sim (1 - \Phi^{oligomer})^{1.6}$ [15]. Thus, the PCL oligomer can be regarded as a good solvent for PCL200. This is expected, since the oligomer should be an athermal solvent with only excluded volume repulsion. The entanglement time τ_e also depends on the concentration of the used solvent, since the oligomer has a lower T_g and thus acts as plasticizer. The upper and lower limits of τ_e , necessary for the back-extrapolation of the residual dipolar coupling of the oligomer-diluted PCL melt, can be calculated via [15]

$$\tau_e \sim (1 - \Phi^{oligomer})^{-2.3} \quad (\text{A.12})$$

using $1.4 \cdot 10^{-3}$ and $1 \cdot 10^{-4}$ (derived in chapter A.1 of the appendix) as starting values

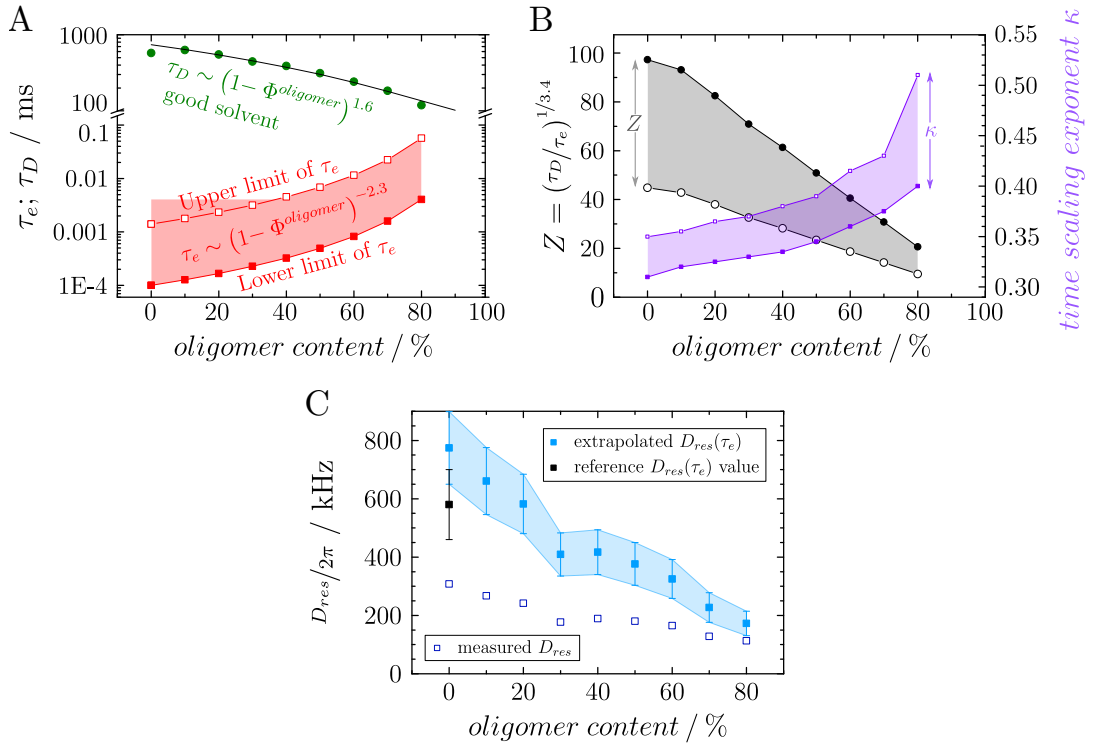


Figure A.5: A) Dependence of the disentanglement times τ_D (measured, green circles) and the upper and lower limit of τ_e (calculated; closed and open red circles) on the oligomer content. B) Calculated number of entanglements strands Z (open and closed black circles) and the corresponding time scaling exponents κ (open and closed violet squares) according to references [109, 136, 141]. C) Measured (blue open squares) and back-extrapolated residual dipolar couplings (bright blue, closed squares) of polymer/oligomer mixtures up to 80 % oligomer dilution, measured in the melt at 53 °C. The black square for zero oligomer content indicates the reference value of the residual dipolar coupling as derived in chapter A.1.

for the upper and lower limits of the entanglement time. The τ_D - and τ_e -dependencies are shown in Figure A.5. For the back extrapolation of the residual dipolar coupling at τ_e , the time scaling exponent κ , which depends on the number of entanglements strands Z in the high- M_w PCL, is needed. By rearranging equation A.2, the values for Z can be derived and allow to assign the corresponding κ -values [109, 136, 141]. Both dependencies on the oligomer concentration are shown in Figure A.5 B.

Double-quantum measurements in the melt were performed on all polymer/oligomer mixtures and the pure samples. In the molten oligomer, the isotropic motions averages the dipolar coupling to zero. Results for the 10/90 mixture could not be analyzed, since the detected I_{DQ} -intensity was too low. The determined and back-extrapolated residual dipolar couplings are presented in Figure A.5 C. The back-extrapolated values display a pronounced decrease for increasing oligomer content. Thus, the oligomer-dilution of long chain PCL results in the expected reduction of the entanglement density in the melt prior to crystallization.

In the following part the impact of the reduced entanglement density on the crystallization of polymer/oligomer mixtures is discussed.

Simultaneous and co-crystallization in oligomer-diluted PCL

The PCL polymer/oligomer mixtures were crystallized at 35, 45 and 53 °C. The temperature-dependent crystalline fractions are shown for all crystallization and measurement temperatures in Figure A.6. Please note, that the intermediate fraction, which is not shown here, is similar for all samples and temperatures with $f_i \sim 0.1$. The transverse relaxation time $T_{2,i}^* \approx 20 - 30 \mu\text{s}$ indicates, that the intermediate phase is rigid. The crystalline fraction increases upon oligomer-dilution by $\sim 25\%$ at $T_c = 35^\circ\text{C}$ and by $\sim 15\%$ at $T_c = 45^\circ\text{C}$, respectively. At $T_c = 53^\circ\text{C}$, the crystalline fractions are similar, but with a lower melting point for higher dilutions. In general the crystalline fraction decreases with increasing crystallization temperature and increases with higher oligomer content.

The polymer and oligomer component are capable of crystallizing, and thus, the detected crystalline fraction is the sum of both components. To determine the crystalline fraction of polymer and oligomer separately, several parameters of the pure samples can be used: the temperature-dependent amount of defects in the pure polymer sample $\varphi^{\text{polymer}}(T)$ and the percentage of oligomer chains within a crystal lamellae, $\chi_{\text{lamellae}}^{\text{oligomer}} = 74\%$. The amount of non-crystallized oligomer chains, $X_{\text{non}}^{\text{oligomer}}$, in the mixtures can be calculated by subtracting the temperature-dependent amount of defects of the pure polymer sample, φ^{polymer} (as shown in Figure A.3), multiplied with the polymer weight fraction Φ^{polymer} , from the detected amount of defects in

A.2 Effects on crystallization and entanglement density caused by oligomer dilution of poly(ϵ -caprolactone)

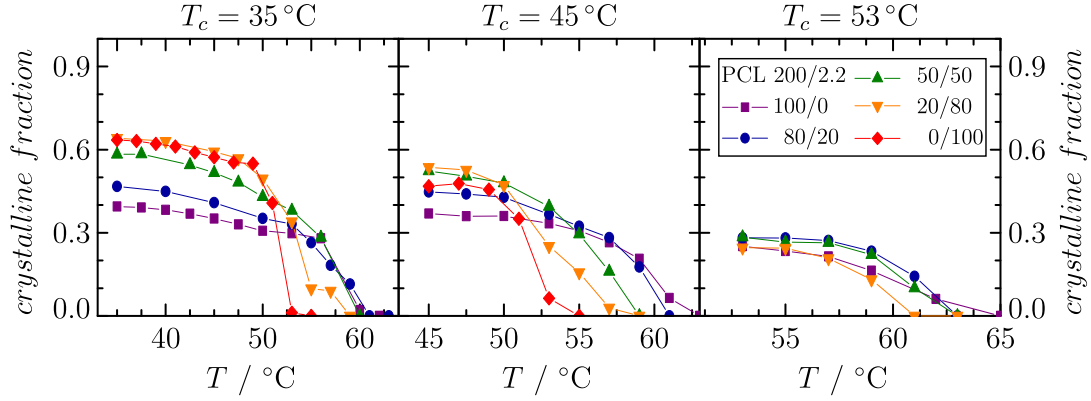


Figure A.6: Temperature dependent crystalline fractions of the pure oligomer and polymer as well as the 80/20, 50/50 and 20/80 composition, crystallized at 35, 45 and 53 °C.

the mixtures $\varphi^{mixture}$

$$X_{non}^{oligomer} = \varphi^{mixture} - \Phi^{polymer} \cdot \varphi^{polymer}(T) \quad (A.13)$$

The amount of constrained oligomer chains is then given by

$$X_{con.}^{oligomer} = \Phi^{oligomer} - X_{non}^{oligomer} \quad (A.14)$$

with $\Phi^{oligomer}$ describing the oligomer weight fraction. Under the assumption that the percentage of the oligomer chains within the lamellae, $\chi_{lamellae}^{oligomer}$, does not change in the mixed samples, one can calculate the rigid fraction of the oligomer, $f_{rigid}^{oligomer}$, via

$$\begin{aligned} f_{rigid}^{oligomer} &= X_{con.}^{oligomer} \cdot 0.74 \\ rel. f_{rigid}^{oligomer} &= \frac{f_{rigid}^{oligomer}}{\Phi^{oligomer}} \end{aligned} \quad (A.15)$$

The relative fraction $rel. f_{rigid}^{oligomer}$ yields the percentage of oligomer within a rigid environment and allows for a better comparison of different mixing ratios. The crystalline fraction of the PCL200 component is given by the difference of the rigid fraction of the mixture $f_c + f_i$ (determined by the 1H FID analysis) and $f_{rigid}^{oligomer}$

$$\begin{aligned} f_{rigid}^{polymer} &= f_c + f_i - f_{rigid}^{oligomer} \\ rel. f_{rigid}^{polymer} &= \frac{f_{rigid}^{polymer}}{\Phi^{polymer}} \end{aligned} \quad (A.16)$$

The percentage of constrained oligomer chains in the the PCL mixtures for all crystallization temperatures are shown in Figure A.7. The amount of constrained oligomers exceeds 85% for the two lower crystallization and measurement temperatures, reveal-

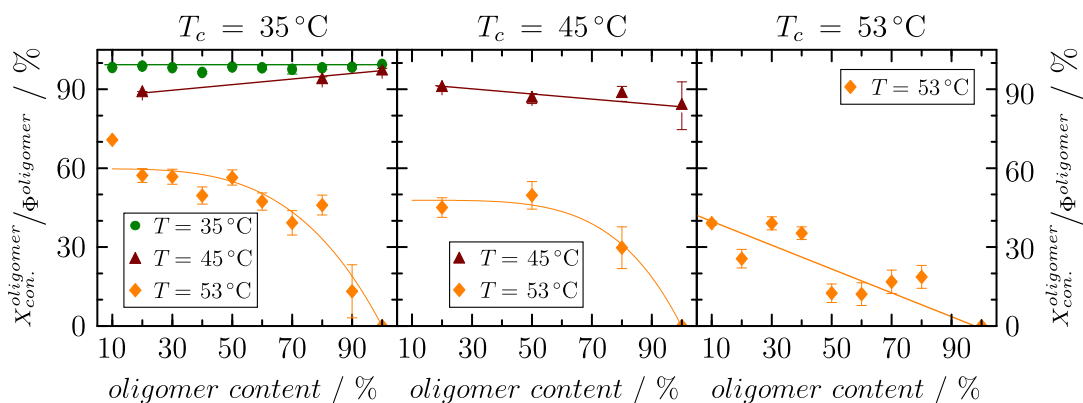


Figure A.7: The percentage of constrained PCL oligomers in a given polymer/oligomer mixture, which were crystallized at 35 °C (left), 45 °C (middle) and 53 °C (right). For crystallization and/or measurement temperatures below 53 °C, more than 80 % of the oligomer chains in the mixtures are part of the crystalline structure. Heating to or crystallizing at 53 °C reduces this amount.

ing that nearly all oligomer chains in the blend participate in the formation of the lamellae. Crystallizing at or increasing the temperature to 53 °C reduces the amount of constrained oligomers, since pure oligomer crystals are molten at this temperature. However, a considerable proportion of oligomers remains in a crystalline environment, indicating the formation of shared polymer/oligomer crystals.

Based on this analysis the (relative) rigid fractions of the oligomer and polymer content in the mixtures can be calculated. The results are shown in Figure A.8. For mixtures crystallized at 35 °C the rigid fractions of PCL2.2 increase linearly, while the rigid fractions of PCL200 decrease upon dilution. The relative rigid fractions of the oligomer is constant at 70 % over the complete composition range, whereas the relative rigid fractions of the polymer increase for a higher oligomer content. The error for $rel. f_{rigid}^{polymer}$ also increases strongly with decreasing polymer content. Step-wise heating to 45 °C reduces the overall crystallinity by approximately 10 %, whereby $rel. f_{rigid}^{oligomer}$ and $rel. f_{rigid}^{polymer}$ are both slightly reduced. At 53 °C pure oligomer crystals are molten. The overall crystallinity of the sample is nearly constant at ~ 40 % up to 80 % oligomer dilution. The crystalline fraction has contributions of both, polymer as well as oligomer. The remaining oligomer crystalline fraction of the oligomers must arise from shared polymer/oligomer crystals.

A nearly similar trend, but with a reduced crystallinity, can be seen for the polymer/oligomer mixtures crystallized and measured at 45 °C. The relative oligomer rigid fractions lie between 60 and 65 %. Heating to 53 °C reduces the crystalline fraction, but a certain amount of oligomer chain remain crystalline.

At 53 °C all samples, independent of T_c , have a similar crystalline fraction and dependence on the oligomer content. However, the presence of a rigid PCL2.2 fraction at 53 °C reveals the existence of mixed polymer/oligomer crystals. The amount of

A.2 Effects on crystallization and entanglement density caused by oligomer dilution of poly(ϵ -caprolactone)

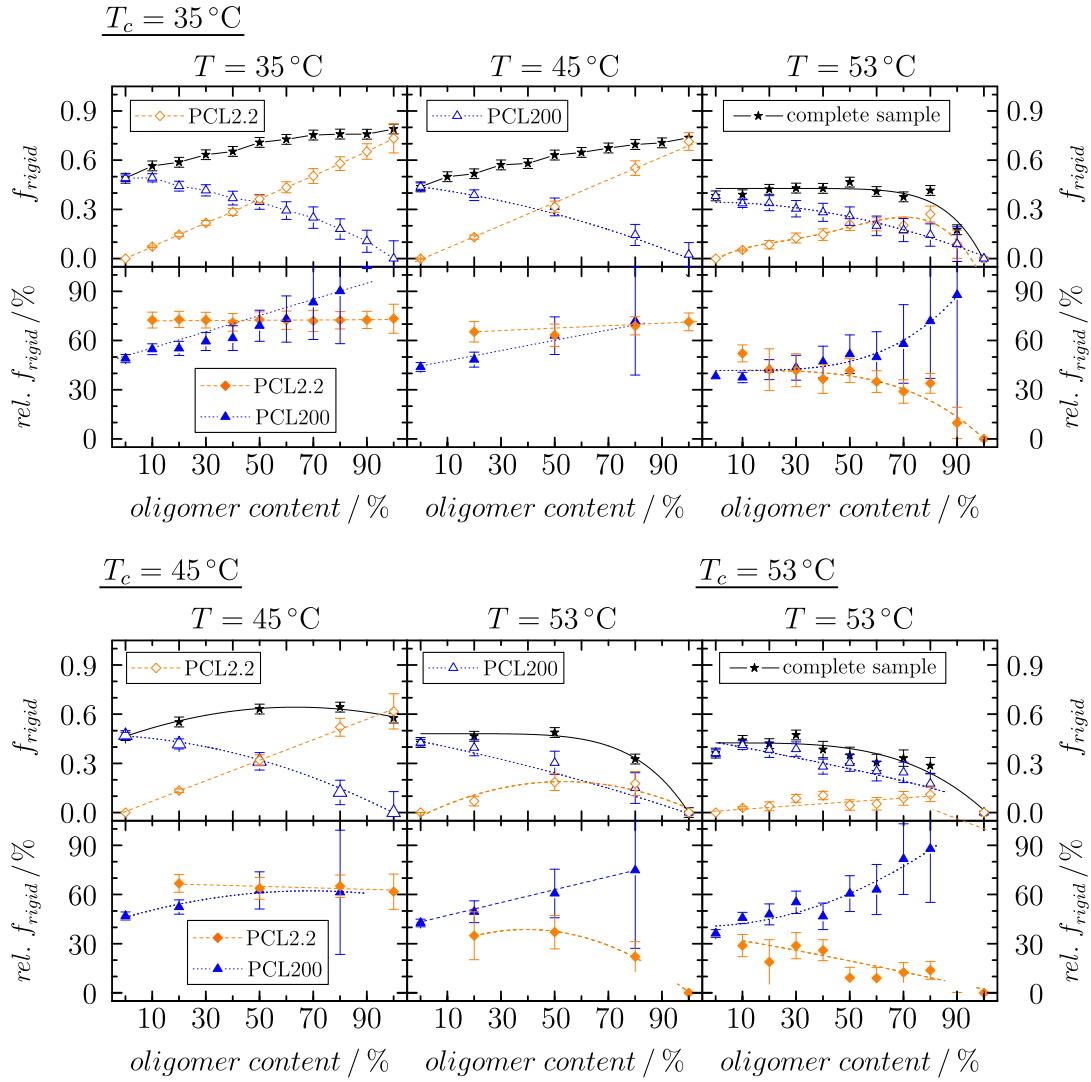


Figure A.8: PCL polymer/oligomer mixtures crystallized at 35 (top), 45 and 53 °C (bottom). In each graph the top rows depicts the measured rigid (crystalline + intermediate) fraction f_{rigid} (black stars) as well as the calculated rigid fractions of the polymer (blue, open triangles) and oligomer (orange, open diamonds) for all mixtures, respectively. The bottom row shows the calculated relative rigid fractions $rel. f_{rigid}$ of PCL200 (blue, closed triangles) and PCL2.2 (orange closed diamonds).

oligomer in a mixed crystal are higher for lower crystallization temperatures. Even for temperatures T above 53 °C a rigid oligomer fraction is detectable and supports the assumption of mixed crystals. These temperature-dependent results of the 80/20, 50/50 and 20/80 mixtures, which were crystallized at at 35, 45 and 53 °C are shown in Figure A.9.

In all investigated mixtures crystallized at $T_c = 35$ and 45 °C more than 90 % of the oligomer chains are partially crystalline at the crystallization temperature. The amount of constrained PCL chains start to decrease for $T \geq 45$ °C and reaches zero close to the melting temperature of the mixed sample, which is $\sim 3 - 7$ degree higher than the melting temperature of pure oligomer crystals $T_{melt}^{oligomer} = 53$ °C (drawn

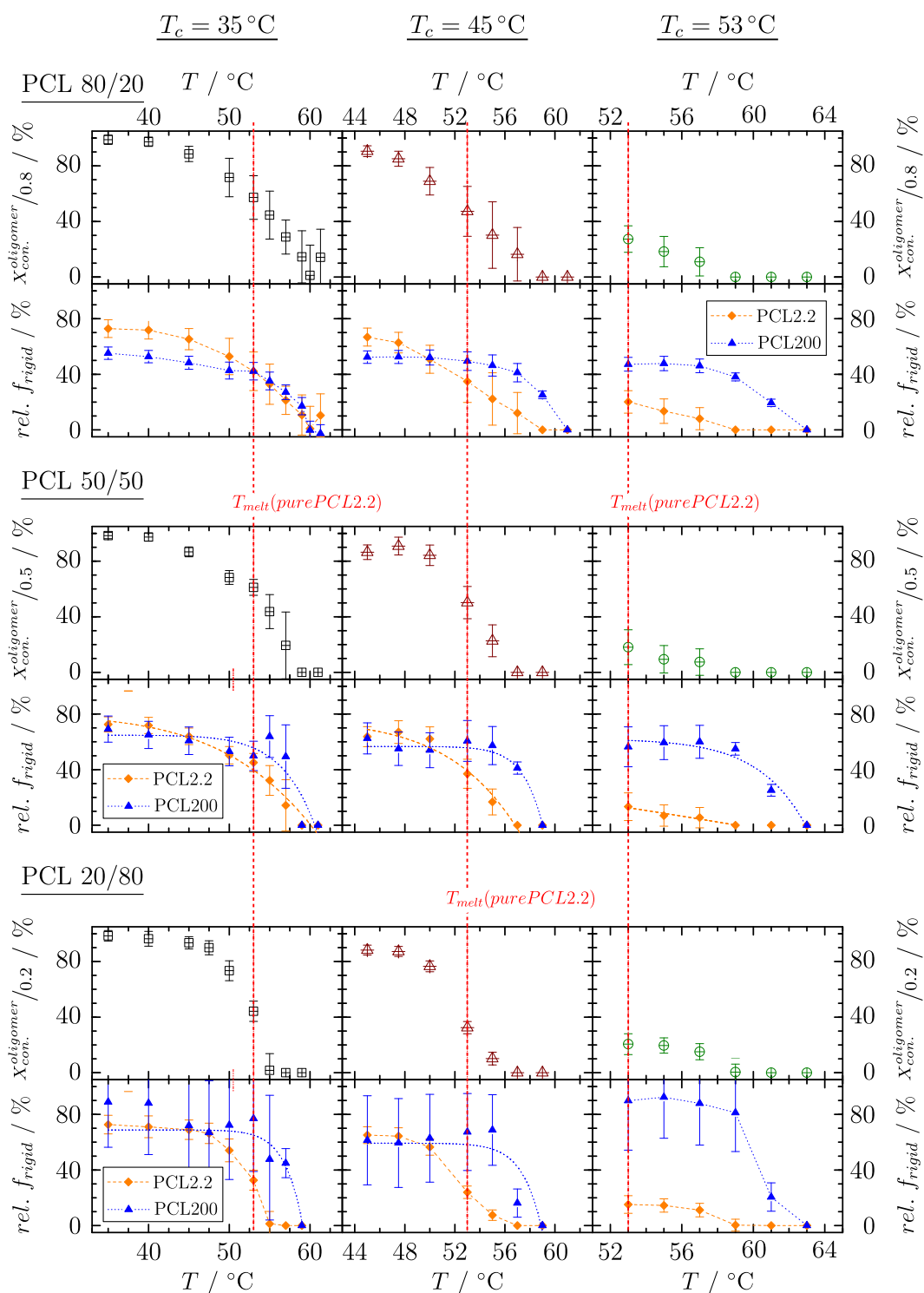


Figure A.9: Top: PCL 80/20; middle: PCL 50/50 and bottom PCL 20/80. In each graph the top row shows the temperature-dependent amount of constrained oligomer chains $X_{con}^{oligomer}$ crystallized at 35, 45 and 53 °C (from left to right), respectively. The bottom row show the calculated relative rigid fractions f_{rigid} , of oligomer (orange diamonds) and polymer (blue triangles). The red dashed-dotted line in each graph at 53 °C indicates the melting temperature of pure oligomer crystals. Error bars arise from fitting uncertainties (defects) and propagation of uncertainty (relative rigid fraction). The orange, dashed and blue, dotted lines serve as guide to the eye.

as a dashed red line in Figure A.9). At 53 °C approximately 30 % (PCL 20/80, $T_c = 45$ °C,) to 60 % (PCL 80/20, $T_c = 35$ °C,) of the oligomer chains remain in a crystalline environment. Mixtures crystallized at 53 °C have a lower amount of constrained oligomer chains, with $\sim 20 - 30$ % at the crystallization temperature. The amount of constrained oligomer chains decreases gradually during heating. In general, the mixture melting temperatures are lower for higher oligomer concentrations. Nonetheless, for all mixtures and crystallization temperatures at least 20 % of the oligomer chains remain in a crystalline environment at 53 °, where pure oligomers are molten.

The relative rigid fraction of PCL2.2 follows a similar temperature-dependence as the amount of constrained oligomer chains, starting at 70 to 80 % for $T_c = 35$ and 45 °C and 10 to 20 % for $T_c = 53$ °C followed by a gradual reduction upon heating. The relative rigid fraction of the long-chain polymer is, within the error, constant at 50 to 60 % for all crystallization temperatures and mixtures in the relevant temperature range. The error for f_{rigid}^{PCL200} is rather high in the 20/80 mixture, which is caused by the low polymer content. Nonetheless, the calculated values follow the same trend as the other two mixtures.

In the crystallized oligomer, a residual dipolar coupling in the amorphous phase is detected, even though no entanglements are present. The coupling is caused by anisotropic motions of the dangling chain ends. In the polymer/oligomer mixtures it is not possible to distinguish between couplings arising from dangling (oligomer) chain ends or entanglements of the long polymer chains. This prevents an analysis of the polymer/oligomer mixtures with regard to their entanglement density or a possible entanglement enhancement. However, the amorphous thickness d_a is always larger [143, 144] than the estimated tube diameter of 3.9 nm [72] and thus the condition for an investigation of the entanglements in the amorphous phase would be fulfilled.

A.3 Effect of the crystallization conditions on the pseudo-eutectic behavior in statistical PBSA copolyesters

Random isodimorphic copolyesters display a pseudo-eutectic behavior in a material-dependent composition range. In the pseudo-eutectic range both comonomer units can form separate coexisting crystals. Pérez-Camargo et al. [26] report, that in the complete composition range of the random, isodimorphic copolymer, poly(butanediol-succinate/butanediol-adipate) (PBSA), the inclusion or exclusion of co-units is influenced by the crystallization condition, e.g. cooling rate.

Here, the effect of different cooling rates on the crystallization of PBSA copolymers in the pseudoeutectic range, PBSA 50/50 and 40/60, is investigated with ^1H FID analysis

and ^{13}C T_1 relaxation studies. The copolymers are named after their BS/BA fractions. The samples were cooled from the melt to -40°C (^1H FID analysis) and $\sim -20^\circ\text{C}$ (^{13}C relaxation studies) with cooling rates of less than 2 K/min (slow), approximately 5 K/min (intermediate) and faster than 20 K/min (fast). Proton FID measurements were performed using step-wise heating. Torchia experiments, used to determine the ^{13}C T_1 relaxation times, were performed at 6 and 30°C for the 50/50 composition and 6 and 40°C for PBSA 40/60, respectively. The difference in the minimum temperatures for both techniques is caused by the experimental setup.

The obtained results will be compared to the published findings on the asymmetric inclusion of co-units in the copolymers PBSA 20/80 and 60/40, presented in chapter 4.2. The published results were obtained on PBSA copolymers with composition on either side of the pseudoeutectic range, where only one crystalline phase (BA- or BS-rich) is formed. It was found that BA-units are excluded from the bulk BS-crystal, whereas the BS-units are included into the BA-rich crystal. An investigation on PBSA 40/60 and 50/50 focusing on a possible inclusion of co-units is more complicated, since both crystalline structures coexist.

FID analysis

The cooling rate dependent signal fractions (crystalline: red stars; intermediate green circles; amorphous: violet triangles) of PBSA 50/50 and 40/60 are shown in Figure A.10. Both samples display a two-step melting, independent from the applied cooling rate. For temperatures around 0°C , the crystalline fractions develop a “plateau”-like region (highlighted in blue) with slowly decaying crystalline fractions. This overall crystallinity arises from the sum of BA- and BS-rich crystals. An exception to this behavior is observed for the 50/50 composition after slow cooling. For this sample no plateau-like region around 0°C is detected. Increasing the temperature results in the first sequential melting of BA-rich crystals and potentially of smaller, less stable BS-rich crystals. In this temperature range, the crystalline signal fraction decreases more significantly. This first melting step is followed by a second “plateau”-like region (highlighted in orange), whose signal arises from BS-rich crystals. A further increase of the temperature results in the final melting. For both composition the intermediate fraction is independent on the cooling rate and reaches a rather high value with approximately 15 to 20%. The dependence of the overall crystalline (and thus also on the amorphous fraction) on the cooling rate is differently pronounced for the two samples.

In Table A.2 the results of the FID analysis are summarized and the overall crystallinity as well as the fractions arising from BA-rich and BS-rich crystals are listed. The crystalline fractions of BA-rich crystal are given by the difference of the overall

A.3 Effect of the crystallization conditions on the pseudo-eutectic behavior in statistical PBSA copolyesters

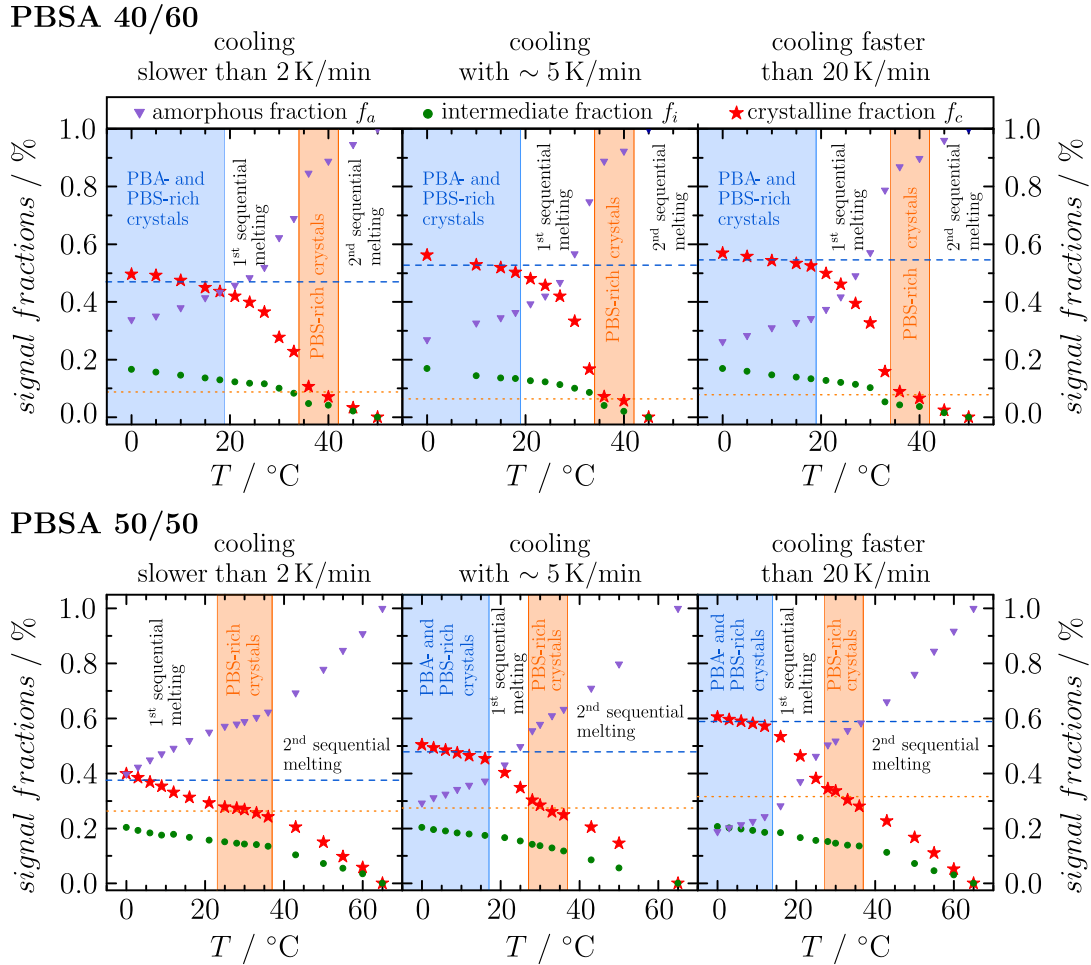


Figure A.10: Temperature-dependent amorphous (violet triangles), intermediate (green circles) and crystalline (red stars) fractions of PBSA 40/60 (*top*) and PBSA 50/50 (*bottom*). The applied cooling rates range from slow (<2 K/min), intermediate with ~ 5 K/min to fast (> 20 K/min). Temperature ranges, where BA- and BS-rich crystals coexist are highlighted in blue. After the first sequential melting only BS-rich crystals remain, these regions are highlighted in orange.

Table A.2: Detected and calculated crystallinities of BS- and BA-rich crystals of PBSA 40/60 and 50/50. The crystalline fractions are determined by the average values in the highlighted temperature ranges shown in Figure A.10. The amount of BA-rich crystals is given by the difference of the overall crystallinity and the amount of BS-rich crystals. The error of the crystallinities is the standard deviation of the calculated averages.

cooling rate	BA and BS-rich crystals	BA-rich crystals	BS-rich crystals
40/60			
<2 K/min	47.0 ± 2.6	38.2 ± 5.1	8.8 ± 2.5
5 K/min	52.8 ± 2.6	46.4 ± 3.6	6.4 ± 1.0
>20 K/min	54.6 ± 1.8	46.8 ± 3.4	7.8 ± 1.6
50/50			
<2 K/min	36.7 ± 2.0	10.3 ± 4.2	26.3 ± 1.5
5 K/min	47.9 ± 1.9	20.5 ± 4.4	27.4 ± 2.5
>20 K/min	58.9 ± 1.3	27.3 ± 4.3	31.6 ± 3.0

crystallinity and the fraction of BS-rich crystals detected after the first sequential melting. In this calculation it is assumed that only BA-units melt during the first sequential melting process. The loss of crystalline signal caused by the melting of (potentially) included BS-units in the BA-rich crystals or of small, less stable BS-crystals cannot be accounted for.

The overall crystallinity of the 40/60 composition increases only slightly from 47 to 55 (volume) percent upon higher cooling rates. BA-rich crystals melt in the temperature range between 18 and 35 °C. The remaining signals of the BS-rich crystals are, within the error margins, constant at $7.6 \pm 1.2\%$ for all cooling rates.

In the 50/50 composition the dependence of the overall crystallinity and the BS-rich crystalline fraction on the cooling rates is more pronounced. For cooling rates with less than 2 K/min the lowest overall crystallinity is detected. Additionally, the crystalline fraction does not develop a “plateau”-like region for the BA and BS-rich crystals. Instead, it decreases steadily from $\sim 37\%$ at 0 °C upon heating, until the plateau-like region of the BS-rich crystals, in the temperature range from 23 to 37 °C, are reached. For faster cooling rates the overall crystallinity increases from $\sim 48\%$ for cooling with 5 K/min to $\sim 59\%$ for fast cooling. For both cooling rates a “plateau”-like region in the temperature range, where BA and BS-rich crystals coexist, is detected. Again, the crystalline signals arising from the BS-rich crystals depend only slightly on all applied cooling rates and increases from $\sim 26\%$ to $\sim 32\%$ upon faster cooling.

It seems that the change of the cooling rates mainly affects the crystallization of BA-rich crystals, which crystallize after the formation of BS-rich crystals. In the following, this assumption will be further analyzed via ^{13}C T_1 relaxation studies.

^{13}C T_1 relaxation studies

^{13}C T_1 relaxation studies were performed on both samples for fast and slow cooling; the intermediate case with a cooling rate of 5 K/min was not investigated. The intensity decay of ^{13}C T_1 -filtered MAS CP spectra are used to identify crystalline or immobilized regions of both comonomer units, similar to the relaxation studies used in chapter 4.2. The cross polarization times were set to 100 μs , thus only signals from intermediate and crystalline regions are detected. Signals arising from crystalline phases are characterized by relaxation times longer than $\sim 10\text{s}$, relaxation times of an intermediate phase have values of a few seconds. Even faster relaxations are characteristic for mobile regions. Temperature-dependent spectra of fast and slow cooled PBSA 40/60 and 50/50 with a 5 s T_1 -filter are shown in Figure A.11. A difference in the chemical shifts of both comonomers allows to separately analyze the BA (*A* resonance at ~ 34.5 ppm) and BS (*S* resonance at ~ 29.5 ppm) signals.

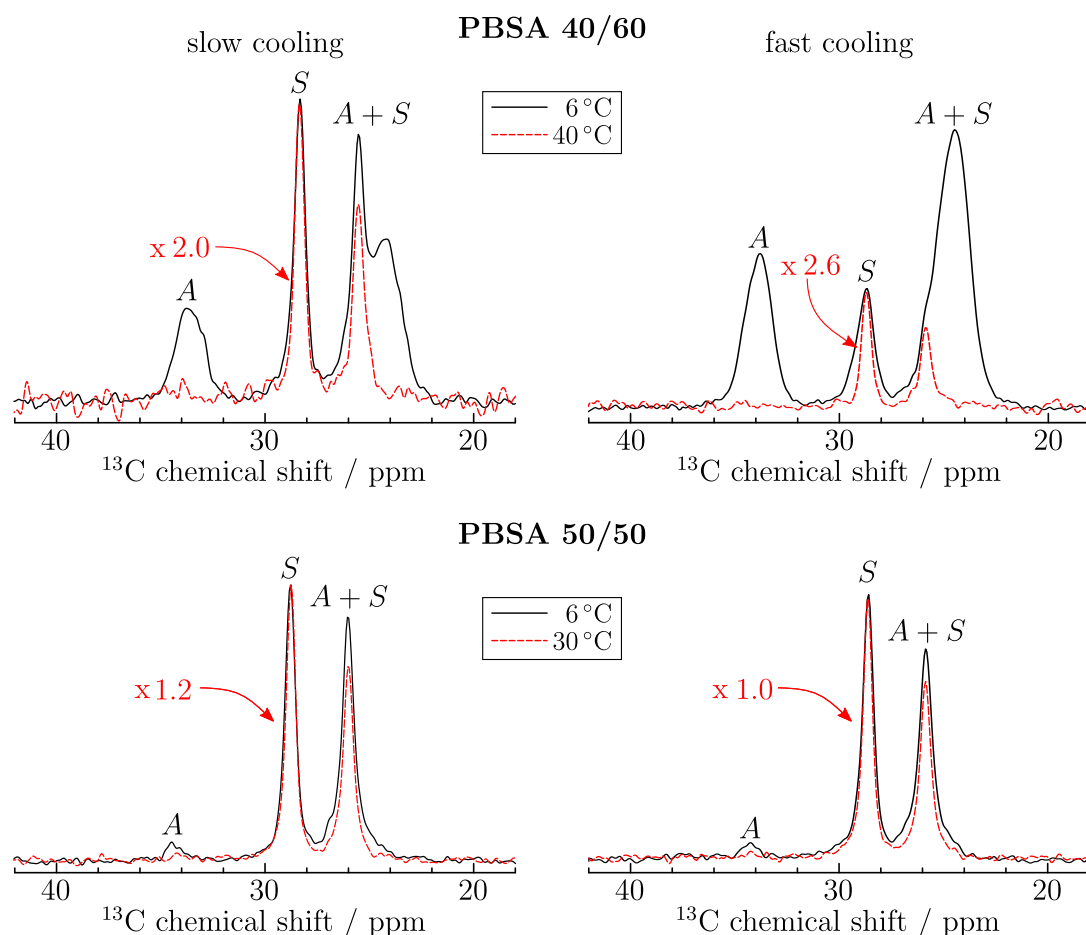


Figure A.11: ^{13}C MAS $100\ \mu\text{s}$ -CP spectra after a $5\ \text{s}$ T_1 -filter. *Top*: spectra of PBSA 40/60 detected at $6\ ^\circ\text{C}$ (black line) and $40\ ^\circ\text{C}$ (red dashed line) after slow (*left*) and fast (*right*) cooling. *Bottom*: spectra of PBSA 50/50 detected at $6\ ^\circ\text{C}$ (black line) and $30\ ^\circ\text{C}$ (red dashed line) after slow (*left*) and fast (*right*) cooling. The spectra detected at the elevated temperature are scaled by factor, as indicated for each spectra.

The spectra were detected at temperatures within the two “plateau”-like regions determined with the FID analysis. This allows a conclusion about a possible co-unit inclusion.

The ^{13}C MAS CP spectra of PBSA 40/60 (Figure A.11 *top*), obtained after slow and fast cooling at $6\ ^\circ\text{C}$ (BA and BS-rich crystals) and $40\ ^\circ\text{C}$ (only BS-rich crystals), show a clear difference. For slow cooling the S resonance has a much higher intensity than the A peak, indicating that a higher amount of BS-units is in a crystalline environment. At $40\ ^\circ\text{C}$, BA-rich crystals are molten and no rigid A resonance is detected and the intensity of the S resonance is reduced. After scaling the $40\ ^\circ\text{C}$ spectrum by a factor of two, one clearly sees that the overall shape of the S resonance is similar for both temperatures. This is an indication for exclusion or very limited incorporation of BS-units in the BA-rich crystals, since the included BS-units would resonate at a slightly different chemical shift as shown in chapter 4.2. The spectra detected after fast cooling, reveal that more BA than BS-units are crystalline

at 6 °C. This could be explained by a higher amount of included BS-units in the BA-rich crystals. This is supported by the broader *S* resonance at 6 °C as compared to the scaled 40 °C spectrum.

The determined relaxation times and the amplitudes, obtained from the Torchia experiments, are listed in Table A.3. Signals associated with a crystalline phase are printed in bold. The amplitudes are normalized such that the intensity of the combined *A* and *S* resonances are equal to one. At 6 °C, the longitudinal relaxation times associated with a crystalline phase of BA and BS-units in the 40/60 composition range between 21.5 s and 43.6 s. This reveals that both comonomers are in a crystalline environment. For slow cooling both crystalline T_1 times are longer. Relaxation times in the range of a few seconds are attributed to segments with an intermediate mobility. After heating to 40 °C, the relaxation times of the *A* resonances indicate an intermediate mobility for all BA-units, whereas a certain amount of BS-segments remain in a crystalline environment but without BA co-unit inclusion.

The results on PBSA 40/60 are in agreement with the findings presented in chapter 4.2. No crystalline *A* resonance and intermediate relaxation for the elevated temperature suggest that BA-units are excluded from the BS-crystals. Indications for a more pronounced BS co-unit inclusion in BA-rich crystals under fast cooling is given by the differences of the temperature-dependent spectra as well as a higher BA crystalline fraction in comparison to slow cooling.

In PBSA 50/50 the relaxation times of the *S* resonance at 6 °C exceed 20s for both cooling rates, whereas the relaxation times of the *A* resonance are lower with

Table A.3: Amplitudes *A* and longitudinal relaxation times T_1 obtained from the intensity decay detected with the Torchia pulse sequence.

^a Error: ± 0.05 , ^b Error: 10-20 %

	slow cooling				fast cooling			
	<i>S</i> resonance		<i>A</i> resonance		<i>S</i> resonance		<i>A</i> resonance	
	<i>A</i> ^a	T_1 / s						
40/60	0.30 0.20	37.5^b 2.25	0.20 0.30	43.6^b 1.4	0.25 0.18	21.5^b 0.60	0.44 0.13	27.9^b 0.55
40 °C	0.45 0.20	17.2^b 0.12	0.02 0.33	22.2^b 0.31	0.58 0.03	15.0^b 0.16	0 0.07	- 1.08
50/50	0.42 0.25	52.2^b 1.21	0.05 0.28	6.1 0.70	0.40 0.24	23.0^b 0.82	0.03 0.17	13.0^b 1.22
30 °C	0.40 0.24	55.0^b 1.21	0 0.08	- 1.91	0.47 0.17	18.4^b 0.64	0 0.14	- 1.51
			0.28	0.26			0.22	0.23

6.1 s for slow and 13.0 s for fast cooling. In the latter case, the crystallization of BA-rich crystals may not be complete. According to DSC results [146] the sample needs to be cooled to $-40\text{ }^{\circ}\text{C}$ for a complete crystallization of BA-rich crystals. In the Torchia experiments the sample was only cooled to $-20\text{ }^{\circ}\text{C}$. This could explain the low relaxation times and the small amplitude of BA-rich crystals. In the FID experiments the minimum temperature was $-40\text{ }^{\circ}\text{C}$, therefore the crystallization of BA-rich crystals can be assumed to be complete. The detected relaxation times at $30\text{ }^{\circ}\text{C}$ display an intermediate mobility for the BA-units, whereas BS-units remain crystalline. No indication for BA co-unit inclusion is given. However, for cooling with less than 2 K/min a minimum temperature of $-20\text{ }^{\circ}\text{C}$ is sufficient for the crystallization of BA-rich crystals. Thus, the low relaxation time could either be attributed to the formation of small BA-crystals or a thickening process of BS-crystals with the formation of BA-units in pocket-like structures, similar to the results of PBSA 60/40 presented in chapter 4.2. Upon heating to $30\text{ }^{\circ}\text{C}$, no crystalline *A* resonance is detected and the BS-units remain crystalline. The ^{13}C spectra of PBSA 50/50 are similar for both cooling rates. Upon heating no *A* resonance is detected. The shape of the *S* resonance remains the same, indicating no or only marginal BS-unit inclusion.

Comparison of ^{13}C T_1 relaxation studies and FID analysis

In Figure A.12 quantitative signal fractions (^1H FID analysis) of the amorphous (f_a), intermediate (f_i) and crystalline f_i phases of fast and slow cooled PBSA 40/60 and 50/50 are illustrated as a bar diagram. Additionally, the crystalline fraction (red bar) is divided into their BA/BS composition according to the FID analysis as well as the results of the ^{13}C T_1 relaxation studies at $6\text{ }^{\circ}\text{C}$. The FID analysis yields signals arising from BS- (orange) and BA-rich (blue) crystals, whereas the Torchia experiments allows the quantification of BS and BA-units within a crystalline phase. This distinction between the detected signals with both methods is important and yield an explanation for the difference in the BA/BS assignment.

The values from Table A.2 are used for the BA/BS assignment in Figure A.12 according to the FID analysis. It is distinguished between BA- and BS-rich crystals. But the fraction of BA-rich crystal also includes the signal of potentially included BS co-units and vice versa. Additional errors, which results in a unrealistically high BA-rich fraction, are caused by a possible partial melting of BS-units during the first sequential melting. Thus, in the FID analysis the amount of BA-rich crystals may be overrepresented. Nonetheless, the FID analysis allows a quantitative determination of the three signal fractions, while ^{13}C CP spectra are only qualitative.

The crystal compositions, determined with the results from the Torchia experiments, are based on the analysis of the ^{13}C CP spectra, where BS and BA units can be

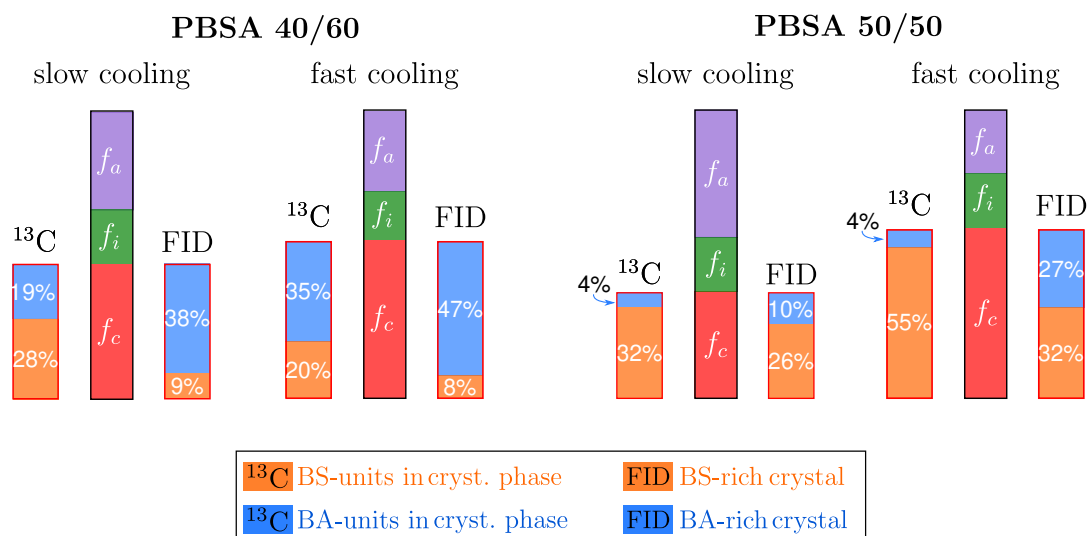


Figure A.12: Bar diagram showing the overall signal composition of slow and fast cooled PBSA 40/60 and 50/50 (at approximately 6°C) into amorphous f_a , intermediate f_i and crystalline f_c fractions, obtained with the FID analysis. The BA/BS assignment of the crystalline fraction are determined with results of the FID analysis and the Torchia method. The FID analysis allows the distinction between BA-rich and BS-rich crystals according to Table A.2. A comparison of the amplitudes associated with a crystalline environment, derived with ^{13}C T_1 relaxation studies at 6°C (Torchia) yields the amount of BA and BS-units in a crystalline environment.

separately evaluated. By comparing the amplitudes, listed in Table A.3, with long T_1 relaxation times the volume fraction of BS and BA-units in a crystalline environment at a given temperature can be estimated. In comparison to the FID analysis a higher amount of BS-units are crystalline when the results of the ^{13}C T_1 relaxation studies are used. This holds true for both compositions and cooling rates.

In summary, the differences of the crystal compositions, as shown in Figure A.12, can be explained by the two applied methods and yields additional insight in the morphology of PBSA copolymers at the pseudoeutectic range. The higher amount of BS-units, determined with the Torchia experiment, is explained by a partial melting of BS-units in a crystal environment during the first sequential melting. It is hypothesized that crystalline BS-units form extended BS-crystals, but may also exist as small crystals or as co-unit inclusion in BA-rich crystals.

The comparison of temperature-dependent spectra allows to assign a BS co-unit inclusion in BA-rich crystals as a relevant factor for the morphology of fast cooled PBSA 40/60. In slowly cooled PBSA 40/60 no indication of co-unit inclusion can be seen in the spectra. Melting of small BS-crystals could explain the differences of the BA/BS crystal assignment. The formation of small BS and BA crystals would also explain the experimental findings of the slowly cooled 50/50 composition. The possible incomplete crystallization of the BA-crystals in fast cooled PBSA 50/50 prevents an evaluation with respect to a BS co-unit inclusion.

The results presented here are in general agreement with the results presented in chapter 4.2, where a BS co-unit inclusion in BA crystals and an exclusion of BA-units from the bulk BS crystal was observed. However, the investigated samples in chapter 4.2 were on either side of and not in the pseudoeutectic range. Additionally, the thermal history of the samples was different. As shown here, the cooling rate has indeed a strong influence on the BS co-unit inclusion in PBSA 40/60. Fast cooling seems to allow for a higher amount of included co-units. In PBSA 50/50 no evidence for a pronounced BS co-unit inclusion was found. However, the detection of a small amount of included BS-units is not feasible since the signal may be too small in comparison to the resonance corresponding to the BS-rich crystals. For neither sample nor thermal history a BA co-unit inclusion in BS-crystals was detected. Thus, the results presented here agree with the already published results.

Bibliography

- (1) Staudinger, H. (1929). Über die Konstitution der hochmolekularen Stoffe. *Naturwissenschaften* 17, 141–144.
- (2) Braun, D., *Kleine Geschichte der Kunststoffe*, 2nd ed.; Hanser: München, 2017.
- (3) Baekeland, L. H. (1909). The Synthesis, Constitution, and Uses of Bakelite. *Macromolecules* 1, 149–161.
- (4) Kaiser, W., *Kunststoffchemie für Ingenieure: Von der Synthese zur Anwendung*, 4th ed.; Carl Hanser Verlag GmbH & Company KG: 2015.
- (5) Andrady, A. L., and Neal, M. A. (2009). Applications and societal benefits of plastics. *Phil. Trans. R. Soc. B* 364, 1977–1984.
- (6) Thompson, R. C., Swan, S. H., Moore, C. J., and vom Saal, F. S. (2009). Our plastic age. *Phil. Trans. R. Soc. B* 364, 1973–1976.
- (7) Staudinger, H. (1955). Über die Grundlagen der makromolekularen Chemie. *Naturwissenschaften* 42, 221–230.
- (8) Mie, G., Hengstenberg, J., Staudinger, H., Johner, H., Lüthy, M., and Signer, R. (1927). Der polymere Formaldehyd, ein Modell der Cellulose. *Naturwissenschaften* 16, 379–380.
- (9) Iwata, T., and Doi, Y. (1999). Crystal structure and biodegradation of aliphatic polyester crystals. *Macromol. Chem. Phys.* 200, 2429–2442.
- (10) Pan, P., and Inoue, Y. (2009). Polymorphism and isomorphism in biodegradable polyesters. *Prog. Polym. Sci.* 34, 605–640.
- (11) Piorkowska, E., and Rutledge, G. C., *Handbook of Polymer Crystallization*, 1st ed.; John Wiley & Sons: Hoboken, New Jersey, 2013.
- (12) Bovey, F. A., and Winslow, F. H. In *Macromolecules, an Introduction to Polymer Science*, Bovey, F. A., and Winslow, F. H., Eds.; Academic Press: New York, 1979; Chapter 1.
- (13) Allegra, G., and Bassi, I. W. (1969). Isomorphism in Synthetic Macromolecular Systems. *Adv. Polymer Sci.* 6, 549–574.

- (14) Natta, G., Corradini, P., Sianesi, D., and Morero, D. (1961). Isomorphism Phenomena in Macromolecules. *J. Polym. Sci.* 51, 527–539.
- (15) Rubinstein, M. and Colby, R., *Polymer Physics*; Oxford University Press: Oxford, 2003.
- (16) Hu, W.-G., and Schmidt-Rohr, K. (1999). Polymer ultradrawability: the crucial role of α_c -relaxation chain mobility in the crystallites. *Acta Polym.* 50, 271–285.
- (17) Ballauff, M. (1989). Stiff-chain polymers - Structure, phase-behavior, and properties. *Angew. Chem., Int. Ed. Engl.* 28, 253–267.
- (18) Strobl, G., *The Physics of Polymers*, 3rd ed.; Springer: Berlin, 2007.
- (19) Morgan, P. W. (1977). Synthesis and Properties of Aromatic and Extended Chain Polyamides. *Macromolecules* 10, 1381–1390.
- (20) Kwolek, S. L., Morgan, P., Schaeffgen, J. R., and Gulrich, L. (1977). Synthesis, Anisotropic Solutions, and Fibers of Poly(1,4-benzamide). *Macromolecules* 10, 1390–1396.
- (21) Milner, S. T. (2020). Unified Entanglement Scaling for Flexible, Semiflexible, and Stiff Polymer Melts and Solutions. *Macromolecules* 53, 1314–1325.
- (22) Ballauff, M. (1986). Rigid rod polymers having flexible side chains. 1. Thermotropic pol(1,4-phenylene 2,5-dialkoxyterephthalate)s. *Makromol. Chem., Rapid Commun.* 7, 407–414.
- (23) De Rosa, C., and Auriemma, F. In *Handbook of Polymer Crystallization*, Piorkowska, G. C., E. and Rutledge, Ed., 1st ed.; John Wiley & Sons: Hoboken, New Jersey, 2013; Chapter 2.
- (24) Staudinger, H. (1934). Der Aufbau der hochmolekularen organischen Verbindungen. *Naturwissenschaften* 22, 65–71.
- (25) Pérez-Camargo, R. A., Arandia, I., Safari, M., Cavallo, D., Lotti, N., Soccio, M., and Müller, A. J. (2018). Crystallization of isodimorphic aliphatic random copolyesters: Pseudo-eutectic behavior and double-crystalline materials. *Eur. Polym. J.* 101, 233–247.
- (26) Pérez-Camargo, R. A., Liu, D., G. Cavallo, Wang, D., and Müller, A. J. (2020). Effect of the crystallization conditions on the exclusion/inclusion balance in biodegradable poly(butylene succinate-ran-butylene adipate) copolymers. *Biomacromolecules* 21, 3420–3435.
- (27) Hoffman, J. D., and Lauritzen, J. I. (1961). Crystallization of Bulk Polymers With Chain Folding: Theory of Growth of Lamellar Spherulites. *J. Res. Natl. Bur. Stand. A Phys. Chem.* 65A, 297–336.

-
- (28) Gedde, U. G., *Polymer Physics*, 4th ed.; Kluwer Academic Publishers: Dordrecht, 2001.
- (29) Hu, W., Frenkel, D., and Mathot, V. B. F. (2003). Intramolecular Nucleation Model for Polymer Crystallization. *Macromolecules* *36*, 8178–8183.
- (30) Hu, W. (2018). Growth rate equations of lamellar polymer crystals. *Polymer Crystallization* *1:e25831*.
- (31) Hikosaka, M. (1987). Unified theory of nucleation of folded-chain crystals and extended-chain crystals of linear-chain polymers. *Polymer* *28*, 1257–1264.
- (32) Robelin-Souffaché, E., and Rault, J. (1989). Origin of the Long Period and Crystallinity in Quenched Semicrystalline Polymers. 1. *Macromolecules* *22*, 3581–3594.
- (33) Strobl, G. (2000). From the melt via mesomorphic and granular crystalline layers to lamellar crystallites: A major route followed in polymer crystallization? *Eur. Phys. J. E* *3*, 165–183.
- (34) Iwata, K. (2002). Role of entanglement in crystalline polymers 1. Basic theory. *Polymer* *43*, 6609–6626.
- (35) Strobl, G. (2009). Colloquium: Laws controlling crystallization and melting in bulk polymers. *81*, 1287–1300.
- (36) Stepanow, S. (2014). Kinetic mechanism of chain folding in polymer crystallization. *Phys. Rev. E - Stat. Nonlinear, Soft Matter Phys.* *90*, 1–5.
- (37) Jiang, X., Reiter, G., and Hu, W. (2016). How Chain-Folding Crystal Growth Determines the Thermodynamic Stability of Polymer Crystals. *J. Phys. Chem. B* *120*, 566–571.
- (38) Hong, Y., Koga, T., and Miyoshi, T. (2015). Chain Trajectory and Crystallization Mechanism of a Semicrystalline Polymer in Melt- and Solution-Grown Crystals As Studied Using ^{13}C - ^{13}C Double-Quantum NMR. *Macromolecules* *48*, 3282–3293.
- (39) Luo, C., and Sommer, J.-U. (2016). Role of Thermal History and Entanglement Related Thickness Selection in Polymer Crystallization. *ACS Macro Lett.* *5*, 30–34.
- (40) Strobl, G. (2006). Crystallization and melting of bulk polymers: New observations, conclusions and a thermodynamic scheme. *Prog. Polym. Sci.* *31*, 398–442.
- (41) Luo, C., and Sommer, J.-U. (2014). Frozen Topology: Entanglements Control Nucleation and Crystallization in Polymers. *Phys. Rev. Lett.* *49*, 195702.

- (42) Luo, C., and Sommer, J.-U. (2013). Disentanglements of Linear Polymer Chains Toward Unentangled Crystals. *ACS Macro Lett.* *2*, 31–34.
- (43) Yao, Y., and Chen, Q. In *Annu. Reports NMR Spectrosc.* 1st ed.; 10; Elsevier Ltd.: 2010; Chapter 4, pp 199–224.
- (44) Schulz, M., Seidlitz, A., Kurz, R., Bärenwald, R., Petzold, A., Saalwächter, K., and Thurn-Albrecht, T. (2018). The Underestimated Effect of Intracrystalline Chain Dynamics on the Morphology and Stability of Semicrystalline Polymers. *Macromolecules* *51*, 8377–8385.
- (45) Boyd, R. H. (1985). Relaxation processes in crystalline polymers. *Polymer* *26*, 323–347.
- (46) Schulz, M., Seidlitz, A., Petzold, A., and Thurn-Albrecht, T. (2020). The effect of intracrystalline chain dynamics on melting and reorganization during heating in semicrystalline polymers. *Polymer* *196*, 122441.
- (47) Sisti, L., Totaro, G., and Marchese, P. In *Biodegradable and Biobased Polymers for Environmental and Biomedical Applications*, Kalia, S., and Avérous, L., Eds.; Scrivener Publishing & John Wiley and Sons: Hoboken, 2016; Chapter 7.
- (48) Plate, N. A., and Shibaev, V. P. (1974). Comb-like polymers - Structure and properties. *J. Polymer Sci.: Macromol. Reviews* *8*, 117–253.
- (49) Danke, V., Gupta, G., Reimann, S., Binder, W. H., and Beiner, M. (2018). Structure formation in nanophase-separated systems with lamellar morphology: Comb-like vs. linear precision polymers. *Eur. Polym. J.* *103*, 116–123.
- (50) Danke, V., Gupta, G., Reimann, S., Binder, W. H., and Beiner, M. (2017). Tuning layered superstructures in precision polymers. *J. Phys. Chem. B* *121*, 4583–4591.
- (51) Clauss, J., Schmidt-Rohr, K., Adam, A., Boeffel, C., and Spiess, H. W. (1992). Stiff macromolecules with aliphatic side chains: side-chain mobility, conformation, and organization from 2D solid-state NMR spectroscopy. *Macromolecules* *25*, 5208–5214.
- (52) Babur, T., Gupta, G., and Beiner, M. (2016). About different packing states of alkyl groups in comb-like polymers with rigid backbone. *Soft Matter* *12*, 8093–8097.
- (53) Zheng, W.-Y., Levon, K., Laakso, J., and Oesterholm, J.-E. (1994). Characterization and Solid-State Properties of Processable N-Alkylated Polyanilines in the Neutral State. *Macromolecules* *27*, 7754–7768.

-
- (54) Meille, A. V., Romita, V., Caronna, T., Lovinger, A. J., Catellani, M., and Belobrzecakaja, L. (1927). Influence of Molecular Weight and Regioregularity on the Polymorphic Behavior of Poly(3-decylthiophenes). *Macromolecules* *30*, 7898–7905.
- (55) Levitt, M. H., *Spin Dynamics*, 2nd ed.; John Wiley & Sons: Chichester, 2008.
- (56) Reichert, D., and Saalwächter, K. In *Encyclopedia of Nuclear Magnetic Resonance (NMR Crystallography)*, Harris, R. K., Wasylchen, R. E., and Duer, M. J., Eds., Chichester, 2009.
- (57) de Gennes, P. G. (1971). Reptation of a Polymer Chain in the Presence of Fixed Obstacles. *J. Chem. Phys.* *55*, 572–579.
- (58) Doi, M. (1981). Explanation for the 3.4 power law of viscosity of polymeric liquids on the basis of the tube model. *J. Polym. Sci. B Polym. Lett. Ed.* *19*, 265–273.
- (59) Doi, M. (1983). Explanation for the 3.4 power law of viscosity of polymeric liquids on the basis of the tube model. *J. Polym. Sci. Pol. Phys.* *21*, 667–684.
- (60) Graessley, W. W. (1980). Some phenomenological consequences of the Doi-Edwards theory of viscoelasticity. *J. Polym. Sci. Pol. Phys.* *18*, 27–34.
- (61) de Gennes, P. G. (1976). Dynamics of Entangled Polymer Solutions. I. The Rouse Model. *Macromolecules* *9*, 587–593.
- (62) Viovy, J. L., Rubinstein, M., and Colby, R. H. (1991). Constraint Release in Polymer Melts: Tube Reorganization versus Tube Dilation. *Macromolecules* *24*, 7754–7768.
- (63) Okada, K. N., and Hikosaka, M. In *Handbook of Polymer Crystallization*, Piorkowska, E., and Rutledge, G. C., Eds., 1st ed.; John Wiley & Sons: Hoboken, New Jersey, 2013; Chapter 4.
- (64) Tahsiro, K. In *Handbook of Polymer Crystallization*, Piorkowska, E., and Rutledge, G. C., Eds., 1st ed.; John Wiley & Sons: Hoboken, New Jersey, 2013; Chapter 5.
- (65) Fritzsche, K. J., Mao, K., and Schmidt-Rohr, K. (2017). Avoidance of Density Anomalies as a Structural Principle for Semicrystalline Polymers: The Importance of Chain Ends and Chain Tilt. *Macromolecules* *50*, 1521–1540.
- (66) Martinez-Salazar, J., Barham, P. J., and Keller, A. (1984). Studies on Polyethylene Crystallized at Unusually High Supercoolings: Fold Length, Habit, Growth, Rate, Epitaxy. *J. Polym. Sci. Polym. Phys. Ed.* *22*, 1085–1096.
- (67) Mandelkern, L. (1990). The Structure of Crystalline Polymers. *Acc. Chem. Res.* *23*, 380–386.

- (68) Stack, G. M., Voigt-Martin, I. G., and Mandelkern, L. (1984). Crystallization, Melting, and Morphology of Low Molecular Weight Polyethylene Fractions. *Macromolecules* 17, 1283–1302.
- (69) Voigt-Martin, I. G., Alamo, R., and Mandelkern, L. (1986). Constraint Release in Polymer Melts: Tube Reorganization versus Tube Dilation. *J. Polym. Sci. Polym. Phys. Ed.* 24, 1283–1302.
- (70) Mutter, R., Stille, W., and Strobl, G. (1993). Transition Regimes and Surface Melting in Partially Crystalline Polyethylene: A Raman Spectroscopic Study. *J. Polym. Sci. B Polym. Phys.* 31, 99–105.
- (71) Albrecht, T., and Strobl, G. (1996). Observation of the Early Stages of Crystallization in Polyethylene by Time-Dependent SAXS: Transition from Individual Crystals to Stacks of Lamellae. *Macromolecules* 29, 783–785.
- (72) Kurz, R., Schulz, M., Scheliga, F., Men, Y., Seidlitz, A., Thurn-Albrecht, T., and Saalwächter, K. (2018). Interplay between Crystallization and Entanglements in the Amorphous Phase of the Crystal-Fixed Polymer Poly(ϵ -caprolactone). *Macromolecules* 51, 5831–5842.
- (73) Hikosaka, M. (1990). Unified theory of nucleation of folded-chain crystals (FCCs) and extended-chain crystals (ECCs) of linear-chain polymers: 2. Origin of FCC and ECC. *Polymer* 31, 458–468.
- (74) Anwar, M., Berryman, J. T., and Schilling, T. (2014). Crystal nucleation mechanism in melts of short polymer chains under quiescent conditions and under shear flow. *J. Chem. Phys.* 141, 124910.
- (75) Iwata, K., and Edwards, S. F. (1988). New Entanglement Model of Condensed Linear Polymers: Localized Gauss Integral Model. *Macromolecules* 21, 2901–2904.
- (76) Fischer, E. W. (1967). Das Grenzflächenschmelzen der Kristallite in teilkristallisierten Hochpolymeren. *Kolloid - Z. u. Z. Polymere* 218, 97–114.
- (77) Albrecht, T., and Strobl, G. (1995). Temperature-Dependent Crystalline-Amorphous Structures in Linear Polyethylene: Surface Melting and the Thickness of the Amorphous Layer. *Macromolecules* 28, 5828–5833.
- (78) Mansfield, M. L. (1987). Temperature-Dependent Changes in the Structure of the Amorphous Domains of Semicrystalline Polymers. *Macromolecules* 20, 1384–1393.
- (79) Rieger, J., and Mansfield, M. L. (1989). Comments on "Temperature-Dependent Changes in the Structure of the Amorphous Domains of Semicrystalline Polymers". *Macromolecules* 22, 3810–3812.

-
- (80) Luo, C., and Sommer, J.-U. (2011). Growth Pathway and Precursor States in Single Lamellar Crystallization: MD Simulations. *Macromolecules* 44, 1523–1529.
- (81) Luo, C., Kröger, M., and Sommer, J.-U. (2016). Entanglements and Crystallization of Concentrated Polymer Solutions: Molecular Dynamics Simulations. *Macromolecules* 49, 9017–9025.
- (82) Luo, C., Kröger, M., and Sommer, J.-U. (2016). Molecular dynamics simulations of polymer crystallization under confinement: Entanglement effect. *Polymer* 109, 71–84.
- (83) Pracella, M. In *Handbook of Polymer Crystallization*, Piorkowska, E. and Rutledge, G. C., Ed., 1st ed.; John Wiley & Sons: Hoboken, New Jersey, 2013; Chapter 10.
- (84) Krumme, A., Lehtinen, A., and Viikna, A. (2004). Crystallisation behaviour of high density polyethylene blends with bimodal molar mass distribution 1. Basic characteristics and isothermal crystallisation. *Eur. Polym. J.* 40, 359–369.
- (85) Krumme, A., Lehtinen, A., and Viikna, A. (2004). Crystallisation behaviour of high density polyethylene blends with bimodal molar mass distribution 2. Non-isothermal crystallisation. *Eur. Polym. J.* 40, 371–378.
- (86) Shen, H., Xie, B., Yang, W., and Yang, M. (2013). Non-isothermal crystallization of polyethylene blends with bimodal molecular weight distribution. *Polym. Test.* 32, 1385–1391.
- (87) Zhai, Z., Morthomas, J., Fusco, C., Perez, M., and Lame, O. (2019). Crystallization and Molecular Topology of Linear Semicrystalline Polymers: Simulation of Uni- and Bimodal Molecular Weight Distribution Systems. *Macromolecules* 52, 4196–4208.
- (88) Li, S., and Register, R. A. In *Handbook of Polymer Crystallization*, Piorkowska, E., and Rutledge, G. C., Eds., 1st ed.; John Wiley & Sons: Hoboken, New Jersey, 2013; Chapter 11.
- (89) Alamo, R. G., and Mandelkern, L. (1994). Temperature-Dependent Crystalline-Amorphous Structures in Linear Polyethylene: Surface Melting and the Thickness of the Amorphous Layer. *Thermochim. Acta* 238, 155–201.
- (90) Howard, P. R., and Crist, B. (1989). Unit Cell Dimensions in Model Ethylene-Butene-1 Copolymers. *J. Polym. Sci. B Polym. Phys.* 27, 2269–2282.
- (91) Flory, P. J. (1955). Theory of Crystallization in Copolymers. *Trans. Faraday Soc.* 51, 848–857.

- (92) Basterretxea, A., Gabirondo, E., Flores, I., Etxeberria, A., Gonzalez, A., Müller, A. J., Mecerreyes, D., Coulembier, O., and Sardon, H. (2019). *Macromolecules* 52, 3506–3515.
- (93) Lenz, R. W. (1985). Structure-order relationships in liquid crystalline polyesters. *Pure & Appl. Chem.* 57, 1537–1544.
- (94) Lenz, R. W. (1985). Balancing Mesogenic and Non-mesogenic Groups in the Design of Thermotropic Polyesters. *Faraday Discuss. Chem. Soc.* 79, 21–32.
- (95) Ballauff, M. (1986). Phase Equilibria in Rodlike Systems with Flexible Side Chains. *Macromolecules* 19, 1366–1374.
- (96) Ballauff, M., and Schmidt, G. F. (1987). Rigid rod polymers with flexible side chains, 2. Observation of a novel type of layered mesophase. *Makromol. Chem., Rapid Commun.* 8, 93–97.
- (97) Ballauff, M., and Schmidt, G. F. (1987). Rigid rod polymers with flexible side chains, 3. Structural Investigations on a Novel Layered Mesophase Formed by Thermotropic Poly(1,4-phenylene-2,5-dialkoxy terephthalate)s. *Mol. Cryst. Liq. Cryst.* 147, 163–177.
- (98) Wenzel, M., Ballauff, M., and Wegner, G. (1987). Rigid rod polymers with flexible side chains, 4. Synthesis, structure and phase behaviour of polyimides prepared from pyromellitic anhydride and 2,5-di-n-alkoxy-1,4-phenylene diisocyanates. *Makromol. Chem* 188, 2865–2873.
- (99) Berger, K., and Ballauff, M. (1988). Rigid rod polymers with flexible side chains, 5. Structure and phase behavior of thermotropic Poly(2-n-alkyl-1,4-phenylene terephthalate)s. *Mol Cryst. Liq. Cryst. Inc. Nonlin. Opt.* 157, 109–123.
- (100) Duran, R., Ballauff, M., Wenzel, M., and Wegner, G. (1988). Rigid rod polymers with flexible side chains, 6. Ordered Phases from Solid Solutions of Two-Component Blends as Investigated by Wide-Angle X-ray Scattering. *Macromolecules* 21, 2897–2899.
- (101) Duer, M. J. In *Solid-State NMR Spectroscopy Principles and Application*, Duer, M. J., Ed., 1st ed.; Blackwell Science: Oxford, 2002; Chapter 2.
- (102) deAzevedo, E. R., Hu, W.-G., Bonagamba, T. J., and Schmidt-Rohr, K. (1999). Centerband-Only Detection of Exchange: Efficient Analysis of Dynamics in Solids by NMR. *J. Am. Chem. Soc.* 121, 8411–8412.

-
- (103) Schäler, K., Roos, M., Micke, P., Golitsyn, Y., Seidlitz, A., Thurn-Albrecht, T., Schneider, H., Hempel, G., and Saalwächter, K. (2015). Basic principles of static proton low-resolution spin diffusion NMR in nanophase-separated materials with mobility contrast. *Solid State Nucl. Magn. Reson.* *72*, 50–63.
- (104) Papon, A., Saalwächter, K., Schäler, K., Guy, L., Lequeux, L., and Montes, H. (2011). Low-Field NMR Investigations of Nanocomposites: Polymer Dynamics and Network Effects. *Macromolecules* *44*, 913–922.
- (105) Demco, D. E., Johansson, A., and Tegenfeldt, J. (1995). Proton spin diffusion for spatial heterogeneity and morphology investigations of polymers. *Solid State Nucl. Magn. Reson.* *4*, 13–38.
- (106) Anderson, P. W., and Weiss, P. R. (1953). Exchange Narrowing in Paramagnetic Resonance. *RMP* *25*, 269–276.
- (107) Fedotov, V. D., Chernov, V. M., and Khazanovich, T. N. (1978). Effect of slow molecular motion on damping of transverse nuclear magnetization in amorphous polymers. *Polym. Sci. U. S. S. R.* *20*, 1037–1045.
- (108) Saalwächter, K. (2007). Proton Multiple-Quantum NMR for the study of chain dynamics and structural constraints in polymeric soft materials. *Prog. Nucl. Mag. Reson. Spectrosc.* *51*, 50–63.
- (109) Chávez, F. V., and Saalwächter, K. (2011). Time-Domain NMR Observation of Entangled Polymer Dynamics; Universal Behavior of Flexible Homopolymers and Applicability of the Tube Model. *Macromolecules* *44*, 1549–1559.
- (110) Chávez, F. V., and Saalwächter, K. (2011). Time-Domain NMR Observation of Entangled Polymer Dynamics: Analytical Theory of Signal Functions. *Macromolecules* *44*, 1560–1569.
- (111) Saalwächter, K., Ziegler, K., Spyckerelle, O., Haidar, B., Vidal, A., and Sommer, J.-U. (2003). ^1H multiple-quantum nuclear magnetic resonance investigations of molecular order distributions in poly(dimethylsiloxane) networks: Evidence for a linear mixing law in bimodal systems. *J. Chem. Phys.* *119*, 3468–3482.
- (112) Baum, J., and Pines, A. (1986). NMR studies of clustering in solids. *J. Am. Chem. Soc.* *108*, 7447–7454.
- (113) Mordvinkin, A., and Saalwächter, K. (2017). Microscopic observation of the segmental orientation autocorrelation function for entangled polymer chains. *J. Chem. Phys.* *146*, 094902.

- (114) Mordvinkin, A., and Saalwächter, K. (2018). Erratum: “Microscopic observation of the segmental orientation autocorrelation function for entangled and constrained polymer chain” [J. Chem. Phys. 146, 094902 (2017)]. *J. Chem. Phys.* 148, 089901.
- (115) Duer, M. J. In *Solid-State NMR Spectroscopy Principles and Application*, Duer, M. J., Ed., 2nd ed.; Blackwell Science: Oxford, 2002; Chapter 2.
- (116) Lee, M., and Goldberg, W. I. (1965). Nuclear-Magnetic Resonance Line Narrowing by a Rotating rf Field. *Phys. Rev.* 140, 1261–1271.
- (117) Mote, K. R., Agarwal, V., and Madhu, P. K. (2016). Five decades of homonuclear dipolar broadening in solid-state NMR: Status and outlook. *Prog. Nucl. Magn. Reson. Spectrosc.* 97, 1–39.
- (118) Metz, G., Wu, X., and Smith, S. O. (1994). Ramped-Amplitude Cross Polarization in Magic-Angle-Spinning NMR. *J. Magn. Reson.* 110, 219–277.
- (119) Morris, G. A., and Freeman, R. (1979). Enhancement of nuclear magnetic resonance signals by polarization transfer. *J. Am. Chem. Soc.* 101, 760–762.
- (120) Torchia, D. A. (1978). The measurement of proton-enhanced carbon-13 T1 values by a method which suppresses artifacts. *J. Magn. Reson.* 30, 613–616.
- (121) Raya, J., Perrone, B., Bechinger, B., and Hirschinger, J. (2011). Chemical shift powder spectra obtained by using Rotor-Directed Exchange of Orientations Cross Polarization (RODEO-CP). *Chem. Phys. Lett.* 508, 155–164.
- (122) Kurz, R., Cobo, M. F., deAzevedo, E. R., Sommer, M., Wicklein, A., Thelakkat, M., Hempel, G., and Saalwächter, K. (2013). Avoiding bias effects in NMR experiments for Heteronuclear Dipole-Dipole Coupling Determinations: Principles and Applications to Organic Semiconductor Materials. *Chem. Phys. Chem.* 14, 3146–3155.
- (123) Munowitz, M. G., Griffin, R. G., Bodenhausen, G., and Huang, T. H. (1981). Two-Dimensional Rotational Spin-Echo Nuclear Magnetic Resonance in Solids: Correlation of chemical shift and Dipolar Interactions. *J. Am. Chem. Soc.* 103, 2529–2533.
- (124) deAzevedo, E. R., Saalwächter, K., Pascui, O., de Souza, A. A., Bonagamba, T. J., and Reichert, D. (2008). Intermediate motions as studied by solid-state separated local field NMR experiments. *J. Chem. Phys.* 128, 155–164.
- (125) Hirschinger, J. (2006). A simple analytical model to describe dynamic magic-angle spinning experiments. *Concepts Magn. Reson.*, 28A, 307–320.
- (126) Scheler, U. In *Solid-State NMR Spectroscopy Principles and Application*, Duer, M. J., Ed., 2nd ed.; Blackwell Science: Oxford, 2002; Chapter 10.

-
- (127) Goldman, M., and Shen, L. (1966). Spin-Spin Relaxation in LaF_3 . *Phys. Rev.* *144*, 321–331.
- (128) Kumashiro, K. K., Schmidt-Rohr, K., Murphy III, O. J., Ouellette, K. L., Cramer, W. A., and Thompson, L. K. (1998). A Novel Tool for Probing Membrane Protein Structure: Solid-State NMR with Proton Spin Diffusion and X-Nucleus Detection. *J. Am. Chem. Soc.* *120*, 5043–5051.
- (129) Hsiao, B. S., Zuo, F., Mao, Y., and Schick, C. In *Handbook of Polymer Crystallization*, Piorkowska, E., and Rutledge, G. C., Eds., 1st ed.; John Wiley & Sons: Hoboken, New Jersey, 2013; Chapter 1.
- (130) Kurz, R., Achilles, A., Chen, W., Schäfer, M., Seidlitz, A., Golitsyn, Y., Kressler, J., Paul, W., Hempel, G., Miyoshi, T., Thurn-Albrecht, T., and Saalwächter, K. (2017). Intracrystalline Jump Motion in Poly(ethylene oxide) Lamellae of Variable Thickness: A Comparison of NMR Methods. *Macromolecules* *50*, 3890–3902.
- (131) Schulz, M., Schäfer, M., Saalwächter, K., and Thurn-Albrecht, T. (2021). Intracrystalline chain dynamics as the relevant factor governing lamellar thickness in semicrystalline polymers. *Macromolecules*, submitted.
- (132) Fetters, L. J., Lohse, D. J., and Colby, R. H. In *Physical Properties of Polymers Handbook*, Mark, J. E., Ed., 2nd ed.; Springer: New York, 2007; Chapter 25.
- (133) Seidlitz, A. Einfluss von Kristallisationskinetik und Dynamik im Kristall und in der Schmelze auf die Strukturbildung teilkristalliner Polymere, Ph.D. Thesis, Martin-Luther-Universität Halle Wittenberg, 2016.
- (134) Kurz, R. Charakterisierung von kristalliner und amorpher Phase teilkristalliner Polymere mittels Festkörper NMR, Ph.D. Thesis, Martin-Luther-Universität Halle Wittenberg, 2018.
- (135) Chávez, F. V., and Saalwächter, K. (2010). NMR Observation of Entangled Polymer Dynamics: Tube Model Predictions and Constraint Release. *Phys. Rev. Lett.* *104*, 198305.
- (136) Trutschel, M.-L., Mordvinkin, A., Furtado, F., Willner, L., and Saalwächter, K. (2018). Time-Domain NMR Observation of Entangled Polymer Dynamics: Focus on All Tube-Model Regimes, Chain Center and Matrix Effects. *Macromolecules* *51*, 4108–4117.
- (137) Graessley, W. W., *The entanglement concept in polymer rheology*; Springer: Berlin, Heidelberg, 1974.

- (138) Doi, M. and Edwards, S. F., *The Theory of Polymer Dynamics*; Clarendon Press: Oxford, 1986.
- (139) Ball, R. C., Callaghan, P. T., and Samulski, E. T. (1999). A simplified approach to the interpretation of nuclear spin correlations in entangled polymeric liquids. *J. Chem. Phys.* *106*, 7352–7361.
- (140) Kimmich, R., and Fatkullin, N. In *NMR • 3D Analysis • Photopolymerization*, Abe, A. et al., Eds.; Springer: Berlin, Heidelberg, 2004, pp 1–113.
- (141) Furtado, F., Damron, J., Trutschel, M.-L., Franz, C., Schröter, K., R. C., B., Saalwächter, K., and Panja, D. (2014). NMR Observation of Entangled Polymer Dynamics: Focus on Tagged Chain Rotational Dynamics and Confirmation from a Simulation Model. *Macromolecules* *47*, 256–268.
- (142) Córdova, M. E., Lorenzo, A. T., Müller, A. J., Hoskins, J. N., and Grayson, S. M. (2011). A Comparative Study on the Crystallization Behavior of Analogous Linear and Cyclic Poly(ϵ -caprolactone). *Macromolecules* *44*, 1742–1746.
- (143) Wang, Z., personal communication, 31.01.2020.
- (144) Wang, Z., personal communication, 04.06.2020.
- (145) Wang, Z., personal communication, 18.09.2020.
- (146) Pérez-Camargo, R. A., Fernández-d’Arlas, B., Cavallo, D., Lotti, N., Debuissy, T., Pollet, E., Avérous, L., and Müller, A. J. Tailoring the Structure, Morphology, and Crystallization of Isodimorphic Poly(butylene succinate-*ran*-butylene adipate) Random Copolymers by Changing Composition and Thermal History. *Macromolecules* *50*, 597–608.

Remarks on the format of citations within this thesis (excluding the reprinted articles)

An in-text citation [1000] directly *following* a word, e.g. chemical compound, refers to specifically this (compound), while an in-text citation *preceding* an ”.” (period) refers to the whole sentence [1001]. An citation *after* an ”.” (period) refers to the sentences since the previous citation. This type of referencing is used for longer paraphrased content (multiple sentences), not necessary coinciding with the end of an paragraph. [1002] These types exclude the cases where a citation is used before a ”:” (colon) [1003]: this indicates, that the information following the colon is based on reference [1003]. This also excludes the case where a whole (new) paragraph is introduced, e.g. with ”Meier et al. [1004] summarized ...” or the case of a direct quotation with quotation marks, e.g. ”...” [1004] or Meier et al. [1004] stated that ”...”.

Erklärung

Hiermit versichere ich, die vorliegende Arbeit selbstständig und ohne fremde Hilfe verfasst und keine anderen als die von mir angegebenen Quellen und Hilfsmittel verwendet zu haben. Die den benutzten Werken wörtlich oder inhaltlich entnommenen Stellen habe ich als solche kenntlich gemacht.

Ich erkläre, keine anderweitigen Promotionsversuche unternommen und die vorliegende Dissertation weder in der jetzigen noch in einer anderen Fassung einer anderen wissenschaftlichen Einrichtung vorgelegt zu haben.

Halle (Saale), den

Mareen Schäfer

Acknowledgements

I would like to thank and acknowledge all the people who supported me during my doctoral studies.

Prof. Dr. Kay Saalwächter for the opportunity to work in this interesting field of research and his continuous support and encouragement during my time at the NMR group at the Martin-Luther-Universität Halle-Wittenberg. I am also grateful for the possibility to participate in international conferences and for enabling my research stay at the laboratory of Prof. Dr. Klaus Schmidt-Rohr.

Dr. Tiago Mendes Ferreira and Dr. Günter Hempel for the technical assistance with the NMR spectrometers and the numerous insightful discussions on NMR theory.

Dr. Ricardo Kurz for introducing me to this research project and for explanations regarding the initial experimental setup.

My sincere thanks to **all members of the NMR group** for the comfortable and also often fun atmosphere at work or at private gatherings. A special “thank you” to **Dr. Tiago Mendes Ferreira** and **Mozhdeh Abbasi** for the pleasant office atmosphere.

Prof. Dr. Thomas Thurn-Albrecht (Experimentelle Polymerphysik, MLU Halle-Wittenberg) for the fruitful discussions of our results on polymer crystallization as well as his constructive feedback, further insights and suggestions.

Dr. Albrecht Petzold and Dr. Zefan Wang for our successful collaborative work on diluted PCL samples and the helpful explanations and interpretations of the SAXS results.

My sincere thanks goes to **Martha Schulz**, not only for the constructive and very pleasant collaboration during the last years, but also for further support in the “PhD-life” and entertaining evenings at iRTG workshops and at conferences, which I enjoyed very much.

The collaboration and the interactions with **the Thurn-Albrecht group and its members**, also at various conferences, was delightful—thanks!

Varun Danke (former PhD student at the Fraunhofer IMWS, Halle) for the straightforward collaboration on the studies of comb-like polymers.

Niklas Wallstein for the smooth cooperative work and his help regarding the implementation and analysis of NMR experiments.

Prof. Dr. Klaus Schmidt-Rohr (Brandeis University, Waltham, Massachusetts, USA) for granting me the opportunity to work in his research group.

Dr. Shichen Yuan for the support and help during my stay in the group of Klaus Schmidt-Rohr.

Prof. Dr. Mario Beiner for being my mentor in the graduate school of the iRTG.

Dr. Ann-Kristin Flieger and Dr. Thomas Michael for administrative support and organization of the SFB workshops, soft-skill courses, advanced training modules and the doctoral students seminars.

The funding of the project within the framework of the Deutsche Forschungsgemeinschaft (DFG) SFB/TRR 102 project A01 is highly appreciated.

My sincere thanks goes to **Josef Eichhorn** and **Achim Schaller** for additional proofreading of the thesis.

List of publications

1. R. Kurz, A. Achilles, W. Chen, **M. Schäfer**, A. Seidlitz, Y. Golitsyn, J. Kressler, W. Paul, G. Hempel, T. Miyoshi, T. Thurn-Albrecht and Kay Saalwächter. “Intracrystalline Jump Motion in Poly(ethylene oxide) Lamellae of Variable Thickness: A Comparison of NMR Methods.” *Macromolecules* **50** 3890-3902 (2017)
2. L. Jakisch, M. Garaleh **M. Schäfer**, A. Mordvinkin, K. Saalwächter and F. Böhme. “Synthesis and Structural NMR Characterization of Novel PPG/PCL Conetworks based upon Heterocomplementary Coupling Reactions.” *Macromol. Chem. Phys.* **219** 1700327 (2018)
3. V. Danke, M. Beiner, K. Saalwächter and **M. Schäfer***. “Structure and Dynamics in a Polymorphic Nanophase-Separated Stiff Comblike Polymer.” *Macromolecules* **52** 6943-6952 (2019)
4. **M. Schäfer***, N. Wallstein, M. Schulz, T. Thurn-Albrecht and K. Saalwächter. “Intracrystalline Dynamics in Oligomer-Diluted Poly(Ethylene Oxide).” *Macromol. Chem. Phys.* **221** 1900393 (2020)
5. Y. Qiao, M. Schulz, H. Wang, R. Cheng, **M. Schäfer**, T. Thurn-Albrecht and Y. Men. “Hierarchical structure of polybutene-1 in crystal blocks resulting from the form II to I solid-to-solid transition as revealed by small-angle X-ray scattering.” *Polymer* **195** 122425 (2020)
6. **M. Schäfer***, S. Yuan, A. Petzold, R. A. Pérez-Camargo, A. J. Müller, T. Thurn-Albrecht, K. Saalwächter and K. Schmidt-Rohr. “Asymmetric co-unit inclusion in statistical copolyesters.” *Macromolecules* **54** 835-845 (2021)
7. M. Schulz, **M. Schäfer**, K. Saalwächter and T. Thurn-Albrecht. “Lamellar thickness in semicrystalline polymers as a result of the competition between crystal growth and intracrystalline chain dynamics.” submitted to *Macromolecules* (2021)

Curriculum vitae

Personal data

Family name:	Schäfer
First name:	Mareen
Date of birth:	29.07.1991
Place of birth:	Regensburg
Nationality:	German

Education

03/2016 - present	Doctural studies Martin-Luther Universtität Halle-Wittenberg Institute of Physics (NMR group) Supervisor: Kay Saalwächter
10/2013 - 02/2016	Master studies in Physics (Master of Science) Universität Regensburg
10/2010 - 09/2013	Bachelor studies in Physics (Bachelor of Science) Universität Regensburg
09/07/2010	Fachgebundene Hochschulreife Staatliche Fachoberschule und Berufsoberschule Regensburg

Halle (Saale), den

Mareen Schäfer